

# Low-complexity stochastic modeling of wall-bounded shear flows

A DISSERTATION  
SUBMITTED TO THE FACULTY OF THE GRADUATE SCHOOL  
OF THE UNIVERSITY OF MINNESOTA  
BY

Armin Zare

IN PARTIAL FULFILLMENT OF THE REQUIREMENTS  
FOR THE DEGREE OF  
Doctor of Philosophy

Professor Mihailo R. Jovanović, advisor

December 2016

Low-complexity stochastic modeling  
of wall-bounded shear flows

Copyright © 2016

by

Armin Zare

ALL RIGHTS RESERVED

*To Samira, my parents, and my sister*

# Acknowledgements

Many people have contributed to my success over the years, and I cannot adequately express my deep appreciation for their help, support and encouragement.

First and foremost, I would like to thank my Ph.D. advisor, Professor Mihailo Jovanović, for giving me the opportunity to embark on this journey as a graduate student, for his constant support and guidance, and for his generosity and patience in teaching me all I needed to know. Most importantly, he taught me how to be critical of myself, in conducting research and in presenting my work. His diligence and passion has always been a source of inspiration and motivation, driving me to not only be a better researcher, but also a better person with higher professional skills. I would also like to extend my sincerest appreciation for his flexibility, open-mindedness, and true understanding of my concerns during my graduate studies.

I would like to thank Professors Georgiou, Haupt, Longmire, and Nichols for serving on my doctoral committee. I have received invaluable comments and feedback from all of them. Professor Georgiou has been exceptionally kind and supportive from my early days in Minnesota, and even before I came to the US. It has been a privilege to collaborate with him on several publications that I am very proud of. His scholarly attitude, maturity, unique personality and broad knowledge have critically influenced how I think, write, and communicate my work. Professor Nichols has been truly supportive and generous in sharing his ideas and providing great feedback on my research. I look forward to many fruitful discussions and collaborations with him in the near future. I am also grateful to my excellent teachers at the University of Minnesota, Professors Giannakis, Longmire, Luo, Mahesh, Saad, Salapaka, and Seiler.

I was extremely lucky to interact with Professors Chernyshenko, Hwang, and Schmid during my visit to Imperial College, London, in 2015. I greatly benefited from their vision, ideas, and insights. Many thanks to Professor Chernyshenko and his student Sacha Ghebali for being exceptional hosts during this visit. I would also like to thank Professor Moin for his interest in our work and for providing the opportunity for me and my advisor to participate in the 2014 and 2016 CTR Summer Programs from which I immensely benefited.

Throughout my graduate studies, I had the opportunity to collaborate with several individuals. I would especially like to extend my gratitude to Dr. Yongxin Chen, Dr. Philipp Hack, Christian Grussler, and Wei Ran for being great research collaborators and true friends.

It has been an honor to get to know and work with my colleagues in the controls research group: Drs. Rashad Moarref, Fu Lin, and Binh Lieu who played a critical role in my transition to the U of M when I joined in 2010, and the rest of my office mates Dr. Yongxin Chen, Dr. Neil Dhingra, Dr. Xiaofan Wu, Sepideh Hassan Moghaddam, Wei Ran, Dongsheng Ding, Hamza Farooq, Dr. Kaoru Yamamoto, Dr. Lipeng Ning, Dr. Xianhua Jiang, Harshad Deshmane, Eric Dahlberg, and Professor Donatello Materassi who made my life in Minnesota all the more enjoyable and interesting. I am eternally grateful to Dr. Rashad Moarref who served as my main mentor during the first few years at the U of M and has been a great source of advice throughout the years. I would also like to thank Dr. Binh Lieu for teaching me how to run numerical simulations of fluid flows and for always taking the initiative in hosting many memorable events.

I am incredibly fortunate to have met many wonderful individuals, the group of friends that I often refer to as my second family, particularly: Mehdi Lamee, Behnaz Forootaninia, Farnaz Forootaninia, Meisam Razaviyayn, Maral Mousavi, Morteza Mardani, Maziar Sanjabi, Pardees Azodanloo, Karen Khatamifard, Sepideh Hassan Moghaddam, Mostafa Toloui, Mohammadreza Nasiri, Roushanak Navvab, Mojtaba Kadkhodaei, Ali Ghoreyshi, Sepehr Salehi, Nazila Haratipour, Mehrdad Hairani, Pooya Rezaei, Saghar Sadeghpour, Neil Dhingra, Xiaofan Wu, Kaoru Yamamoto, Sayan Ghosal, Rohit Gupta, Sei Zhen Khong, Milad Siami, Rojin Hajian, Elnaz Ziaie, Fatemeh Sheikholeslami, Mohsen Mahmoodi, Mohsen Saadat, Fazel Zare Bidoki, Shahrouz Takyar, Shayesteh Kiaei, and all of the passionate members of the Palangs soccer team.

My warmest thanks go to my family, the source of my confidence and pride. They have always carried me through the lows and celebrated the highs. They have sacrificing so much for me to be the person I am today and I am thankful for each and everyone of them. I am indebted to my parents, Ziba and Shahram, and to my little sister, Azin, for their infinite love and support. I am grateful to my wonderful wife, Samira, for her unconditional love and patience throughout my Ph.D. studies, and for preserving my sanity, especially in my final year. Finally, I would like to thank my grandparents, aunts, uncles, cousins, and family-in-laws for their encouragement and love over the years.

# Abstract

Turbulent flows are ubiquitous in nature and they appear in many engineering applications. Transition to turbulence, in general, increases skin-friction drag in air/water vehicles compromising their fuel-efficiency and reduces the efficiency and longevity of wind turbines. While traditional flow control techniques combine physical intuition with costly experiments, their effectiveness can be significantly enhanced by control design based on low-complexity models and optimization. In this dissertation, we develop a theoretical and computational framework for the low-complexity stochastic modeling of wall-bounded shear flows.

Part I of the dissertation is devoted to the development of a modeling framework which incorporates data-driven techniques to refine physics-based models. We consider the problem of completing partially known sample statistics in a way that is consistent with underlying stochastically driven linear dynamics. Neither the statistics nor the dynamics are precisely known. Thus, our objective is to reconcile the two in a parsimonious manner. To this end, we formulate optimization problems to identify the dynamics and directionality of input excitation in order to explain and complete available covariance data. For problem sizes that general-purpose solvers cannot handle, we develop customized optimization algorithms based on alternating direction methods. The solution to the optimization problem provides information about critical directions that have maximal effect in bringing model and statistics in agreement.

In Part II, we employ our modeling framework to account for statistical signatures of turbulent channel flow using low-complexity stochastic dynamical models. We demonstrate that white-in-time stochastic forcing is not sufficient to explain turbulent flow statistics and develop models for colored-in-time forcing of the linearized Navier-Stokes equations. We also examine the efficacy of stochastically forced linearized NS equations and their parabolized equivalents in the receptivity analysis of velocity fluctuations to external sources of excitation as well as capturing the effect of the slowly-varying base flow on streamwise streaks and Tollmien-Schlichting waves.

In Part III, we develop a model-based approach to design surface actuation of turbulent channel flow in the form of streamwise traveling waves. This approach is capable of identifying the drag reducing trends of traveling waves in a simulation-free manner. We also use the stochastically forced linearized NS equations to examine the Reynolds number independent effects of spanwise wall oscillations on drag reduction in turbulent channel flows. This allows us to extend the predictive capability of our simulation-free approach to high Reynolds numbers.

# Contents

|   |               |
|---|---------------|
| <b>Acknowledgements</b>   | <b>iv</b>     |
| <b>Abstract</b>   | <b>vi</b>     |
| <b>List of Figures</b>  | <b>xi</b>     |
| <b>1 Introduction</b>   | <b>1</b>      |
| 1.1 Low-complexity modeling of turbulent flows . . . . .  | 4             |
| 1.2 Matrix completion problems . . . . .  | 5             |
| 1.2.1 Nuclear norm formulation . . . . .  | 6             |
| 1.2.2 $r^*$ norm formulation . . . . .  | 7             |
| 1.2.3 Matrix factorization formulation . . . . .  | 8             |
| 1.2.4 Structured matrix completion problems . . . . .   | 9             |
| 1.3 Flow control . . . . .  | 10            |
| 1.4 Dissertation structure . . . . .  | 12            |
| 1.5 Preview of main results and contributions . . . . .   | 13            |
| <br><b>I Low-complexity modeling of partially available second-order statistics: theory and efficient optimization algorithms</b> | <br><b>16</b> |
| <b>2 Low-complexity modeling of partially available second-order statistics</b>   | <b>17</b>     |
| 2.1 Introduction . . . . .  | 17            |
| 2.2 Linear stochastic models and state statistics . . . . .   | 18            |
| 2.2.1 Algebraic constraints on admissible covariances . . . . .   | 19            |
| 2.2.2 Power spectrum of input process . . . . .   | 20            |
| 2.2.3 Stochastic control interpretation . . . . .   | 22            |
| 2.3 Covariance completion and model complexity . . . . .  | 23            |
| 2.3.1 The signature of $Z$ . . . . .  | 24            |
| 2.3.2 Decomposition of $Z$ into $BH^* + HB^*$ . . . . .   | 27            |
| 2.3.3 Covariance completion problem . . . . .   | 28            |

|          |  |           |
|----------|--|-----------|
| <b>3</b> | <b>Optimization algorithms for structured covariance completion problems</b>       | <b>31</b> |
| 3.1      | Introduction . . . . .   | 31        |
| 3.2      | Rearrangement of constraints . . . . .   | 32        |
| 3.3      | SDP formulation and the dual problem . . . . .                                     | 33        |
| 3.4      | Alternating Minimization Algorithm (AMA) . . . . .                                 | 35        |
| 3.4.1    | Solution to the $X$ -minimization problem (3.7a) . . . . .                         | 36        |
| 3.4.2    | Solution to the $Z$ -minimization problem (3.7b) . . . . .                         | 36        |
| 3.4.3    | Lagrange multiplier update . . . . .   | 37        |
| 3.4.4    | Choice of step-size for the dual update (3.7c), (3.7d) . . . . .                   | 37        |
| 3.4.5    | Computational complexity . . . . .   | 38        |
| 3.4.6    | AMA as a proximal gradient on the dual . . . . .                                   | 38        |
| 3.4.7    | Convergence analysis . . . . .   | 41        |
| 3.5      | Alternating Direction Method of Multipliers (ADMM) . . . . .                       | 43        |
| 3.5.1    | Computational complexity . . . . .   | 45        |
| 3.5.2    | Accelerated ADMM . . . . .   | 45        |
| 3.6      | Computational experiments . . . . .  | 46        |
| <b>4</b> | <b>The use of the <math>r^*</math> heuristic in covariance completion problems</b> | <b>52</b> |
| 4.1      | Introduction . . . . .   | 52        |
| 4.2      | Problem Formulation . . . . .  | 53        |
| 4.3      | Low-rank approximation . . . . .   | 56        |
| 4.3.1    | Preliminaries . . . . .  | 56        |
| 4.3.2    | Convex reformulation . . . . .   | 58        |
| 4.4      | Examples . . . . .   | 59        |
| 4.4.1    | Two-dimensional heat equation . . . . .  | 59        |
| 4.4.2    | Mass-spring-damper system . . . . .  | 62        |
| <b>5</b> | <b>Perturbation of system dynamics and the covariance completion problem</b>       | <b>67</b> |
| 5.1      | Introduction . . . . .   | 67        |
| 5.2      | Background . . . . .   | 68        |
| 5.3      | Covariance completion via minimum energy control . . . . .                         | 72        |
| 5.3.1    | Identification of essential input channels . . . . .                               | 72        |
| 5.3.2    | Polishing step . . . . .   | 74        |
| 5.4      | An example . . . . .   | 74        |
| <b>6</b> | <b>Conclusions and future directions</b>   | <b>80</b> |

|            |  |            |
|------------|--|------------|
| <b>II</b>  | <b>Stochastic modeling of wall-bounded shear flows</b>                               | <b>82</b>  |
| <b>7</b>   | <b>Stochastic modeling of turbulent channel flow</b>                                 | <b>83</b>  |
| 7.1        | Introduction . . . . .   | 83         |
| 7.2        | Linearized Navier-Stokes equations and flow statistics . . . . .                     | 89         |
| 7.2.1      | The Navier-Stokes equations and second-order statistics . . . . .                    | 89         |
| 7.2.2      | Stochastically forced linearized NS equations . . . . .                              | 91         |
| 7.2.3      | Second-order statistics of the linearized Navier-Stokes equations . . . . .          | 92         |
| 7.3        | Completion of partially known turbulent flow statistics . . . . .                    | 94         |
| 7.3.1      | Covariance completion problem . . . . .  | 94         |
| 7.3.2      | Filter design: dynamics of stochastic forcing . . . . .                              | 96         |
| 7.4        | Application to turbulent channel flow . . . . .                                      | 100        |
| 7.4.1      | Necessity for the colored-in-time forcing . . . . .                                  | 101        |
| 7.4.2      | Reproducing available and completing unavailable velocity correlations . . . . .     | 101        |
| 7.4.3      | Verification in stochastic linear simulations . . . . .                              | 107        |
| 7.4.4      | Reproducing statistics at higher Reynolds numbers . . . . .                          | 110        |
| 7.5        | Spatio-temporal analysis of the linear model . . . . .                               | 110        |
| 7.5.1      | Spatio-temporal frequency responses . . . . .  | 114        |
| 7.5.2      | Temporal two-point correlations . . . . .  | 119        |
| <b>8</b>   | <b>Stochastic modeling of spatially evolving flows</b>                               | <b>123</b> |
| 8.1        | Introduction . . . . .   | 123        |
| 8.2        | Background . . . . .   | 125        |
| 8.2.1      | Stochastically forced linearized NS equations . . . . .                              | 125        |
| 8.2.2      | Second-order statistics and computation of energy amplification . . . . .            | 126        |
| 8.3        | Local and global analysis of stochastically forced linearized NS equations . . . . . | 126        |
| 8.3.1      | Parallel Blasius boundary layer flow subject to free-stream turbulence . . . . .     | 127        |
| 8.3.2      | Global analysis of stochastically forced linearized NS equations . . . . .           | 128        |
| 8.4        | Stochastically forced linear parabolized stability equations . . . . .               | 129        |
| 8.4.1      | Linear parabolized stability equations . . . . .                                     | 131        |
| 8.4.2      | Streamwise evolution of a two-dimensional TS wave . . . . .                          | 132        |
| <b>9</b>   | <b>Conclusions and future directions</b>   | <b>137</b> |
| <b>III</b> | <b>Flow control</b>  | <b>143</b> |
| <b>10</b>  | <b>Turbulent drag reduction by streamwise traveling waves</b>                        | <b>144</b> |
| 10.1       | Introduction . . . . .   | 144        |
| 10.2       | Problem formulation . . . . .  | 145        |

|           |  |            |
|-----------|--|------------|
| 10.2.1    | Governing equations . . . . .  | 145        |
| 10.2.2    | Navier-Stokes equations augmented with turbulent viscosity . . .   | 146        |
| 10.3      | Turbulent mean velocity in flow with $\nu_{T0}$ . . . . .  | 147        |
| 10.4      | Dynamics of velocity fluctuations . . . . .  | 150        |
| 10.4.1    | Linearized Navier-Stokes equations . . . . .   | 150        |
| 10.4.2    | Second-order statistics of velocity fluctuations . . . . .   | 151        |
| 10.4.3    | Influence of fluctuations on turbulent viscosity and skin-friction<br>drag . . . . .                                   | 152        |
| 10.4.4    | Results: turbulent drag reduction and net efficiency . . . . .   | 153        |
| <b>11</b> | <b>Model-based analysis of the effect of spanwise wall oscillations on drag<br/>reduction at high Reynolds numbers</b> | <b>155</b> |
| 11.1      | Introduction . . . . .   | 155        |
| 11.2      | Background . . . . .   | 156        |
| 11.2.1    | Second-order statistics of velocity fluctuations in the presence of<br>control . . . . .                               | 158        |
| 11.2.2    | Turbulent viscosity model and drag reduction . . . . .   | 159        |
| 11.3      | High Reynolds number trends . . . . .  | 160        |
| 11.3.1    | Turbulent energy spectrum of uncontrolled flow . . . . .   | 160        |
| 11.3.2    | Effect of control on the production and dissipation of turbulent<br>kinetic energy at high Reynolds numbers . . . . .  | 160        |
| 11.4      | Drag reduction in higher Reynolds numbers flows . . . . .  | 162        |
| <b>12</b> | <b>Conclusions and future directions</b>   | <b>167</b> |
|           | <b>References</b>  | <b>170</b> |
|           | <b>Appendix A.</b>   | <b>194</b> |
| A.1       | Proof of Lemma 1 . . . . .   | 194        |
| A.2       | Proof of Proposition 2 . . . . .   | 195        |
| A.3       | Proof of Lemma 2 . . . . .   | 196        |
| A.4       | Proof of Lemma 3 . . . . .   | 196        |
| A.5       | Proof of Lemma 4 . . . . .   | 198        |
|           | <b>Appendix B.</b>   | <b>201</b> |
| B.1       | Change of coordinates . . . . .  | 201        |
| B.2       | Interpretation of the matrix $H$ solving (7.12) . . . . .  | 202        |
| B.3       | The role of the regularization parameter $\gamma$ . . . . .  | 202        |

# List of Figures

|     |  |    |
|-----|--|----|
| 1.1 | Turbulence increases the fuel consumption of (a) submarines, (b) passenger aircrafts and (c) ships. It also reduces the energy efficiency of (d) wind farms and (e) tidal turbines. . . . .  | 2  |
| 1.2 | Visualization of a flat-plate boundary-layer flow. The flow direction is from left to right. (a) Laminar flow; (b) Transition to turbulent flow. . .   | 2  |
| 1.3 | The number of full scale wing tests in Boeing's aircraft design procedure over three decades. . . . .  | 3  |
| 1.4 | (a) An array of distributed hot-film shear-stress sensors and wall-deformation actuators for feedback flow control; (b) Sketch of a riblet-mounted surface; (c) Sketch of a superhydrophobic surface; (d) Wall transpiration in the form of streamwise traveling wave; (e) Spanwise wall oscillations. . .             | 11 |
| 2.1 | (a) A cascade connection of an LTI system with a linear filter that is designed to account for the sampled steady-state covariance matrix $X$ ; (b) An equivalent feedback representation of the cascade connection in (a). 20   |    |
| 3.1 | The saturation operator $\mathcal{T}_\tau$ is related to the soft-thresholding operator $\mathcal{S}_\tau$ via identity (3.10). . . . .  | 37 |
| 3.2 | Mass-spring-damper system with $n$ masses. . . . .   | 46 |
| 3.3 | Partially available correlations of the MSD system. . . . .  | 47 |
| 3.4 | (a) The $\gamma$ -dependence of the relative error (percents) between the solution $X$ to (2.18) and the true covariance $\Sigma_{xx}$ for the MSD system with 50 masses; (b) singular values of the solution $Z$ to (2.18) for $\gamma = 2.2$ . . . .   | 48 |
| 3.5 | Performance of AMA <sub>BB</sub> for the MSD system with 50 masses, $\gamma = 2.2$ , $\epsilon_1 = 0.005$ , and $\epsilon_2 = 0.05$ . (a) The dual objective function $J_d(Y_1, Y_2)$ of (2.18); (b) the duality gap, $ \Delta_{\text{gap}} $ ; and (c) the primal residual, $\Delta_p$ . . .                          | 49 |
| 3.6 | Convergence curves showing performance of ADMM ( $\circ$ ) and AMA with ( $-$ ) and without ( $\triangle$ ) BB step-size initialization vs. (a) the number of iterations; and (b) solve times for the MSD system with 50 masses and $\gamma = 2.2$ . Here, $J_d^*$ is the value of the optimal dual objective. . . . . | 49 |
| 3.7 | Diagonals of (a) position and (b) velocity covariances for the MSD system with 50 masses; Solid black lines show diagonals of $\Sigma_{xx}$ and red circles mark solutions of optimization problem (2.18). . . . .   | 50 |

|     |   |    |
|-----|---|----|
| 3.8 | Time evolution of the variance of the MSD system's state vector for twenty realizations of white-in-time forcing to (2.9b). The variance averaged over all simulations is marked by the thick black line. . . . .   | 51 |
| 3.9 | The true covariance $\Sigma_{pp}$ of the MSD system and the covariance $X_{pp}$ resulting from linear stochastic simulations of (2.9b). Available one-point correlations of the position of masses used in (2.18) are marked along the main diagonals. . . . .  | 51 |
| 4.1 | A cascade connection of an LTI system with a linear filter that is designed to account for the sampled steady-state covariance matrix $X$ . . . . .   | 55 |
| 4.2 | Discretized mesh on the unit square. The input enters the state equations through designated sides. . . . .   | 60 |
| 4.3 | Interpolated colormap of the true steady-state covariance $\Sigma_{xx}$ of the discretized heat equation. Available correlations used in (4.7) and (4.8) are marked by black lines. . . . .   | 61 |
| 4.4 | (a) The $r$ -dependence of the relative Frobenius norm error (percents) between the solution $X$ to (4.7) and the true covariance $\Sigma_{xx}$ for the discretized 2D heat equation discretized using 16 points. (b) The $\gamma$ -dependence of the relative error between the solution to (4.8) and the true covariance. . . . . | 62 |
| 4.5 | The recovered state covariance matrix of the heat equation resulting from problem (4.7) (a, b), and problem (4.8) (c, d). (a) $r = 1$ ; (b) $r = 2$ ; (c) $\gamma = 0$ ; (d) $\gamma = 8.46$ . . . . .  | 63 |
| 4.6 | The steady-state covariance matrices of the (a) position $\Sigma_{pp}$ , and (b) velocity $\Sigma_{vv}$ , of masses in the MSD system with $n = 20$ masses. Available one-point correlations used in problems (4.7) and (4.8) are marked by black lines. . . . .  | 64 |
| 4.7 | (a) The $r$ -dependence of the relative error between the solution $X$ to (4.7) and the true covariance $\Sigma_{xx}$ for the MSD system with $n = 20$ masses. (b) The $\gamma$ -dependence of the error between the solution to (4.8) and the true covariance. . . . .   | 64 |
| 4.8 | The recovered covariance matrices of position and velocity in the MSD system with $n = 20$ masses resulting from problem (4.7) (a, b, c, d), and problem (4.8) (e, f, g, h). (a, b) $r = 1$ ; (c, d) $r = 10$ ; (e, f) $\gamma = 0$ ; (g, h) $\gamma = 0.19$ . . . . .  | 66 |
| 5.1 | (a) A cascade connection of an LTI system with a linear filter that is designed to account for the sampled steady-state covariance matrix $X$ ; (b) An equivalent feedback representation of the cascade connection in (a). . . . .   | 71 |
| 5.2 | Geometry of a three-dimensional pressure-driven channel flow. . . . .   | 75 |
| 5.3 | Structure of the output covariance matrix $\Phi$ . Available one-point velocity correlations in the wall-normal direction represent diagonal entries of the blocks in the velocity covariance matrix $\Phi$ . . . . .   | 76 |

|     |  |     |
|-----|--|-----|
| 5.4 | True covariance matrices of the output velocity field (a, c, e, g), and covariance matrices resulting from solving optimization problem (5.9) with $\gamma = 10^4$ followed by a polishing step (b, d, f, h). (a, b) Streamwise $\Phi_{11}$ , (c, d) wall-normal $\Phi_{22}$ , (e, f) spanwise $\Phi_{33}$ , and (g, h) the streamwise/wall-normal $\Phi_{12}$ two-point correlation matrices at $(k_x, k_z) = (0, 1)$ . The one-point correlation profiles that are used as problem data in (5.9) are marked by black lines along the main diagonals. . . . . | 77  |
| 5.5 | The $\gamma$ -dependence of the relative Frobenius norm error between the true state covariance $\Sigma_{xx}$ and the solution $X$ to (5.9) before ( $\circ$ ) and after ( $\Delta$ ) polishing, for the channel flow with $N = 11$ collocation points in channel height. . . . .  | 78  |
| 5.6 | Retained columns of the input matrix $B$ as $\gamma$ increases. A black dot indicates the presence of the corresponding input channel. The top row ( $\gamma = 0$ ) shows the use of all channels, and the bottom row ( $\gamma = 10^4$ ) shows the least number of channels required for accounting for the observed statistics. . . . .  | 78  |
| 5.7 | The $\gamma$ -dependence of the number of retained input channels after solving problem (5.9) in the case of iterative reweighting ( $\circ$ ) and in the case of constant weights ( $\Delta$ ). . . . .   | 79  |
| 7.1 | A spatio-temporal filter is designed to provide colored stochastic input to the linearized NS equations in order to reproduce partially available second-order statistics of turbulent channel flow. . . . .   | 88  |
| 7.2 | Geometry of a pressure-driven turbulent channel flow. . . . .  | 90  |
| 7.3 | Structure of the matrix $\Phi$ in optimization problem (7.19). At each pair of wavenumbers $\mathbf{k} = (k_x, k_z)$ , available second-order statistics are given by one-point correlations in the wall-normal direction, i.e., the diagonal entries of the blocks in the velocity covariance matrix $\Phi$ . The data is obtained from <a href="http://torroja.dmt.upm.es/channels/data/">http://torroja.dmt.upm.es/channels/data/</a> . . . . .   | 96  |
| 7.4 | (a) Spatio-temporal filter (7.20) is designed to provide colored stochastic input to the linearized NS equations (7.6) in order to reproduce partially available second-order statistics of turbulent channel flow. The dynamics of this cascade connection are governed by the evolution model (7.24); (b) An equivalent reduced-order representation of (7.24) is given by (7.27). . . . .   | 98  |
| 7.5 | An equivalent feedback representation of the cascade connection in figure 7.4a. . . . .  | 99  |
| 7.6 | Positive eigenvalues of the matrix $A(\mathbf{k})X_{\text{dns}}(\mathbf{k}) + X_{\text{dns}}(\mathbf{k})A^*(\mathbf{k})$ , for channel flow with $R_\tau = 186$ and $\mathbf{k} = (2.5, 7)$ , indicate that turbulent velocity covariances cannot be reproduced by the linearized NS equations with white-in-time stochastic forcing; cf. equation (7.11). . . . .   | 102 |

|      |  |     |
|------|--|-----|
| 7.7  | (a) Correlation profiles of normal and (b) shear stresses resulting from DNS of turbulent channel flow with $R_\tau = 186$ (–) and from the solution to (7.19); $uu$ ( $\circ$ ), $vv$ ( $\square$ ), $ww$ ( $\triangle$ ), $-uv$ ( $\diamond$ ). We observe perfect matching of all one-point velocity correlations that result from integration over wall-parallel wavenumbers. Note: plot markers are sparse for data presentation purposes and do not indicate grid resolution. . . . .  | 103 |
| 7.8  | Pre-multiplied one-dimensional energy spectrum of streamwise (a,b), wall-normal (c,d), spanwise (e,f) velocity fluctuations, and the Reynolds stress co-spectrum (g,h) in terms of streamwise (left) and spanwise (right) wavelengths and the wall-normal coordinate (all in inner units). Color plots: DNS-generated spectra of turbulent channel flow with $R_\tau = 186$ . Contour lines: spectra resulting from the solution to (7.19). . . . .  | 104 |
| 7.9  | Covariance matrices resulting from DNS of turbulent channel flow with $R_\tau = 186$ (left plots); and the solution to optimization problem (7.19) with $\gamma = 300$ (right plots). (a, b) Streamwise $\Phi_{uu}$ , (c, d) wall-normal $\Phi_{vv}$ , (e, f) spanwise $\Phi_{ww}$ , and the streamwise/wall-normal $\Phi_{uv}$ two-point correlation matrices at $\mathbf{k} = (2.5, 7)$ . The one-point correlation profiles that are used as problem data in (7.19) are marked by black lines along the main diagonals. . . . . | 105 |
| 7.10 | Quadrant II of the spanwise covariance matrices resulting from (a) DNS of turbulent channel flow with $R_\tau = 186$ , and (b) the solution to optimization problem (7.19) with $\gamma = 300$ at $\mathbf{k} = (2.5, 7)$ . The horizontal black lines mark $y^+ = 15$ . (c) Comparison of the two-point correlation $\Phi_{ww}$ at $y^+ = 15$ with other wall-normal locations: DNS (–); solution of (7.19) ( $\triangle$ ). . . . .  | 106 |
| 7.11 | Singular values of the solution $Z$ to (7.19) in turbulent channel flow with $R_\tau = 186$ , $\mathbf{k} = (2.5, 7)$ , and $N = 127$ for (a) $\gamma = 300$ ; and (b) $\gamma = 10^4$ . . . . .   | 107 |
| 7.12 | Time evolution of fluctuation's kinetic energy for twenty realizations of the forcing to the modified linearized dynamics (7.27) with $R_\tau = 186$ and $\mathbf{k} = (2.5, 7)$ ; the energy averaged over all simulations is marked by the thick black line. . . . .   | 108 |
| 7.13 | Normal stress profiles in the (a) streamwise, (b) wall-normal, (c) spanwise direction, and (d) shear stress profile resulting from DNS of turbulent channel flow with $R_\tau = 186$ at $\mathbf{k} = (2.5, 7)$ (–) and stochastic linear simulations ( $\circ$ ). . . . .   | 109 |
| 7.14 | Normalized normal (left) and shear (right) stress profiles resulting from DNS (–) and from the solution to (7.19) with $\gamma = 300$ at $\lambda_x^+ = 1000$ and $\lambda_z^+ = 100$ (in inner units); $uu$ ( $\circ$ ), $vv$ ( $\square$ ), $ww$ ( $\triangle$ ), $-uv$ ( $\diamond$ ). (a, b) $R_\tau = 547$ ; (c, d) $R_\tau = 934$ ; (e, f) $R_\tau = 2003$ . . . . .   | 111 |
| 7.15 | Singular values of the matrix $Z$ resulting from the solution to (7.19) with $\gamma = 300$ at $R_\tau = 549$ ( $\circ$ ), $934$ ( $\diamond$ ), and $2003$ ( $\square$ ). . . . .   | 112 |

|      |  |     |
|------|--|-----|
| 7.16 | (a) Power spectral density $\Pi_{\mathbf{v}}(\mathbf{k}, \omega)$ and (b) worst-case amplification $G_{\mathbf{v}}(\mathbf{k}, \omega)$ as a function of temporal frequency $\omega$ in turbulent channel flow with $R_\tau = 186$ and $\mathbf{k} = (2.5, 7)$ , resulting from the linearized NS model (7.6) (black curve), an eddy-viscosity-enhanced linearized NS model (blue curve), and the modified linearized dynamics (7.27) (red curve).   | 114 |
| 7.17 | The one-dimensional energy density $E_{\mathbf{v}\mathbf{v}}$ as a function of $y^+$ and $c$ computed using the linearized NS equations (7.6) (a, d), an eddy-viscosity-enhanced linearized NS model (b, e), and the modified dynamics (7.27) (c, f) for turbulent channel flow with $R_\tau = 186$ . Plots (d-f) show the energy density normalized by its maximum value over $y$ for fixed values of $c$ . The colors are in logarithmic scale. The turbulent mean velocity is marked by the black curve in (d-f). | 115 |
| 7.18 | Contribution of the response directions $\tilde{\xi}_j$ to the total energy in turbulent channel flow with $R_\tau = 2003$ and $\mathbf{k} = (1, 6)$ . The modified dynamics (7.27) are driven by harmonic excitation with temporal frequency (a) $\omega = 21.4$ and (b) $\omega = 26.5$ .  | 117 |
| 7.19 | Spatial structure of the principal response directions of the frequency response $T_{\mathbf{v}\mathbf{w}}(\mathbf{k}, \omega)$ in turbulent channel flow with $R_\tau = 2003$ , $\mathbf{k} = (1, 6)$ , at $t = 0$ for (a,b) $\omega = 21.4$ and (c,d) $\omega = 26.5$ . (a,c) Isosurfaces of the streamwise velocity; red and blue colors denote regions of high and low velocity at 60% of their largest values. (b,d) Spatial structure of the streamwise velocity (color plots) and vorticity (contour lines).  | 118 |
| 7.20 | Spatial structure of the principal response of the operator $B(\mathbf{k})T_f(\mathbf{k}, \omega)$ in turbulent channel flow with $R_\tau = 2003$ , $\mathbf{k} = (1, 6)$ , at $t = 0$ for (a,b) $\omega = 21.4$ and (c,d) $\omega = 26.5$ . (a,c) Isosurfaces of the streamwise velocity; red and blue colors denote regions of high and low velocity at 60% of their largest values. (b,d) Spatial structure of the streamwise component of the response (color plots) and vorticity (contour lines).              | 120 |
| 7.21 | (a) The steady-state autocovariance $\Phi_{uu}(\mathbf{k}, \tau)$ resulting from the modified dynamics (7.27) for turbulent channel flow with $R_\tau = 186$ and $\mathbf{k} = (2.5, 7)$ . (b) The same quantity plotted at $y^+ = 15$ .   | 121 |
| 7.22 | (a) Estimates of the streamwise convection velocity for $\mathbf{k} = (2.5, 7)$ computed using (7.36) ( $\circ$ ) and (7.37) ( $\triangle$ ) as a function of wall distance $y^+$ for turbulent channel flow with $R_\tau = 186$ . The mean velocity profile is plotted for comparison ( $-$ ). (b) Enlargement of the same plot for $y^+ < 40$ .  | 122 |
| 8.1  | Geometry of a transitional boundary layer flow subject to stochastic forcing.  | 125 |
| 8.2  | Plots of $\log_{10}(E(\mathbf{k}))$ in the Blasius boundary layer flow with $Re_0 = 400$ subject to white-in-time stochastic excitation in different wall-normal regions; (a) $y_1 = 0$ , $y_2 = 5$ (b) $y_1 = 5$ , $y_2 = 10$ in equation (8.5).  | 128 |

|      |   |     |
|------|---|-----|
| 8.3  | Principal modes with $k_z = 0.4$ , resulting from excitation in the vicinity (a,c,e) ( $y_1 = 0$ and $y_2 = 5$ in (8.5)) and away from the wall (b,d,f) ( $y_1 = 5$ and $y_2 = 10$ in (8.5)). (a,b) Streamwise velocity components; (c,d) streamwise velocity at $z = 0$ ; (e,f) $y$ - $z$ slice of streamwise velocity (color plots) and vorticity (contour lines) at $x = 1150$ . . . . .                         | 130 |
| 8.4  | Amplitude of TS waves at $\omega = 0.0344$ in a flat-plate boundary layer flow; nonlinear PSE (solid), linear PSE without forcing (dashed), linear PSE with white forcing ( $\Delta$ ), and linear PSE with white, but $x$ -dependent forcing designed using the procedure explained in Section 8.4.2 ( $\circ$ ). . .  | 133 |
| 8.5  | Velocity covariance matrices at $x = 2800$ resulting from (a,c) simulation of nonlinear PSE, and (b,d) from propagation of equation (8.7) in Blasius boundary layer flow with TS mode initialization. (a,b) The streamwise correlation matrix $X_{v_1 v_1}$ , and (c,d) the streamwise/wall-normal cross correlation matrix $X_{v_1 v_2}$ . . . . .   | 135 |
| 8.6  | Relative error in matching the amplitude of streamwise velocity (solid) and in matching the state covariance $X(x)$ (dashed) using the linear PSE with $x$ -dependent white stochastic forcing in the spatial evolution of a 2D TS wave with $\omega = 0.0344$ . . . . .  | 136 |
| 8.7  | The amplitude of the streamwise component of a 2D TS waves with $\omega = 0.0344$ at (a) $x = 1840$ and (b) $x = 2800$ , which results from nonlinear PSE (solid) and linear PSE with $x$ -dependent stochastic forcing (dashed). . . . .   | 136 |
| 9.1  | (a) Nonlinear NS equations as a feedback interconnection of the linearized dynamics with the nonlinear term; (b) Stochastically-driven linearized NS equations with low-rank state-feedback modification. The two representations can be made equivalent, at the level of second-order statistics, by proper selection of $B$ and $C_f$ . . . . .   | 138 |
| 9.2  | Partitioning the state in (7.27) as $\psi = (v, \eta)$ , and conformably the forcing $B\mathbf{w}$ as $(f_v, f_\eta)$ , the term $BC_f$ in (7.27) modifies the Orr-Sommerfeld, Squire, and coupling operators into $\tilde{A}_{11}$ , $\tilde{A}_{22}$ , and $\tilde{A}_{21}$ , respectively. It also introduces an additional feedback term $\tilde{A}_{12}$ . . . . .   | 140 |
| 9.3  | For the linearized dynamics of fluctuations around turbulent mean velocity, the appropriate forcing is sought to reproduce partially available velocity correlations and complete the statistical signature of the turbulent flow field. Completed second-order statistics can then be brought into the mean flow equations in order to give turbulent mean velocity and provide equilibrium configuration. . . . . | 141 |
| 10.1 | (a) Pressure driven turbulent channel flow. (b) Boundary actuation of blowing and suction along the walls. . . . .  | 146 |

|      |   |     |
|------|---|-----|
| 10.2 | Second-order correction to the skin-friction drag $D_2$ as a function of traveling wave speed $c$ and frequency $\omega_x$ : (a) upstream traveling waves; and (b) downstream traveling waves. Predictions are obtained using the solution to (10.6)-(10.7) with turbulent viscosity determined by (10.5). . .  | 148 |
| 10.3 | Drag variation, $\Delta D = D - D_0$ , as a function of wave amplitude $\alpha$ for an upstream traveling wave with $c = -2$ and $\omega_x = 0.5$ . Predictions are obtained from the solution to (10.6)-(10.7) with turbulent viscosity determined by (10.5) using terms up to a second order in $\alpha$ ( $\circ$ ), fourth order in $\alpha$ ( $\nabla$ ), and Newton's method (solid curve). . . . .   | 151 |
| 10.4 | Drag in a turbulent channel flow obtained from high-fidelity simulations with $R_\tau = 186$ subject to an upstream traveling wave ( $c = -2$ , $\omega_x = 0.5$ ) at three wave amplitudes, $\alpha = 0.01$ (blue), $\alpha = 0.05$ (red), and $\alpha = 0.125$ (green). The black dots denote the drag computed using the model-based framework of Section 10.4. Also shown are the laminar drag (dashed line) and turbulent drag in the absence of control (black solid line). . . . . | 154 |
| 11.1 | (a) Pressure driven turbulent channel flow, and (b) channel flow subject to spanwise wall oscillations of amplitude $\alpha$ and period $T$ . . . . .   | 157 |
| 11.2 | Premultiplied energy spectrum of uncontrolled flow from DNS of turbulent channel flow in terms of streamwise (left) and spanwise (right) wavelengths and the wall-normal coordinate (all in inner units) at (a, b) $R_\tau = 186$ , (c, d) $R_\tau = 547$ , (e, f) $R_\tau = 934$ , and (g, h) $R_\tau = 2003$ . . . .  | 161 |
| 11.3 | Ratio of contribution to kinetic energy production to bulk production. As the Reynolds number increases, contribution to the production of kinetic energy shifts from structures that lie in the near-wall region to those that lie farther away from the wall and in the logarithmic region. . . . .   | 162 |
| 11.4 | Premultiplied second-order correction to the kinetic energy spectrum of velocity fluctuations in turbulent channel flow subject to spanwise wall oscillations with period $T^+ = 100$ ; $k_x k_2(y, k_x)$ (left) and $k_z k_2(y, k_z)$ (right). (a, b) $R_\tau = 186$ , (c, d) $R_\tau = 547$ , (e, f) $R_\tau = 934$ , and (g, h) $R_\tau = 2003$ . . . . .  | 163 |
| 11.5 | Premultiplied second-order correction to the dissipation of kinetic energy in turbulent channel flow subject to spanwise wall oscillations with period $T^+ = 100$ ; $k_x \epsilon_2(y, k_x)/R_\tau^2$ (left) and $k_z \epsilon_2(y, k_z)/R_\tau^2$ (right). (a, b) $R_\tau = 186$ , (c, d) $R_\tau = 547$ , (e, f) $R_\tau = 934$ , and (g, h) $R_\tau = 2003$ . . . . .   | 164 |
| 11.6 | Turbulent drag reduction normalized by $\alpha^2$ at $R_\tau = 934$ (black), $R_\tau = 2003$ (blue), and $R_\tau = 4000$ (green) in terms of period of oscillations $T^+$ . . . . .   | 165 |
| 12.1 | Block diagram representing the various steps involved in the simulation-free approach for determining the effect of control on skin-friction drag in turbulent flows. . . . .   | 169 |
| B.1  | The $\gamma$ -dependence of (a) the relative error (B.8); and (b) the rank of the matrix $Z$ resulting from (7.19) for turbulent channel flow with $R_\tau = 186$ and $\mathbf{k} = (2.5, 7)$ . . . . .   | 203 |

# Chapter 1

## Introduction

A growing awareness of the global energy crisis has motivated vigorous research on fuel-efficient vehicles and renewable energy generation, such as wind and tidal energy harvesting. While much progress has been made in alternative energy development, turbulence has presented a major obstacle. Turbulence, in general, increases skin-friction drag in air and water vehicles compromising their fuel-efficiency [1, 2]. It also reduces efficiency and longevity of turbines in wind and tidal energy generation. It is thus of critical importance to understand the physics of turbulent flows and incorporate this knowledge in the design of vehicles and turbine blades.

Turbulent flows are at the center of many key processes in nature and engineering applications. As viscous stresses are overcome by the fluids inertia and the Reynolds number<sup>1</sup> increases, smooth and ordered (laminar) motion becomes complex and disordered (turbulent); see figure 1.2. In this process, which is known as transition to turbulence, velocity and pressure fluctuations undergo rapid variations with a broad range of spatial and temporal scales and the motion becomes inherently three dimensional and unsteady. In boundary layers, large fluctuations caused by turbulence lead to an increase in the dissipation of kinetic energy. This increases resistance to motion in turbulent boundary layers relative to laminar boundary layers. While in applications such as air transportation or wind power generation it is desired to suppress turbulence for the purpose of drag reduction, other applications necessitate its promotion for the purpose of mixing chemical species or preventing separation [3]. In both scenarios, a fundamental understanding of the physics of turbulent flows is critical in developing efficient flow control strategies.

---

<sup>1</sup>In fluid mechanics, the Reynolds number is a dimensionless quantity that represents the ratio of inertial to viscous forces.

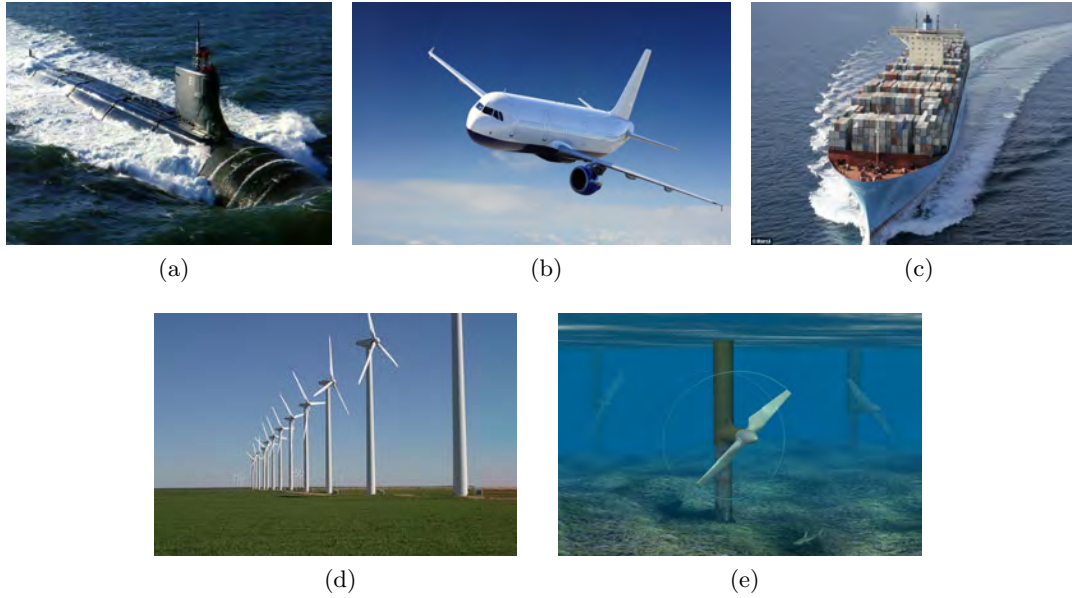


Figure 1.1: Turbulence increases the fuel consumption of (a) submarines, (b) passenger aircrafts and (c) ships. It also reduces the energy efficiency of (d) wind farms and (e) tidal turbines.

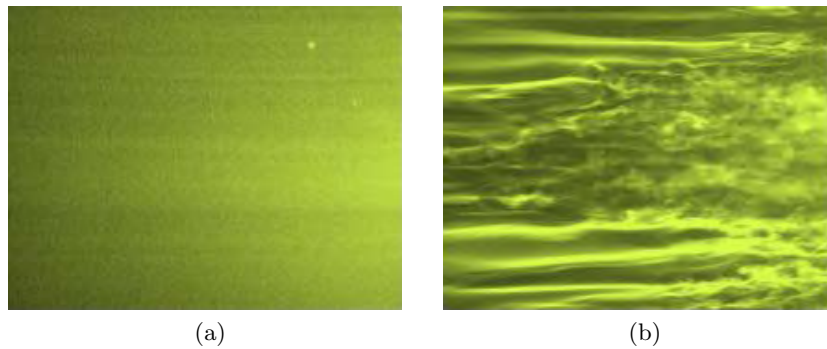


Figure 1.2: Visualization of a flat-plate boundary-layer flow [4]. The flow direction is from left to right. (a) Laminar flow; (b) Transition to turbulent flow.

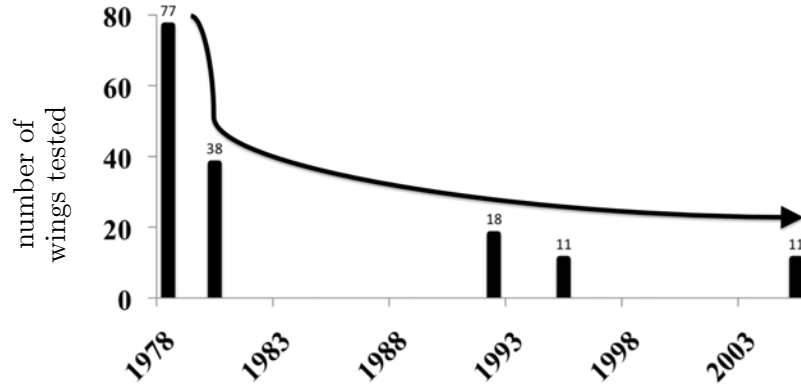


Figure 1.3: The number of full scale wing tests in Boeing's aircraft design procedure over three decades.

In the late 1970's, Boeing built and tested over 70 prototype wings in the design and test procedure for the 767. These full scale wind tunnel tests were not only costly but they significantly delayed the design and manufacturing process. With the rise of computational fluid mechanics and supercomputers, numerical simulations were incorporated into the early design stages [3]. This brought the number of full scale wing tests down to 11 by 1995. However, the limitations of numerical simulations and the absence of reliable turbulence models have caused this trend to plateau; see figure 1.3. Large-eddy simulation is rapidly advancing in its modeling and implementation, but the computational cost for external flows at high Reynolds numbers is still too high for it to be incorporated into aerodynamic design [5]. Without a tractable model to capture the complex nature of turbulence, current practice is largely empirical, and relies on numerical simulations and experiments in an attempt to mitigate turbulence. Although these offer valuable insights into the performance of control strategies, they are costly, time-consuming, and not amenable to systematic controller design.

In this dissertation, we utilize tools from systems theory, fluid mechanics and optimization to develop low-complexity models that capture the complex dynamics of turbulent flows in a way that is tractable for analysis, optimization, and control design. The remainder of this introductory chapter is organized as follows. In Section 1.1, we briefly overview various aspects of low-complexity modeling for turbulent flows. In Section 1.2, we provide a preliminary discussion on matrix completion problems. In Section 1.3, we discuss different classes of flow control strategies. In Section 1.4, we provide an outline of the dissertation. Finally, a preview of our main results and contributions is provided in Section 1.5.

## 1.1 Low-complexity modeling of turbulent flows

Turbulence modeling involves the development of mathematical models that approximate the physical behavior of turbulent flows and is a key element in computational fluid dynamics. A shared quality among notable turbulence models is their simplicity and agreement with physical intuition. An ideal model is commonly described as one that requires the least amount of complexity to capture the essence of the relevant physics [6]. Turbulence is an inherently three dimensional and time dependent phenomenon. Therefore, an enormous amount of information is necessary to describe all details of a turbulent flow. However, a complete time history over all spatial coordinates for every flow property is rarely required. The level of complexity of a model qualitatively scales with the sufficient amount of detail required in the turbulent flow application. It is thus important to identify the relevant properties that must be captured by the mathematical model.

In recent years, due to the advent of advanced measurement techniques and the availability of parallel computing resources, experimentally and numerically generated data sets are becoming increasingly available for a wide range of flow configurations and Reynolds numbers. An accurate statistical description of turbulent flows may provide insights into flow physics and will be instrumental in model-based control design for suppressing or promoting turbulence. Thus, it is increasingly important to understand how structural and statistical features of turbulent flows can be embedded in models of low-complexity that are suitable for analysis, optimization, and control design.

Nonlinear dynamical models of wall-bounded shear flows that are based on the Navier-Stokes equations typically have a large number of degrees of freedom. This makes them unsuitable for analysis and control synthesis. On the other hand, the existence of coherent structures in turbulent wall-bounded shear flows [7–9] has inspired the development of data-driven techniques for reduced-order modeling of the Navier-Stokes equations. These include proper orthogonal decomposition (POD) [10–12], balanced POD [13, 14], Koopman modes [15–18], dynamic mode decomposition [19–21], and low-order Galerkin models [22–25]. However, in all of these modeling schemes, control actuation and sensing may significantly alter the identified modes. This introduces nontrivial challenges for model-based control design [26, 27].

In contrast, linearization of the Navier-Stokes equations around the mean velocity gives rise to models that are well-suited for analysis and synthesis using tools of modern robust control. These tools allow the designer to ensure satisfactory performance even when the real physical system deviates from the model used for control design. Furthermore, when driven by stochastic excitation, such models are capable of qualitatively and quantitatively replicating structural features of both transitional [28–30] and turbulent [31–35] wall-bounded shear flows of Newtonian fluids. The utility of such tools

extends to more complex flows and geometries including flows of non-Newtonian viscoelastic fluids [36–40], multiphase flows at low Reynolds numbers [41], and high-speed aeroacoustic flows associated with turbulent jets [42].

In this dissertation, we develop low-complexity stochastic dynamical models that are based on the linearized Navier-Stokes equations and are statistically consistent with experimental measurements and the result of numerical simulations. In our modeling framework, complexity is quantified by the number of degrees of freedom in the linearized evolution model that are directly influenced by stochastic excitation sources. We develop models for colored-in-time stochastic forcing using a maximum entropy formulation together with a regularization that serves as a proxy for rank minimization. Effectively, our method provides a low-rank modification to the generator of the linearized Navier-Stokes dynamics around the turbulent mean velocity. Our modeling framework relies heavily on tools from convex optimization. It is also closely related to the field of low-rank matrix completion in that it allows for the completion of unavailable statistics in a way that is consistent with the linearized dynamics. Due to this close relationship, we provide a brief overview of matrix completion problems in the next section.

A value of our method is that it provides a data-driven refinement of models that originate from first principles. Our method captures complex dynamics in a way that is tractable for analysis, optimization and control design. While not intended to eliminate the need for high-fidelity numerical simulations and experiments, low-complexity models are anticipated to significantly reduce the overall cost and the time of design and validation.

## 1.2 Matrix completion problems

The low-rank matrix completion problem considers the recovery of an unknown low-rank matrix from only a subset of its entries. In many modern applications, due to experimental/numerical limitations or even the large size of datasets, it is often the case that data matrices are only partially known. Moreover, low-rank models have demonstrated utility in many applications for the purpose of extracting useful information from “big data”. As a result, the matrix completion problem has attracted a significant amount of attention in recent years with applications in recommendation systems (e.g. the Netflix Prize competition) [43, 44], compressive sensing [45–48], global positioning in sensor networks [49–51], phase retrieval [52], system identification [53, 54], computer vision [55, 56], multi-class learning in machine learning [57, 58], robust spectral compressive sensing [59], and many other areas of research [60, 61]. It is also closely related to robust principal component analysis [62–65], non-negative matrix factorization [66], and the tensor completion problem [67, 68].

The problem of completing a partially observed low-rank matrix can be expressed as the following non-convex feasibility problem

$$\begin{aligned} & \text{find} && Z \in \mathbb{R}^{m \times n} \\ & \text{subject to} && \text{rank}(Z) \leq r, \\ & && Z_{ij} = M_{ij}, \quad (i, j) \in \mathcal{I}, \end{aligned} \tag{1.1}$$

where  $\mathcal{I}$  denotes the set of indices of the known entries in the true matrix  $M$ . Since it may be difficult to handle the constraint set in (1.1), the following two reformulations can be considered:

$$\begin{aligned} & \underset{Z}{\text{minimize}} && \text{rank}(Z) \\ & \text{subject to} && Z_{ij} = M_{ij}, \quad (i, j) \in \mathcal{I}, \end{aligned} \tag{1.2}$$

which penalizes the violation of the first constraint in (1.1), and

$$\begin{aligned} & \underset{Z}{\text{minimize}} && \|\mathcal{P}_{\mathcal{I}}(M - Z)\|_F^2 \\ & \text{subject to} && \text{rank}(Z) \leq r \end{aligned} \tag{1.3}$$

which penalizes the violation of the second constraint in (1.1). Here,  $\mathcal{P}_{\mathcal{I}}$  denotes a projection onto the set of indices represented by  $\mathcal{I}$ . Since the rank function is a discrete function and is thus intractable, various studies have considered reformulations of problems (1.2) and (1.3), which can be classified by how they deal with the rank function: nuclear norm approximation or matrix factorization. The nuclear norm formulation provides a convex approximation and can be solved to global optima, whereas the matrix factorization formulation encodes the low-rankness explicitly through the product of two smaller matrices but is non-convex. While most theoretical developments for the matrix completion problem are based on the nuclear norm formulation [45–48, 69], big data applications are generally based on matrix factorization [44]. Surprisingly, in many numerical experiments algorithms for the non-convex matrix factorization formulation can exactly recover the unknown low-rank matrix. Moreover, a number of studies have established theoretical guarantees for low-rank matrix recovery using the matrix factorization formulation [70, 71]. We next briefly summarize these two approaches.

### 1.2.1 Nuclear norm formulation

Recent studies have demonstrated that the minimization of the nuclear norm (i.e., the sum of the singular values)

$$\|Z\|_* := \sum_i \sigma_i(Z),$$

represents a good proxy for rank minimization [45, 72, 73]. Based on this, problem (1.2) can be relaxed into the following nuclear norm minimization

$$\begin{aligned} & \underset{Z}{\text{minimize}} && \|Z\|_* \\ & \text{subject to} && Z_{ij} = M_{ij}, \quad (i, j) \in \mathcal{I}. \end{aligned} \tag{1.4}$$

For  $M \in \mathbb{R}^{n \times n}$ , it has been shown that if  $\mathbf{card}(\mathcal{I}) \geq cn^{1.2} \text{rank}(Z) \log(n)$ , where  $\mathbf{card}(\mathcal{I})$  is the cardinality of  $\mathcal{I}$  (number of observations) and  $c$  is a constant, then with high probability the solution to (1.4) is a solution to (1.2) [45]. In addition, it has been shown that problem (1.4) recovers the lowest rank solution [73]. In other words, one cannot find a matrix of lower rank with entries matching the partial observations denoted by  $\mathcal{I}$ .

When the entries denoted by  $\mathcal{I}$  are not precisely known, a variation of (1.4) can be considered to address noisy matrix completion [60]

$$\begin{aligned} & \underset{Z}{\text{minimize}} && \|Z\|_* \\ & \text{subject to} && \sum_{(i,j) \in \mathcal{I}} (Z_{ij} - M_{ij})^2 \leq \epsilon. \end{aligned} \tag{1.5}$$

It has been shown that the reconstruction error for noisy matrix completion is proportional to the initial observation error [60].

Problems (1.4) and (1.5) can be reformulated as a semidefinite programs (SDP) and solved to global optima by standard SDP solvers for small-size problems. For larger problems, first-order algorithms that rely on the singular value thresholding algorithm [74] and several variants of the proximal gradient method [75, 76] have been proposed. While the linear convergence of these algorithms has been established [77, 78], the per-iteration cost, which requires either exact or inexact singular value decomposition, is still high making these algorithms rather slow. Another drawback of these algorithms is that they require storage of large  $m$  by  $n$  matrices.

### 1.2.2 $r^*$ norm formulation

Recently, various benefits and applications of the so-called “ $r^*$  norm” (also called “ $k$ -support norm”), as a natural extension of the nuclear norm, have been demonstrated [79–86]. In particular, its relation with the optimal rank  $r$  approximation under convex constraints has been investigated [79, 85]. When the magnitudes of unknown entries are significantly smaller than that of the known ones, the nuclear norm often creates regions of large entries which deviate from the ground truth. In such cases, the  $r^*$  norm has shown to be more suitable for the purpose of matrix completion, especially

if the objective is to penalize both the rank and the Frobenius norm of the unknown matrix [85, 86].

For  $Z \in \mathbb{R}^{m \times n}$  and  $1 \leq r \leq q := \min\{m, n\}$ . The  $r$  norm of the matrix  $Z$

$$\|Z\|_r := \sqrt{\sum_{i=1}^r \sigma_i^2(Z)}$$

is unitarily-invariant and its dual-norm is the  $r^*$  norm

$$\|Z\|_{r^*} := \max_{\|X\|_r \leq 1} \langle Z, X \rangle.$$

It also holds that

- $\|Z\|_1 \leq \dots \leq \|Z\|_q = \|Z\|_F = \|Z\|_{q^*} \leq \dots \leq \|Z\|_{1^*}$
- $\text{rank}(Z) \leq r$  if and only if  $\|Z\|_r = \|Z\|_F = \|Z\|_{r^*}$ ,

where  $\|\cdot\|_F$  denotes the Frobenius norm. Based on this, problem (1.2) can be relaxed into the following  $r^*$  norm minimization

$$\begin{aligned} & \underset{Z}{\text{minimize}} && \|Z\|_{r^*} \\ & \text{subject to} && Z_{ij} = M_{ij}, \quad (i, j) \in \mathcal{I}. \end{aligned}$$

Here, the  $r^*$  norm adds an additional layer of flexibility and can play the role of a tuning parameter. Interestingly, it has also been shown that  $r$  need not be an integer and that for particular applications (see Chapter 4) sweeping over real-valued  $r \geq 1$  can potentially improve the quality of completion without adding to the rank of the solution [85–87].

### 1.2.3 Matrix factorization formulation

Problem (1.3), which penalizes the violation of the second constraint in (1.1), can be rewritten as

$$\underset{X, Y}{\text{minimize}} \quad \|\mathcal{P}_{\mathcal{I}}(M - XY^T)\|_F^2 \quad (1.6)$$

where  $X \in \mathbb{R}^{m \times r}$  and  $Y \in \mathbb{R}^{n \times r}$ . This formulation uncovers the matrix  $Z = XY^T$  with rank no more than  $r$ . In addition, an alternative formulation has been proposed which regulates the norms of  $X$  and  $Y$

$$\underset{X, Y}{\text{minimize}} \quad \|\mathcal{P}_{\mathcal{I}}(M - XY^T)\|_F^2 + \lambda (\|X\|_F^2 + \|Y\|_F^2). \quad (1.7)$$

This can be obtained by maximum a posteriori (MAP) estimation under a certain probabilistic model of the low-rank matrix [88].

In the matrix factorization approach, the low-rank requirement is automatically fulfilled by decomposing the rank  $r$  matrix  $Z$  into smaller matrices  $X$  and  $Y$ . Problem (1.7) is a non-convex fourth-order polynomial optimization problem, which is NP-hard. However, by exploiting the structure of the problem, standard gradient methods in conjunction with alternating minimization methods [44, 89, 90] or stochastic gradient descent [44, 91–94] can be used to efficiently obtain the optimal solution. These methods have less storage requirements and smaller per-iteration computational costs. Empirical studies have shown that these algorithms work very well for the matrix factorization approach. However, apart from a few cases [70, 71, 95], theoretical guarantees for exact recovery are rather underdeveloped.

#### 1.2.4 Structured matrix completion problems

The focus of this section has so far been on the recovery of low-rank matrices based on independently sampled entries. Another line, relevant to classes of covariance completion problems that arise in our modeling framework (cf. Section 2), considers problems where a subset of the rows and columns of an approximately low-rank matrix are observed and the goal is to reconstruct the whole matrix based on the observed data. Such problems are denominated structured matrix completion problems.

The covariance completion problem that arises from our modeling framework aims at the recovery of a covariance matrix based on a structured subset of observed statistics. We use the nuclear norm as a convex surrogate to the rank function. As previously mentioned, the nuclear norm is the convex envelope of the rank function over the unit ball  $\|Z\|_2 \leq 1$  and in conjunction with incoherence conditions has been utilized to provide theoretical guarantees for standard matrix completion problems [73]. However, these theoretical results do not apply to the more structured observation model associated with our optimization framework. Consequently, direct application of existing matrix completion results yields pessimistic bounds on the number of observations.

In the covariance completion problem, even though only a small subset of highly structured observations are available, our numerical experiments show reasonable recovery of state covariances. As will be discussed in the following chapters, such high recovery is not possible without incorporating the physics of the linearized dynamics as a structural constraint into the optimization framework.

### 1.3 Flow control

As mentioned in Section 1.1, a fundamental understanding of the physics of turbulent flows is critical in developing efficient flow control strategies. Flow control strategies are devised to either mitigate the unfavorable effects of turbulence, e.g., large skin-friction drag, or to promote turbulence and they can be classified into two main categories of feedback and sensorless control strategies.

The advent of micro-electro-mechanical systems (MEMS) technology has enabled the fabrications of integrated circuits with the necessary micro-sensors, control logic and actuators that can be mounted on the surface of air/water vehicles as well as wind/tidal turbines [96–99]. The relevant flow quantities such as pressure and shear stresses are measured by sensors and the flow is actuated by wall-deformation actuators and compliant surfaces via a feedback rule; see figure 1.4a. This allows for the actuation of small eddies that reside close to the solid surface and are responsible for turbulent drag.

Despite recent advances in the area of MEMS, the extremely small spatial and temporal scales of flow fluctuations at high Reynolds numbers has hindered the utility of feedback control strategies in turbulent flow applications [1, 100]. A more feasible alternative is to consider sensorless flow control strategies that are commonly inspired by nature [101] and rely on our understanding of the fundamental flow physics. Examples of such control strategies are riblet-mounted [102] and superhydrophobic (super water repellent) surfaces [103]; see figures 1.4b and 1.4c. The skin of sharks is textured with riblet-shaped denticles, which help them swim with reduced friction [104]; similarly, the water repellent properties of lotus leaves have motivated the design of superhydrophobic surface coatings [103]. In aerospace applications, a self-adhesive plastic film with V-shaped riblets, manufactured by 3M, was applied over the fuselage and the wings of an Airbus A320 aircraft, and a net drag reduction of about 2% was reported [105]. In this dissertation, we touch upon the design of two other sensorless schemes: wall transpiration in the form of streamwise traveling waves and spanwise wall oscillations; see figures 1.4d and 1.4e. Instead of actuating the flow, sensorless control strategies modify the geometrical properties of the flow. As a result they inhibit the motion of eddies by preventing them from coming very close to the surface and thereby influence the exchange of energy between the flow and the surface. This ultimately leads to a reduction in skin-friction drag.

In the past two decades, many studies have focused on model-based flow control design using techniques from linear systems theory [33, 106–110]. In Part III, we develop a model-based approach to designing streamwise traveling waves for turbulent drag reduction in channel flow. This approach is capable of identifying the drag reducing trends of traveling waves in a simulation-free manner. We also use the stochastically forced linearized Navier-Stokes equations to examine the Reynolds number independent effects of spanwise wall oscillations on drag reduction in turbulent channel flows. This

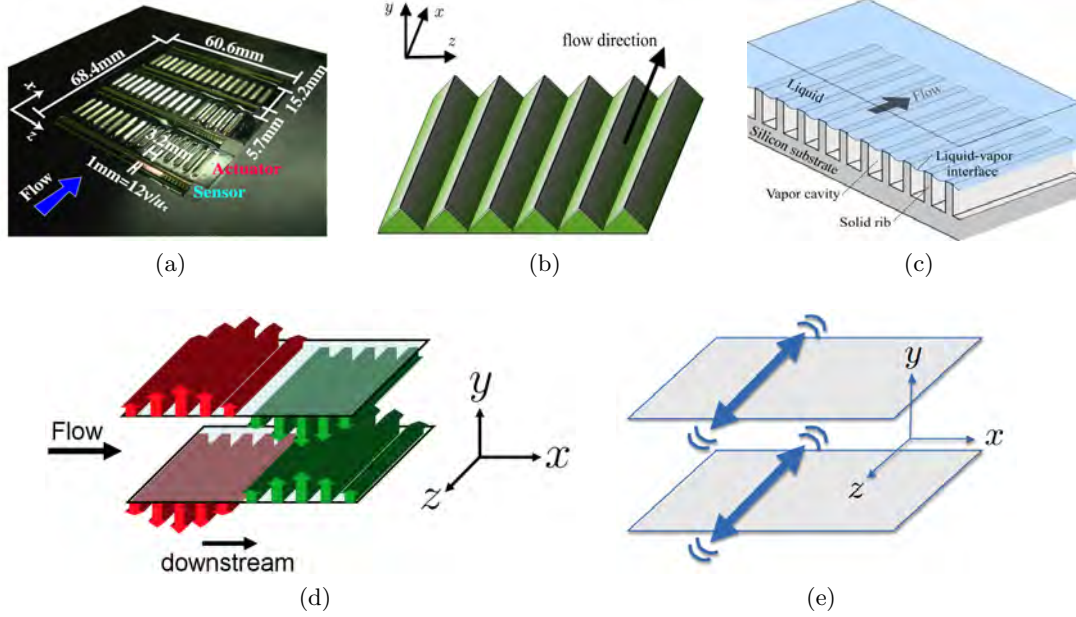


Figure 1.4: (a) An array of distributed hot-film shear-stress sensors and wall-deformation actuators for feedback flow control [96]; (b) Sketch of a riblet-mounted surface; (c) Sketch of a superhydrophobic surface; (d) Wall transpiration in the form of streamwise traveling waves; (e) Spanwise wall oscillations.

allows us to extend the predictive capability of our approach to high Reynolds numbers.

## 1.4 Dissertation structure

This dissertation is organized into three parts and two appendices. Each part contains individual chapters that are self-contained and describe various projects that were carried out in my graduate studies. At the end of each part, the main contributions are summarized and future research directions are discussed.

Part I of the dissertation is devoted to the theoretical and algorithmic development of low-complexity models that account for partially observed second-order statistics. In Chapter 2, we consider the problem of completing partially known sample statistics in a way that is consistent with the underlying stochastically driven linear dynamics. The theoretical developments of this chapter lead to the formulation of a covariance completion optimization problem whose solution provides spectral information about

critical directions that have maximal effect in bringing model and statistics in agreement. In Chapter 3, we develop efficient customized optimization algorithms for solving the covariance completion problem. In Chapter 4, we examine the utility of the  $r^*$  norm approximation in improving the quality of covariance completion relative to the nuclear norm formulation. In Chapter 5, we provide an alternative approach to the covariance completion problem based on low-rank dynamical perturbations to the underlying stochastically driven linear dynamics. In Chapter 6, we summarize the main contributions of Part I and discuss extensions and future research directions.

Part II is devoted to the low-complexity modeling of transitional and turbulent shear flows. In Chapter 7, we utilize the modeling framework developed in Part I for the stochastic modeling of turbulent channel flow. In Chapter 8, we investigate the efficacy of the stochastically forced linearized Navier-Stokes equations and their parabolized equivalents in modeling the transitional boundary layer. In Chapter 9, we conclude Part II by discussing broader implications of our framework as well as outlining possible extensions.

Part III considers the model-based control of turbulent channel flow using passive surface actuation. In Chapter 10, we develop a model-based framework to analyze turbulent drag reduction in channel flow subject to streamwise traveling blowing and suction. Chapter 11 is devoted to the model-based analysis of the effect of spanwise wall oscillations on drag reduction in high Reynolds number turbulent channel flows. In Chapter 12, we summarize Part III and discuss open research problems.

Appendix A provides proofs to the lemmas and propositions of Chapters 2 and 3. Finally, in Appendix B we provide additional details related to the developments of Chapter 7.

## 1.5 Preview of main results and contributions

In what follows, we provide an overview of the main contributions of this dissertation.

### Part I

**Low-complexity modeling of partially available second-order statistics.** We consider the problem of completing partially known sample statistics in a way that is consistent with the underlying stochastically driven linear dynamics. Neither the statistics nor the dynamics are precisely known. Thus, our objective is to reconcile the two in a parsimonious manner. More specifically, we seek to explain correlation data with the least number of possible input disturbance channels. We formulate this inverse problem as rank minimization, and for its solution, we employ a convex relaxation based on the nuclear norm. This gives rise to a class of structured covariance completion problems.

The solution to the covariance completion problem provides spectral information about critical directions that have maximal effect in bringing model and statistics in agreement. An additional contribution is the design of a class of linear filters that realize suitable colored-in-time excitation to account for the observed state statistics. These filters solve a non-standard stochastic realization problem with partial covariance information. Finally, we show that the effect of the resulting colored-in-time input process is precisely equivalent to a perturbation of the system dynamics, without any need to increase the state dimension.

**Optimization algorithms for structured covariance completion problems.** We cast the covariance completion problem as a semidefinite program that can be solved using general-purpose solvers. For problem sizes that these solvers cannot handle, we develop two customized algorithms based on alternating direction methods; the Alternating Minimization Algorithm (AMA) and the Alternating Direction Method of Multipliers (ADMM). We draw a contrast between AMA and ADMM by showing that AMA leads to explicit, easily computable updates of both primal and dual optimization variables. We interpret AMA as a proximal gradient for the dual problem and establish convergence for our customized AMA with fixed step-size. Moreover, we utilize a Barzilai-Borwein step-size initialization followed by backtracking to achieve sufficient dual ascent. This enhances convergence relative to theoretically proven sub-linear convergence rates for AMA with fixed step-size. We also provide an example that illustrates the utility of our modeling and optimization framework and draw contrast between AMA and the commonly used ADMM algorithm.

The MATLAB source codes for our customized ADMM and AMA algorithms can be found at:

<http://www.ece.umn.edu/users/mihailo/software/ccama/>

**The use of the  $r^*$  heuristic in covariance completion problems.** We use the  $r^*$  norm as an alternative to the nuclear norm approximation in the covariance completion problem. Relative to the nuclear norm relaxation, the  $r^*$  norm exploits an additional degree of freedom which is useful in the completion of diagonally dominant covariances. While the nuclear norm relaxation yields forcing models of low-complexity, in some cases it can result in unreasonable completion of second-order statistics. Our numerical experiments show that the use of the  $r^*$  norm can indeed result in better covariance completion without adding to the rank of the solution to our optimization problem.

**Perturbation of system dynamics and the covariance completion problem.** We formulate the problem to match available covariance data while minimizing the energy required to adjust the dynamics by a suitable low-rank perturbation. More specifically, in the context of covariance completion via stochastically forced linear dynamics, we start from a pre-specified set of input channels and pose an optimization

problem that allows us to identify a small subset of these channels that can explain partially observed second-order statistics via suitable feedback interactions. To cope with the combinatorial complexity of our optimization problem, we utilize a convex characterization that has been used in the context of optimal sensor and actuator selection, which also allows us to cast our problem as a semidefinite program. This work provides an alternative interpretation for our covariance completion framework as a static state-feedback synthesis approach to an inverse problem that identifies dynamical feedback interactions which account for available statistical signatures.

## Part II

**Stochastic modeling of turbulent channel flow.** We employ our modeling framework to account for second-order statistics of turbulent channel flow using stochastic dynamical models of low complexity that are based on the linearized Navier-Stokes equations. We demonstrate that white-in-time stochastic forcing is not sufficient to explain turbulent flow statistics and develop models for colored-in-time forcing of the linearized dynamics. In addition, we show that colored-in-time excitation of the Navier-Stokes equations can also be interpreted as a low-rank modification to the generator of the linearized dynamics. Although our models are based on matching one-point velocity correlations, we demonstrate good recovery of two-point correlations. We also analyze the spatio-temporal responses of our model to stochastic and deterministic excitation sources. In particular, by examining the power spectral density of velocity fluctuations, we have shown that the dynamical modification attenuates the amplification over all temporal frequencies. A similar effect has been observed in the eddy-viscosity-enhanced linearization of the Navier-Stokes equations. Finally, we have computed two-point temporal correlations resulting from our model to demonstrate that the essential features of the convection velocities of individual modes are reproduced. Our method provides a data-driven refinement of models that originate from first principles and captures complex dynamics of turbulent flows in a way that is tractable for analysis, optimization, and control design.

**Stochastic modeling of spatially evolving flows.** We examine the efficacy of stochastically forced linearized Navier-Stokes equations and the parabolized stability equations in studying the dynamics of flow fluctuations in the transitional boundary layer. We utilize a parallel flow assumption in the Blasius boundary layer to analyze the receptivity of velocity fluctuations to stochastic excitation sources (e.g., free-stream turbulence and surface roughness). We also conduct a global analysis by examining the energetically dominant flow structures that arise from stochastic excitation of the linearized Navier-Stokes equations around a streamwise varying base flow profile. To account for the effect of linear diffraction, we introduce stochastic forcing into the linear parabolized stability equations and examine the interaction of the slowly-varying

base flow with streamwise streaks and Tollmien-Schlichting waves. Our results demonstrate the necessity for spatially correlated stochastic excitation of the linear PSE for the purpose of capturing transient peaks in the streamwise intensity of the flow.

### Part III

**Turbulent drag reduction by streamwise traveling waves.** For a turbulent channel flow with zero-net-mass-flux surface actuation in the form of streamwise traveling waves we develop a model-based approach to design control parameters that can reduce skin-friction drag. Our simulation-free approach is capable of identifying drag reducing trends in traveling waves with various control parameters. We also use high-fidelity simulations to verify the quality of our theoretical predictions.

**Model-based analysis of the effect of spanwise wall oscillations on drag reduction at high Reynolds numbers.** We use the stochastically forced linearized Navier-Stokes equations to study the Reynolds number independent effects of spanwise wall oscillations on drag reduction in turbulent channel flows. We show that the influence of wall oscillations at low Reynolds numbers is confined to the streamwise and spanwise wavelengths that correspond to the universal inner-scaled eddies in wall turbulence. Since wall oscillations do not suppress large-scale eddies, which are responsible for increased drag in the uncontrolled flow, we conclude that wall oscillations have weaker influence on drag reduction at higher Reynolds numbers. Our observations extend the predictive capability of our simulation-free approach and enable predictions of drag reduction at high Reynolds numbers.

## Part I

# Low-complexity modeling of partially available second-order statistics: theory and efficient optimization algorithms

## Chapter 2

# Low-complexity modeling of partially available second-order statistics

State statistics of linear systems satisfy certain structural constraints that arise from the underlying dynamics and the directionality of input disturbances. In this chapter, we study the problem of completing partially known state statistics. Our aim is to develop tools that can be used in the context of control-oriented modeling of large-scale dynamical systems. For the type of applications we have in mind, the dynamical interaction between state variables is known while the directionality and dynamics of input excitation is often uncertain. Thus, the goal of the mathematical problem that we formulate is to identify the dynamics and directionality of input excitation in order to explain and complete observed sample statistics. More specifically, we seek to explain correlation data with the least number of possible input disturbance channels. We formulate this inverse problem as rank minimization, and for its solution, we employ a convex relaxation based on the nuclear norm. In the next chapter, we develop customized algorithms based on alternating direction methods that are well-suited for problem sizes that cannot be handled by general-purpose solvers.

### 2.1 Introduction

Motivation for this work stems from control-oriented modeling of systems with a large number of degrees of freedom. Indeed, dynamics governing many physical systems are prohibitively complex for purposes of control design and optimization. Thus, it is

common practice to investigate low-dimensional models that preserve the essential dynamics. To this end, stochastically driven linearized models often represent an effective option that is also capable of explaining observed statistics. Further, such models are well-suited for analysis and synthesis using tools from modern robust control.

An example that illustrates the point is the modeling of fluid flows. In this, the Navier-Stokes equations are prohibitively complex for control design [106]. On the other hand, linearization of the equations around the mean-velocity profile in the presence of stochastic excitation has been shown to qualitatively replicate structural features of shear flows [28–30, 33, 107–109, 111, 112]. However, it has also been recognized that a simple white-in-time stochastic excitation cannot reproduce important statistics of the fluctuating velocity field [113, 114]. In this chapter, we introduce a mathematical framework to consider stochastically driven linear models that depart from the white-in-time restriction on random disturbances. Our objective is to identify low-complexity disturbance models that account for partially available second-order statistics of large-scale dynamical systems.

Thus, herein, we formulate a covariance completion problem for linear time-invariant (LTI) systems with uncertain disturbance dynamics. The complexity of the disturbance model is quantified by the number of input channels. We relate the number of input channels to the rank of a certain matrix which reflects the directionality of input disturbances and the correlation structure of excitation sources. We address the resulting optimization problem using the nuclear norm as a surrogate for rank [45, 46, 60, 70, 72, 73, 115, 116].

The solution to the covariance completion problem gives rise to a class of linear filters that realize colored-in-time disturbances and account for the observed state statistics. This is a non-standard stochastic realization problem with partial spectral information [117–120]. The class of modeling filters that we generate for the stochastic excitation is generically minimal in the sense that it has the same number of degrees of freedom as the original linear system. Furthermore, we demonstrate that the covariance completion problem can be also interpreted as an identification problem that aims to explain available statistics via suitable low-rank dynamical perturbations.

Our presentation is organized as follows. We summarize key results regarding the structure of state covariances and its relation to the power spectrum of input processes in Section 2.2. In Section 2.3, we characterize admissible signatures for matrices that parametrize disturbance spectra and formulate the covariance completion problem.

## 2.2 Linear stochastic models and state statistics

We now discuss algebraic conditions that state covariances of LTI systems satisfy. For white-in-time stochastic inputs state statistics satisfy an algebraic Lyapunov equation. A similar algebraic characterization holds for LTI systems driven by colored stochastic processes [121, 122]. This characterization provides the foundation for the covariance completion problem that we study in this chapter.

Consider a linear time-invariant system

$$\begin{aligned}\dot{x} &= Ax + Bu \\ y &= Cx\end{aligned}\tag{2.1}$$

where  $x(t) \in \mathbb{C}^n$  is a state vector,  $y(t) \in \mathbb{C}^p$  is the output, and  $u(t) \in \mathbb{C}^m$  is a zero-mean stationary stochastic input. The dynamic matrix  $A \in \mathbb{C}^{n \times n}$  is Hurwitz,  $B \in \mathbb{C}^{n \times m}$  is the input matrix with  $m \leq n$ , and  $(A, B)$  is a controllable pair. Let  $X$  be the steady-state covariance of the state vector of system (2.1),  $X = \lim_{t \rightarrow \infty} \mathbf{E}(x(t)x^*(t))$ , with  $\mathbf{E}$  being the expectation operator. We next review key results and provide new insights into the following questions:

- (i) What is the algebraic structure of  $X$ ? In other words, given a positive definite matrix  $X$ , under what conditions does it qualify to be the steady-state covariance of (2.1)?
- (ii) Given the steady-state covariance  $X$  of (2.1), what can be said about the power spectra of input processes that are consistent with these statistics?

### 2.2.1 Algebraic constraints on admissible covariances

The steady-state covariance matrix  $X$  of the state vector in (2.1) satisfies [121, 122]

$$\text{rank} \begin{bmatrix} AX + XA^* & B \\ B^* & 0 \end{bmatrix} = \text{rank} \begin{bmatrix} 0 & B \\ B^* & 0 \end{bmatrix}.\tag{2.2a}$$

An equivalent characterization is that there is a solution  $H \in \mathbb{C}^{n \times m}$  to the equation

$$AX + XA^* = -BH^* - HB^*.\tag{2.2b}$$

Either of these conditions, together with the positive definiteness of  $X$ , completely characterize state covariances of linear dynamical systems driven by white or colored stochastic processes [121, 122]. When the input  $u$  is white noise with covariance  $W$ ,  $X$  satisfies the algebraic Lyapunov equation

$$AX + XA^* = -BWB^*.$$

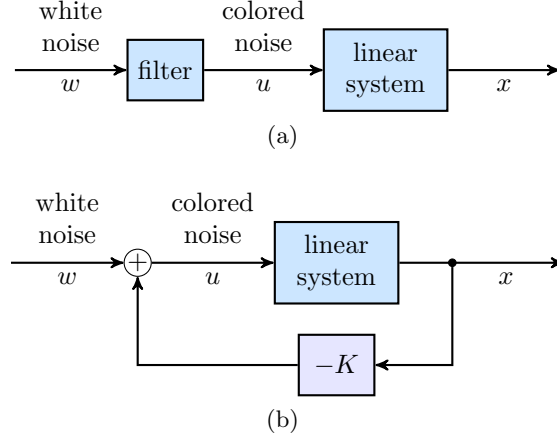


Figure 2.1: (a) A cascade connection of an LTI system with a linear filter that is designed to account for the sampled steady-state covariance matrix  $X$ ; (b) An equivalent feedback representation of the cascade connection in (a).

In this case,  $H$  in (2.2b) is determined by  $H = \frac{1}{2}BW$  and the right-hand-side  $-BWB^*$  is sign-definite. In fact, except for this case when the input is white noise, the matrix  $Z$  defined by

$$Z := -(AX + XA^*) \quad (2.3a)$$

$$= BH^* + HB^* \quad (2.3b)$$

may have both positive and negative eigenvalues. Additional discussion on the structure of  $Z$  is provided in Section 2.3.1.

### 2.2.2 Power spectrum of input process

For stochastically driven LTI systems the state statistics can be obtained from knowledge of the system model and the input statistics. Herein, we are interested in the converse: starting from the steady-state covariance  $X$  and the system dynamics (2.1), we want to identify the power spectrum of the input process  $u$ . As illustrated in figure 2.1a, we seek to construct a filter which, when driven by white noise, produces a suitable stationary input  $u$  to (2.1) so that the state covariance is  $X$ . Next, we characterize a class of filters with degree at most  $n$ .

Consider the linear filter given by

$$\dot{\xi} = (A - BK)\xi + Bw \quad (2.4a)$$

$$u = -K\xi + w \quad (2.4b)$$

where  $w$  is a zero-mean white stochastic process with covariance  $\Omega \succ 0$  and

$$K = \frac{1}{2} \Omega B^* X^{-1} - H^* X^{-1}, \quad (2.4c)$$

for some  $H$  that satisfies (2.2b). The power spectrum of  $u$  is determined by

$$\Pi_{uu}(\omega) = \Psi(j\omega) \Omega \Psi^*(j\omega)$$

where

$$\Psi(s) = I - K(sI - A + BK)^{-1}B$$

is the transfer function of the filter (2.4). To verify this, consider the cascade connection shown in figure 2.1a, with state space representation

$$\begin{aligned} \begin{bmatrix} \dot{x} \\ \dot{\xi} \end{bmatrix} &= \begin{bmatrix} A & -BK \\ 0 & A - BK \end{bmatrix} \begin{bmatrix} x \\ \xi \end{bmatrix} + \begin{bmatrix} B \\ B \end{bmatrix} w \\ x &= \begin{bmatrix} I & 0 \end{bmatrix} \begin{bmatrix} x \\ \xi \end{bmatrix}. \end{aligned} \quad (2.5)$$

This representation has twice as many states as linear system (2.1), but it is not controllable and therefore not minimal. The coordinate transformation

$$\begin{bmatrix} x \\ \phi \end{bmatrix} = \begin{bmatrix} I & 0 \\ -I & I \end{bmatrix} \begin{bmatrix} x \\ \xi \end{bmatrix}$$

brings system (2.5) into the following form

$$\begin{aligned} \begin{bmatrix} \dot{x} \\ \dot{\phi} \end{bmatrix} &= \begin{bmatrix} A - BK & -BK \\ 0 & A \end{bmatrix} \begin{bmatrix} x \\ \phi \end{bmatrix} + \begin{bmatrix} B \\ 0 \end{bmatrix} w \\ x &= \begin{bmatrix} I & 0 \end{bmatrix} \begin{bmatrix} x \\ \phi \end{bmatrix}. \end{aligned}$$

Clearly, the input  $w$  does not enter into the equation for  $\phi$  and

$$\dot{x} = (A - BK)x + Bw \quad (2.6)$$

provides a minimal realization of the transfer function from white-in-time  $w$  to  $x$ ,  $(sI - A + BK)^{-1}B$ . In addition, the corresponding algebraic Lyapunov equation in

conjunction with (2.4c) yields

$$\begin{aligned}
& (A - BK)X + X(A - BK)^* + B\Omega B^* \\
&= AX + XA^* + B\Omega B^* - BKX - XK^*B^* \\
&= AX + XA^* + BH^* + HB^* \\
&= 0.
\end{aligned}$$

This shows that (2.4) generates a process  $u$  that is consistent with  $X$ .

As we elaborate next, compact representation (2.6) offers an equivalent interpretation of colored-in-time stochastic input processes as a *dynamical perturbation* to system (2.1).

### 2.2.3 Stochastic control interpretation

The class of power spectra described by (2.4) is closely related to the covariance control problem, or the covariance assignment problem, studied in [123, 124]. To illustrate this, let us consider

$$\dot{x} = Ax + Bv + Bw \quad (2.7a)$$

where  $w$  is again white with covariance  $\Omega$ ; see figure 2.1b. In the absence of a control input ( $v = 0$ ), the steady-state covariance satisfies the Lyapunov equation

$$AX + XA^* + B\Omega B^* = 0.$$

A choice of a non-zero process  $v$  can be used to assign different values for  $X$ . Indeed, for

$$v = -Kx \quad (2.7b)$$

and  $A - BK$  Hurwitz,  $X$  satisfies

$$(A - BK)X + X(A - BK)^* + B\Omega B^* = 0. \quad (2.8)$$

It is easy to see that any  $X \succ 0$  satisfying (2.8) also satisfies (2.2b) with  $H = -XK^* + \frac{1}{2}B\Omega$ . Conversely, if  $X \succ 0$  satisfies (2.2b), for  $K = \frac{1}{2}\Omega B^*X^{-1} - H^*X^{-1}$ , then  $X$  also satisfies (2.8) and  $A - BK$  is Hurwitz. Thus, the following statements are equivalent:

- A matrix  $X \succ 0$  qualifies as the stationary state covariance of (2.7a) via a suitable choice of state-feedback (2.7b).
- A matrix  $X \succ 0$  is a state covariance of (2.1) for some stationary stochastic input  $u$ .

To clarify the connection between  $K$  and the corresponding modeling filter for  $u$ , let

$$u = -Kx + w. \quad (2.9a)$$

Substitution of (2.7b) into (2.7a) yields

$$\begin{aligned}\dot{x} &= (A - BK)x + Bw \\ &= Ax + Bu\end{aligned}\tag{2.9b}$$

which coincides with (2.1). Thus,  $X$  can also be achieved by driving (2.1) with  $u$  given by (2.9a). The equivalence of (2.4) and (2.9) is evident. Equation (2.9b) shows that a colored-in-time stochastic input process  $u$  can be interpreted as a dynamical perturbation to system (2.1). This offers advantages from a computational standpoint, e.g., when conducting stochastic simulations; see Section 5.4.

In general, there is more than one choice of  $K$  that yields a given feasible  $X$ . A criterion for the selection of an optimal feedback gain  $K$ , can be to minimize

$$\lim_{t \rightarrow \infty} \mathbf{E}(v^*(t)v(t)).$$

This optimality criterion relates to information theoretic notions of distance (Kullback-Leibler divergence) between corresponding models with and without control [125–127]. Based on this criterion, the optimal feedback gain  $K$  can be obtained by minimizing trace( $KXK^*$ ), subject to the linear constraint (2.8). This choice of  $K$  characterizes an optimal filter of the form (2.9). This filter is used in Section 5.4 where we provide an illustrative example.

## 2.3 Covariance completion and model complexity

In Section 2.2, we presented the structural constraints on the state covariance  $X$  of an LTI system. We also proposed a method to construct a class of linear filters that generate the appropriate input process  $u$  to account for the statistics in  $X$ . In many applications, the dynamical generator  $A$  in (2.1) is known. For example, in turbulent fluid flows the mean velocity can be obtained using numerical simulations of the Navier-Stokes equations and linearization around this equilibrium profile yields  $A$  in (2.1). On the other hand, stochastic excitation often originates from disturbances that are difficult to model directly. To complicate matters, the state statistics may be only partially known, i.e., only certain correlations between a limited number of states may be available. For example, such second-order statistics may reflect partial output correlations obtained in numerical simulations or experiments of the underlying physical system. Thus, we now introduce a framework for completing unknown elements of  $X$  in a manner that is consistent with state-dynamics and, thereby, obtaining information about the spectral content and directionality of input disturbances to (2.1).

For colored-in-time disturbance  $u$  that enters into the state equation in *all directions*, through the identity matrix, condition (2.2a) is trivially satisfied. Indeed, any sample

covariance  $X$  can be generated by a linear model (2.1) with  $B = I$ . In this case, the Lyapunov-like constraint (2.2b) simplifies to

$$AX + XA^* = -H^* - H.$$

Clearly, this equation is satisfied with  $H^* = -AX$ . With this choice of the cross-correlation matrix  $H$ , the dynamics represented by (2.9b) can be equivalently written as

$$\dot{x} = -\frac{1}{2}X^{-1}x + w$$

with a white disturbance  $w$ . This demonstrates that *colored-in-time* forcing  $u$  which *excites all degrees of freedom* can *completely overwrite the original dynamics*. Thus, such an input disturbance can trivially account for the observed statistics *but* provides no useful information about the underlying physics.

In our setting, the structure and size of the matrix  $B$  in (2.1) is not known *a priori*, which means that the direction of the input disturbances are not given. In most physical systems, disturbance can directly excite only a limited number of directions in the state space. For instance, in mechanical systems where inputs represent forces and states represent position and velocity, disturbances can only enter into the velocity equation. Hence, it is of interest to identify a disturbance model that involves a small number of input channels. This requirement can be formalized by restricting the input to enter into the state equation through a matrix  $B \in \mathbb{C}^{n \times m}$  with  $m < n$ . Thus, our objective is to identify matrices  $B$  and  $H$  in (2.2b) to reproduce a partially known  $X$  while striking an optimal balance with the complexity of the model; the complexity is reflected in the rank of  $B$ , i.e., the number of input channels. This notion of complexity is closely related to the signature of  $Z$ , which we discuss next.

### 2.3.1 The signature of $Z$

As mentioned in Section 2.2, the matrix  $Z$  in (2.3) is not necessarily positive semidefinite. However, it is not arbitrary. We next examine admissible values of the *signature* on  $Z$ , i.e., the number of positive, negative, and zero eigenvalues. In particular, we show that the number of positive and negative eigenvalues of  $Z$  impacts the number of input channels in the state equation (2.1).

There are two sets of constraints on  $Z$  arising from (2.3a) and (2.3b), respectively. The first one is a standard Lyapunov equation with Hurwitz  $A$  and a given Hermitian  $X \succ 0$ . The second provides a link between the signature of  $Z$  and the number of input channels in (2.1).

First, we study the constraint on the signature of  $Z$  arising from (2.3a) which we repeat here,

$$AX + XA^* = -Z. \tag{2.10}$$

The unique solution to this Lyapunov equation, with Hurwitz  $A$  and Hermitian  $X$  and  $Z$ , is given by

$$X = \int_0^\infty e^{At} Z e^{A^*t} dt. \quad (2.11)$$

Lyapunov theory implies that if  $Z$  is positive definite then  $X$  is also positive definite. However, the converse is not true. Indeed, for a given  $X \succ 0$ ,  $Z$  obtained from (2.10) is not necessarily positive definite. Clearly,  $Z$  cannot be negative definite either, otherwise  $X$  obtained from (2.11) would be negative semidefinite. We can thus conclude that (2.10) does in fact introduce a constraint on the signature of  $Z$ . In what follows, the signature is defined as the triple

$$\text{In}(Z) = (\pi(Z), \nu(Z), \delta(Z))$$

where  $\pi(Z)$ ,  $\nu(Z)$ , and  $\delta(Z)$  denote the number of positive, negative, and zero eigenvalues of  $Z$ , respectively.

Several authors have studied constraints on signatures of  $A$ ,  $X$ , and  $Z$  that are linked through a Lyapunov equation [128–130]. Typically, such studies focus on the relationship between the signature of  $X$  and the eigenvalues of  $A$  for a given  $Z \succeq 0$ . In contrast, [131] considers the relationship between the signature of  $Z$  and eigenvalues of  $A$  for  $X \succ 0$  and we make use of these results.

Let  $\{\lambda_1, \dots, \lambda_l\}$  denote the eigenvalues of  $A$ ,  $\mu_k$  denote the geometric multiplicity of  $\lambda_k$ , and

$$\mu(A) := \max_{1 \leq k \leq l} \mu_k.$$

The following result is a special case of [131, Theorem 2].

**Proposition 1.** *Let  $A$  be Hurwitz and let  $X$  be positive definite. For  $Z = -(AX + XA^*)$ ,*

$$\pi(Z) \geq \mu(A). \quad (2.12)$$

To explain the nature of the constraint  $\pi(Z) \geq \mu(A)$ , we first note that  $\mu(A)$  is *the least number of input channels that are needed for system (2.1) to be controllable* [132, p. 188]. Now consider the decomposition

$$Z = Z_+ - Z_-$$

where  $Z_+$ ,  $Z_-$  are positive semidefinite matrices, and accordingly  $X = X_+ - X_-$  with  $X_+$ ,  $X_-$  denoting the solutions of the corresponding Lyapunov equations. Clearly, unless the above constraint (2.12) holds,  $X_+$  cannot be positive definite. Hence,  $X$  cannot be positive definite either. Interestingly, there is no constraint on  $\nu(Z)$  other than

$$\pi(Z) + \nu(Z) \leq n$$

which comes from the dimension of  $Z$ .

To study the constraint on the signature of  $Z$  arising from (2.3b), we begin with a lemma, whose proof is provided in the appendix.

**Lemma 1.** *For a Hermitian matrix  $Z$  decomposed as*

$$Z = S + S^*$$

*the following holds*

$$\pi(Z) \leq \text{rank}(S).$$

Clearly, the same bound applies to  $\nu(Z)$ , that is,

$$\nu(Z) \leq \text{rank}(S).$$

The importance of these bounds stems from our interest in decomposing  $Z$  into summands of small rank. A decomposition of  $Z$  into  $S + S^*$  allows us to identify input channels and power spectra by factoring  $S = BH^*$ . The rank of  $S$  coincides with the rank of  $B$ , that is, with the number of input channels in the state equation. Thus, it is of interest to determine the minimum rank of  $S$  in such a decomposition and this is given in Proposition 2 (the proof is provided in the appendix).

**Proposition 2.** *For a Hermitian matrix  $Z$  having signature  $(\pi(Z), \nu(Z), \delta(Z))$ ,*

$$\min \{\text{rank}(S) \mid Z = S + S^*\} = \max \{\pi(Z), \nu(Z)\}.$$

We can now summarize the bounds on the number of positive and negative eigenvalues of the matrix  $Z$  defined by (2.3). By combining Proposition 1 with Lemma 1 we show that these upper bounds are dictated by the number of inputs in the state equation (2.1).

**Proposition 3.** *Let  $X \succ 0$  denote the steady-state covariance of the state  $x$  of a stable linear system (2.1) with  $m$  inputs. If  $Z$  satisfies the Lyapunov equation (2.10), then*

$$\begin{aligned} 0 &\leq \nu(Z) \leq m \\ \mu(A) &\leq \pi(Z) \leq m. \end{aligned}$$

*Proof.* From Section 2.2, a state covariance  $X$  satisfies

$$AX + XA^* = -BH^* - HB^*.$$

Setting  $S = BH^*$ ,

$$Z = BH^* + HB^* = S + S^*.$$

From Lemma 1,

$$\max\{\pi(Z), \nu(Z)\} \leq \text{rank}(S) \leq \text{rank}(B) = m.$$

The lower bounds follow from Proposition 1.  $\square$

### 2.3.2 Decomposition of $Z$ into $BH^* + HB^*$

Proposition 2 expresses the possibility to decompose the matrix  $Z$  into  $BH^* + HB^*$  with  $S = BH^*$  of minimum rank equal to  $\max\{\pi(Z), \nu(Z)\}$ . Here, we present an algorithm that achieves this objective. Given  $Z$  with signature  $(\pi(Z), \nu(Z), \delta(Z))$ , we can choose an invertible matrix  $T$  to bring  $Z$  into the following form<sup>1</sup>

$$\hat{Z} := TZT^* = 2 \begin{bmatrix} I_\pi & 0 & 0 \\ 0 & -I_\nu & 0 \\ 0 & 0 & 0 \end{bmatrix} \quad (2.14)$$

where  $I_\pi$  and  $I_\nu$  are identity matrices of dimension  $\pi(Z)$  and  $\nu(Z)$  [133, pages 218–223]. We first present a factorization of  $Z$  for  $\pi(Z) \leq \nu(Z)$ . With

$$\hat{S} = \begin{bmatrix} I_\pi & -I_\pi & 0 & 0 \\ I_\pi & -I_\pi & 0 & 0 \\ 0 & 0 & -I_{\nu-\pi} & 0 \\ 0 & 0 & 0 & 0 \end{bmatrix} \quad (2.15)$$

we clearly have  $\hat{Z} = \hat{S} + \hat{S}^*$ . Furthermore,  $\hat{S}$  can be written as  $\hat{S} = \hat{B}\hat{H}^*$ , where

$$\hat{B} = \begin{bmatrix} I_\pi & 0 \\ I_\pi & 0 \\ 0 & I_{\nu-\pi} \\ 0 & 0 \end{bmatrix}, \quad \hat{H} = \begin{bmatrix} I_\pi & 0 \\ -I_\pi & 0 \\ 0 & -I_{\nu-\pi} \\ 0 & 0 \end{bmatrix}.$$

In case  $\nu(Z) = \pi(Z)$ ,  $I_{\nu-\pi}$  and the corresponding row and column are empty. Finally, the matrices  $B$  and  $H$  are determined by  $B = T^{-1}\hat{B}$  and  $H = T^{-1}\hat{H}$ .

Similarly, for  $\pi(Z) > \nu(Z)$ ,  $Z$  can be decomposed into  $BH^* + HB^*$  with  $B = T^{-1}\hat{B}$ ,  $H = T^{-1}\hat{H}$ , and

$$\hat{B} = \begin{bmatrix} I_{\pi-\nu} & 0 \\ 0 & I_\nu \\ 0 & I_\nu \\ 0 & 0 \end{bmatrix}, \quad \hat{H} = \begin{bmatrix} I_{\pi-\nu} & 0 \\ 0 & I_\nu \\ 0 & -I_\nu \\ 0 & 0 \end{bmatrix}.$$

---

<sup>1</sup>The choice of  $T$  represents a standard congruence transformation that brings  $Z$  into canonical form.

Note that both  $B$  and  $H$  are full column-rank matrices.

### 2.3.3 Covariance completion problem

Given the dynamical generator  $A$  and partially observed state correlations, we want to obtain a low-complexity model for the disturbance that can explain the observed entries of  $X$ . Here the complexity is reflected by the number of input channels, i.e., the rank of the input matrix  $B$ . Clearly,  $\text{rank}(B) \geq \text{rank}(S)$ . Furthermore, any  $S$  can be factored as  $S = BH^*$  with  $\text{rank}(B) = \text{rank}(S)$  via, e.g., singular value decomposition. Thus, we focus on minimizing the rank of  $S$ .

Rank minimization is a difficult problem because  $\text{rank}(\cdot)$  is a non-convex function. Recent advances have demonstrated that the minimization of the nuclear-norm (i.e., the sum of the singular values)

$$\|S\|_* := \sum_{i=1}^n \sigma_i(S)$$

represents a good proxy for rank minimization [45, 46, 60, 70, 72, 73, 115, 116]. We thus formulate the following matrix completion problem:

*Given a Hurwitz  $A$  and the matrix  $G$ , determine matrices  $X = X^*$  and  $Z = S + S^*$  from the solution to*

$$\begin{aligned} & \underset{S, X}{\text{minimize}} && \|S\|_* \\ & \text{subject to} && AX + XA^* + S + S^* = 0 \\ & && (C X C^*) \circ E - G = 0 \\ & && X \succeq 0. \end{aligned} \tag{2.16}$$

In the above, the matrices  $A$ ,  $C$ ,  $E$ , and  $G$  represent problem data, while  $S$ ,  $X \in \mathbb{C}^{n \times n}$  are optimization variables. The entries of the Hermitian matrix  $G$  represent partially known second-order statistics which reflect output correlations provided by numerical simulations or experiments of the underlying physical system. The symbol  $\circ$  denotes elementwise matrix multiplication and the matrix  $E$  is the structural identity defined by

$$E_{ij} = \begin{cases} 1, & G_{ij} \text{ is available} \\ 0, & G_{ij} \text{ is unavailable.} \end{cases}$$

The constraint set in (2.16) represents the intersection of the positive semidefinite cone and two linear subspaces. These are specified by the Lyapunov-like constraint, which is imposed by the linear dynamics, and the linear constraint which relates  $X$  to the

available entries of the steady-state output covariance matrix

$$\lim_{t \rightarrow \infty} \mathbf{E}(y(t) y^*(t)) = C X C^*.$$

As shown in Proposition 2, *minimizing the rank of  $S$  is equivalent to minimizing  $\max\{\pi(Z), \nu(Z)\}$* . Given  $Z$ , there exist matrices  $Z_+ \succeq 0$  and  $Z_- \succeq 0$  with  $Z = Z_+ - Z_-$  such that  $\text{rank}(Z_+) = \pi(Z)$  and  $\text{rank}(Z_-) = \nu(Z)$ . Furthermore, any such decomposition of  $Z$  satisfies  $\text{rank}(Z_+) \geq \pi(Z)$  and  $\text{rank}(Z_-) \geq \nu(Z)$ . Thus, instead of (2.16), we can alternatively consider the following convex optimization problem, which aims at minimizing  $\max\{\pi(Z), \nu(Z)\}$ ,

$$\begin{aligned} & \underset{X, Z_+, Z_-}{\text{minimize}} && \max\{\text{trace}(Z_+), \text{trace}(Z_-)\} \\ & \text{subject to} && A X + X A^* + Z_+ - Z_- = 0 \\ & && (C X C^*) \circ E - G = 0 \\ & && X \succeq 0, Z_+ \succeq 0, Z_- \succeq 0. \end{aligned} \tag{2.17}$$

Both (2.16) and (2.17) can be solved efficiently using standard SDP solvers [134, 135] for small- and medium-size problems. Note that (2.16) and (2.17) are obtained by relaxing the rank function to the nuclear norm and the signature to the trace, respectively. Thus, even though the original non-convex optimization problems are equivalent to each other, the resulting convex relaxations (2.16) and (2.17) are not, in general.

In Chapter 3, we develop an efficient customized algorithm which solves the following *covariance completion* problem

$$\begin{aligned} & \underset{X, Z}{\text{minimize}} && -\log \det X + \gamma \|Z\|_* \\ & \text{subject to} && A X + X A^* + Z = 0 \\ & && (C X C^*) \circ E - G = 0. \end{aligned} \tag{2.18}$$

For any  $Z$  there exists a decomposition  $Z = Z_+ - Z_-$  with  $Z_+, Z_- \succeq 0$  such that

$$\|Z\|_* = \text{trace}(Z_+) + \text{trace}(Z_-).$$

Since

$$\text{trace}(Z_+) + \text{trace}(Z_-) \geq \max\{\text{trace}(Z_+), \text{trace}(Z_-)\},$$

the solution to (2.18) provides a possibly suboptimal solution to (2.17).

We have also considered (2.18) in the absence of the logarithmic barrier function [136, 137]. However, in that case, the corresponding semidefinite  $X$  is not suitable for synthesizing the input filter (2.4) because  $X^{-1}$  appears in the expression for  $K$ ; cf. (2.4c). Furthermore, as we show in Chapter 3, another benefit of using the logarithmic barrier

is that it ensures strong convexity of the smooth part of the objective function in (2.18). We exploit this property to develop efficient algorithms for solving optimization problem (2.18). To highlight the theoretical developments of this section we provide an example in Section 3.6.

## Chapter 3

# Optimization algorithms for structured covariance completion problems

In this chapter, we first cast the covariance completion problem as a semidefinite program that can be solved using general-purpose solvers. For problem sizes that these solvers cannot handle, we develop two customized algorithms based on alternating direction methods; the Alternating Minimization Algorithm (AMA) and the Alternating Direction Method of Multipliers (ADMM). Our customized algorithms allow us to exploit the respective structure of the logarithmic barrier function and the nuclear norm, thereby leading to an efficient implementation that is well-suited for large systems. We interpret AMA as a proximal gradient for the dual problem and prove sub-linear convergence for our customized AMA with fixed step-size. We conclude with an example that illustrates the utility of our modeling and optimization framework and draw contrast between AMA and the commonly used ADMM algorithm.

### 3.1 Introduction

The relaxed optimization problem (2.18) is convex and can be cast as a semidefinite program (SDP) which is readily solvable by standard software for small-size problems. A further contribution is to specifically address larger problems that general-purpose solvers cannot handle. To this end, we first bring problem (2.18) into a form that is convenient for alternating direction methods. We exploit the problem structure, derive the Lagrange dual, and develop an efficient customized Alternating Minimization Algorithm

(AMA). Specifically, we show that AMA is a proximal gradient for the dual and establish convergence for the covariance completion problem. We utilize a Barzilai-Borwein (BB) step-size initialization followed by backtracking to achieve sufficient dual ascent. This enhances convergence relative to theoretically-proven sub-linear convergence rates for AMA with fixed step-size. We also draw contrast between AMA and the commonly used Alternating Direction Method of Multipliers (ADMM) by showing that AMA leads to explicit, easily computable updates of both primal and dual optimization variables.

The alternating minimization algorithm was originally developed by Tseng [138] and its enhanced variants have been recently presented in [139, 140] and used, in particular, for estimation of sparse Gaussian graphical models [140]. On the other hand, the more commonly known ADMM has been effectively employed in low-rank matrix recovery [141], sparse covariance selection [142], image denoising and magnetic resonance imaging [143], sparse feedback synthesis [144–146], system identification [54, 147, 148], and many other applications [139, 149–151].

We demonstrate that AMA, which effectively works as a proximal gradient algorithm on the dual problem is more efficient in handling covariance completion problems of large sizes.

In Section 3.2, we express the constraint set in a form amenable to alternating optimization methods. In Section 3.3, we cast optimization problem (2.18) as a SDP, present the optimality conditions and derive the dual problem. In Section 3.4, we provide details of our customized AMA and show that AMA can be equivalently interpreted as a proximal gradient algorithm on the dual problem. This also enables a principled step-size selection aimed at achieving sufficient dual ascent. We also establish theoretical results regarding the convergence of our customized algorithm in Section 3.4.7. In Section 3.5, we develop a customized ADMM algorithm for solving problem (2.18) and draw contrast between AMA and ADMM. To highlight the theoretical and algorithmic developments of Chapters 2 and 3, we provide an example in Section 3.6.

## 3.2 Rearrangement of constraints

In (2.18),  $\gamma$  determines the importance of the nuclear norm relative to the logarithmic barrier function. The convexity of (2.18) follows from the convexity of the objective function

$$J_p(X, Z) := -\log \det X + \gamma \|Z\|_*$$

and the convexity of the constraint set. Problem (2.18) can be equivalently expressed as follows,

$$\begin{aligned} & \underset{X, Z}{\text{minimize}} && -\log \det X + \gamma \|Z\|_* \\ & \text{subject to} && \mathcal{A}X + \mathcal{B}Z - \mathcal{C} = 0, \end{aligned} \quad (3.1)$$

where the constraints are now given by

$$\begin{bmatrix} \mathcal{A}_1 \\ \mathcal{A}_2 \end{bmatrix} X + \begin{bmatrix} I \\ 0 \end{bmatrix} Z - \begin{bmatrix} 0 \\ G \end{bmatrix} = 0.$$

Here,  $\mathcal{A}_1 : \mathbb{C}^{n \times n} \rightarrow \mathbb{C}^{n \times n}$  and  $\mathcal{A}_2 : \mathbb{C}^{n \times n} \rightarrow \mathbb{C}^{p \times p}$  are linear operators, with

$$\begin{aligned} \mathcal{A}_1(X) &:= AX + XA^* \\ \mathcal{A}_2(X) &:= (CXC^*) \circ E \end{aligned}$$

and their adjoints, with respect to the standard inner product  $\langle M_1, M_2 \rangle := \text{trace}(M_1^* M_2)$ , are given by

$$\begin{aligned} \mathcal{A}_1^\dagger(Y) &= A^*Y + YA \\ \mathcal{A}_2^\dagger(Y) &= C^*(E \circ Y)C. \end{aligned}$$

### 3.3 SDP formulation and the dual problem

By splitting  $Z$  into positive and negative definite parts,

$$Z = Z_+ - Z_-, \quad Z_+ \succeq 0, \quad Z_- \succeq 0$$

it can be shown [72, Section 5.1.2] that (3.1) can be cast as an SDP,

$$\begin{aligned} & \underset{X, Z_+, Z_-}{\text{minimize}} && -\log \det X + \gamma (\text{trace}(Z_+) + \text{trace}(Z_-)) \\ & \text{subject to} && \mathcal{A}_1(X) + Z_+ - Z_- = 0 \\ & && \mathcal{A}_2(X) - G = 0 \\ & && Z_+ \succeq 0, \quad Z_- \succeq 0. \end{aligned} \quad (3.2)$$

We next use this SDP formulation to derive the Lagrange dual of the covariance completion problem (3.1).

**Proposition 4.** *The Lagrange dual of (3.2) is given by*

$$\begin{aligned} & \underset{Y_1, Y_2}{\text{maximize}} \quad \log \det \left( \mathcal{A}_1^\dagger(Y_1) + \mathcal{A}_2^\dagger(Y_2) \right) - \langle G, Y_2 \rangle + n \\ & \text{subject to} \quad \|Y_1\|_2 \leq \gamma \end{aligned} \quad (3.3)$$

where Hermitian matrices  $Y_1, Y_2$  are the dual variables associated with the equality constraints in (3.2).

*Proof.* The Lagrangian of (3.2) is given by

$$\begin{aligned} \mathcal{L}(X, Z_\pm; Y_1, Y_2, \Lambda_\pm) = & -\log \det X + \gamma \text{trace}(Z_+ + Z_-) - \langle \Lambda_+, Z_+ \rangle - \langle \Lambda_-, Z_- \rangle + \\ & \langle Y_1, \mathcal{A}_1(X) + Z_+ - Z_- \rangle + \langle Y_2, \mathcal{A}_2(X) - G \rangle \end{aligned} \quad (3.4)$$

where Hermitian matrices  $Y_1, Y_2$ , and  $\Lambda_\pm \succeq 0$  are Lagrange multipliers associated with the equality and inequality constraints in (3.2). Minimizing the Lagrangian with respect to  $Z_+$  and  $Z_-$  yields

$$\begin{aligned} \gamma I - \Lambda_+ + Y_1 & \succeq 0, & Z_+ & \succeq 0 \\ \gamma I - \Lambda_- - Y_1 & \succeq 0, & Z_- & \succeq 0. \end{aligned}$$

Because of the positive semi-definiteness of the dual variables  $\Lambda_+$  and  $\Lambda_-$ , we also have that

$$\begin{aligned} Y_1 + \gamma I & \succeq \Lambda_+ \succeq 0 \\ -Y_1 + \gamma I & \succeq \Lambda_- \succeq 0, \end{aligned}$$

which yields the constraint in (3.3)

$$-\gamma I \preceq Y_1 \preceq \gamma I \iff \|Y_1\|_2 \leq \gamma. \quad (3.5)$$

On the other hand, minimization of  $\mathcal{L}$  with respect to  $X$  yields

$$X^{-1} = \mathcal{A}_1^\dagger(Y_1) + \mathcal{A}_2^\dagger(Y_2) \succ 0. \quad (3.6)$$

Substitution of (3.6) into (3.4) in conjunction with complementary slackness conditions

$$\begin{aligned} \langle \gamma I - \Lambda_+ + Y_1, Z_+ \rangle &= 0 \\ \langle \gamma I - \Lambda_- - Y_1, Z_- \rangle &= 0 \end{aligned}$$

can be used to obtain the Lagrange dual function

$$\begin{aligned} J_d(Y_1, Y_2) &= \inf_{X, Z_+, Z_-} \mathcal{L}(X, Z_\pm; Y_1, Y_2, \Lambda_\pm) \\ &= \log \det \left( \mathcal{A}_1^\dagger(Y_1) + \mathcal{A}_2^\dagger(Y_2) \right) - \langle G, Y_2 \rangle + n. \end{aligned}$$

□

The dual problem (3.3) is a convex optimization problem with variables  $Y_1 \in \mathbb{C}^{n \times n}$  and  $Y_2 \in \mathbb{C}^{p \times p}$ . These variables are dual feasible if the constraint in (3.3) is satisfied. In the case of primal and dual feasibility, any dual feasible pair  $(Y_1, Y_2)$  gives a lower bound on the optimal value  $J_p^*$  of the primal problem (3.2). As we show next, the alternating minimization algorithm of Section 3.4 can be interpreted as a proximal gradient algorithm on the dual problem and is developed to achieve sufficient dual ascent and satisfy (3.6).

### 3.4 Alternating Minimization Algorithm (AMA)

The logarithmic barrier function in (2.18) is strongly convex over any compact subset of the positive definite cone [152]. This makes it well-suited for the application of AMA, which requires strong convexity of the smooth part of the objective function [138].

The augmented Lagrangian associated with (3.1) is

$$\begin{aligned} \mathcal{L}_\rho(X, Z; Y_1, Y_2) = & -\log \det X + \gamma \|Z\|_* + \langle Y_1, \mathcal{A}_1(X) + Z \rangle + \langle Y_2, \mathcal{A}_2(X) - G \rangle + \\ & \frac{\rho}{2} \|\mathcal{A}_1(X) + Z\|_F^2 + \frac{\rho}{2} \|\mathcal{A}_2(X) - G\|_F^2 \end{aligned}$$

where  $\rho$  is a positive scalar and  $\|\cdot\|_F$  is the Frobenius norm.

AMA consists of the following steps:

$$X^{k+1} := \underset{X}{\operatorname{argmin}} \mathcal{L}_0(X, Z^k; Y_1^k, Y_2^k) \quad (3.7a)$$

$$Z^{k+1} := \underset{Z}{\operatorname{argmin}} \mathcal{L}_\rho(X^{k+1}, Z; Y_1^k, Y_2^k) \quad (3.7b)$$

$$Y_1^{k+1} := Y_1^k + \rho \left( \mathcal{A}_1(X^{k+1}) + Z^{k+1} \right) \quad (3.7c)$$

$$Y_2^{k+1} := Y_2^k + \rho \left( \mathcal{A}_2(X^{k+1}) - G \right). \quad (3.7d)$$

These terminate when the duality gap

$$\Delta_{\text{gap}} := -\log \det X^{k+1} + \gamma \|Z^{k+1}\|_* - J_d(Y_1^{k+1}, Y_2^{k+1})$$

and the primal residual

$$\Delta_p := \|\mathcal{A}X^{k+1} + \mathcal{B}Z^{k+1} - \mathcal{C}\|_F$$

are sufficiently small, i.e.,  $|\Delta_{\text{gap}}| \leq \epsilon_1$  and  $\Delta_p \leq \epsilon_2$ . In the  $X$ -minimization step (3.7a),

AMA minimizes the Lagrangian  $\mathcal{L}_0$  with respect to  $X$ . This step is followed by a  $Z$ -minimization step (3.7b) in which the augmented Lagrangian  $\mathcal{L}_\rho$  is minimized with respect to  $Z$ . Finally, the Lagrange multipliers,  $Y_1$  and  $Y_2$ , are updated based on the primal residuals with the step-size  $\rho$ .

In contrast to the Alternating Direction Method of Multipliers [150] (cf. Section 3.5), which minimizes the augmented Lagrangian  $\mathcal{L}_\rho$  in both  $X$ - and  $Z$ -minimization steps, AMA updates  $X$  via minimization of the standard Lagrangian  $\mathcal{L}_0$ . As shown below, in (3.8), use of AMA leads to a *closed-form expression* for  $X^{k+1}$ . Another differentiating aspect of AMA is that it works as a proximal gradient on the dual function; see Section 3.4.6. This allows us to select the step-size  $\rho$  in order to achieve sufficient dual ascent.

### 3.4.1 Solution to the $X$ -minimization problem (3.7a)

At the  $k$ th iteration of AMA, minimizing the Lagrangian  $\mathcal{L}_0$  with respect to  $X$  for fixed  $\{Z^k, Y_1^k, Y_2^k\}$  yields

$$X^{k+1} = \left( \mathcal{A}^\dagger(Y_1^k, Y_2^k) \right)^{-1} = \left( \mathcal{A}_1^\dagger(Y_1^k) + \mathcal{A}_2^\dagger(Y_2^k) \right)^{-1}. \quad (3.8)$$

### 3.4.2 Solution to the $Z$ -minimization problem (3.7b)

For fixed  $\{X^{k+1}, Y_1^k, Y_2^k\}$ , the augmented Lagrangian  $\mathcal{L}_\rho$  is minimized with respect to  $Z$ ,

$$\underset{Z}{\text{minimize}} \quad \gamma \|Z\|_* + \frac{\rho}{2} \|Z - V^k\|_F^2. \quad (3.9)$$

By computing the singular value decomposition of the symmetric matrix

$$V^k := -\left( \mathcal{A}_1(X^{k+1}) + (1/\rho)Y_1^k \right) = U \Sigma U^*,$$

where  $\Sigma$  is the diagonal matrix of the singular values  $\sigma_i$  of  $V^k$ , the solution to (3.9) is obtained by singular value thresholding [74],

$$Z^{k+1} = \mathcal{S}_{\gamma/\rho}(V^k).$$

The soft-thresholding operator  $\mathcal{S}_\tau$  is defined as

$$\mathcal{S}_\tau(V^k) := U \mathcal{S}_\tau(\Sigma) U^*, \quad \mathcal{S}_\tau(\Sigma) = \text{diag}((\sigma_i - \tau)_+)$$

with  $a_+ := \max\{a, 0\}$ .

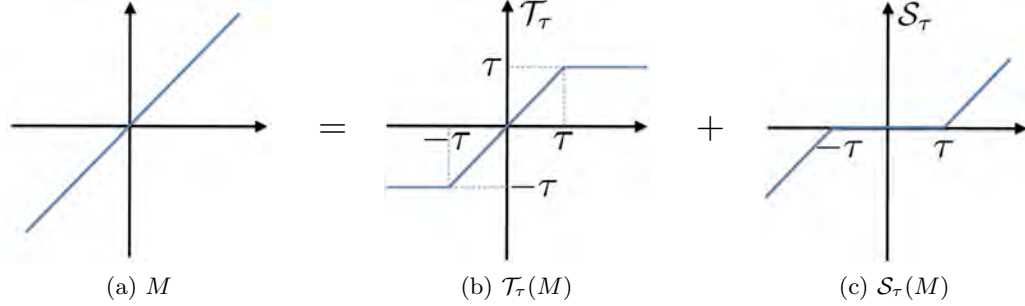


Figure 3.1: The saturation operator  $\mathcal{T}_\tau$  is related to the soft-thresholding operator  $\mathcal{S}_\tau$  via identity (3.10).

### 3.4.3 Lagrange multiplier update

The expressions for  $X^{k+1}$  and  $Z^{k+1}$  can be used to bring (3.7c) and (3.7d) into the following form

$$\begin{aligned} Y_1^{k+1} &= \mathcal{T}_\gamma(Y_1^k + \rho \mathcal{A}_1(X^{k+1})) \\ Y_2^{k+1} &= Y_2^k + \rho(\mathcal{A}_2(X^{k+1}) - G). \end{aligned}$$

For Hermitian matrix  $M$  with singular value decomposition  $M = U \Sigma U^*$ ,  $\mathcal{T}_\tau$  is the saturation operator,

$$\begin{aligned} \mathcal{T}_\tau(M) &:= U \mathcal{T}_\tau(\Sigma) U^* \\ \mathcal{T}_\tau(\Sigma) &= \text{diag}(\min(\max(\sigma_i, -\tau), \tau)) \end{aligned}$$

which restricts the singular values of  $M$  between  $-\tau$  and  $\tau$ . As illustrated in figure 3.1, the saturation and soft-thresholding operators are related via

$$M = \mathcal{T}_\tau(M) + \mathcal{S}_\tau(M). \quad (3.10)$$

The above updates of Lagrange multipliers guarantee dual feasibility at each iteration, i.e.,  $\|Y_1^{k+1}\|_2 \leq \gamma$  for all  $k$ , which justifies the choice of stopping criteria in ensuring primal feasibility of the solution.

### 3.4.4 Choice of step-size for the dual update (3.7c), (3.7d)

We follow an enhanced variant of AMA [140] which utilizes an adaptive BB step-size selection [153] in (3.7b), (3.7c), and (3.7d) to guarantee sufficient dual ascent and positive definiteness of  $X$ . Our numerical experiments indicate that this heuristic provides

substantial acceleration relative to the use of a fixed step-size. Since the standard BB step-size may not always satisfy the feasibility or the sufficient ascent conditions, we employ backtracking to determine an appropriate step-size.

At the  $k$ th iteration of AMA, an initial step-size,

$$\rho_{k,0} = \frac{\sum_{i=1}^2 \|Y_i^{k+1} - Y_i^k\|_F^2}{\sum_{i=1}^2 \left\langle Y_i^{k+1} - Y_i^k, \nabla J_d(Y_i^k) - \nabla J_d(Y_i^{k+1}) \right\rangle}, \quad (3.11)$$

is adjusted through a backtracking procedure to guarantee positive definiteness of the subsequent iterate of (3.7a) and sufficient ascent of the dual function,

$$\mathcal{A}^\dagger(Y_1^{k+1}, Y_2^{k+1}) \succ 0 \quad (3.12a)$$

$$J_d(Y_1^{k+1}, Y_2^{k+1}) \geq J_d(Y^k) + \sum_{i=1}^2 \left( \left\langle \nabla J_d(Y_i^k), Y_i^{k+1} - Y_i^k \right\rangle + \frac{1}{2\rho_k} \|Y_i^{k+1} - Y_i^k\|_F^2 \right). \quad (3.12b)$$

Here,  $\nabla J_d$  is the gradient of the dual function and the right-hand-side of (3.12b) is a local quadratic approximation of the dual objective around  $Y_1^k$  and  $Y_2^k$ . Furthermore, (3.12a) guarantees the positive definiteness of  $X^{k+1}$ ; cf. (3.8).

Our customized AMA is summarized as Algorithm 1.

### 3.4.5 Computational complexity

The  $X$ -minimization step in AMA involves a matrix inversion, which takes  $O(n^3)$  operations. Similarly, the  $Z$ -minimization step amounts to a singular value decomposition and it requires  $O(n^3)$  operations. Since this step is embedded within an iterative backtracking procedure for selecting the step-size  $\rho_k$  (cf. Section 3.4.4), if the step-size selection takes  $q$  inner iterations the total computational cost for a single iteration of AMA is  $O(qn^3)$ . In contrast, the worst-case complexity of standard SDP solvers is  $O(n^6)$ .

### 3.4.6 AMA as a proximal gradient on the dual

In the follow up section, Section 3.4.7, we show that the gradient of the dual objective function over a convex domain is Lipschitz continuous. In the present section, we denote

---

**Algorithm 1** Customized Alternating Minimization Algorithm

---

**input:**  $A, G, \gamma > 0$ , tolerances  $\epsilon_1, \epsilon_2$ , and backtracking constant  $\beta \in (0, 1)$ .

**initialize:**  $k = 0$ ,  $\rho_{0,0} = 1$ ,  $\Delta_{\text{gap}} = \Delta_{\text{p}} = 2\epsilon_1$ ,  $Y_2^0 = O_{n \times n}$ , and choose  $Y_1^0$  such that  $\mathcal{A}_1^\dagger(Y_1^0) = (\gamma / \|Y_1^0\|_2) I_{n \times n}$ .

**while:**  $|\Delta_{\text{gap}}| > \epsilon_1$  and  $\Delta_{\text{p}} > \epsilon_2$ ,

$X^{k+1} = (\mathcal{A}^\dagger(Y_1^k, Y_2^k))^{-1}$

compute  $\rho_k$ : Largest feasible step in  $\{\beta^j \rho_{k,0}\}_{j=0,1,\dots}$

such that  $Y_1^{k+1}$  and  $Y_2^{k+1}$  satisfy (3.12)

$Z^{k+1} = \underset{Z}{\operatorname{argmin}} \mathcal{L}_{\rho_k}(X^{k+1}, Z, Y_1^k, Y_2^k)$

$Y_1^{k+1} = Y_1^k + \rho \left( \mathcal{A}_1(X^{k+1}) + Z^{k+1} \right)$

$Y_2^{k+1} = Y_2^k + \rho \left( \mathcal{A}_2(X^{k+1}) - G \right)$

$\Delta_{\text{p}} = \|\mathcal{A} X^{k+1} + \mathcal{B} Z^{k+1} - \mathcal{C}\|_F$

$\Delta_{\text{gap}} = -\log \det X^{k+1} + \gamma \|Z^{k+1}\|_* - J_d(Y_1^{k+1}, Y_2^{k+1})$

$k = k + 1$

choose  $\rho_{k,0}$  based on (3.11)

**endwhile**

**output:**  $\epsilon$ -optimal solutions,  $X^{k+1}$  and  $Z^{k+1}$ .

---

a bound on the Lipschitz constant by  $L$ , and prove that AMA with step-size  $\rho = 1/L$  works as a proximal gradient on the dual problem. This implies that (3.7c) and (3.7d) are equivalent to the updates obtained by applying the proximal gradient algorithm to (3.3).

The dual problem (3.3) takes the following form

$$\underset{Y_1, Y_2}{\text{minimize}} \quad f(Y_1, Y_2) + g(Y_1, Y_2) \quad (3.13)$$

where  $f(Y_1, Y_2) = -\log \det \mathcal{A}^\dagger(Y_1, Y_2) - \langle G, Y_2 \rangle$  and  $g(Y_1, Y_2)$  denotes the indicator function

$$\mathcal{I}(Y_1) = \begin{cases} 0, & \|Y_1\|_2 \leq \gamma \\ +\infty, & \text{otherwise.} \end{cases}$$

Both  $f: (\mathbb{C}^{n \times n}, \mathbb{C}^{p \times p}) \rightarrow \mathbb{R}$  and  $g: (\mathbb{C}^{n \times n}, \mathbb{C}^{p \times p}) \rightarrow \mathbb{R} \cup \{+\infty\}$  are closed proper convex functions and  $f$  is continuously differentiable. For  $Y_1 \in \mathbb{C}^{n \times n}$  and  $Y_2 \in \mathbb{C}^{p \times p}$ , the proximal operator of  $g$ ,  $\text{prox}_g: (\mathbb{C}^{n \times n}, \mathbb{C}^{p \times p}) \rightarrow (\mathbb{C}^{n \times n}, \mathbb{C}^{p \times p})$  is given by

$$\text{prox}_g(V_1, V_2) = \underset{Y_1, Y_2}{\text{argmin}} \quad g(Y_1, Y_2) + \frac{1}{2} \sum_{i=1}^2 \|Y_i - V_i\|_F^2$$

where  $V_1$  and  $V_2$  are fixed matrices. For (3.13), the proximal gradient method [154] determines the updates as

$$\left( Y_1^{k+1}, Y_2^{k+1} \right) := \text{prox}_{\rho g} \left( Y_1^k - \rho \nabla_{Y_1} f(Y_1^k, Y_2^k), Y_2^k - \rho \nabla_{Y_2} f(Y_1^k, Y_2^k) \right)$$

where  $\rho > 0$  is the step-size. For  $\rho \in (0, 1/L]$  this method converges with rate  $O(1/k)$  [155].

Application of the proximal gradient method to the dual problem (3.13) yields

$$Y_1^{k+1} := \underset{Y_1}{\text{argmin}} \left\langle \nabla_{Y_1} (-\log \det \mathcal{A}^\dagger(Y_1^k, Y_2^k)), Y_1 \right\rangle + \mathcal{I}(Y_1) + \frac{L}{2} \|Y_1 - Y_1^k\|_F^2 \quad (3.14a)$$

$$Y_2^{k+1} := \underset{Y_2}{\text{argmin}} \left\langle \nabla_{Y_2} (-\log \det \mathcal{A}^\dagger(Y_1^k, Y_2^k)), Y_2 \right\rangle + \langle G, Y_2 \rangle + \frac{L}{2} \|Y_2 - Y_2^k\|_F^2 \quad (3.14b)$$

The gradient in (3.14a) is determined by

$$\nabla_{Y_1} (-\log \det \mathcal{A}^\dagger(Y_1^k, Y_2^k)) = -\mathcal{A}_1(\mathcal{A}^\dagger(Y_1^k, Y_2^k)^{-1})$$

and we thus have

$$Y_1^{k+1} := \underset{Y_1}{\text{argmin}} \quad \mathcal{I}(Y_1) + \frac{L}{2} \|Y_1 - (Y_1^k + \frac{1}{L} \mathcal{A}_1(\mathcal{A}^\dagger(Y_1^k, Y_2^k)^{-1}))\|_F^2. \quad (3.15)$$

Since  $X^{k+1} = \mathcal{A}^\dagger(Y_1^k, Y_2^k)^{-1}$ , it follows that the dual update  $Y_1^{k+1}$  given by (3.7c) solves (3.15) with  $\rho = 1/L$ . This is because the saturation operator  $\mathcal{T}_\gamma$  represents the proximal mapping for the indicator function  $\mathcal{I}(Y_1)$  [154]. Finally, using the first order optimality conditions for (3.14b) it follows that the dual update

$$Y_2^{k+1} = Y_2^k + \frac{1}{L}(\mathcal{A}_2(\mathcal{A}^\dagger(Y_1^k, Y_2^k)^{-1}) - G)$$

is equivalent to (3.7d) with  $\rho = 1/L$ .

### 3.4.7 Convergence analysis

In this section we use the equivalence between AMA and the proximal gradient algorithm (on the dual problem) to prove convergence of our customized AMA. Before doing so, we first establish Lipschitz continuity of the gradient of the logarithmic barrier in the dual objective function over a pre-specified convex domain, and show that the dual iterates are bounded within this domain. These two facts allow us to establish sub-linear convergence of AMA for (2.18). Proofs of all technical statements presented here are provided in the appendix.

We define the ordered pair  $Y = (Y_1, Y_2) \in \mathbb{H}^n \times \mathbb{H}^p$  where

$$\mathbb{H}^n \times \mathbb{H}^p = \{(Y_1, Y_2) \mid Y_1 \in \mathbb{H}^n \text{ and } Y_2 \in \mathbb{H}^p\},$$

with  $\mathbb{H}^n$  denoting the set of Hermitian matrices of dimension  $n$ . We also assume the existence of an optimal solution  $\bar{Y} = (\bar{Y}_1, \bar{Y}_2)$  which is a fixed point of the dual updates (3.7c) and (3.7d), i.e.,

$$\begin{aligned}\bar{Y}_1 &= \mathcal{T}_\gamma(\bar{Y}_1 + \rho \mathcal{A}_1(\bar{X})) \\ \bar{Y}_2 &= \bar{Y}_2 + \rho(\mathcal{A}_2(\bar{X}) - G)\end{aligned}$$

where  $\bar{X} = \mathcal{A}^\dagger(\bar{Y})^{-1}$ . Since the proof of optimality for  $\bar{Y}$  follows a similar line of argument made in [140], we refrain from including further details.

While the gradient of  $J_d$  is not Lipschitz continuous over the entire domain of  $\mathbb{H}^n \times \mathbb{H}^p$ , we show its Lipschitz continuity over the convex domain

$$\mathcal{D}_{\alpha\beta} = \{Y \in \mathbb{H}^n \times \mathbb{H}^p \mid 0 < \alpha I \preceq \mathcal{A}^\dagger(Y) \preceq \beta I < \infty\} \quad (3.16)$$

for any  $0 < \alpha < \beta < \infty$ . This is stated in the next lemma, and its proof given in the appendix relies on showing that the Hessian of  $J_d$  is bounded from above.

**Lemma 2.** *For  $Y \in \mathcal{D}_{\alpha\beta}$ , the function  $\log \det \mathcal{A}^\dagger(Y)$  has a Lipschitz continuous gradient with Lipschitz constant  $L = \sigma_{\max}^2(\mathcal{A}^\dagger)/\alpha^2$ , where  $\sigma_{\max}(\mathcal{A}^\dagger)$  is the largest singular value*

of the operator  $\mathcal{A}^\dagger$ .

We next show that the dual AMA iterations (3.7c) and (3.7d) are contractive, which is essential in establishing that the iterates are bounded within the domain  $\mathcal{D}_{\alpha\beta}$ .

**Lemma 3.** *Consider the map  $Y \mapsto Y^+$*

$$Y_1^+ = \mathcal{T}_\gamma(Y_1 + \rho \mathcal{A}_1(\mathcal{A}^\dagger(Y)^{-1})) \quad (3.17a)$$

$$Y_2^+ = Y_2 + \rho(\mathcal{A}_2(\mathcal{A}^\dagger(Y)^{-1}) - G), \quad (3.17b)$$

where  $Y = (Y_1, Y_2)$ . Let  $0 < \alpha < \beta < \infty$  be such that

$$\alpha I \preceq \mathcal{A}^\dagger(\bar{Y}) \preceq \beta I,$$

where  $\bar{Y} = (\bar{Y}_1, \bar{Y}_2)$  denotes a fixed point of (3.17). Then, for any  $0 < \rho \leq \frac{2\alpha^4}{\beta^2 \sigma_{\max}^2(\mathcal{A})}$ , the map (3.17) is contractive over  $\mathcal{D}_{\alpha\beta}$ , that is,

$$\|Y^+ - \bar{Y}\|_F \leq \|Y - \bar{Y}\|_F \quad \text{for any } Y \in \mathcal{D}_{\alpha\beta}.$$

As noted above, it follows that the dual AMA iterates  $\{Y^k\}$  belong to the domain  $\mathcal{D}_{\alpha\beta}$ . This is stated explicitly next in Lemma 4. In fact, the lemma establishes universal lower and upper bounds on  $\mathcal{A}^\dagger(Y^k)$  for all  $k$ . These bounds guarantees that the dual iterates  $\{Y^k\}$  belong to the domain  $\mathcal{D}_{\alpha\beta}$  and that Lipschitz continuity of the gradient of the dual function is preserved through the iterations.

**Lemma 4.** *Given a feasible initial condition  $Y^0$ , i.e.,  $Y^0$  satisfies  $\mathcal{A}^\dagger(Y^0) \succ 0$  and  $\|Y_1^0\|_2 \leq \gamma$ , let  $\alpha, \beta > 0$*

$$\beta = \sigma_{\max}(\mathcal{A}^\dagger) \|Y^0 - \bar{Y}\|_F + \|\mathcal{A}^\dagger(\bar{Y})\|_2$$

$$\alpha = \det \mathcal{A}^\dagger(Y^0) \beta^{1-n} e^{-\langle G, Y_2^0 \rangle - \gamma \sqrt{n} \sigma_{\max}(\mathcal{A}_1^\dagger) \text{trace}(\bar{X})}.$$

Then, for any positive step-size  $\rho \leq \frac{2\alpha^4}{\beta^2 \sigma_{\max}^2(\mathcal{A})}$ , we have

$$\alpha I \preceq \mathcal{A}^\dagger(Y^k) \preceq \beta I \quad \text{for all } k \geq 0.$$

Since AMA works as a proximal gradient on the dual problem its convergence properties follow from standard theoretical results for proximal gradient methods [155]. In particular, it can be shown that the proximal gradient algorithm with step-size  $\rho = 1/L$  ( $L$  being the Lipschitz constant in Lemma 2) falls into a general family of *majorization-minimization* algorithms for which convergence properties are well-established [156].

The logarithmic barrier in the dual function is convex and continuously differentiable. Furthermore, its gradient is Lipschitz continuous over the domain  $\mathcal{D}_{\alpha\beta}$ . Therefore, starting from the pair  $Y^0 = (Y_1^0, Y_2^0)$  a positive step-size

$$\rho \leq \min \left\{ \frac{2\alpha^4}{\beta^2 \sigma_{\max}^2(\mathcal{A})}, \frac{\alpha^2}{\sigma_{\max}^2(\mathcal{A}^\dagger)} \right\}$$

guarantees that  $\{Y^k\}$  converges to  $\bar{Y}$  at a sub-linear rate that is no worse than  $O(1/k)$ ,

$$J_d(Y^k) - J_d(\bar{Y}) \leq O(1/k).$$

Since  $\mathcal{A}^\dagger$  is not an invertible mapping,  $-\log \det \mathcal{A}^\dagger(Y)$  cannot be strongly convex over  $\mathcal{D}_{\alpha\beta}$ . Thus, in general, AMA with a constant step-size cannot achieve a linear convergence rate [157, 158]. In computational experiments, we observe that a heuristic step-size selection (BB step-size initialization followed by backtracking) can improve the convergence of AMA; see Section 3.6.

### 3.5 Alternating Direction Method of Multipliers (ADMM)

Another splitting method that can be used to solve the optimization problem (2.18) is the Alternating Direction Method of Multipliers (ADMM). In contrast to AMA, ADMM minimizes the augmented Lagrangian  $\mathcal{L}_\rho$  in each step of the iterative procedure,

$$X^{k+1} := \underset{X}{\operatorname{argmin}} \mathcal{L}_\rho(X, Z^k; Y_1^k, Y_2^k) \quad (3.18a)$$

$$Z^{k+1} := \underset{Z}{\operatorname{argmin}} \mathcal{L}_\rho(X^{k+1}, Z; Y_1^k, Y_2^k) \quad (3.18b)$$

$$Y_1^{k+1} := Y_1^k + \rho \left( \mathcal{A}_1(X^{k+1}) + Z^{k+1} \right) \quad (3.18c)$$

$$Y_2^{k+1} := Y_2^k + \rho \left( \mathcal{A}_2(X^{k+1}) - G \right). \quad (3.18d)$$

These terminate when the primal and dual residuals are sufficiently small [150, Section 3.3], i.e.,

$$\begin{aligned} \|\mathcal{A}X^{k+1} + \mathcal{B}Z^{k+1} - \mathcal{C}\|_F &\leq \epsilon \\ \|\rho \mathcal{A}_1^\dagger (Z^{k+1} - Z^k)\|_F &\leq \epsilon. \end{aligned}$$

In addition, ADMM does not have efficient step-size selection rules. Typically, either a constant step-size is selected or the step-size is adjusted to keep the norms of primal and dual residuals within a constant factor of one another [150].

While the  $Z$ -minimization step is equivalent to that of AMA, the  $X$ -update in ADMM

is obtained by minimizing the augmented Lagrangian. This amounts to solving the following optimization problem

$$\underset{X}{\text{minimize}} \quad -\log \det X + \frac{\rho}{2} \sum_{i=1}^2 \|\mathcal{A}_i(X) - U_i^k\|_F^2 \quad (3.19)$$

where  $U_1^k := -(Z^k + (1/\rho)Y_1^k)$  and  $U_2^k := G - (1/\rho)Y_2^k$ . From first order optimality conditions we have

$$-X^{-1} + \rho \mathcal{A}_1^\dagger(\mathcal{A}_1(X) - U_1^k) + \rho \mathcal{A}_2^\dagger(\mathcal{A}_2(X) - U_2^k) = 0.$$

Since  $\mathcal{A}_1^\dagger \mathcal{A}_1$  and  $\mathcal{A}_2^\dagger \mathcal{A}_2$  are not unitary operators, the  $X$ -minimization step *does not have an explicit solution*.

In what follows, we use a proximal gradient method [154] to update  $X$ . By linearizing the quadratic term in (3.19) around the current inner iterate  $X_i$  and adding a quadratic penalty on the difference between  $X$  and  $X_i$ ,  $X_{i+1}$  is obtained as the minimizer of

$$-\log \det X + \rho \sum_{j=1}^2 \left\langle \mathcal{A}_j^\dagger \left( \mathcal{A}_j(X_i) - U_j^k \right), X \right\rangle + \frac{\mu}{2} \|X - X_i\|_F^2. \quad (3.20)$$

To ensure convergence of the proximal gradient method [154], the parameter  $\mu$  has to satisfy  $\mu \geq \rho \lambda_{\max}(\mathcal{A}_1^\dagger \mathcal{A}_1 + \mathcal{A}_2^\dagger \mathcal{A}_2)$ , where we use power iteration to compute the largest eigenvalue of the operator  $\mathcal{A}_1^\dagger \mathcal{A}_1 + \mathcal{A}_2^\dagger \mathcal{A}_2$ .

By taking the variation of (3.20) with respect to  $X$ , we obtain the first order optimality condition

$$\mu X - X^{-1} = \mu X_i - \rho \sum_{j=1}^2 \mathcal{A}_j^\dagger \left( \mathcal{A}_j(X_i) - U_j^k \right). \quad (3.21)$$

The solution to (3.21) is given by

$$X_{i+1} = V \text{diag}(g) V^*,$$

where the  $j$ th entry of the vector  $g \in \mathbb{R}^n$  is given by

$$g_j = \frac{\lambda_j}{2\mu} + \sqrt{\left(\frac{\lambda_j}{2\mu}\right)^2 + \frac{1}{\mu}}.$$

Here,  $\lambda_j$ 's are the eigenvalues of the matrix on the right-hand-side of (3.21) and  $V$  is the matrix of the corresponding eigenvectors. As it is typically done in proximal gradient algorithms [154], starting with  $X_0 := X^k$ , we obtain  $X^{k+1}$  by repeating inner iterations until the desired accuracy is reached.

### 3.5.1 Computational complexity

The above described method involves an eigenvalue decomposition in each inner iteration of the  $X$ -minimization problem, which requires  $O(n^3)$  operations. Therefore, if the  $X$ -minimization step takes  $q$  inner iterations to converge, a single outer iteration of ADMM requires  $O(qn^3)$  operations. Thus, ADMM and AMA have similar computational complexity; cf. Section 3.4.5. However, in Section 3.6 we demonstrate that, relative to ADMM, customized AMA provides significant speed-up via a heuristic step-size selection (i.e., a BB step-size initialization followed by backtracking).

### 3.5.2 Accelerated ADMM

When both parts of the objective function are strongly convex, an accelerated variant of ADMM can be employed [139]. The accelerated algorithm is simply ADMM with a Nesterov-type (predictor-corrector) acceleration step. However, the presence of the nuclear norm in (2.18) prevents us from using such techniques. For weakly convex objective functions, restart rules in conjunction with acceleration techniques can be used to reduce oscillations that are often encountered in first-order iterative methods [139, 159].

The accelerated ADMM algorithm is given by,

$$\begin{aligned}
X^k &:= \operatorname{argmin}_X \mathcal{L}_\rho(X, \hat{Z}^k; \hat{Y}_1^k, \hat{Y}_2^k) \\
Z^k &:= \operatorname{argmin}_Z \mathcal{L}_\rho(X^{k+1}, Z; \hat{Y}_1^k, \hat{Y}_2^k) \\
Y_1^k &:= \hat{Y}_1^k + \rho \left( \mathcal{A}_1(X^{k+1}) + Z^{k+1} \right) \\
Y_2^k &:= \hat{Y}_2^k + \rho \left( \mathcal{A}_2(X^{k+1}) - G \right). \\
c_k &:= \frac{1}{\rho} \|Y_1^k - \hat{Y}_1^k\|_F^2 + \frac{1}{\rho} \|Y_2^k - \hat{Y}_2^k\|_F^2 + \rho \|Z^k - \hat{Z}^k\|_F^2 \\
&\text{if } c_k < \eta c_{k-1}, \\
&\quad \alpha_{k+1} := (1 + \sqrt{1 + 4\alpha_k^2})/2 \\
&\quad \hat{Z}^{k+1} := Z^k + \frac{\alpha_k - 1}{\alpha_{k+1}} (Z^k - Z^{k-1}) \\
&\quad \hat{Y}_1^{k+1} := Y_1^k + \frac{\alpha_k - 1}{\alpha_{k+1}} (Y_1^k - Y_1^{k-1}) \\
&\quad \hat{Y}_2^{k+1} := Y_2^k + \frac{\alpha_k - 1}{\alpha_{k+1}} (Y_2^k - Y_2^{k-1}) \\
&\text{else} \\
&\quad \alpha_{k+1} = 1, \hat{Z}^{k+1} = Z^{k-1}, \hat{Y}_1^{k+1} = Y_1^{k-1}, \hat{Y}_2^{k+1} = Y_2^{k-1} \\
&\quad c_k \leftarrow \eta^{-1} c_{k-1}
\end{aligned}$$

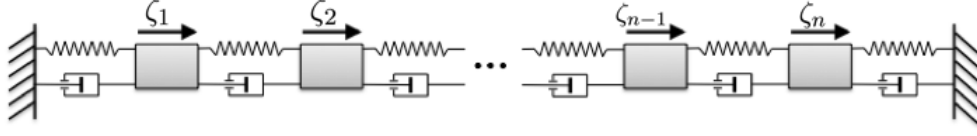


Figure 3.2: Mass-spring-damper system with  $n$  masses.

Following [139], the algorithm is initialized with  $Z^{-1} = \hat{Z}^0$ ,  $Y_1^{-1} = \hat{Y}_1^0$ ,  $Y_2^{-1} = \hat{Y}_2^0$ ,  $\rho > 0$ ,  $\alpha_1 = 1$ , and terminated using similar criteria as in the ADMM algorithm.

Since our computational experiments do not suggest a significant improvement using restart rules, we refrain from further discussing this variant of ADMM in Section 3.6 and refer the interested reader to our previously published conference paper [160].

### 3.6 Computational experiments

We provide an example to demonstrate the utility of our modeling and optimization framework. This is based on a stochastically-forced mass-spring-damper (MSD) system; see figure 3.2. Stochastic disturbances are generated by a low-pass filter,

$$\text{low-pass filter: } \dot{\zeta} = -\zeta + d \quad (3.22a)$$

where  $d$  represents a zero-mean unit variance white process. The state space representation of the MSD system is given by

$$\text{MSD system: } \dot{x} = Ax + B_\zeta \zeta \quad (3.22b)$$

where the state vector  $x = [p^* \ v^*]^*$ , contains position and velocity of masses. Accordingly, the state and input matrices are

$$A = \begin{bmatrix} O & I \\ -T & -I \end{bmatrix}, \quad B_\zeta = \begin{bmatrix} 0 \\ I \end{bmatrix}$$

where  $O$  and  $I$  are zero and identity matrices of suitable sizes, and  $T$  is a symmetric tridiagonal Toeplitz matrix with 2 on the main diagonal and  $-1$  on the first upper and lower sub-diagonals.

The steady-state covariance of system (3.22) can be found as the solution to the Lyapunov equation

$$\tilde{A}\Sigma + \Sigma\tilde{A}^* + \tilde{B}\tilde{B}^* = 0$$

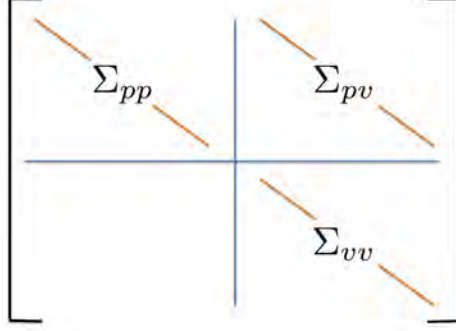


Figure 3.3: Partially available correlations of the MSD system.

where

$$\tilde{A} = \begin{bmatrix} A & B_\zeta \\ O & -I \end{bmatrix}, \quad \tilde{B} = \begin{bmatrix} 0 \\ I \end{bmatrix}$$

and

$$\Sigma = \begin{bmatrix} \Sigma_{xx} & \Sigma_{x\zeta} \\ \Sigma_{\zeta x} & \Sigma_{\zeta\zeta} \end{bmatrix}.$$

The matrix  $\Sigma_{xx}$  denotes the state covariance of the MSD system, partitioned as,

$$\Sigma_{xx} = \begin{bmatrix} \Sigma_{pp} & \Sigma_{pv} \\ \Sigma_{vp} & \Sigma_{vv} \end{bmatrix}.$$

We assume knowledge of one-point correlations of the position and velocity of masses, i.e., the diagonal elements of matrices  $\Sigma_{pp}$ ,  $\Sigma_{vv}$ , and  $\Sigma_{pv}$ . Thus, in order to account for these available statistics, we seek a state covariance  $X$  of the MSD system which agrees with the available statistics whose structure is displayed in figure 3.3.

Additional information about our computational experiments, along with MATLAB source codes, can be found at:

<http://www.ece.umn.edu/users/mihailo/software/ccama/>

Recall that in (2.18),  $\gamma$  determines the importance of the nuclear norm relative to the logarithmic barrier function. While larger values of  $\gamma$  yield solutions with lower rank, they may fail to provide reliable completion of the “ideal” state covariance  $\Sigma_{xx}$ . For various problem sizes, minimum error in matching  $\Sigma_{xx}$  is achieved with  $\gamma \approx 1.2$  and for larger values of  $\gamma$  the error gradually increases. For MSD system with 50 masses, figure 3.4a shows the relative error in matching  $\Sigma_{xx}$  as a function of  $\gamma$ . The smallest error is obtained for  $\gamma = 1.2$ , but this value of  $\gamma$  does not yield a low-rank input correlation  $Z$ . For  $\gamma = 2.2$  reasonable matching is obtained (82.7% matching) and the resulting  $Z$

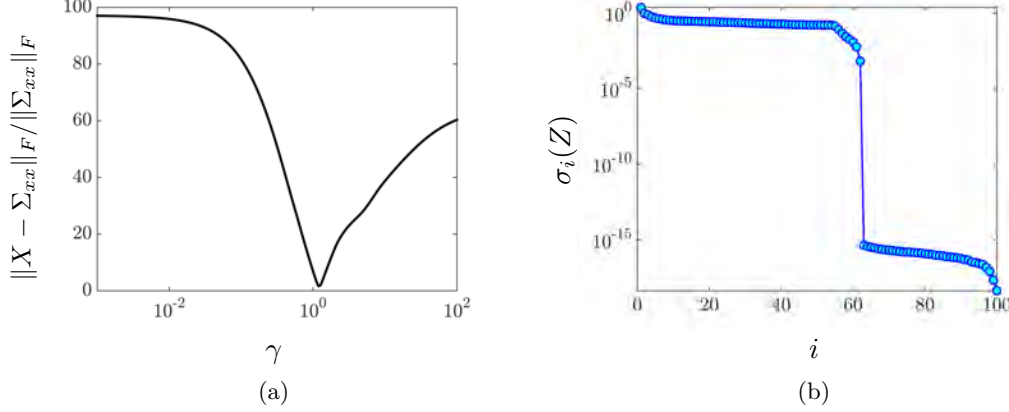


Figure 3.4: (a) The  $\gamma$ -dependence of the relative error (percents) between the solution  $X$  to (2.18) and the true covariance  $\Sigma_{xx}$  for the MSD system with 50 masses; (b) singular values of the solution  $Z$  to (2.18) for  $\gamma = 2.2$ .

Table 3.1: Solve times (in seconds) for different number of masses and  $\gamma = 2.2$ .

| n   | CVX   | ADMM   | AMA    | AMA <sub>BB</sub> |
|-----|-------|--------|--------|-------------------|
| 10  | 28.4  | 2      | 1.3    | 0.5               |
| 20  | 419.7 | 54.7   | 30.7   | 2.2               |
| 50  | —     | 3442.9 | 3796.7 | 52.7              |
| 100 | —     | 40754  | 34420  | 5429.8            |

displays a clear-cut in its singular values with 62 of them being nonzero; see figure 3.4b.

For  $\gamma = 2.2$ , Table 3.1 compares solve times of CVX [134] and the customized algorithms of Sections 3.4 and 3.5. All algorithms were implemented in MATLAB and executed on a 3.4 GHz Core(TM) i7-2600 Intel(R) machine with 12GB RAM. Each method stops when an iterate achieves a certain distance from optimality, i.e.,  $\|X^k - X^*\|_F / \|X^*\|_F < \epsilon_1$  and  $\|Z^k - Z^*\|_F / \|Z^*\|_F < \epsilon_2$ . The choice of  $\epsilon_1, \epsilon_2 = 0.01$ , guarantees that the primal objective is within 0.1% of  $J_p(X^*, Z^*)$ . For  $n = 50$  and  $n = 100$ , CVX ran out of memory. Clearly, for large problems, AMA with BB step-size initialization significantly outperforms both regular AMA and ADMM.

For a MSD system with 50 masses and  $\gamma = 2.2$ , we now focus on the convergence of AMA. Figure 3.5a shows monotonic increase of the dual objective function. The absolute

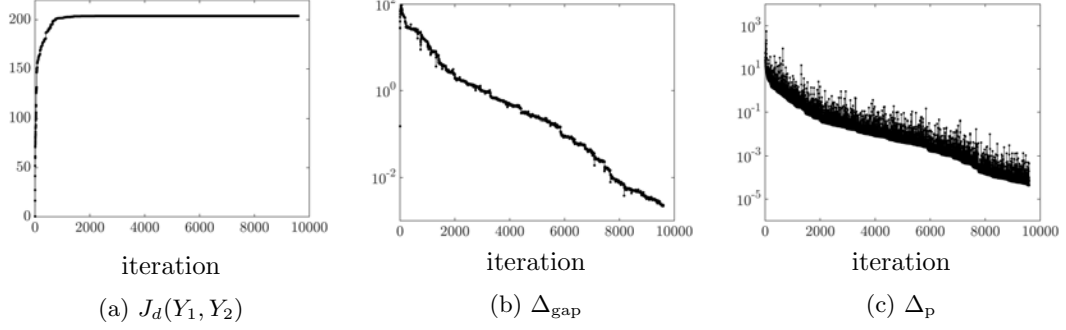


Figure 3.5: Performance of AMA<sub>BB</sub> for the MSD system with 50 masses,  $\gamma = 2.2$ ,  $\epsilon_1 = 0.005$ , and  $\epsilon_2 = 0.05$ . (a) The dual objective function  $J_d(Y_1, Y_2)$  of (2.18); (b) the duality gap,  $|\Delta_{\text{gap}}|$ ; and (c) the primal residual,  $\Delta_p$ .

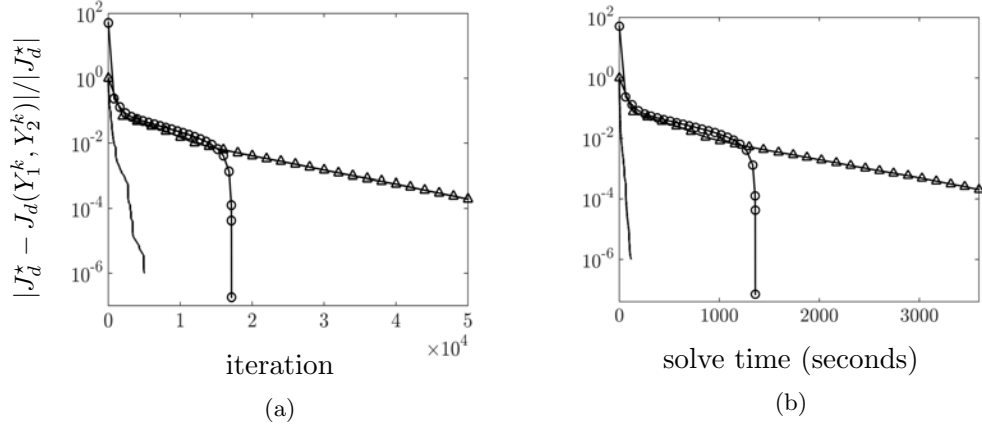


Figure 3.6: Convergence curves showing performance of ADMM ( $\circ$ ) and AMA with ( $-$ ) and without ( $\triangle$ ) BB step-size initialization vs. (a) the number of iterations; and (b) solve times for the MSD system with 50 masses and  $\gamma = 2.2$ . Here,  $J_d^*$  is the value of the optimal dual objective.

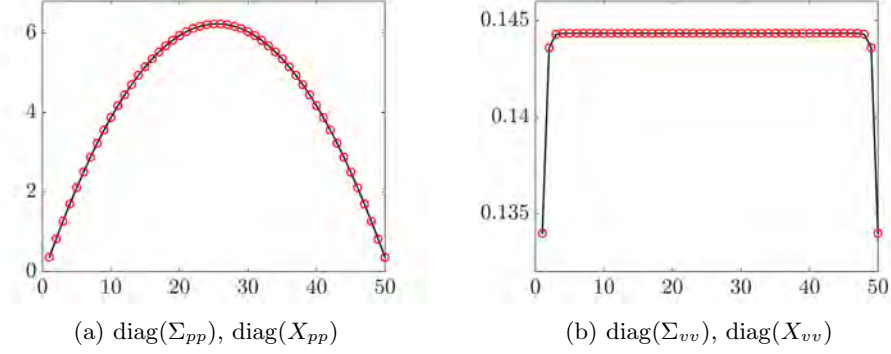


Figure 3.7: Diagonals of (a) position and (b) velocity covariances for the MSD system with 50 masses; Solid black lines show diagonals of  $\Sigma_{xx}$  and red circles mark solutions of optimization problem (2.18).

value of the duality gap  $|\Delta_{\text{gap}}|$  and the primal residual  $\Delta_p$  demonstrate convergence of our customized algorithm; see figures 3.5b and 3.5c. In addition, figure 3.6a shows that regular AMA converges linearly to the optimal solution and that AMA with BB step-size initialization outperforms both regular AMA and ADMM. Thus, heuristic step-size initialization can improve the theoretically-established convergence rate. Similar trends are observed when convergence curves are plotted as a function of time; see 3.6b. Finally, figure 3.7 demonstrates feasibility of the optimization problem (2.18) and perfect recovery of the available diagonal elements of the covariance matrix.

For  $\gamma = 2.2$ , the spectrum of  $Z$  contains 50 positive and 12 negative eigenvalues. Based on Proposition 2,  $Z$  can be decomposed into  $BH^* + HB^*$ , where  $B$  has 50 independent columns. In other words, the identified  $X$  can be explained by driving the state-space model with 50 stochastic inputs  $u$ . The algorithm presented in Section 2.3.2 is used to decompose  $Z$  into  $BH^* + HB^*$ . For the identified input matrix  $B$ , the design parameter  $K$  is then chosen to satisfy the optimality criterion described in Section 2.2.3. This yields the optimal filter (2.9) that generates the stochastic input  $u$ . We use this filter to validate our approach as explained next.

We conduct linear stochastic simulations of system (2.9b) with zero-mean unit variance input  $w$ . Figure 3.8 shows the time evolution of the state variance of the MSD system. Since proper comparison requires ensemble-averaging, we have conducted twenty stochastic simulations with different realizations of the stochastic input  $w$  to (2.9b). The variance, averaged over all simulations, is given by the thick black line. Even though the responses of individual simulations differ from each other, the average of twenty sample sets asymptotically approaches the correct steady-state variance.

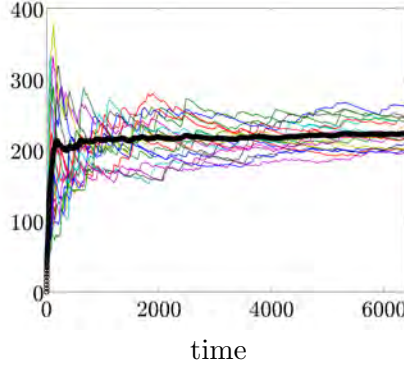


Figure 3.8: Time evolution of the variance of the MSD system's state vector for twenty realizations of white-in-time forcing to (2.9b). The variance averaged over all simulations is marked by the thick black line.

The recovered covariance matrix of mass positions  $X_{pp}$  resulting from the ensemble-averaged simulations of (2.9b) is shown in figure 3.9b. We note that (i) only diagonal elements of this matrix (marked by the black line) are used as data in the optimization problem (2.18), and that (ii) the recovery of the off-diagonal elements is remarkably consistent. This is to be contrasted with typical matrix completion techniques that require incoherence in sampling entries of the covariance matrix. The key in our formulation of structured covariance completion is the Lyapunov-like structural constraint (2.2b) in (2.18). Indeed, it is precisely this constraint that retains the relevance of the system dynamics and, thereby, the physics of the problem.

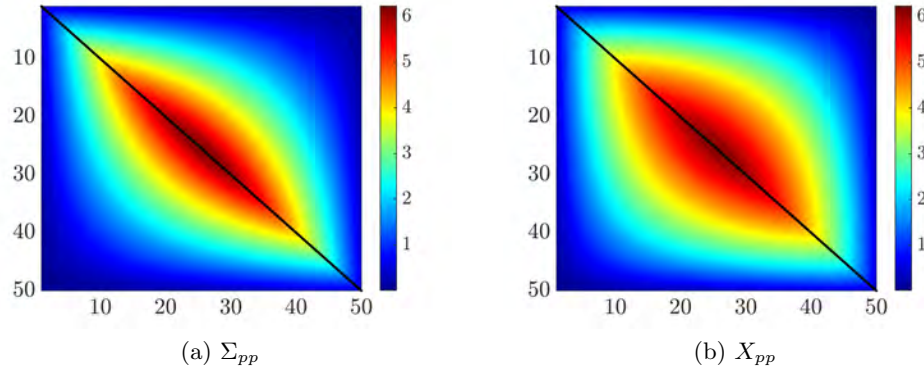


Figure 3.9: The true covariance  $\Sigma_{pp}$  of the MSD system and the covariance  $X_{pp}$  resulting from linear stochastic simulations of (2.9b). Available one-point correlations of the position of masses used in (2.18) are marked along the main diagonals.

## Chapter 4

# The use of the $r^*$ heuristic in covariance completion problems

As described in previous chapters, the covariance completion problem aims to complete partially known sample statistics in a way that is consistent with the underlying linear dynamics. The statistics of stochastic inputs are unknown and sought to explain the given correlations. Such inverse problems admit many solutions for the forcing correlations, but can be interpreted as an optimal low-rank approximation problem for identifying forcing models of low complexity. On the other hand, the quality of completion can be improved by utilizing information regarding the magnitude of unknown entries. In this chapter, we generalize theoretical results regarding the  $r^*$  norm approximation and demonstrate the performance of this heuristic in completing partially available statistics using stochastically-driven linear models.

### 4.1 Introduction

Matrix completion problems emerge in many applications (cf. [45, 46, 60]). In this chapter, we are interested in a class of structured covariance completion problems which arise as inverse problems in low-complexity modeling of complex dynamical systems. A particular class of models that can be used for this purpose are stochastically-driven linear models. Motivation for this choice arises in the modeling of fluid flows where the stochastically-forced linearized Navier-Stokes equations have proven capable of replicating structural features of wall-bounded shear flows [28–30, 33, 34, 113].

The problem of estimating covariances at the output of known linear systems has been previously addressed [161–163]. More recently, a modeling and optimization framework was proposed for designing stochastic forcing models of low complexity which account for

partially observed statistical signatures [164]. In this setup, the complexity is related to the rank of input correlation structures [164, 165]. This gives rise to a class of structured covariance completion problems that aim to complete partially observed statistical signatures in a way that is consistent with the assumed linear dynamics. In addition, the use of the nuclear norm as a convex surrogate for rank minimization [72, 73] has allowed for the development of efficient customized algorithms that handle large-size problems [160, 164]. This approach has particularly proven successful in the low-complexity modeling of turbulent fluid flows [34, 137, 166].

Recently, various benefits and applications of the so-called “ $r^*$  norm” (also called “ $k$ -support-norm”), as a natural extension of the nuclear norm, have been demonstrated [79–86]. In particular, its relation with the optimal rank  $r$  approximation under convex constraints has been investigated [79, 85]. Herein, we utilize these theoretical results to address the covariance completion problem as a special case of low-rank approximation. We demonstrate the ability of this approach in improving the quality of completion while maintaining (or even lowering) the complexity of the required forcing model compared to the nuclear norm relaxation.

The outline of this chapter is as follows. In Section 5.2, we provide a detailed background of the considered covariance completion problem and motivate the use of the  $r^*$  norm, which is formally introduced in Section 4.3.1. Subsequently, we present two new convex relaxations to our problem in Section 4.3.2. In Section 4.4, we provide illustrative examples to support our theoretical developments.

## 4.2 Problem Formulation

Consider the linear time-invariant (LTI) system with state-space representation

$$\begin{aligned}\dot{x} &= Ax + Bu \\ y &= Cx\end{aligned}\tag{4.1}$$

where  $x(t) \in \mathbb{C}^n$  is the state vector,  $y(t) \in \mathbb{C}^p$  is the output,  $u(t) \in \mathbb{C}^m$  is a zero-mean stationary stochastic process,  $A \in \mathbb{C}^{n \times n}$  is Hurwitz, and  $B \in \mathbb{C}^{n \times m}$  is the input matrix with  $m \leq n$ . For controllable  $(A, B)$ , a positive-definite matrix  $X$  qualifies as the steady-state covariance matrix of the state vector  $x(t)$  if and only if the Lyapunov-like equation

$$AX + XA^* = -(BH^* + HB^*),\tag{4.2}$$

is solvable for  $H \in \mathbb{C}^{n \times m}$  [121, 122]. Equation (4.2) provides an algebraic characterization of state covariances of linear dynamical systems driven by white or colored stochastic processes. For white noise  $u$  with covariance  $W$ ,  $H = BW/2$  and (4.2) simplifies to

the standard algebraic Lyapunov equation

$$A X + X A^* = -B W B^*. \quad (4.3)$$

The main difference between (4.2) and (4.3) is that the right-hand-side,  $-B W B^*$  in (4.3) is negative semi-definite.

We are interested in the setup where the matrix  $A$  in (4.1) is known but due to experimental or numerical limitations, only partial correlations between a limited number of state components are available. Moreover, it is often the case that the origin and directionality of the stochastic excitation  $u$  is unknown. Interestingly, the solvability of (4.2) can be shown to be equivalent to the following rank condition:

$$\text{rank} \begin{bmatrix} A X + X A^* & B \\ B^* & 0 \end{bmatrix} = \text{rank} \begin{bmatrix} 0 & B \\ B^* & 0 \end{bmatrix}.$$

This implies that any positive-definite matrix  $X$  is admissible as a covariance of the LTI system (4.1) if the input matrix  $B$  is full row rank [121], which eliminates the role of the dynamics inherent in  $A$ . Hence, it is desirable to limit the rank of the input matrix  $B$ .

In [164], an optimization framework was developed to account for partially known sampled second-order statistics using stochastically-forced LTI models. In this framework, the complexity of the model is reflected by the rank of the input matrix  $B$ , which is bounded by the rank of [164, 165]

$$Z := -(A X + X A^*).$$

Based on this, the structured covariance completion problem is given by

$$\begin{aligned} & \underset{X, Z}{\text{minimize}} && \text{rank}(Z) \\ & \text{subject to} && A X + X A^* + Z = 0 \\ & && (C X C^*) \circ E - G = 0 \\ & && X \succ 0, \end{aligned} \quad (4.4)$$

in which matrices  $A$ ,  $C$ ,  $E$ , and  $G$  are problem data, and Hermitian matrices  $X$ ,  $Z \in \mathbb{C}^{n \times n}$  are optimization variables. While the steady-state covariance matrix  $X$  is required to be positive definite, the matrix  $Z$  may have both positive and negative eigenvalues. This is in contrast to the case of white-in-time input  $u$  where the matrix  $Z$  is positive semi-definite. Entries of  $G$  represent partially available second-order statistics and  $C$ , the output matrix, establishes the relationship between entries of the matrix  $X$  and partially available statistics resulting from experiments or simulations. The symbol  $\circ$

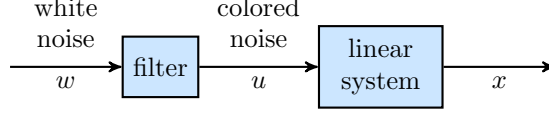


Figure 4.1: A cascade connection of an LTI system with a linear filter that is designed to account for the sampled steady-state covariance matrix  $X$ .

denotes elementwise matrix multiplication and  $E$  is the structural identity matrix,

$$E_{ij} = \begin{cases} 1, & \text{if } G_{ij} \text{ is available} \\ 0, & \text{if } G_{ij} \text{ is unavailable.} \end{cases}$$

Due to the non-convexity of the rank function, problem (4.4) is difficult to solve. Typically, the nuclear norm, i.e., the sum of singular values of a matrix,  $\|Z\|_* := \sum_i \sigma_i(Z)$ , is used as a proxy for rank minimization [72, 73]. This prompts the following convex reformulation:

$$\begin{aligned} & \underset{X, Z}{\text{minimize}} && \|Z\|_* \\ & \text{subject to} && AX + XA^* + Z = 0 \\ & && (CXC^*) \circ E - G = 0 \\ & && X \succ 0, \end{aligned}$$

The solution is used to construct spatio-temporal filters that generate colored-in-time forcing correlations that account for the observed statistics [121, 122, 164]; see Figure 4.1.

The nuclear norm is the convex envelope of the rank function over the unit ball  $\|Z\|_2 \leq 1$  and in conjunction with incoherence conditions has been utilized to provide theoretical guarantees for standard matrix completion problems [73]. However, for problem (4.4), the additional structural constraint that arises from the Lyapunov-like equation prevents us from taking advantage of these standard theoretical results. In addition, even though the nuclear norm heuristic achieves a low-rank solution for  $Z$  with a clear-cut in its singular values, it may not give good completion of the covariance matrix  $X$ . It is thus important to examine more refined convex relaxations that may result in better completion.

In [85], it has been demonstrated that when the magnitudes of unknown entries are significantly smaller than that of the known ones, the nuclear norm often creates regions of large entries which deviate from the ground truth. In the next section, we demonstrate that the  $r^*$  norm is more suitable if the objective is to keep both the rank and the Frobenius norm of the correlation structures small.

### 4.3 Low-rank approximation

We next introduce the  $r^*$  norm and provide a brief summary of its properties. A more elaborate presentation of these theoretical developments can be found in [85].

#### 4.3.1 Preliminaries

In the following, let  $\sigma_1(M) \geq \dots \geq \sigma_{\min\{m,n\}}(M)$  denote the increasingly sorted singular values of  $M \in \mathbb{R}^{n \times m}$ , counted with multiplicity. Moreover, given a singular value decomposition  $M = \sum_{i=1}^{\min\{m,n\}} \sigma_i(M) u_i v_i^T$  of  $M$ , we define  $\text{svd}_r(M) := \sum_{i=1}^r \sigma_i(M) u_i v_i^T$ .

**Lemma 5.** *Let  $M \in \mathbb{R}^{n \times m}$  and  $1 \leq r \leq q := \min\{m, n\}$ . The  $r$  norm of the matrix  $M$*

$$\|M\|_r := \sqrt{\sum_{i=1}^r \sigma_i^2(M)}$$

*is unitarily-invariant and its dual-norm is the  $r^*$  norm*

$$\|M\|_{r^*} := \max_{\|X\|_r \leq 1} \langle M, X \rangle.$$

*It holds that*

- $\|M\|_1 \leq \dots \leq \|M\|_q = \|M\|_F = \|M\|_{q^*} \leq \dots \leq \|M\|_{1^*}$
- $\text{rank}(M) \leq r$  if and only if  $\|M\|_r = \|M\|_F = \|M\|_{r^*}$ ,

*where  $\|\cdot\|_F$  denotes the Frobenius norm.*

The nuclear norm and the  $r^*$  norm coincide for  $r = 1$ . Thus, minimizing  $\|\cdot\|_{r^*}$  with  $r > 1$  can have a more significant influence on decreasing  $\|\cdot\|_F$  than  $\|\cdot\|_{1^*}$ . This is also motivated by the following Proposition.

**Proposition 5.** *Let  $\mathcal{C} \subset \mathbb{R}^{n \times m}$  be a closed convex set, then*

$$\begin{aligned} \inf_{\substack{M \in \mathcal{C} \\ \text{rank}(M) \leq r}} \|M\|_F^2 &\geq \max_{D \in \mathcal{C}^*} \left[ \inf_{M \in \mathcal{C}} \langle D, M \rangle - \|D\|_r^2 \right] \\ &= \min_{M \in \mathcal{C}} \|M\|_{r^*}^2 \end{aligned} \tag{4.5}$$

*where  $\mathcal{C}^* := \{D \in \mathbb{R}^{n \times m} : \inf_{M \in \mathcal{C}} \langle D, M \rangle > -\infty\}$ . Let the maximum and the minimum in (4.5) be achieved by  $D^* \in \mathcal{C}^*$  and  $M^*$ , respectively.*

- *If  $\sigma_r(D^*) \neq \sigma_{r+1}(D^*)$ , then the infimum on the left equals the maximum on the right and  $M^* = \text{svd}_r(D^*)$ .*

- If  $\sigma_r(D^*) = \dots = \sigma_{r+s}(D^*) > \sigma_{r+s+1}(D^*) \neq 0$  for some  $s \geq 1$  then  $\text{rank}(M^*) \leq r + s$ .

*Proof.* See [85].

Hence, in an ideal situation, i.e.  $\sigma_r(D^*) \neq \sigma_{r+1}(D^*)$ ,  $r$  has a strong correlation with the true rank of the matrix that one aims to complete. This will be seen in several examples in Section 4.4.

We next concentrate on the case of  $\sigma_r(D_r^*) = \sigma_{r+1}(D_r^*)$ , i.e.,  $\text{rank}(M_r^*) > r$  where we define

$$M_r^* := \underset{M \in \mathcal{C}}{\text{argmin}} \|M\|_{r^*}^2$$

$$D_r^* := \underset{D \in \mathcal{C}^*}{\text{argmax}} \left[ \inf_{M \in \mathcal{C}} \langle D, M \rangle - \|D\|_r^2 \right]$$

for  $1 \leq r \leq \min\{m, n\}$ . Assume that  $r + 1 \leq \text{rank}(M_r^*) < \text{rank}(M_{r+1}^*)$  and  $\|M_r^*\|_F > \|M_{r+1}^*\|_F$ . In this very common situation (cf. Section 4.4),  $M_r$  may still be of sufficiently small rank but too high cost. Conversely,  $M_{r+1}$  may have sufficiently small cost but too high rank. Therefore, a trade-off between these two solutions is desired, which can be achieved by allowing for a non-integer valued  $r$ , i.e.

$$\|\cdot\|_r := \sqrt{\sum_{i=1}^{\lfloor r \rfloor} \sigma_i^2(\cdot) + (r - \lfloor r \rfloor) \sigma_{\lfloor r \rfloor}^2(\cdot)},$$

where  $\lfloor r \rfloor := \max\{z \in \mathbb{Z} : z \leq r\}$  and  $\lceil r \rceil := \min\{z \in \mathbb{Z} : z \geq r\}$ . Letting  $M_r^*$  and  $D_r^*$  be also defined for  $r \in \mathbb{R}$ , it remains true that  $\text{rank}(M_r^*) \leq \lceil r \rceil + s$  if  $\sigma_{\lceil r \rceil}(D_r^*) = \dots = \sigma_{\lceil r \rceil + s}(D_r^*) > \sigma_{\lceil r \rceil + s + 1}(D_r^*)$ . Moreover, for  $r \in \mathbb{N}$  and  $\alpha \in [0, 1]$ ,  $\|\cdot\|_{r+1-\alpha}^2$  is given by the convex combination of  $\|\cdot\|_r^2$  and  $\|\cdot\|_{r+1}^2$ ,

$$\|\cdot\|_{r+1-\alpha}^2 = \alpha \|\cdot\|_r^2 + (1 - \alpha) \|\cdot\|_{r+1}^2.$$

This indicates the usefulness of the real-valued  $r$  norm to achieve the desired trade-off. In conjunction with Lemma 5 it follows that

$$F(D, r) := \inf_{M \in \mathcal{C}} \langle D, M \rangle - \|D\|_r^2$$

is concave. Thus, Berge's Maximum Theorem (see [167, page 116]) implies that the

parameter depending set

$$\mathcal{C}^*(r) := \operatorname{argmax}_{D \in \mathcal{C}^*} \left[ \inf_{M \in \mathcal{C}} \langle D, M \rangle - \|D\|_r^2 \right]$$

is upper hemicontinuous in  $r$ , i.e. for all  $r \in [1, \min\{m, n\}]$  and all  $\varepsilon > 0$ , there exists  $\delta > 0$  such that for all  $t \geq 1$

$$|t - r| < \delta \Rightarrow \mathcal{C}^*(t) \subset \mathcal{B}_\varepsilon(\mathcal{C}^*(r)),$$

where  $\mathcal{B}_\varepsilon(\mathcal{C}^*(r)) := \{X : \exists D \in \mathcal{C}^*(r) : \|X - D\|_F < \varepsilon\}$ . Assume for simplicity that  $D_r^*$  is unique, then it follows that a sufficiently small increase of  $r$  cannot increase  $s$ . Therefore, as for the nuclear regularization [72], one often expects  $\operatorname{rank}(M_t^*)$  to look like a staircase function of  $t \in [r, r + 1]$ .

### 4.3.2 Convex reformulation

Based on these theoretical developments, the  $r^*$  norm can be employed as a convex proxy for the rank function. This prompts the following convex relaxation of the covariance completion problem (4.4),

$$\begin{aligned} & \underset{X, Z}{\text{minimize}} && \|Z\|_{r^*} \\ & \text{subject to} && AX + XA^* + Z = 0 \\ & && (CXC^*) \circ E - G = 0 \\ & && X \succ 0. \end{aligned} \tag{4.6}$$

which can be formulated as the semi-definite program (SDP)

$$\begin{aligned} & \underset{X, Z}{\text{minimize}} && \operatorname{trace}(W) \\ & \text{subject to} && \begin{bmatrix} I - P & Z \\ Z^* & W \end{bmatrix} \succeq 0 \\ & && \operatorname{trace}(P) - n + r = 0 \\ & && AX + XA^* + Z = 0 \\ & && (CXC^*) \circ E - G = 0 \\ & && X \succ 0 \quad P \succeq 0. \end{aligned} \tag{4.7}$$

Problem (4.7) results from taking the Lagrange dual of the SDP characterization of the  $r$  norm; see [79] for details.

In the next section we present illustrative examples which demonstrate the benefit of using the  $r^*$  norm over the nuclear norm. Based on the discussion in Section 4.3.1, and

for a fair comparison, we also consider the alternative formulation

$$\begin{aligned}
& \underset{X, Z}{\text{minimize}} && \|Z\|_F^2 + \gamma \|Z\|_* \\
& \text{subject to} && AX + XA^* + Z = 0 \\
& && (CXC^*) \circ E - G = 0 \\
& && X \succ 0.
\end{aligned} \tag{4.8}$$

This formulation has been discussed earlier in [74]. It intends to mimic the behavior of the  $r^*$  norm and allows us to achieve a trade-off using the tuning parameter  $\gamma$ . Here,  $\|Z\|_F^2$  is regularized by the nuclear norm of  $Z$  and the parameter  $\gamma$  determines the weight on the nuclear norm.

## 4.4 Examples

### 4.4.1 Two-dimensional heat equation

We provide an example to compare the performance of the relaxation in problem (4.6) with the performance of the hybrid objective considered in problem (4.8). This is based on the two-dimensional heat equation

$$\dot{T} = \Delta T = \frac{\partial^2}{\partial x^2} T + \frac{\partial^2}{\partial y^2} T$$

on the unit square. Inputs are introduced through the Dirichlet boundary conditions of the four edges, i.e.,  $\xi = [\xi_1 \cdots \xi_4]^T$ . Finite difference discretization of the Laplacian operator on a uniform grid with step-size  $h = \frac{1}{n+1}$  gives

$$\Delta T_{ij} \approx -\frac{1}{h^2}(4T_{ij} - T_{i+1,j} - T_{i,j+1} - T_{i-1,j} - T_{i,j-1}),$$

where  $T_{ij}$  is the temperature of the inner grid point on the  $i$ th row and  $j$ th column of the mesh. Based on this, the dynamic matrix  $A$  denotes an  $n^2 \times n^2$  Poisson-matrix and the input matrix  $B_\xi := [b_{ij}] \in \mathbb{R}^{n^2 \times 4}$  models the boundary conditions as inputs into the state dynamics. Here,  $b_{ij} = 0$  except for the following cases:

$$\begin{aligned}
b_{i1} &:= 1, & \text{for } i = 1, 2, \dots, n \\
b_{i2} &:= 1, & \text{for } i = n, 2n, \dots, n^2 \\
b_{i3} &:= 1, & \text{for } i = n(n-1) + 1, n(n-1) + 2, \dots, n^2 \\
b_{i4} &:= 1, & \text{for } i = 1, n+1, \dots, n(n-1) + 1
\end{aligned}$$

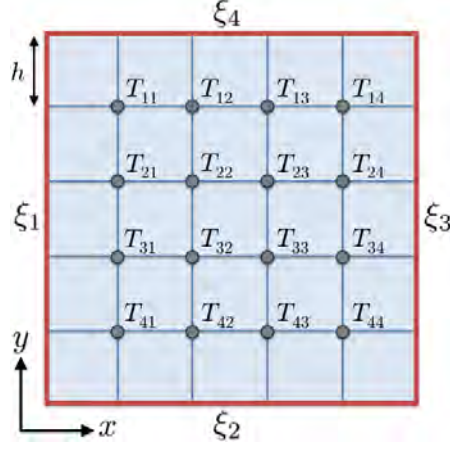


Figure 4.2: Discretized mesh on the unit square. The input enters the state equations through designated sides.

The dynamics of the discretized heat equation have the following state-space representation

$$\dot{x} = \frac{1}{h^2} A x + \frac{1}{h^2} B_{\xi} \xi, \quad (4.9a)$$

where  $x \in \mathbb{R}^{n^2}$  denotes the state. We assume that four input disturbances are generated by the low-pass filter

$$\dot{\xi} = -\xi + d. \quad (4.9b)$$

Here,  $d$  denotes a zero-mean unit variance white process.

The steady-state covariance of system (5.11) can be found as the solution to the Lyapunov equation

$$\tilde{A} \Sigma + \Sigma \tilde{A}^* + \tilde{B} \tilde{B}^* = 0$$

where

$$\tilde{A} = \begin{bmatrix} A & B_{\xi} \\ O & -I \end{bmatrix}, \quad \tilde{B} = \begin{bmatrix} 0 \\ I \end{bmatrix}$$

and

$$\Sigma = \begin{bmatrix} \Sigma_{xx} & \Sigma_{x\xi} \\ \Sigma_{\xi x} & \Sigma_{\xi\xi} \end{bmatrix}.$$

Here, the sub-covariance  $\Sigma_{xx}$  denotes the state covariance of the discretized heat equation (4.9a).

We use 16 points to discretize the square region ( $n = 4$ ), and restrict the input to enter through two sides by setting the second and fourth columns of  $B_{\xi}$  to zero. The

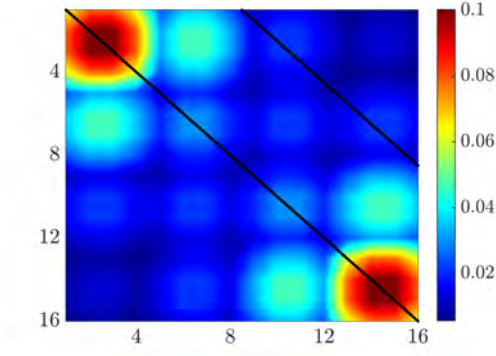


Figure 4.3: Interpolated colormap of the true steady-state covariance  $\Sigma_{xx}$  of the discretized heat equation. Available correlations used in (4.7) and (4.8) are marked by black lines.

covariance matrix of the state in (4.9a) is shown in figure 4.3 where black lines indicate known correlations that are used as problem data. We conduct a parametric study to determine the influence of  $r$  and  $\gamma$  on the solutions of (4.7) and (4.8).

Figures 4.4a and 4.4b respectively show the  $r$ -dependence and  $\gamma$ -dependence of the relative error of solutions to (4.7) and (4.8). For problem (4.7), minimum relative error is achieved with  $r = 2$ , as expected for a system with two inputs. On the other hand,  $\gamma = 8.46$  gives the best completion in problem (4.8). We note that the optimal solution for (4.7) results in a relative error which is about a third smaller (4.83% vs. 7.26%) with a corresponding matrix  $Z$  of lower rank (2 vs. 3).

Figure 4.5 shows the recovered covariance matrix of the discretized heat equation resulting from problems (4.7) and (4.8) and for various values of  $r$  and  $\gamma$ . Figures 4.5a and 4.5b correspond to the case of nuclear norm minimization ( $r = 1$ ) and optimal covariance completion ( $r = 2$ ) for problem (4.7). On the other hand, Figures 4.5c and 4.5d correspond to the solution of the Frobenius norm minimization ( $\gamma = 0$ ) and optimal covariance completion ( $\gamma = 8.46$ ) for problem (4.8). It is notable that the Frobenius norm minimization does not result in reasonable completion of the covariance matrix. Moreover, the nuclear norm creates off-diagonal spots of relatively large entries where the true covariance matrix is close to zero.

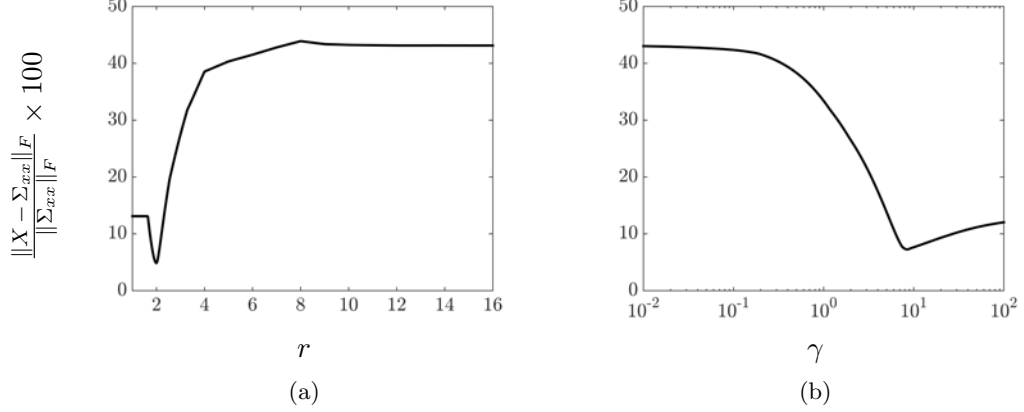


Figure 4.4: (a) The  $r$ -dependence of the relative Frobenius norm error (percents) between the solution  $X$  to (4.7) and the true covariance  $\Sigma_{xx}$  for the discretized 2D heat equation discretized using 16 points. (b) The  $\gamma$ -dependence of the relative error between the solution to (4.8) and the true covariance.

#### 4.4.2 Mass-spring-damper system

We provide an example of a stochastically-forced mass-spring-damper (MSD) system to demonstrate the utility of the  $r^*$  norm in the completion of diagonally dominant covariance matrices. The state space representation of the MSD system is given by

$$\dot{x} = Ax + B_\xi \xi$$

$$A = \begin{bmatrix} 0 & I \\ -T & -I \end{bmatrix}, \quad B_\xi = \begin{bmatrix} 0 \\ I \end{bmatrix}.$$

Here, the state vector contains the position and velocity of masses,  $x = [p^T \ v^T]^T$ ,  $0$  and  $I$  are zero and identity matrices of suitable sizes, and  $T$  is a symmetric tridiagonal Toeplitz matrix with 2 on the main diagonal and  $-1$  on the first upper and lower sub-diagonals.

Stochastic disturbances are generated by a similar low-pass filter as in the previous example and the steady-state covariance matrix of  $x$  is partitioned as

$$\Sigma_{xx} = \begin{bmatrix} \Sigma_{pp} & \Sigma_{pv} \\ \Sigma_{vp} & \Sigma_{vv} \end{bmatrix}.$$

We assume that stochastic forcing affects all masses. For  $n = 20$  masses, figure 4.6 shows the covariance matrices of positions  $\Sigma_{pp}$  and velocities  $\Sigma_{vv}$ . We assume knowledge of one-point correlations, i.e., diagonal entries of  $\Sigma_{pp}$  and  $\Sigma_{vv}$ . Note that in this example

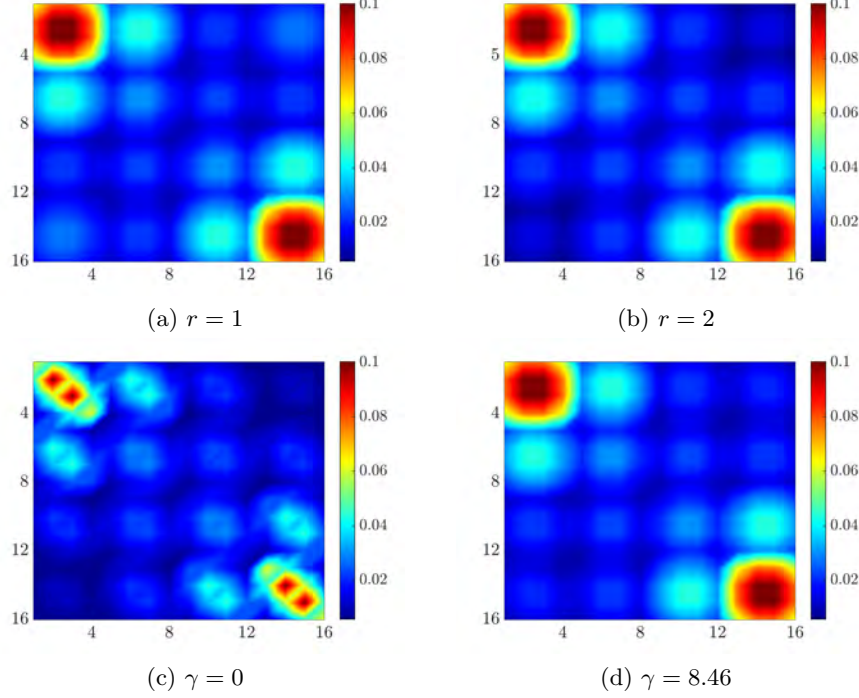


Figure 4.5: The recovered state covariance matrix of the heat equation resulting from problem (4.7) (a, b), and problem (4.8) (c, d). (a)  $r = 1$ ; (b)  $r = 2$ ; (c)  $\gamma = 0$ ; (d)  $\gamma = 8.46$ .

the covariance matrices are diagonally dominant, especially  $\Sigma_{vv}$ .

Again, we study the respective effect of  $r$  and  $\gamma$  on the solutions of (4.7) and (4.8). As shown in figure 4.7, these dependencies are monotonic and minimization of the Frobenius norm, which corresponds to solving problem (4.7) with  $r = 2n$  and problem (4.8) with  $\gamma = 0$ , results in the best covariance completion (77% recovery). However, in this case the matrix  $Z$  is not rank deficient. On the other hand, nuclear norm minimization, which corresponds to solving (4.7) with  $r = 1$  and (4.8) with  $\gamma = \infty$ , results in the worst completion (46%).

Figure 4.8 shows the recovered covariance matrices of position  $X_{pp}$  and velocity  $X_{vv}$  resulting from optimization problems (4.7) and (4.8) with various values of  $r$  and  $\gamma$ . While nuclear norm minimization yields poor recovery of the diagonally dominant covariance matrix of velocities  $\Sigma_{vv}$  (cf. figure 4.8b), minimization of the Frobenius norm results in best overall recovery (cf. figures 4.8e and 4.8f). However, as aforementioned, lack of a surrogate for rank minimization leads to a full-rank matrix  $Z$ . An intermediate state

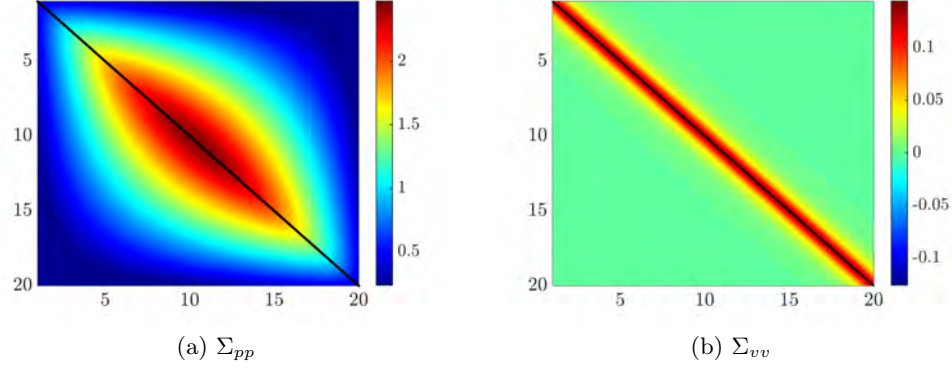


Figure 4.6: The steady-state covariance matrices of the (a) position  $\Sigma_{pp}$ , and (b) velocity  $\Sigma_{vv}$ , of masses in the MSD system with  $n = 20$  masses. Available one-point correlations used in problems (4.7) and (4.8) are marked by black lines.

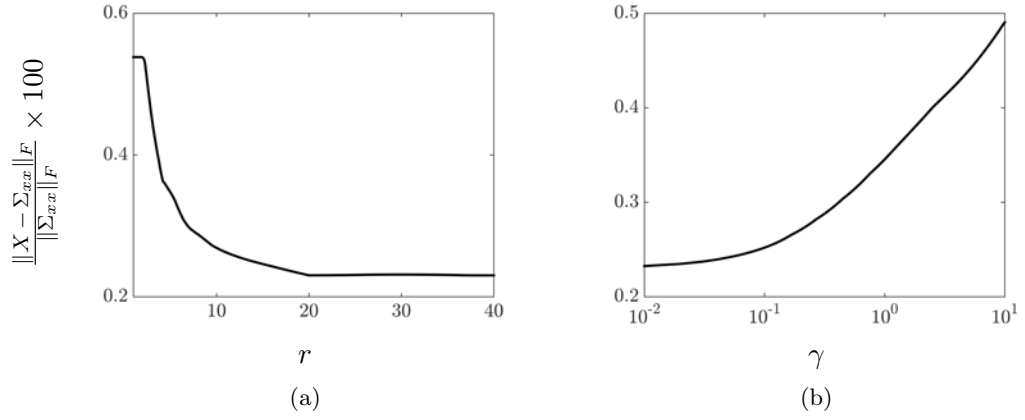


Figure 4.7: (a) The  $r$ -dependence of the relative error between the solution  $X$  to (4.7) and the true covariance  $\Sigma_{xx}$  for the MSD system with  $n = 20$  masses. (b) The  $\gamma$ -dependence of the error between the solution to (4.8) and the true covariance.

with reasonable recovery (73%) can be achieved by solving (4.7) with  $r = 10$  (figures 4.8c and 4.8d) and (4.8) with  $\gamma = 0.19$  (figures 4.8g and 5.4d). While the quality of recovery is the same, the matrix  $Z$  which results from solving problem (4.7) is of lower rank (10 vs. 18). Moreover, if one intended to get a solution of rank 18, choosing  $r = 18$  would be successful here and by Proposition 5 there is no other solution of smaller Frobenius norm.

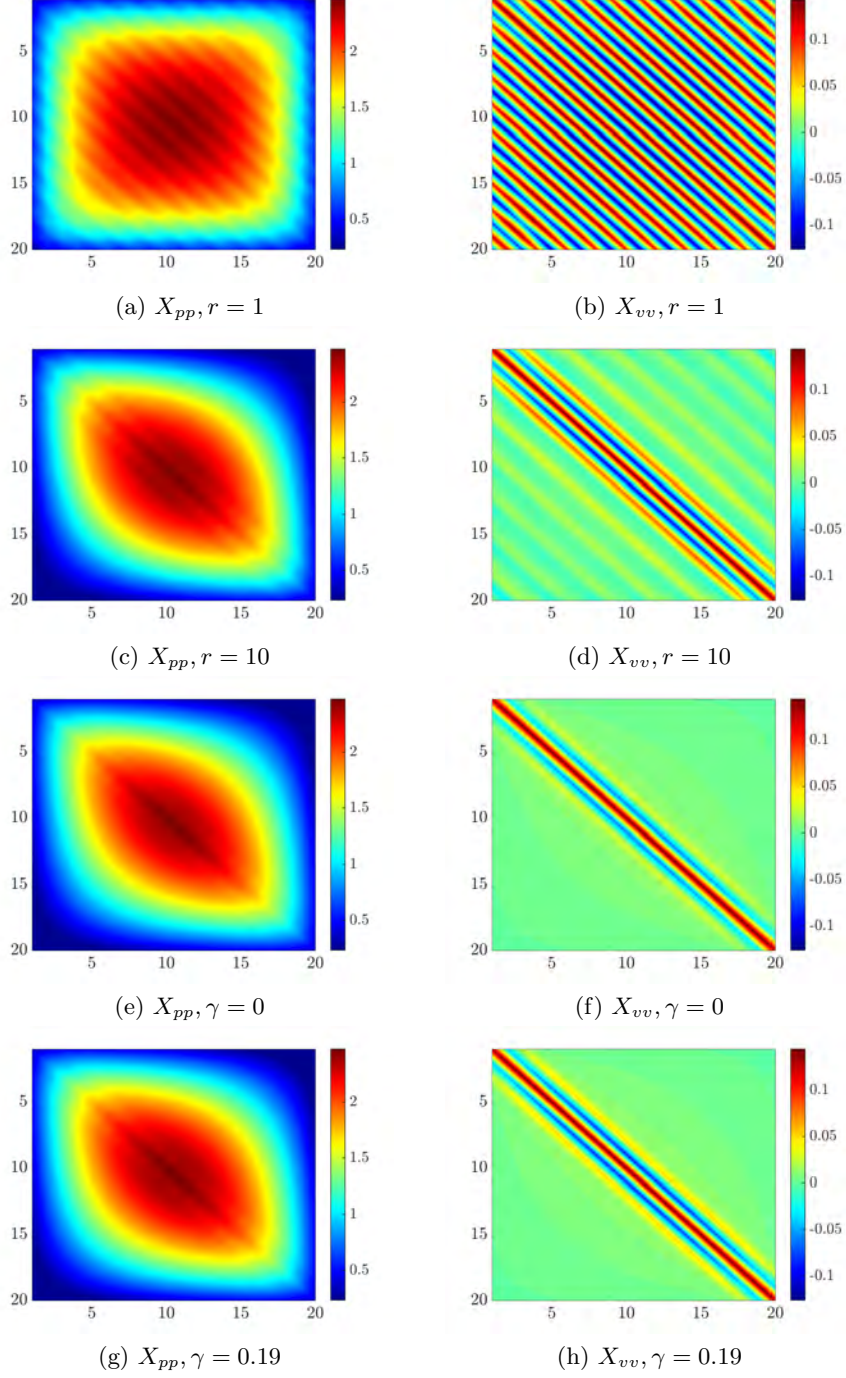


Figure 4.8: The recovered covariance matrices of position and velocity in the MSD system with  $n = 20$  masses resulting from problem (4.7) (a, b, c, d), and problem (4.8) (e, f, g, h). (a, b)  $r = 1$ ; (c, d)  $r = 10$ ; (e, f)  $\gamma = 0$ ; (g, h)  $\gamma = 0.19$ .

## Chapter 5

# Perturbation of system dynamics and the covariance completion problem

In this chapter, we again consider the problem of completing partially known sample statistics in a way that is consistent with underlying stochastically driven linear dynamics. Neither the statistics nor the dynamics are precisely known. Thus, our objective is to reconcile the two in a parsimonious manner. Herein, we formulate a convex optimization problem to match available covariance data while minimizing the energy required to adjust the dynamics by a suitable low-rank perturbation. The solution to the optimization problem provides information about critical directions that have maximal effect in bringing model and statistics in agreement.

### 5.1 Introduction

Our topic begins with a simplified model of a complex dynamical process together with an incomplete set of covariance statistics. The observed partial statistical signature of the process carries useful information about the underlying dynamics. Thus, our goal is to reconcile the available covariance data with our model by an economical refinement of both, the model and the estimated statistics.

The history and motivation for this subject root in the modeling of fluid flows. In this, the stochastically-forced linearized Navier-Stokes equations around the mean velocity profile have been shown to qualitatively replicate the structural features of shear flows [28–30, 33]. This chapter represents an extension of the theoretical developments presented in Chapter 2, where we introduced nontrivial (colored) stochastic forcing

into linear dynamics in order to account for a partially known output covariance; also see [34, 137, 160, 164, 165]. We were motivated by the fact that white-in-time stochastic forcing is often insufficient to explain observed correlations [113, 114]. However, insights from that earlier work suggest that the effect of a colored-in-time input process is precisely *equivalent* to a perturbation of the system dynamics, *without* any need to increase the state dimension [34, 164].

Any perturbations in state dynamics can be equivalently represented by state-feedback interactions. Parsimony in our methodology dictates that we penalize both the magnitude as well as the directionality of corresponding correction terms. Thereby, we formulate the problem to match available covariance data while minimizing the energy required to adjust the dynamics by a suitable low-rank perturbation. The solution to the convex optimization problem that we formulate provides information about critical directions that have maximal effect in bringing model and statistics in agreement.

Starting from a pre-specified set of input channels our objective is to identify a small subset that can explain partially-observed second-order statistics via suitable feedback interactions. In general, this is a combinatorial optimization problem. To cope with the combinatorial complexity, we utilize convex characterization that was recently used in the context of optimal sensor and actuator selection [168, 169]. This allows us to cast our problem as a semidefinite program.

Our problem can be viewed as having a dual interpretation. It can be considered as a static state-feedback synthesis approach to an inverse problem that identifies dynamical feedback interactions which account for available statistical signatures. On the other hand, it can also be considered as an identification problem that aims to explain available statistics via suitable low-rank perturbations of the linear dynamics.

The rest of this chapter is organized as follows. In Section 5.2, we provide a brief summary of the covariance completion problem and draw connections to covariance control problems. In Section 5.3, we pose the problem as a state-feedback synthesis and provide a convex formulation. In Section 5.4, we offer an example to highlight the utility of our approach.

## 5.2 Background

Consider a linear time-invariant (LTI) system with state-space representation

$$\begin{aligned}\dot{x} &= Ax + Bf \\ y &= Cx\end{aligned}\tag{5.1}$$

where  $x(t) \in \mathbb{C}^n$  is the state vector,  $y(t) \in \mathbb{C}^p$  is the output,  $f(t) \in \mathbb{C}^m$  is a stationary zero-mean stochastic process,  $A \in \mathbb{C}^{n \times n}$  is the dynamic matrix, and  $B \in \mathbb{C}^{n \times m}$  is the input matrix with  $m \leq n$ . For Hurwitz  $A$  and controllable  $(A, B)$ , a positive definite matrix  $X$  qualifies as the steady-state covariance matrix of the state vector

$$X := \lim_{t \rightarrow \infty} \mathbf{E}(x(t) x^*(t)),$$

if and only if the linear equation

$$A X + X A^* = -(B H^* + H B^*), \quad (5.2)$$

is solvable for  $H \in \mathbb{C}^{n \times m}$  [121, 122]. Here,  $\mathbf{E}$  is the expectation operator,  $H$  is a matrix that contains spectral information about the stochastic input process and is related to the cross-correlation between the input  $f$  and the state  $x$  [34, Appendix B], and  $*$  denotes the complex conjugate transpose. For a white-in-time input  $f$  with covariance  $W$ , the covariance  $X$  satisfies the algebraic Lyapunov equation

$$A X + X A^* = -B W B^*. \quad (5.3)$$

The main difference between (5.2) and (5.3) is that the right-hand-side in (5.2) is allowed to be sign-indefinite, thereby allowing for colored-in-time stochastic inputs. Clearly, for  $H = B W / 2$ , (5.2) simplifies to the Lyapunov equation (5.3).

The algebraic relation between second-order statistics of the state and forcing can be used to explain partially known sampled second-order statistics using stochastically-driven LTI systems [164, 165]. While the dynamical generator  $A$  is known, the origin and directionality of stochastic excitation  $f$  is unknown. It is also important to restrict the complexity of the forcing model. This complexity is quantified by the number of degrees of freedom that are directly influenced by stochastic forcing and translates into the number of input channels or  $\text{rank}(B)$ . It can be shown that the rank of  $B$  is closely related to the signature of the matrix

$$\begin{aligned} Z &:= -(A X + X A^*) \\ &= B H^* + H B^*. \end{aligned}$$

The signature of a matrix is determined by the number of its positive, negative, and zero eigenvalues. In addition, the rank of  $Z$  bounds the rank of  $B$  [164, 165].

Based on this, the problem of identifying low-complexity structures for stochastic forcing

can be formulated as the following structured covariance completion problem [164]

$$\begin{aligned} & \underset{X, Z}{\text{minimize}} && -\log \det(X) + \gamma \|Z\|_* \\ & \text{subject to} && AX + XA^* + Z = 0 \\ & && (CXC^*) \circ E - G = 0. \end{aligned} \tag{5.4}$$

Here,  $\gamma$  is a positive regularization parameter, the matrices  $A$ ,  $C$ ,  $E$ , and  $G$  are problem data, and the Hermitian matrices  $X$ ,  $Z \in \mathbb{C}^{n \times n}$  are optimization variables. Entries of  $G$  represent partially available second-order statistics of the output  $y$ , the symbol  $\circ$  denotes elementwise matrix multiplication, and  $E$  is the structural identity matrix,

$$E_{ij} = \begin{cases} 1, & \text{if } G_{ij} \text{ is available} \\ 0, & \text{if } G_{ij} \text{ is unavailable.} \end{cases}$$

Convex optimization problem (5.4) combines the nuclear norm with an entropy function in order to target low-complexity structures for stochastic forcing and facilitate construction of a particular class of low-pass filters that generate colored-in-time forcing correlations. The nuclear norm, i.e., the sum of singular values of a matrix,  $\|Z\|_* := \sum_i \sigma_i(Z)$ , is used as a proxy for rank minimization [72, 73]. On the other hand, the logarithmic barrier function in the objective is introduced to guarantee the positive definiteness of the state covariance matrix  $X$ .

The solution to (5.4) can be translated into a dynamical representation for colored-in-time stochastic forcing by designing linear filters that provide the suitable forcing into system (5.1); see figure 5.1a. The filter dynamics are given by the state-space representation

$$\dot{\xi} = (A - BK)\xi + Bd \tag{5.5a}$$

$$f = -K\xi + d, \tag{5.5b}$$

where  $d$  is a white stochastic process with covariance  $\Omega \succ 0$  and

$$K = \frac{1}{2} \Omega B^* X^{-1} - H^* X^{-1}. \tag{5.5c}$$

Here, the matrices  $B$  and  $H$  correspond to the factorization of the matrix  $Z$  (cf. (5.2)) which results from solving convex optimization problem (5.4); see [164, 165] for details.

From an alternative viewpoint, the constructed class of filters described by (5.5) are related to the covariance control problem studied in [123, 124]; see [164] for additional details. In other words, the cascade interconnection of the filter and linear dynamics

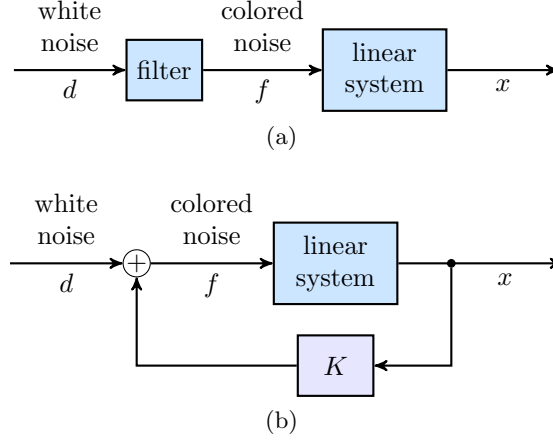


Figure 5.1: (a) A cascade connection of an LTI system with a linear filter that is designed to account for the sampled steady-state covariance matrix  $X$ ; (b) An equivalent feedback representation of the cascade connection in (a).

can be equivalently represented by

$$\dot{x} = Ax + Bu + Bd, \quad (5.6a)$$

where  $d$  is again white with covariance  $\Omega$ , and  $u$  is given by

$$u = -Kx. \quad (5.6b)$$

Substitution of (5.6b) into (5.6a) yields the following state-space representation

$$\dot{x} = (A - BK)x + Bd. \quad (5.6c)$$

In this case, a choice of non-zero  $K$  can be used to assign different values to the covariance matrix  $X$ ; see figure 5.1b. For  $A - BK$  Hurwitz,  $X$  satisfies

$$(A - BK)X + X(A - BK)^* + B\Omega B^* = 0. \quad (5.7)$$

Any  $X \succ 0$  satisfying (5.7) also satisfies (5.2) with  $H = -XK^* + \frac{1}{2}B\Omega$ . Conversely, if  $X \succ 0$  satisfies (5.2), then it also satisfies (5.7) for  $K = \frac{1}{2}\Omega B^* X^{-1} - H^* X^{-1}$  and  $A - BK$  is Hurwitz. Thus, for a stationary state covariance  $X \succ 0$ , the problem of identifying the stochastic input  $f$  in (5.1) is equivalent to assigning the feedback gain matrix  $K$  in (5.6).

### 5.3 Covariance completion via minimum energy control

We next utilize representation (5.6) to propose an alternative method for completing partially known second-order statistics using state-feedback synthesis. In general, there is more than one choice of  $K$  that provides consistency with available steady-state statistics. We propose to select an optimal feedback gain  $K$  that minimizes the control energy in statistical steady-state

$$\lim_{t \rightarrow \infty} \mathbf{E}(u^*(t)u(t)).$$

Such  $K$  can be equivalently obtained by minimizing trace  $(KXK^*)$  subject to (5.7) and a linear constraint that comes from the known output correlations,

$$(CXC^*) \circ E - G = 0.$$

In addition, it is desired to limit the number of degrees of freedom that are directly influenced by the state-feedback  $u$  and stochastic forcing  $d$  in (5.6). This also translates into minimizing the number of input channels or columns of the input matrix  $B$  that perturb the dynamical generator  $A$  in (5.7); see [34, 164] for details.

Herein, we introduce a covariance completion framework which consists of two steps: identification and polishing. In the identification step, we solve the minimum-energy covariance completion problem augmented by a sparsity-promoting regularizer. This allows us to identify a subset of input channels that strike a balance between control energy and the number of used input channels (and thereby the rank of the dynamical perturbation  $BK$ ). In the polishing step, we further reduce the control energy and improve the quality of completion. This is accomplished by solving the minimum-energy covariance completion problem using the identified input channels.

#### 5.3.1 Identification of essential input channels

As aforementioned, the covariance completion problem (5.4) uses a nuclear norm regularization in order to provide a bound on the least number of colored-in-time input channels that are required to account for the known second-order statistics. Herein, we consider the state-space representation

$$\dot{x} = (A - BK)x + Bd$$

where  $d$  is a zero-mean white stochastic process with covariance  $\Omega$ ,  $B$  is the input matrix,  $A$  is Hurwitz, and the pair  $(A, B)$  is controllable. Starting from a given matrix  $B$ , we seek a subset of available input channels that are sufficient for the purpose of

accounting for the observed second-order statistics. This is accomplished by formulating an optimization problem in which the performance index  $\text{trace}(KXK^*)$  is augmented with a term that promotes row-sparsity of the feedback gain matrix  $K$ . When the  $i$ th row of  $K$  is identically equal to zero, the  $i$ th input channel in the matrix  $B$  is not used. Therefore, we can identify a subset of critical input channels by promoting row-sparsity of  $K$ . This approach not only reduces the number of colored-in-time input channels, but it also uncovers the precise dynamical feedback interactions that are required to reconcile the available covariance data with the given linear dynamics.

The regularized minimum-control-energy covariance completion problem can be formulated as,

$$\begin{aligned} \underset{X, K, \Omega}{\text{minimize}} \quad & \text{trace}(KXK^*) + \gamma \sum_{i=1}^n w_i \|e_i^* K\|_2 \\ \text{subject to} \quad & (A - BK)X + X(A - BK)^* + B\Omega B^* = 0 \\ & (CXC^*) \circ E - G = 0 \\ & X \succ 0. \end{aligned} \tag{5.8}$$

Here, matrices  $A$ ,  $B$ ,  $C$ ,  $E$ , and  $G$  are problem data, and matrices  $X \in \mathbb{C}^{n \times n}$ ,  $K \in \mathbb{C}^{m \times n}$ , and  $\Omega \in \mathbb{C}^{m \times m}$  are optimization variables. The regularization parameter  $\gamma > 0$  specifies the relative importance of the sparsity-promoting term,  $w_i$  are nonzero weights, and  $e_i$  is the  $i$ th unit vector in  $\mathbb{R}^m$ .

Since the hermitian matrix  $X$  is positive definite and therefore invertible, the standard change of coordinates  $Y := KX$  brings problem (5.8) into the following form

$$\begin{aligned} \underset{X, Y, \Omega}{\text{minimize}} \quad & \text{trace}(YX^{-1}Y^*) + \gamma \sum_{i=1}^n w_i \|e_i^* Y\|_2 \\ \text{subject to} \quad & AX + XA^* - BY - Y^*B^* + B\Omega B^* = 0 \\ & (CXC^*) \circ E - G = 0 \\ & X \succ 0. \end{aligned} \tag{5.9}$$

Here, we have utilized the equivalence between the row-sparsity of  $K$  and the row-sparsity of  $Y$  [168]. The convexity of (5.9) follows from the convexity of its objective function and the convexity of the constraint set [135]. Furthermore, this optimization problem can be recast as an SDP by taking the Schur complement of  $YX^{-1}Y^*$  [170]. Finally, the optimal feedback gain matrix can be recovered as  $K = YX^{-1}$ .

The SDP characterization of problem (5.9) can be solved efficiently using general-purpose solvers for small-size problems. We are currently developing customized algorithms that exploit the structure of (5.9) in order to gain computational efficiency and improve scalability.

### Iterative reweighting

In optimization problem (5.9) the weighted  $\ell_2$  norm is used to promote row sparsity of the matrix  $Y$ . This choice is inspired by the exact correspondence between the weighted  $\ell_1$  norm, i.e.,  $\sum_i w_i |x_i|$  with  $w_i = 1/|x_i|$  for  $x_i \neq 0$ , and the cardinality function  $\mathbf{card}(x)$ . Since this choice of weights cannot be implemented, the iterative reweighting scheme was proposed instead in [171]. We follow a similar approach and update the weights using

$$w_i^{j+1} = \frac{1}{\|e_i^* Y^j\|_2 + \epsilon}, \quad (5.10)$$

where  $Y^j$  denotes the solution to problem (5.9) in the  $j$ th reweighting step. The small positive parameter  $\epsilon$  ensures that the weights are well-defined.

#### 5.3.2 Polishing step

In the polishing step, we consider the system

$$\dot{x} = (A - B_2 K)x + B d.$$

The matrix  $B_2 \in \mathbb{C}^{n \times q}$  is obtained by eliminating the columns of  $B$  which correspond to the identified row sparsity structure of  $Y$ , where  $q$  denotes the number of retained input channels. For this system, we solve optimization problem (5.9) with  $\gamma = 0$ . This step allows us to identify the optimal matrix  $Y \in \mathbb{C}^{q \times n}$  and subsequently the optimal feedback gain  $K \in \mathbb{C}^{q \times n}$  for a system with a lower number of input control channels. As we demonstrate in our computational experiments, polishing not only reduces the energy of the control input but it can also improve the quality of completion of the covariance matrix  $X$ .

### 5.4 An example

In an incompressible channel-flow, with geometry shown in figure 5.2, we study the dynamics of infinitesimal fluctuations around the parabolic mean velocity profile,  $\bar{\mathbf{u}} = [U(x_2) \ 0 \ 0]^T$  with  $U(x_2) = 1 - x_2^2$ . Here,  $x_1$ ,  $x_2$ , and  $x_3$  denote the streamwise, wall-normal and spanwise coordinates, respectively; see figure 5.2. Finite dimensional approximation of the linearized Navier-Stokes equations around  $\bar{\mathbf{u}}$  results in the following state-space representation

$$\begin{aligned} \dot{x}(\mathbf{k}, t) &= A(\mathbf{k}) x(\mathbf{k}, t) + \xi(\mathbf{k}, t), \\ y(\mathbf{k}, t) &= C(\mathbf{k}) x(\mathbf{k}, t). \end{aligned} \quad (5.11a)$$

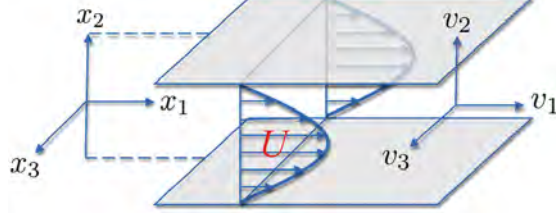


Figure 5.2: Geometry of a three-dimensional pressure-driven channel flow.

Here,  $x = [v_2^T \ \eta^T]^T \in \mathbb{C}^{2N}$  is the state of the linearized model,  $v_2$  and  $\eta = \partial_{x_3} v_1 - \partial_{x_1} v_3$  are the wall-normal velocity and vorticity, the output  $y = [v_1^T \ v_2^T \ v_3^T]^T \in \mathbb{C}^{3N}$  denotes the fluctuating velocity vector,  $\xi$  is a stochastic forcing disturbance,  $\mathbf{k} = [k_x \ k_z]^T$  denotes the vector of horizontal wavenumbers, and the input matrix is the identity  $I_{2N \times 2N}$ . A detailed description of the dynamical matrix  $A$  and output matrix  $C$  can be found in [30].

We assume that the stochastic disturbance  $\xi$  is generated by a low-pass filter with state-space representation

$$\dot{\xi}(\mathbf{k}, t) = -\xi(\mathbf{k}, t) + d(t). \quad (5.11b)$$

Here,  $d$  denotes a zero mean unit variance white process.

The steady-state covariance of system (5.11) can be found as the solution to the Lyapunov equation

$$\tilde{A} \Sigma + \Sigma \tilde{A}^* + \tilde{B} \tilde{B}^* = 0$$

where

$$\tilde{A} = \begin{bmatrix} A & I \\ O & -I \end{bmatrix}, \quad \tilde{B} = \begin{bmatrix} 0 \\ I \end{bmatrix}$$

and

$$\Sigma = \begin{bmatrix} \Sigma_{xx} & \Sigma_{x\xi} \\ \Sigma_{\xi x} & \Sigma_{\xi\xi} \end{bmatrix}.$$

Here, the sub-covariance  $\Sigma_{xx}$  denotes the state covariance of system (5.11a). At any horizontal wavenumber pair  $\mathbf{k}$ , the steady-state covariance matrices of the output  $y$  and the state  $x$  are related by

$$\Phi(\mathbf{k}) = C(\mathbf{k}) \Sigma_{xx}(\mathbf{k}) C^*(\mathbf{k}),$$

Figure 5.3 shows the structure of the output covariance matrix  $\Phi$ .

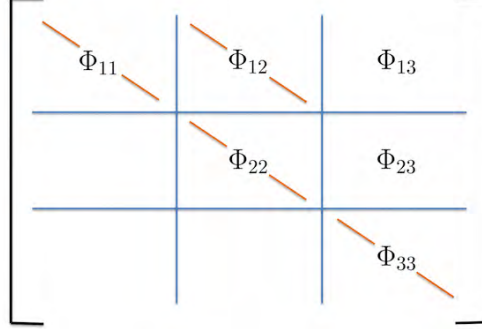


Figure 5.3: Structure of the output covariance matrix  $\Phi$ . Available one-point velocity correlations in the wall-normal direction represent diagonal entries of the blocks in the velocity covariance matrix  $\Phi$ .

For the horizontal wavenumber pair  $(k_x, k_z) = (0, 1)$ , figure 5.4(a, c, e, g) shows the color-plots of the streamwise  $\Phi_{11}$ , wall-normal  $\Phi_{22}$ , spanwise  $\Phi_{33}$ , and the streamwise/wall-normal  $\Phi_{12}$  two-point correlation matrices in the wall-normal direction  $x_2$ . In this example, we assume that the one-point velocity correlations, or diagonal entries of these covariance matrices are available. We set the covariance of white noise disturbances to the identity ( $\Omega = I$ ) and do not treat it as an optimization variable in (5.9). For this example, we use  $N = 11$  collocation points to discretize the differential operators in the wall-normal direction  $x_2$ .

Figure 5.5 shows the  $\gamma$ -dependence of the relative Frobenius norm error in recovering the true covariance  $\Sigma_{xx}$  before and after polishing. As shown in figure 5.5, the polishing step can indeed improve the quality of completion in the covariance matrix  $X$ . The best completion is achieved for high values of  $\gamma$  (96% recovery). Figure 5.4(b, d, f, h) shows the streamwise, wall-normal, spanwise, and the streamwise/wall-normal two-point correlation matrices resulting from solving (5.9) with  $\gamma = 10^4$  followed by polishing.

Figure 5.6 shows the configuration of input channels that are retained as  $\gamma$  is increased. It is evident that as  $\gamma$  increases more control input channels are eliminated. In this example, the initial input matrix is the identity  $I_{2N \times 2N}$ . Since the state is formed as  $x = [v^T \ \eta^T]^T$ , the first and last  $N$  input channels can be considered as entering into the dynamics of wall-normal velocity and wall-normal vorticity, respectively. Notably, input channels that enter the dynamics of wall-normal velocity are more important with more emphasis placed on excitations that are located in the vicinity of channel walls.

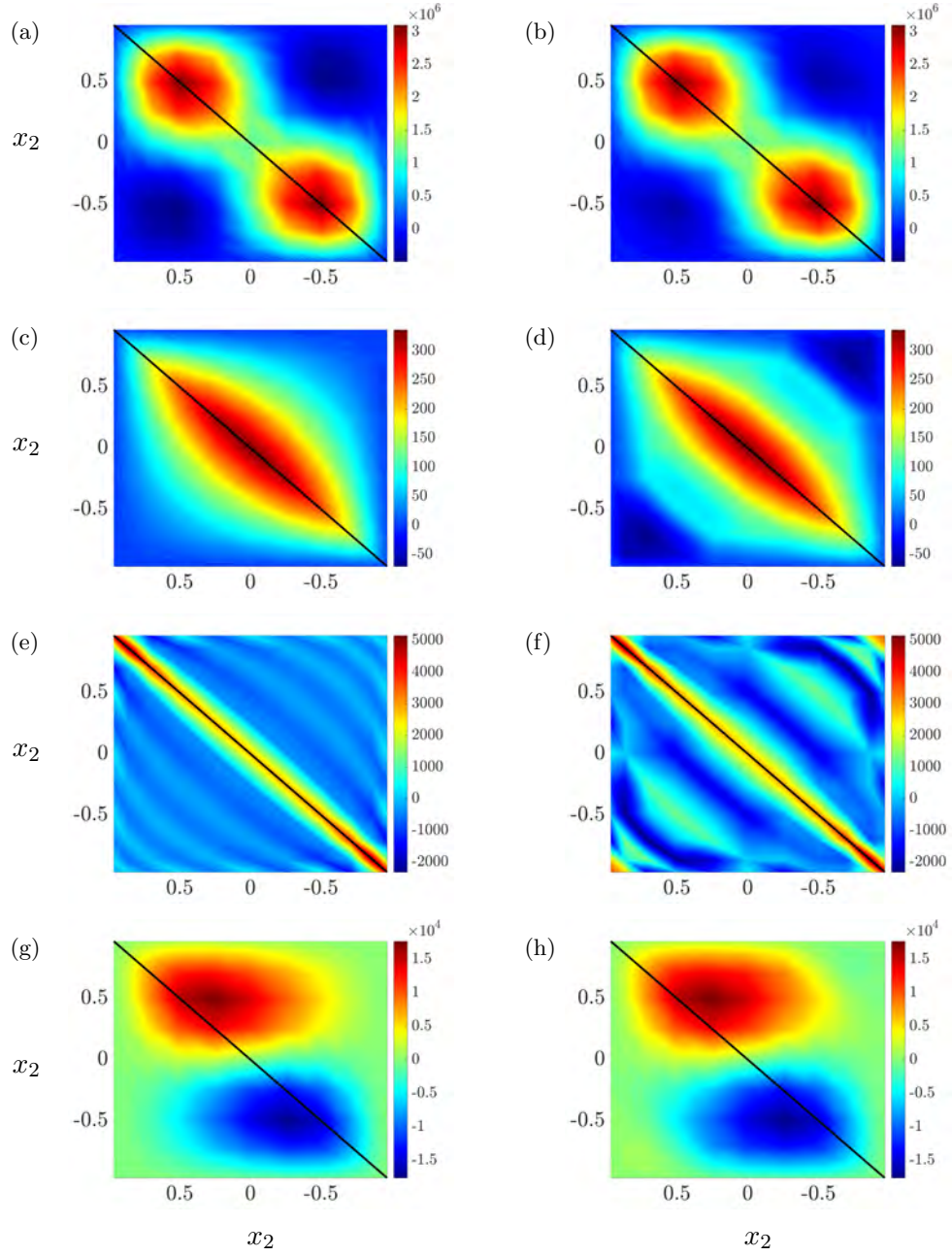


Figure 5.4: True covariance matrices of the output velocity field (a, c, e, g), and covariance matrices resulting from solving optimization problem (5.9) with  $\gamma = 10^4$  followed by a polishing step (b, d, f, h). (a, b) Streamwise  $\Phi_{11}$ , (c, d) wall-normal  $\Phi_{22}$ , (e, f) spanwise  $\Phi_{33}$ , and (g, h) the streamwise/wall-normal  $\Phi_{12}$  two-point correlation matrices at  $(k_x, k_z) = (0, 1)$ . The one-point correlation profiles that are used as problem data in (5.9) are marked by black lines along the main diagonals.

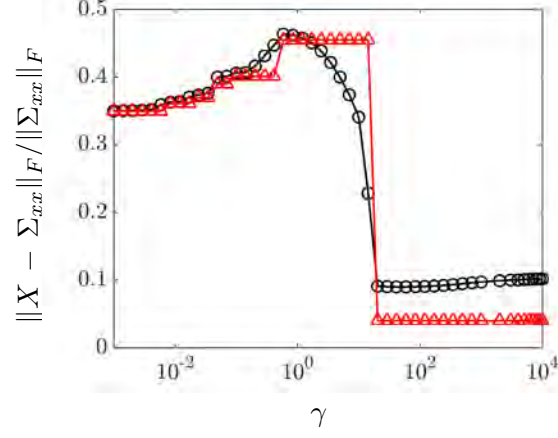


Figure 5.5: The  $\gamma$ -dependence of the relative Frobenius norm error between the true state covariance  $\Sigma_{xx}$  and the solution  $X$  to (5.9) before ( $\circ$ ) and after ( $\triangle$ ) polishing, for the channel flow with  $N = 11$  collocation points in channel height.

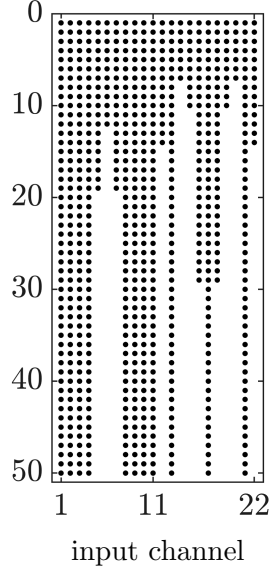


Figure 5.6: Retained columns of the input matrix  $B$  as  $\gamma$  increases. A black dot indicates the presence of the corresponding input channel. The top row ( $\gamma = 0$ ) shows the use of all channels, and the bottom row ( $\gamma = 10^4$ ) shows the least number of channels required for accounting for the observed statistics.

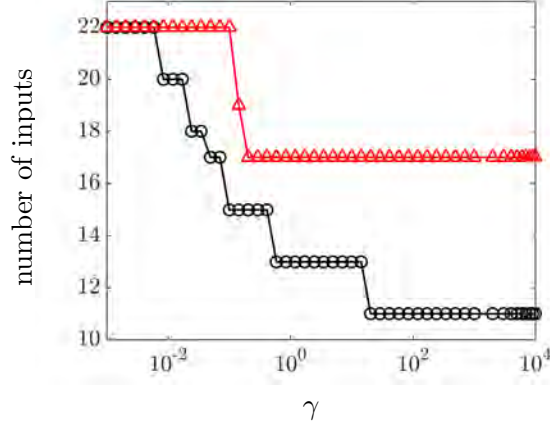


Figure 5.7: The  $\gamma$ -dependence of the number of retained input channels after solving problem (5.9) in the case of iterative reweighting ( $\circ$ ) and in the case of constant weights ( $\triangle$ ).

When the reweighting scheme is employed, for each value of  $\gamma$ , the optimization problem (5.9) is solved 10 times, updating the weights using (5.10) and retaining them as we increase  $\gamma$ . Figure 5.7 illustrates the utility of the iterative reweighting scheme. When constant and uniform sparsity-promoting weights are used, large values of  $\gamma$  are required to eliminate input channels, and even with the highest values of the sparsity-promoting parameter ( $\gamma = 10^4$ ) only 5 input channels were eliminated from the second half of columns of  $B$ . For the same value of  $\gamma$ , problem (5.9) with the iterative reweighting scheme eliminates 11 input channels.

## Chapter 6

# Conclusions and future directions

### Conclusions

We are interested in explaining partially known second-order statistics that originate from experimental measurements or simulations using stochastic linear models. This is motivated by the need for control-oriented models of systems with large number of degrees of freedom, e.g., turbulent fluid flows. In our setup, the linearized approximation of the dynamical generator is known whereas the nature and directionality of disturbances that can explain partially observed statistics are unknown. We thus formulate the problem of identifying appropriate stochastic input that can account for the observed statistics while being consistent with the linear dynamics.

This inverse problem is framed as convex optimization. We utilize nuclear norm minimization to identify noise parameters of low rank and to complete unavailable covariance data. Our formulation relies on drawing a connection between the rank of a certain matrix and the number of disturbance channels into the linear dynamics. An important contribution is the development of a customized alternating minimization algorithm (AMA) that efficiently solves covariance completion problems of large size. In fact, we show that our algorithm works as a proximal gradient on the dual problem and establish a sub-linear convergence rate for the fixed step-size. We also provide comparison with ADMM and demonstrate that AMA yields explicit updates of all optimization variables and a principled procedure for step-size selection. An additional contribution is the design of a class of linear filters that realize suitable colored-in-time excitation to account for the observed state statistics. These filters solve a non-standard stochastic realization problem with partial covariance information.

In Chapter 4, we use the  $r^*$  norm to approximate the rank function in the covariance completion problem. Relative to the nuclear norm relaxation, the  $r^*$  norm exploits an additional degree of freedom which is useful in the completion of diagonally dominant

covariances. While the nuclear norm relaxation yields forcing models of low-complexity, in some cases it can result in unreasonable completion of second-order statistics. Our numerical experiments show that the use of the  $r^*$  norm can indeed improve the quality of completion without increasing the rank of the input correlation structures.

In Chapter 5, we show that the covariance completion problem can be alternatively formulated as a covariance control problem in which we identify the suitable feedback interactions that explain the available statistics. We employ a convenient change of variables through which the problem of minimizing the number of input channels translates into promoting sparsity on the rows of the feedback gain matrix. This allows for the exact identification of critical input directions that have most profound effects in bringing model and statistics in agreement.

## Extensions and future directions

### **The use of the $r^*$ norm in the low-complexity modeling of turbulent flows.**

While the  $r^*$  norm formulation can be cast as an SDP and solved using general purpose solvers, its utility for the purpose of turbulent flow modeling requires the development of customized optimization algorithms that are able to handle larger-size problems. With recent algorithmic developments that have determined the proximal operator for the  $r^*$  norm [85, 86], the customized optimization algorithms developed in Chapter 3 can be used in the context of modeling turbulent fluid flows. We anticipate that the additional layer of flexibility introduced by this heuristic can potentially improve our ability to capture statistical signatures of wall-bounded shear flows.

### **Feedback synthesis for actuator/sensor selection and covariance completion.**

In addition to low-complexity stochastic modeling, the minimum energy covariance completion problem (5.9) can be used for the purpose of optimal sensor and actuator selection (e.g., see [169]). Our ongoing effort is directed toward the development of customized optimization algorithms that efficiently solve these classes of optimal control problems, particularly for large-scale systems.

## Part II

# Stochastic modeling of wall-bounded shear flows

## Chapter 7

# Stochastic modeling of turbulent channel flow

In this chapter, we address the problem of how to account for second-order statistics of turbulent flows using low-complexity stochastic dynamical models based on the linearized Navier-Stokes equations. The complexity is quantified by the number of degrees of freedom in the linearized evolution model that are directly influenced by stochastic excitation sources. For the case where only a subset of velocity correlations are known, we develop a framework to complete unavailable second-order statistics in a way that is consistent with linearization around the turbulent mean velocity. In general, white-in-time stochastic forcing is not sufficient to explain turbulent flow statistics. We develop models for colored-in-time forcing using a maximum entropy formulation together with a regularization that serves as a proxy for rank minimization. We show that colored-in-time excitation of the Navier-Stokes equations can also be interpreted as a low-rank modification to the generator of the linearized dynamics. Our method provides a data-driven refinement of models that originate from first principles and captures complex dynamics of turbulent flows in a way that is tractable for analysis, optimization, and control design.

### 7.1 Introduction

The advent of advanced measurement techniques and the availability of parallel computing have played a pivotal role in improving our understanding of turbulent flows. Experimentally and numerically generated data sets are becoming increasingly available for a wide range of flow configurations and Reynolds numbers. An accurate statistical

description of turbulent flows may provide insights into flow physics and will be instrumental in model-based control design for suppressing or promoting turbulence. Thus, it is increasingly important to understand how structural and statistical features of turbulent flows can be embedded in models of low-complexity that are suitable for analysis, optimization, and control design.

Nonlinear dynamical models of wall-bounded shear flows that are based on the Navier-Stokes (NS) equations typically have a large number of degrees of freedom. This makes them unsuitable for analysis and control synthesis. The existence of coherent structures in turbulent wall-bounded shear flows [7–9] has inspired the development of data-driven techniques for reduced-order modeling of the NS equations. However, control actuation and sensing may significantly alter the identified modes in nonlinear reduced-order modeling schemes. This introduces nontrivial challenges for model-based control design [26, 27]. In contrast, linearization of the NS equations around the mean-velocity gives rise to models that are well-suited for analysis and synthesis using tools of modern robust control. Further, such linearized models, subject to white-in-time stochastic excitation, have been shown to qualitatively replicate structural features of transitional [28–30] and turbulent [31–33] wall-bounded shear flows. However, it has also been recognized that white-in-time stochastic excitation is insufficient to accurately reproduce statistics of the fluctuating velocity field [113, 114].

In this chapter, we build on the theoretical and algorithmic developments of Chapters 2 and 3, and introduce *colored-in-time* stochastic excitation to the linearized NS equations and develop an optimization framework to identify low-complexity models for such excitation sources. We show that these models are suitable to replicate available second-order statistics of wall-bounded shear flows. Our models contain the same number of degrees of freedom as the finite-dimensional approximation of the NS equations. Moreover, they can be interpreted as *low-rank* perturbations of the linearized dynamics.

The linearized NS equations have been effectively used to capture the early stages of transition in wall-bounded shear flows and to identify key mechanisms for subcritical transition. It has been demonstrated that velocity fluctuations around a laminar base flow exhibit high sensitivity to different sources of perturbations. This has provided reconciliation with experimental observations [4, 172–175] that, even in the absence of modal instability, bypass transition can be triggered by large transient growth [176–180] or large amplification of deterministic and stochastic disturbances [29, 30, 112, 181, 182]. The non-normality of the linearized dynamical generator introduces interactions of exponentially decaying normal modes [181, 183], which in turn result in high flow sensitivity. In the presence of mean shear and spanwise-varying fluctuations, vortex tilting induces high sensitivity of the laminar flow and provides a mechanism for the appearance of streamwise streaks and oblique modes [184].

Linear mechanisms also play an important role in the formation and maintenance of

streamwise streaks in turbulent shear flows. Numerical simulations show that, even in the absence of a solid boundary, streaky structures appear in homogeneous turbulence subject to large mean shear [185]. The formation of such structures has been attributed to the linear amplification of eddies that interact with background shear. In addition, linear rapid distortion theory [186] can be used to predict the long time anisotropic behavior as well as the qualitative features of the instantaneous velocity field in homogeneous turbulence [185].

The importance of linear mechanisms in maintaining near-wall streamwise vortices in wall-bounded shear flows was highlighted by [187]. Furthermore, [188] used the linearized NS equations to predict the spacing of near-wall streaks and relate their formation to a combination of lift-up due to the mean profile, mean shear, and viscous dissipation. The linearized NS equations also reveal large transient growth of fluctuations around turbulent mean velocity [189, 190] and a high amplification of stochastic disturbances [191]. Later studies further identified a secondary growth (of the streaks) which may produce much larger transient responses than a secondary instability [192, 193]. All of these studies support the relevance of linear mechanisms in the self-sustaining regeneration cycle [194, 195] and motivate low-complexity dynamical modeling of turbulent shear flows.

Other classes of linear models have also been utilized to study the spatial structure of the most energetic fluctuations in turbulent flows. In particular, augmentation of molecular viscosity with turbulent eddy-viscosity yields the turbulent mean flow as the exact steady-state solution of the modified NS equations [196, 197]. The analysis of the resulting eddy-viscosity-enhanced models reliably predicts the length scales of near-wall structures in turbulent wall-bounded shear flows [198–200]. This model was also used to study the optimal response to initial conditions and body forcing fluctuations in turbulent channel [32] and Couette flows [31], and served as the basis for model-based control design in turbulent channel flow [33].

Recently, a gain-based decomposition of fluctuations around the turbulent mean velocity has been used to characterize energetic structures in terms of their wavelengths and convection speeds [201–204]. For turbulent pipe flow, [201] used resolvent analysis to explain the extraction of energy from the mean flow. Resolvent analysis provides further insight into linear amplification mechanisms associated with critical layers. [204] extended this approach to turbulent channel flow and studied the Reynolds number scaling and geometric self-similarity of the dominant resolvent modes. In addition, they showed that decomposition of the resolvent operator can be used to provide a low-order description of the energy intensity of streamwise velocity fluctuations. Finally, [205] used a weighted sum of a few resolvent modes to approximate the velocity spectra in turbulent channel flow.

The nonlinear terms in the NS equations are conservative and, as such, they do not

contribute to the transfer of energy between the mean flow and velocity fluctuations; they only transfer energy between different Fourier modes [206, 207]. This observation has inspired researchers to *model the effect of nonlinearity* via an *additive stochastic forcing* to the equations that govern the dynamics of fluctuations. Early efforts focused on homogeneous isotropic turbulence [208–211]. In these studies, the conservative nature of the equations was maintained via a balanced combination of dynamical damping and stochastic forcing terms. However, imposing similar dynamical constraints in anisotropic and inhomogeneous flows is challenging and requires significant increase in computational complexity.

The NS equations linearized around the mean velocity capture the interactions between the background flow and velocity fluctuations. In the absence of body forcing and neutrally stable modes, linearized models predict either asymptotic decay or unbounded growth of fluctuations. Thus, without a stochastic source of excitation linearized models around stationary mean profiles cannot generate the statistical responses that are ubiquitous in turbulent flows. For quasi-geostrophic turbulence, linearization around the time-averaged mean profile was used to model heat and momentum fluxes as well as spatio-temporal spectra [212–216]. In these studies, the linearized model was driven with white-in-time stochastic forcing and the dynamical generator was augmented with a source of constant dissipation. In [217], the ability of Markov models (of different orders) subject to white forcing to explain time-lagged covariances of quasi-geostrophic turbulence was examined. Furthermore, singular perturbation methods were employed in an attempt to justify the use of stochastic models for climate prediction [218, 219]. This analysis suggests that more sophisticated models, which involve not only additive but also multiplicative noise sources, may be required. All of these studies demonstrate encouraging agreement between predictions resulting from stochastically driven linearized models and available data and highlight the challenges that arise in modeling dissipation and the statistics of forcing [220, 221].

The authors of [191] examined the statistics of the NS equations linearized around the Reynolds-Tiederman velocity profile subject to white stochastic forcing. It was demonstrated that velocity correlations over a finite interval determined by the eddy turnover time qualitatively agree with second-order statistics of turbulent channel flow. In [113] the NS equations linearized around turbulent mean velocity were studied and the influence of second-order spatial statistics of white-in-time stochastic disturbances on velocity correlations were examined. It was shown that portions of one-point correlations in turbulent channel flow can be approximated by the appropriate choice of forcing covariance. This was done in an *ad hoc* fashion by computing the steady-state velocity statistics for a variety of spatial forcing correlations. This line of work has inspired the development of optimization algorithms for approximation of full covariance matrices using stochastically forced linearized NS equations [161, 222]. Moreover, [33]

demonstrated that the energy spectrum of turbulent channel flow can be exactly reproduced using the linearized NS equations driven by white-in-time stochastic forcing with variance proportional to the turbulent energy spectrum. This choice was motivated by the observation that the second-order statistics of homogeneous isotropic turbulence can be exactly matched by such forcing spectra [114, 223].

Stochastically forced models were also utilized in the context of stochastic structural stability theory to study jet formation and equilibration in barotropic beta-plane turbulence [224–228]. Recently, it was demonstrated that a feedback interconnection of the streamwise-constant NS equations with a stochastically driven streamwise-varying linearized model can generate self-sustained turbulence in Couette and Poiseuille flows [229–231]. Turbulence was triggered by the stochastic forcing and was maintained even after the forcing had been turned off. Even in the absence of stochastic forcing, certain measures of turbulence, e.g., the correct mean velocity profile, are maintained through interactions between the mean flow and a small subset of streamwise varying modes. Even though turbulence can be triggered with white-in-time stochastic forcing, correct statistics cannot be obtained without accounting for the dynamics of the streamwise averaged mean flow or without manipulation of the underlying dynamical modes [232, 233].

As already noted, the linearized NS equations with white-in-time stochastic forcing have been used to predict coherent structures in transitional and turbulent shear flows and to yield statistics that are in qualitative agreement with experiments and simulations. For homogeneous isotropic turbulence, this model can completely recover second-order statistics of the velocity field [114, 223]. For turbulent channel flow, however, we demonstrate that the linearized NS equations with white-in-time stochastic excitation *cannot reproduce* second-order statistics that originate from direct numerical simulations (DNS). This observation exposes the limitations of the white-in-time forcing model.

In the present chapter, we show that *colored-in-time* stochastic forcing provides sufficient flexibility to account for statistical signatures of turbulent channel flow. We develop a systematic method for identifying the spectral content of colored-in-time forcing to the linearized NS equations that allows us to capture second-order statistics of fully developed turbulence. Most of our discussion focuses on channel flow, yet the methodology and theoretical framework are applicable to more complex flow configurations.

We are interested in completing partially available second-order statistics of velocity fluctuations in a way that is consistent with the known dynamics. The statistics of forcing to the linearized equations around turbulent mean velocity are unknown and sought to match the available velocity correlations and to complete any missing data. Our approach utilizes an algebraic relation that characterizes steady-state covariances of linear systems subject to colored-in-time excitation sources [121, 122]. This relation extends the standard algebraic Lyapunov equation, which maps white-in-time forcing

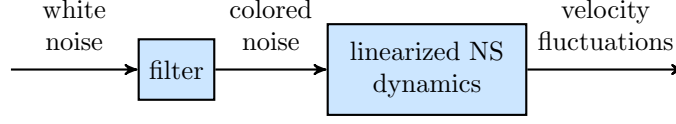


Figure 7.1: A spatio-temporal filter is designed to provide colored stochastic input to the linearized NS equations in order to reproduce partially available second-order statistics of turbulent channel flow.

correlations to state statistics, and it imposes a structural constraint on admissible covariances. We follow a maximum entropy formalism to obtain positive definite velocity covariance matrices and use suitable regularization to identify forcing correlation structures of low rank. This restricts the number of degrees of freedom that are directly influenced by the stochastic forcing and, thus, the complexity of the colored-in-time forcing model [164, 165].

Minimizing the rank, in general, leads to difficult non-convex optimization problems. Thus, instead, we employ nuclear norm regularization as a surrogate for rank minimization [45, 60, 72, 73]. The nuclear norm of a matrix is determined by the sum of its singular values and it provides a means for controlling the complexity of the model for stochastic forcing to the linearized NS equations. The covariance completion problem that we formulate is convex and its globally optimal solution can be efficiently computed using customized algorithms that we recently developed [160, 164].

We use the solution to the covariance completion problem to develop a dynamical model for colored-in-time stochastic forcing to the linearized NS equations (see figure 7.1) and provide a state-space realization for spatio-temporal filters that generate the appropriate forcing. These filters are generically minimal in the sense that their state dimension coincides with the number of degrees of freedom in the finite-dimensional approximation of the NS equations. We also show that colored-in-time stochastic forcing can be equivalently interpreted as a *low-rank modification* to the dynamics of the NS equations linearized around turbulent mean velocity. This dynamical perturbation provides a *data-driven refinement* of a *physics-based model* (i.e., the linearized NS equations) and it guarantees statistical consistency with fully developed turbulent channel flow. This should be compared and contrasted to alternative modifications proposed in the literature, e.g., the eddy-viscosity-enhanced linearization [31, 32, 197–200] or the addition of a dissipation operator [221]; see Chapter 9 for additional details.

We consider the mean velocity profile and one-point velocity correlations in the wall-normal direction at various wavenumbers as available data for our optimization problem. These are obtained using DNS of turbulent channel flow [234–238]. We show that stochastically forced linearized NS equations can be used to exactly reproduce all

one-point correlations (including one-dimensional energy spectra) and to provide good completion of unavailable two-point correlations of the turbulent velocity field. The resulting modified dynamics have the same number of degrees of freedom as the finite-dimensional approximation of the linearized NS equations. Thus, they are convenient for conducting linear stochastic simulations. The ability of our model to account for the statistical signatures of turbulent channel flow is verified using these simulations. We also demonstrate that our approach captures velocity correlations at higher Reynolds numbers. We close the chapter by employing tools from linear systems theory to analyze the spatio-temporal features of our model in the presence of stochastic and deterministic excitation sources.

The rest of this chapter is organized as follows. In Section 7.2, we introduce the stochastically forced linearized NS equations and describe the algebraic relation that linear dynamics impose on admissible state and forcing correlations. In Section 7.3, we formulate the covariance completion problem, provide a state-space realization for spatio-temporal filters, and show that the linearized NS equations with colored-in-time forcing can be equivalently represented as a low-rank modification to the original linearized dynamics. In Section 7.4, we apply our framework to turbulent channel flow and verify our results using linear stochastic simulations. In Section 7.5, we examine spatio-temporal frequency responses of the identified model, visualize dominant flow structures, and compute two-point temporal correlations.

## 7.2 Linearized Navier-Stokes equations and flow statistics

In this section, we present background material on stochastically forced linearized NS equations and second-order statistics of velocity fluctuations. Specifically, we provide an algebraic relation that is dictated by the linearized dynamics and that connects the steady-state covariance of the state in the linearized evolution model to the spectral content of the forcing. We focus on colored-in-time forcing inputs and extend the standard algebraic Lyapunov equation, which maps white-in-time disturbances to state statistics, to this more general case. Even though most of our discussion focuses on turbulent channel flow, the methodology and theoretical framework presented herein are applicable to other flow configurations.

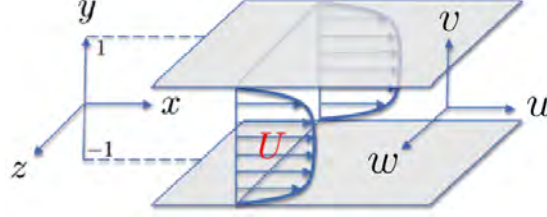


Figure 7.2: Geometry of a pressure-driven turbulent channel flow.

### 7.2.1 The Navier-Stokes equations and second-order statistics

The dynamics of incompressible Newtonian fluids are governed by the NS and continuity equations,

$$\mathbf{u}_t = -(\mathbf{u} \cdot \nabla) \mathbf{u} - \nabla P + \frac{1}{R_\tau} \Delta \mathbf{u}, \quad (7.1a)$$

$$0 = \nabla \cdot \mathbf{u}, \quad (7.1b)$$

where  $\mathbf{u}$  is the velocity vector,  $P$  is the pressure,  $\nabla$  is the gradient, and  $\Delta = \nabla \cdot \nabla$  is the Laplacian. In channel flow with geometry shown in figure 7.2, the friction Reynolds number is  $R_\tau = u_\tau h / \nu$ , where  $h$  is the channel half-height,  $u_\tau = \sqrt{\tau_w / \rho}$  is friction velocity,  $\nu$  is kinematic viscosity,  $\tau_w$  is wall-shear stress (averaged over wall-parallel directions and time),  $\rho$  is the fluid density, and  $t$  is time. In this formulation, spatial coordinates are non-dimensionalized by  $h$ , velocity by  $u_\tau$ , time by  $h/u_\tau$ , and pressure by  $\rho u_\tau^2$ .

The velocity field in (7.1) can be decomposed into the sum of mean,  $\bar{\mathbf{u}}$ , and fluctuating parts,  $\mathbf{v} = [u \ v \ w]^T$ ,

$$\mathbf{u} = \bar{\mathbf{u}} + \mathbf{v}, \quad \bar{\mathbf{u}} = \langle \mathbf{u} \rangle, \quad \langle \mathbf{v} \rangle = 0. \quad (7.2)$$

The components of the velocity fluctuation vector in the streamwise,  $x$ , wall-normal,  $y$ , and spanwise,  $z$ , directions are  $u$ ,  $v$ , and  $w$ , and  $\langle \cdot \rangle$  is the temporal expectation operator.

For turbulent flows, the mean velocity field satisfies the Reynolds-averaged NS equations [186, 206, 207],

$$\bar{\mathbf{u}}_t = -(\bar{\mathbf{u}} \cdot \nabla) \bar{\mathbf{u}} - \nabla \langle P \rangle + \frac{1}{R_\tau} \Delta \bar{\mathbf{u}} - \nabla \cdot \langle \mathbf{v} \mathbf{v}^T \rangle, \quad (7.3a)$$

$$0 = \nabla \cdot \bar{\mathbf{u}}, \quad (7.3b)$$

where  $\langle \mathbf{v} \mathbf{v}^T \rangle$  is the Reynolds stress tensor that arises from the second-order statistics

of velocity fluctuations. Such statistics quantify the transport of momentum and they have profound influence on the mean velocity, and thereby on the resistance to flow motion [206]. The difficulty in determining statistics of fluctuations comes from the nonlinearity in the NS equations which makes the  $n$ th velocity moment depend on the  $(n+1)$ th moment [206]. Statistical theory of turbulence combines physical intuition and empirical observations with rigorous approximation of the flow equations to express the higher-order moments in terms of the lower-order moments [186, 206, 207]. For example, the turbulent viscosity hypothesis [186] relates turbulent fluxes to mean velocity gradients, thereby allowing approximate solutions of (7.3) to be computed.

### 7.2.2 Stochastically forced linearized NS equations

Linearization around the turbulent mean velocity,  $\bar{\mathbf{u}}$ , yields the equations that govern the dynamics of velocity and pressure fluctuations,

$$\mathbf{v}_t = -(\nabla \cdot \bar{\mathbf{u}}) \mathbf{v} - (\nabla \cdot \mathbf{v}) \bar{\mathbf{u}} - \nabla p + \frac{1}{R_\tau} \Delta \mathbf{v} + \mathbf{d}, \quad (7.4a)$$

$$0 = \nabla \cdot \mathbf{v}, \quad (7.4b)$$

where  $\mathbf{d}$  is an additive zero-mean stochastic body forcing. The presence of stochastic forcing can be justified in different ways and there is a rich literature on the subject [28–30, 112]. For our purposes, turbulent flows have a well-recognized statistical signature which we want to reproduce, using perturbations around turbulent mean velocity, by postulating the stochastic model given by (7.4).

A standard conversion yields an evolution form of the linearized equations [239], with the state variable,  $\varphi = [v \ \eta]^T$ , determined by the wall-normal velocity,  $v$ , and vorticity,  $\eta = \partial_z u - \partial_x w$ . In turbulent channels the mean flow takes the form  $\bar{\mathbf{u}} = [U(y) \ 0 \ 0]^T$ , thereby implying translational invariance of (7.4) in the  $x$  and  $z$  directions. Application of the Fourier transform in the wall-parallel directions yields the evolution model,

$$\varphi_t(y, \mathbf{k}, t) = [\mathbf{A}(\mathbf{k}) \varphi(\cdot, \mathbf{k}, t)](y) + [\mathbf{B}(\mathbf{k}) \mathbf{d}(\cdot, \mathbf{k}, t)](y) \quad (7.5a)$$

$$\mathbf{v}(y, \mathbf{k}, t) = [\mathbf{C}(\mathbf{k}) \varphi(\cdot, \mathbf{k}, t)](y), \quad (7.5b)$$

which is parameterized by the spatial wavenumber pair  $\mathbf{k} = (k_x, k_z)$ . The operators  $\mathbf{A}$

and  $\mathbf{C}$  in (7.5) are given by

$$\begin{aligned}\mathbf{A}(\mathbf{k}) &= \begin{bmatrix} \mathbf{A}_{11}(\mathbf{k}) & 0 \\ \mathbf{A}_{21}(\mathbf{k}) & \mathbf{A}_{22}(\mathbf{k}) \end{bmatrix}, \quad \mathbf{C}(\mathbf{k}) = \begin{bmatrix} \mathbf{C}_u(\mathbf{k}) \\ \mathbf{C}_v(\mathbf{k}) \\ \mathbf{C}_w(\mathbf{k}) \end{bmatrix} = \frac{1}{k^2} \begin{bmatrix} ik_x \partial_y & -ik_z \\ k^2 & 0 \\ ik_z \partial_y & ik_x \end{bmatrix}, \\ \mathbf{A}_{11}(\mathbf{k}) &= \Delta^{-1} ((1/R_\tau) \Delta^2 + ik_x (U'' - U\Delta)), \\ \mathbf{A}_{21}(\mathbf{k}) &= -ik_z U', \\ \mathbf{A}_{22}(\mathbf{k}) &= (1/R_\tau) \Delta - ik_x U,\end{aligned}$$

where prime denotes differentiation with respect to the wall-normal coordinate,  $i$  is the imaginary unit,  $\Delta = \partial_y^2 - k^2$ ,  $\Delta^2 = \partial_y^4 - 2k^2 \partial_y^2 + k^4$ , and  $k^2 = k_x^2 + k_z^2$ . In addition, no-slip and no-penetration boundary conditions imply  $v(\pm 1, \mathbf{k}, t) = v'(\pm 1, \mathbf{k}, t) = \eta(\pm 1, \mathbf{k}, t) = 0$ . Here,  $\mathbf{A}_{11}$ ,  $\mathbf{A}_{22}$ , and  $\mathbf{A}_{21}$  are the Orr-Sommerfeld, Squire, and coupling operators [239], and the operator  $\mathbf{C}(\mathbf{k})$ , establishes a kinematic relationship between the components of  $\varphi$  and the components of  $\mathbf{v}$ . The operator  $\mathbf{B}$  specifies the way the external excitation  $\mathbf{d}$  affects the dynamics; see [30] for examples of  $\mathbf{B}$  in the case of channel-wide and near-wall excitations.

Finite-dimensional approximations of the operators in (7.5) are obtained using a pseudospectral scheme with  $N$  Chebyshev collocation points in the wall-normal direction [240]. In addition, we use a change of coordinates to obtain a state-space representation in which the kinetic energy is determined by the Euclidean norm of the state vector; see appendix B.1. The resulting state-space model is given by

$$\dot{\psi}(\mathbf{k}, t) = A(\mathbf{k}) \psi(\mathbf{k}, t) + B(\mathbf{k}) \mathbf{d}(\mathbf{k}, t), \quad (7.6a)$$

$$\mathbf{v}(\mathbf{k}, t) = C(\mathbf{k}) \psi(\mathbf{k}, t), \quad (7.6b)$$

where  $\psi(\mathbf{k}, t)$  and  $\mathbf{v}(\mathbf{k}, t)$  are vectors with complex-valued entries and  $2N$  and  $3N$  components, respectively, and state-space matrices  $A(\mathbf{k})$ ,  $B(\mathbf{k})$ , and  $C(\mathbf{k})$  are discretized versions of the corresponding operators that incorporate the aforementioned change of coordinates.

In statistical steady-state, the covariance matrix

$$\Phi(\mathbf{k}) = \lim_{t \rightarrow \infty} \langle \mathbf{v}(\mathbf{k}, t) \mathbf{v}^*(\mathbf{k}, t) \rangle \quad (7.7)$$

of the velocity fluctuation vector, and the covariance matrix

$$X(\mathbf{k}) = \lim_{t \rightarrow \infty} \langle \psi(\mathbf{k}, t) \psi^*(\mathbf{k}, t) \rangle \quad (7.8)$$

of the state in (7.6), are related as follows:

$$\Phi(\mathbf{k}) = C(\mathbf{k}) X(\mathbf{k}) C^*(\mathbf{k}), \quad (7.9)$$

where  $*$  denotes complex-conjugate-transpose. The matrix  $\Phi(\mathbf{k})$  contains information about all second-order statistics of the fluctuating velocity field, including the Reynolds stresses [241]. The matrix  $X(\mathbf{k})$  contains equivalent information and one can be computed from the other. Our interest in  $X(\mathbf{k})$  stems from the fact that, as we explain next, the entries of  $X(\mathbf{k})$  satisfy tractable algebraic relations that are dictated by the linearized dynamics (7.6) and the spectral content of the forcing  $\mathbf{d}(\mathbf{k}, t)$ .

### 7.2.3 Second-order statistics of the linearized Navier-Stokes equations

For the case where the stochastic forcing is zero-mean and white-in-time with covariance  $W(\mathbf{k}) = W^*(\mathbf{k}) \succeq 0$ , i.e.,

$$\langle \mathbf{d}(\mathbf{k}, t_1) \mathbf{d}^*(\mathbf{k}, t_2) \rangle = W(\mathbf{k}) \delta(t_1 - t_2), \quad (7.10)$$

where  $\delta$  is the Dirac delta function, the steady-state covariance of the state in (7.6) can be determined as the solution to the linear equation,

$$A(\mathbf{k}) X(\mathbf{k}) + X(\mathbf{k}) A^*(\mathbf{k}) = -B(\mathbf{k}) W(\mathbf{k}) B^*(\mathbf{k}). \quad (7.11)$$

Equation (7.11) is standard and it is known as the algebraic Lyapunov equation [242, section 1.11.3]. It relates the statistics of the white-in-time forcing  $W(\mathbf{k})$  to the covariance of the state  $X(\mathbf{k})$  via the system matrices  $A(\mathbf{k})$  and  $B(\mathbf{k})$ .

For the more general case, where the stochastic forcing is colored-in-time, a corresponding algebraic relation was more recently developed by [121, 122]. The new form is

$$A(\mathbf{k}) X(\mathbf{k}) + X(\mathbf{k}) A^*(\mathbf{k}) = -B(\mathbf{k}) H^*(\mathbf{k}) - H(\mathbf{k}) B^*(\mathbf{k}), \quad (7.12)$$

where  $H(\mathbf{k})$  is a matrix that contains spectral information about the colored-in-time stochastic forcing and is related to the cross-correlation between the forcing and the state in (7.6); see section 7.3.2 and appendix B.2 for details. For the special case where the forcing is white-in-time,  $H(\mathbf{k}) = (1/2)B(\mathbf{k})W(\mathbf{k})$  and (7.12) reduces to the standard Lyapunov equation (7.11). It should be noted that the right-hand-side of (7.11) is sign-definite, i.e., all eigenvalues of the matrix  $B(\mathbf{k}) W(\mathbf{k}) B^*(\mathbf{k})$  are nonnegative. In contrast, the right-hand-side of (7.12) is in general sign-indefinite. In fact, except for the case when the input is white noise, the matrix  $Z(\mathbf{k})$  defined by

$$Z(\mathbf{k}) := -(A(\mathbf{k}) X(\mathbf{k}) + X(\mathbf{k}) A^*(\mathbf{k})) \quad (7.13a)$$

$$= B(\mathbf{k}) H^*(\mathbf{k}) + H(\mathbf{k}) B^*(\mathbf{k}) \quad (7.13b)$$

may have both positive and negative eigenvalues.

Both equations, (7.11) and (7.12), in the respective cases, are typically used to compute the state covariance  $X(\mathbf{k})$  from the system matrices and forcing correlations. However, these same equations can be seen as linear algebraic constraints that restrict the values of the admissible covariances. It is in this sense that these algebraic constraints are used in the current chapter. More precisely, while a state-covariance  $X(\mathbf{k})$  is positive definite, not all positive-definite matrices can arise as state-covariances for the specific dynamical model (7.6). As shown by [121, 122], the structure of state-covariances is an inherent property of the linearized dynamics. Indeed, (7.12) provides necessary and sufficient conditions for a positive definite matrix  $X(\mathbf{k})$  to be a state-covariance of (7.6). Thus, given  $X(\mathbf{k})$ , (7.12) has to be solvable for  $H(\mathbf{k})$ . Equivalently, given  $X(\mathbf{k})$ , solvability of (7.12) amounts to the following rank condition:

$$\text{rank} \begin{bmatrix} A(\mathbf{k})X(\mathbf{k}) + X(\mathbf{k})A^*(\mathbf{k}) & B(\mathbf{k}) \\ B^*(\mathbf{k}) & 0 \end{bmatrix} = \text{rank} \begin{bmatrix} 0 & B(\mathbf{k}) \\ B^*(\mathbf{k}) & 0 \end{bmatrix}. \quad (7.14)$$

This implies that any positive-definite matrix  $X$  is admissible as a covariance of a linear time-invariant system if the input matrix  $B$  is full row rank.

In the next section, we utilize this framework to depart from white-in-time restriction on stochastic forcing and present a convex optimization framework for identifying colored-in-time excitations that account for partially available turbulent flow statistics. We also outline a procedure for designing a class of linear filters which generate the appropriate colored-in-time forcing.

### 7.3 Completion of partially known turbulent flow statistics

In high-Reynolds-number flows, only a finite set of correlations is available due to experimental or numerical limitations. Ideally, one is interested in a more complete set of such correlations that provides insights into flow physics. This brings us to investigate the completion of the partially known correlations in a way that is consistent with perturbations of the flow field around turbulent mean velocity. The velocity fluctuations can be accounted for by stochastic forcing to the linearized equations. To this end, we seek stochastic forcing models of low complexity where complexity is quantified by the number of degrees of freedom that are directly influenced by stochastic forcing [164, 165]. Such models arise as solutions to an inverse problem that we address using a regularized maximum entropy formulation. Interestingly, the models we obtain can alternatively be interpreted as a low-rank perturbation to the original linearized dynamics.

### 7.3.1 Covariance completion problem

We begin with the Navier-Stokes equations linearized about the turbulent mean velocity profile (7.6). As explained in Section 7.2.3, the covariance matrix  $X$  of the state  $\psi$  in (7.6), in statistical steady-state, satisfies the Lyapunov-like linear equation

$$AX + XA^* + Z = 0, \quad (7.15)$$

where  $A$  is the generator of the linearized dynamics and  $Z$  is the contribution of the stochastic excitation. For notational convenience, we omit the dependence on the wavenumber vector in this section. A subset of entries of the covariance matrix  $\Phi$  of velocity fluctuations, namely  $\Phi_{ij}$  for a selection of indices  $(i, j) \in \mathcal{I}$ , is assumed available. This yields an additional set of linear constraints for the matrix  $X$ ,

$$(CXC^*)_{ij} = \Phi_{ij}, \quad (i, j) \in \mathcal{I}. \quad (7.16)$$

For instance, these known entries of  $\Phi$  may represent one-point correlations in the wall-normal direction; see figure 7.3 for an illustration. Thus, our objective is to identify suitable choices of  $X$  and  $Z$  that satisfy the above constraints.

It is important to note that  $X$  is a covariance matrix, and hence positive definite, while  $Z$  is allowed to be sign indefinite. Herein, we follow a maximum entropy formalism and minimize  $-\log \det(X)$  subject to the given constraints [243]. Minimization of this logarithmic barrier function guarantees positive definiteness of the matrix  $X$  [135].

The contribution of the stochastic excitation enters through the matrix  $Z$ , cf. (7.13), which is of the form

$$Z = BH^* + HB^*, \quad (7.17)$$

where color of the time-correlations and directionality of the forcing are reflected by the choices of  $B$  and  $H$ . The matrix  $B$  specifies the preferred structure by which stochastic excitation enters into the linearized evolution model while  $H$  contains spectral information about the colored-in-time stochastic forcing. Trivially, when  $B$  is taken to be the full rank, all degrees of freedom are excited and a forcing model that cancels the original linearized dynamics becomes a viable choice; see remark 2. Without additional restriction on the forcing model, minimization of  $-\log \det(X)$  subject to the problem constraints yields a solution where the forcing excites all degrees of freedom in the linearized model. Such an approach may yield a solution that obscures important aspects of the underlying physics; see remark 2. It is thus important to minimize the number of degrees of freedom that can be directly influenced by forcing. This can be accomplished by a suitable regularization, e.g., by minimizing the rank of the matrix  $Z$  [164, 165].

Minimizing the rank, in general, leads to difficult non-convex optimization problems.

Instead, the nuclear norm, i.e., the sum of singular values of a matrix,

$$\|Z\|_* := \sum_i \sigma_i(Z), \quad (7.18)$$

can be used as a *convex* proxy for rank minimization [72, 73]. This leads to the following convex optimization problem

$$\begin{aligned} & \underset{X, Z}{\text{minimize}} && -\log \det(X) + \gamma \|Z\|_* \\ & \text{subject to} && AX + XA^* + Z = 0 \\ & && (CXC^*)_{ij} = \Phi_{ij}, \quad (i, j) \in \mathcal{I}, \end{aligned} \quad (7.19)$$

where the matrices  $A$  and  $C$  as well as the available entries  $\Phi_{ij}$  of the velocity covariance matrix represent problem data, the Hermitian matrices  $X, Z \in \mathbb{C}^{n \times n}$  are the optimization variables, and the regularization parameter  $\gamma > 0$  reflects the relative weight specified for the nuclear norm objective. While minimizing  $-\log \det(X)$  results in the maximum entropy solution, we also confine the complexity of the forcing model via nuclear norm minimization. The objective function in problem (7.19) thus provides a trade-off between the solution to the maximum entropy problem and the complexity of the forcing model.

Convexity of optimization problem (7.19) follows from the convexity of the objective function (which contains entropy and nuclear norm terms) and the linearity of the constraint set. Convexity is important because it guarantees a unique globally optimal solution. In turn, this solution provides a choice for the completed covariance matrix  $X$  and forcing contribution  $Z$  that are consistent with the constraints.

Although optimization problem (7.19) is convex, it is challenging to solve via conventional solvers for large-scale problems that arise in fluid dynamics. To this end, we have developed a scalable customized algorithm [160, 164].

### 7.3.2 Filter design: dynamics of stochastic forcing

We now describe how the solution of optimization problem (7.19) can be translated into a dynamical model for the colored-in-time stochastic forcing that is applied to the linearized NS equations. We recall that, due to translational invariance in the channel flow geometry, optimization problem (7.19) is fully decoupled for different wavenumbers  $\mathbf{k} = (k_x, k_z)$ . For each such pair, the solution matrices  $X(\mathbf{k})$  and  $Z(\mathbf{k})$  provide information about the temporal and wall-normal correlations of the stochastic forcing. We next provide the explicit construction of a linear dynamical model (filter) that generates the appropriate forcing.

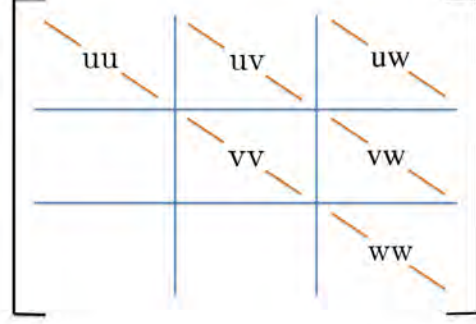


Figure 7.3: Structure of the matrix  $\Phi$  in optimization problem (7.19). At each pair of wavenumbers  $\mathbf{k} = (k_x, k_z)$ , available second-order statistics are given by one-point correlations in the wall-normal direction, i.e., the diagonal entries of the blocks in the velocity covariance matrix  $\Phi$ . The data is obtained from <http://torroja.dmt.upm.es/channels/data/>

The class of linear filters that we consider is generically minimal in the sense that the state dimension of the filter coincides with the number of degrees of freedom in the finite-dimensional approximation of the linearized NS equations (7.6). The input to the filter represents a white-in-time excitation vector  $\mathbf{w}(\mathbf{k}, t)$  with covariance  $\Omega(\mathbf{k}) \succ 0$ . At each  $\mathbf{k}$  the filter dynamics are of the form

$$\dot{\phi}(\mathbf{k}, t) = A_f(\mathbf{k}) \phi(\mathbf{k}, t) + B(\mathbf{k}) \mathbf{w}(\mathbf{k}, t), \quad (7.20a)$$

$$\mathbf{d}(\mathbf{k}, t) = C_f(\mathbf{k}) \phi(\mathbf{k}, t) + \mathbf{w}(\mathbf{k}, t). \quad (7.20b)$$

The generated output  $\mathbf{d}(\mathbf{k}, t)$  provides a suitable *colored-in-time* stochastic forcing to the linearized NS equations that reproduces the observed statistical signature of turbulent flow. As noted earlier, it is important to point out that white-in-time forcing to the linearized NS equations is often insufficient to explain the observed statistics.

The parameters of the filter are computed as follows

$$A_f(\mathbf{k}) = A(\mathbf{k}) + B(\mathbf{k}) C_f(\mathbf{k}), \quad (7.21a)$$

$$C_f(\mathbf{k}) = \left( H^*(\mathbf{k}) - \frac{1}{2} \Omega(\mathbf{k}) B^*(\mathbf{k}) \right) X^{-1}(\mathbf{k}), \quad (7.21b)$$

where the matrices  $B(\mathbf{k})$  and  $H(\mathbf{k})$  correspond to the factorization of  $Z$  into  $Z(\mathbf{k}) = B(\mathbf{k})H^*(\mathbf{k}) + H(\mathbf{k})B^*(\mathbf{k})$ ; see [164, 165] for details. The spectral content of the excitation  $\mathbf{d}(\mathbf{k}, t)$  is determined by the matrix-valued power spectral density

$$\Pi_f(\mathbf{k}, \omega) = T_f(\mathbf{k}, \omega) \Omega(\mathbf{k}) T_f^*(\mathbf{k}, \omega), \quad (7.22)$$

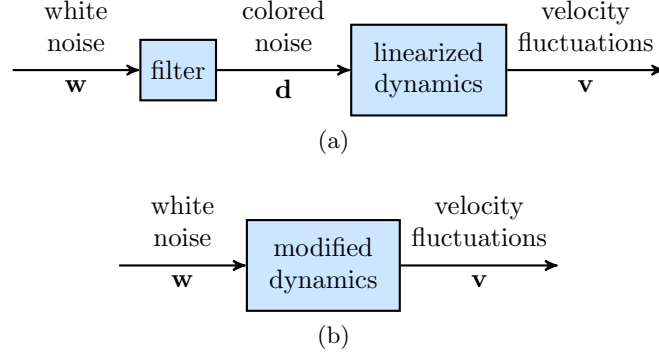


Figure 7.4: (a) Spatio-temporal filter (7.20) is designed to provide colored stochastic input to the linearized NS equations (7.6) in order to reproduce partially available second-order statistics of turbulent channel flow. The dynamics of this cascade connection are governed by the evolution model (7.24); (b) An equivalent reduced-order representation of (7.24) is given by (7.27).

where  $T_f(\mathbf{k}, \omega)$  is the frequency response of the filter, namely,

$$T_f(\mathbf{k}, \omega) = C_f(\mathbf{k}) (i\omega I - A_f(\mathbf{k}))^{-1} B(\mathbf{k}) + I, \quad (7.23)$$

and  $I$  is the identity matrix.

As illustrated in figure 7.4a, the output  $\mathbf{d}(\mathbf{k}, t)$  of the linear filter (7.20) is the input to the linearized NS equations (7.6). This cascade connection can be represented via the evolution model

$$\begin{aligned} \begin{bmatrix} \dot{\psi}(\mathbf{k}, t) \\ \dot{\phi}(\mathbf{k}, t) \end{bmatrix} &= \begin{bmatrix} A(\mathbf{k}) & B(\mathbf{k}) C_f(\mathbf{k}) \\ 0 & A(\mathbf{k}) + B(\mathbf{k}) C_f(\mathbf{k}) \end{bmatrix} \begin{bmatrix} \psi(\mathbf{k}, t) \\ \phi(\mathbf{k}, t) \end{bmatrix} + \begin{bmatrix} B(\mathbf{k}) \\ B(\mathbf{k}) \end{bmatrix} \mathbf{w}(\mathbf{k}, t) \\ \mathbf{v}(\mathbf{k}, t) &= \begin{bmatrix} C(\mathbf{k}) & 0 \end{bmatrix} \begin{bmatrix} \psi(\mathbf{k}, t) \\ \phi(\mathbf{k}, t) \end{bmatrix}, \end{aligned} \quad (7.24)$$

which has twice as many degrees of freedom as the spatial discretization of the original linearized NS model. As shown by [164], due to the presence of uncontrollable modes in (7.24), the coordinate transformation

$$\begin{bmatrix} \psi(\mathbf{k}, t) \\ \chi(\mathbf{k}, t) \end{bmatrix} = \begin{bmatrix} I & 0 \\ -I & I \end{bmatrix} \begin{bmatrix} \psi(\mathbf{k}, t) \\ \phi(\mathbf{k}, t) \end{bmatrix}, \quad (7.25)$$

can be used to bring system (7.24) into the following form

$$\begin{aligned} \begin{bmatrix} \dot{\psi}(\mathbf{k}, t) \\ \dot{\chi}(\mathbf{k}, t) \end{bmatrix} &= \begin{bmatrix} A(\mathbf{k}) + B(\mathbf{k}) C_f(\mathbf{k}) & B(\mathbf{k}) C_f(\mathbf{k}) \\ 0 & A(\mathbf{k}) \end{bmatrix} \begin{bmatrix} \psi(\mathbf{k}, t) \\ \chi(\mathbf{k}, t) \end{bmatrix} + \begin{bmatrix} B(\mathbf{k}) \\ 0 \end{bmatrix} \mathbf{w}(\mathbf{k}, t) \\ \mathbf{v}(\mathbf{k}, t) &= \begin{bmatrix} C(\mathbf{k}) & 0 \end{bmatrix} \begin{bmatrix} \psi(\mathbf{k}, t) \\ \chi(\mathbf{k}, t) \end{bmatrix}. \end{aligned} \quad (7.26)$$

Clearly, the input  $\mathbf{w}(\mathbf{k}, t)$  does not enter into the equation that governs the evolution of  $\chi(\mathbf{k}, t)$ . Thus, the reduced-order representation

$$\begin{aligned} \dot{\psi}(\mathbf{k}, t) &= (A(\mathbf{k}) + B(\mathbf{k}) C_f(\mathbf{k})) \psi(\mathbf{k}, t) + B(\mathbf{k}) \mathbf{w}(\mathbf{k}, t), \\ \mathbf{v}(\mathbf{k}, t) &= C(\mathbf{k}) \psi(\mathbf{k}, t), \end{aligned} \quad (7.27)$$

which has the same number of degrees of freedom as (7.6), completely captures the influence of  $\mathbf{w}(\mathbf{k}, t)$  on  $\psi(\mathbf{k}, t)$ ; see figure 7.4b for an illustration. Furthermore, stability of  $A(\mathbf{k}) + B(\mathbf{k}) C_f(\mathbf{k})$  (see remark 3) implies that the initial conditions  $\psi(\mathbf{k}, 0)$  and  $\phi(\mathbf{k}, 0)$  only influence the transient response and do not have any impact on the steady-state statistics. The corresponding algebraic Lyapunov equation in conjunction with (7.21b) yields

$$\begin{aligned} (A + B C_f) X + X (A + B C_f)^* + B \Omega B^* \\ &= A X + X A^* + B \Omega B^* + B C_f X + X C_f^* B^* \\ &= A X + X A^* + B H^* + H B^* \\ &= 0, \end{aligned} \quad (7.28)$$

which shows that (7.20) generates a stochastic process  $\mathbf{d}(\mathbf{k}, t)$  that is consistent with  $X(\mathbf{k})$ . In what follows, without loss of generality, we choose the covariance matrix of the white noise  $\mathbf{w}(\mathbf{k}, t)$  to be the identity matrix,  $\Omega = I$ .

**Remark 1.** The compact representation (7.27) allows for alternative interpretations of colored-in-time forcing and, at the same time, offers advantages from a computational standpoint. First, the structure of (7.27) suggests that the colored-in-time forcing realized by (7.20) can be equivalently interpreted as a modification of the dynamical generator of the linearized NS equations due to state-feedback interactions; see figure 7.5. This interpretation allows seeking suitable “feedback gains”  $C_f(\mathbf{k})$  that may now be optimal with respect to alternative design criteria [244]. Moreover, the term  $B(\mathbf{k}) C_f(\mathbf{k})$  can be seen as a low-rank modification of the dynamical generator  $A(\mathbf{k})$  of the linearized NS equations. Finally, time-domain simulations require numerical integration of system (7.27) which has half the number of states as compared to system (7.24), thereby offering computational speedup.

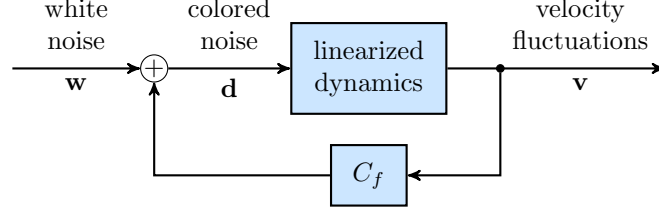


Figure 7.5: An equivalent feedback representation of the cascade connection in figure 7.4a.

**Remark 2.** Important aspects of the underlying physics may be obscured when the forcing is allowed to excite all degrees of freedom in the linearized model. As discussed above, if the nuclear norm of  $Z = BH^* + HB^*$  is not accounted for in (7.19), the resulting input matrix  $B$  will be of full rank. In this case, without loss of generality, we can choose  $B = I$  which simplifies equation (7.12),

$$A(\mathbf{k})X(\mathbf{k}) + X(\mathbf{k})A^*(\mathbf{k}) = -H^*(\mathbf{k}) - H(\mathbf{k}). \quad (7.29)$$

Clearly, this equation is satisfied with  $H^*(\mathbf{k}) = -A(\mathbf{k})X(\mathbf{k})$ . With this choice of  $H(\mathbf{k})$ , the reduced-order representation (7.27) is given by

$$\dot{\psi}(\mathbf{k}, t) = -\frac{1}{2}X^{-1}(\mathbf{k})\psi(\mathbf{k}, t) + \mathbf{w}(\mathbf{k}, t). \quad (7.30)$$

This demonstrates that colored-in-time forcing of the linearized NS equations which excites all degrees of freedom can lead to the complete cancelation of the linearized dynamical generator  $A(\mathbf{k})$ . It is thus crucial to restrict the number of input channels via the nuclear norm penalty in the objective function of optimization problem (7.19).

**Remark 3.** It is known that for channel flow the linearized NS equations around the turbulent mean velocity profile are stable [196, 245]. Interestingly and independently of this fact, the modified dynamical generator,  $A(\mathbf{k}) + B(\mathbf{k})C_f(\mathbf{k})$  in (7.27), can be shown to be stable by standard Lyapunov theory. More specifically, substituting the expression for the matrix  $H(\mathbf{k})$  from (7.21b) into equation (7.12) yields

$$(A(\mathbf{k}) + B(\mathbf{k})C_f(\mathbf{k}))X(\mathbf{k}) + X(\mathbf{k})(A(\mathbf{k}) + B(\mathbf{k})C_f(\mathbf{k}))^* = -B(\mathbf{k})\Omega(\mathbf{k})B^*(\mathbf{k}).$$

This is a standard Lyapunov equation. Since  $(A, B)$  is a controllable pair, so is  $(A + B C_f, B)$ , and therefore  $(A + B C_f, B \Omega^{1/2})$  is controllable as well. Standard Lyapunov theory implies that the positive semi-definiteness of  $B(\mathbf{k})\Omega(\mathbf{k})B^*(\mathbf{k})$  is sufficient to guarantee that all eigenvalues of  $A(\mathbf{k}) + B(\mathbf{k})C_f(\mathbf{k})$  are in the left-half of the complex plane.

## 7.4 Application to turbulent channel flow

In this section, we utilize the modeling and optimization framework developed in Section 7.3 to account for partially observed second-order statistics of turbulent channel flow. In our setup, the mean velocity profile and one-point velocity correlations in the wall-normal direction at various wavenumber pairs  $\mathbf{k}$  are obtained from DNS with  $R_\tau = 186$  [234–237]; see figure 7.3 for an illustration. We show that stochastically forced linearized NS equations can be used to exactly reproduce the available statistics and to complete unavailable two-point correlations of the turbulent velocity field. The *colored-in-time* forcing with the *identified* power spectral density is generated by linear filters that introduce low-rank perturbations to the linearization around turbulent mean velocity; cf. (7.27). As a result of this modification to the linearized NS equations, all one-point correlations are *perfectly matched* and the one-dimensional energy spectra is *completely reconstructed*. In addition, we show that two-point velocity correlations compare favorably with the result of DNS. As aforementioned, the modified dynamics that result from our modeling framework have the same number of degrees of freedom as the finite-dimensional approximation of the linearized NS dynamics and are thus convenient for the purpose of conducting linear stochastic simulations. We utilize these simulations to verify the ability of our model to account for the statistical signatures of turbulent channel flow. Finally, we close this section by showing that our framework can be also used to capture the velocity correlations at higher Reynolds numbers.

### 7.4.1 Necessity for the colored-in-time forcing

For homogeneous isotropic turbulence, [114] showed that the steady-state velocity correlation matrices can be exactly reproduced by the linearized NS equations. This can be achieved with white-in-time solenoidal forcing whose second-order statistics are proportional to the turbulent energy spectrum; for additional details see [223, Appendix C]. For turbulent channel flow, however, we next show that the matrix  $A(\mathbf{k})X_{\text{dns}}(\mathbf{k}) + X_{\text{dns}}(\mathbf{k})A^*(\mathbf{k})$  can fail to be negative semi-definite for numerically generated covariances  $X_{\text{dns}}(\mathbf{k})$  of the state  $\psi$ . Here,  $A(\mathbf{k})$  is the generator of the linearized dynamics around the turbulent mean velocity profile and  $X_{\text{dns}}(\mathbf{k})$  is the steady-state covariance matrix resulting from DNS of turbulent channel flow.

Figure 7.6 shows the eigenvalues of the matrix  $A(\mathbf{k})X_{\text{dns}}(\mathbf{k}) + X_{\text{dns}}(\mathbf{k})A^*(\mathbf{k})$  for channel flow with  $R_\tau = 186$  and  $\mathbf{k} = (2.5, 7)$ . The presence of both positive and negative eigenvalues indicates that the second-order statistics of turbulent channel flow cannot be exactly reproduced by the linearized NS equations with white-in-time stochastic excitation. As we show in the next subsection, this limitation can be overcome by departing from the white-in-time restriction.

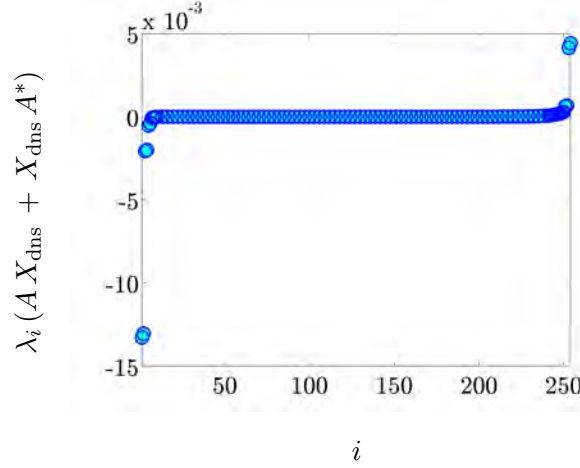


Figure 7.6: Positive eigenvalues of the matrix  $A(\mathbf{k})X_{\text{dns}}(\mathbf{k}) + X_{\text{dns}}(\mathbf{k})A^*(\mathbf{k})$ , for channel flow with  $R_\tau = 186$  and  $\mathbf{k} = (2.5, 7)$ , indicate that turbulent velocity covariances cannot be reproduced by the linearized NS equations with white-in-time stochastic forcing; cf. equation (7.11).

#### 7.4.2 Reproducing available and completing unavailable velocity correlations

We next employ the optimization framework of Section 7.3 to account for second-order statistics of turbulent channel flow with  $R_\tau = 186$  via a low-complexity model. We use  $N = 127$  collocation points in the wall-normal direction and show that all one-point velocity correlations can be exactly reproduced using the linearized NS equations with colored-in-time forcing. Grid convergence is ensured by doubling the number of collocation points. In addition, we demonstrate that an appropriate choice of the regularization parameter  $\gamma$  provides good completion of two-point correlations that are *not* used as problem data in optimization problem (7.19). Appendix B.3 offers additional insight into the influence of this parameter on the quality of completion.

Figures 7.7 and 7.8 show that the solution to optimization problem (7.19) *exactly reproduces* available one-point velocity correlations resulting from DNS at various wavenumbers. At each  $\mathbf{k}$ , the constraint (7.16) restricts all feasible solutions of problem (7.19) to match available one-point correlations. Our computational experiments demonstrate feasibility of optimization problem (7.19) at each  $\mathbf{k}$ . Thus, regardless of the value of the regularization parameter  $\gamma$ , *all available one-point correlations* of turbulent flow can be *recovered* by a stochastically forced linearized model.

Figures 7.7a and 7.7b display perfect matching of all one-point velocity correlations that result from integration over wall-parallel wavenumbers. Since problem (7.19) is

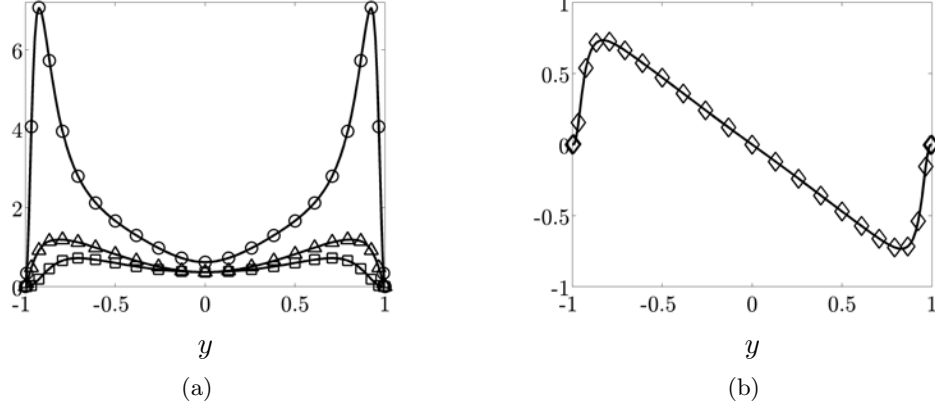


Figure 7.7: (a) Correlation profiles of normal and (b) shear stresses resulting from DNS of turbulent channel flow with  $R_\tau = 186$  (—) and from the solution to (7.19);  $uu$  ( $\circ$ ),  $vv$  ( $\square$ ),  $ww$  ( $\triangle$ ),  $-uv$  ( $\diamond$ ). We observe perfect matching of all one-point velocity correlations that result from integration over wall-parallel wavenumbers. Note: plot markers are sparse for data presentation purposes and do not indicate grid resolution.

not feasible for  $Z \geq 0$ , this cannot be achieved with white-in-time stochastic forcing; see Section 7.4.1. In contrast, colored-in-time forcing enables recovery of the one dimensional energy spectra of velocity fluctuations resulting from DNS; in figure 7.8, pre-multiplied spectra are displayed as a function of the wall-normal coordinate, stream-wise (left plots), and spanwise (right plots) wavelengths. All of these are given in inner (viscous) units with  $y^+ = R_\tau(1 + y)$ ,  $\lambda_x^+ = 2\pi R_\tau/k_x$ , and  $\lambda_z^+ = 2\pi R_\tau/k_z$ .

Our results should be compared and contrasted to [205], where a gain-based low-order decomposition was used to approximate the velocity spectra of turbulent channel flow. Twelve optimally weighted resolvent modes approximated the Reynolds shear stress, streamwise, wall-normal, and spanwise intensities with 25%, 20%, 17%, and 6% error, respectively. While the results presented here are at a lower Reynolds number ( $R_\tau = 186$  vs.  $R_\tau = 2003$ ), our computational experiments demonstrate feasibility of optimization problem (7.19) at all wavenumber pairs. Thus, all one-point correlations can be perfectly matched with colored-in-time stochastic forcing. As we show in Section 7.4.4, this holds even at higher Reynolds numbers.

We next demonstrate that the solution to optimization problem (7.19) also provides good recovery of two-point velocity correlations. We examine the wavenumber pair

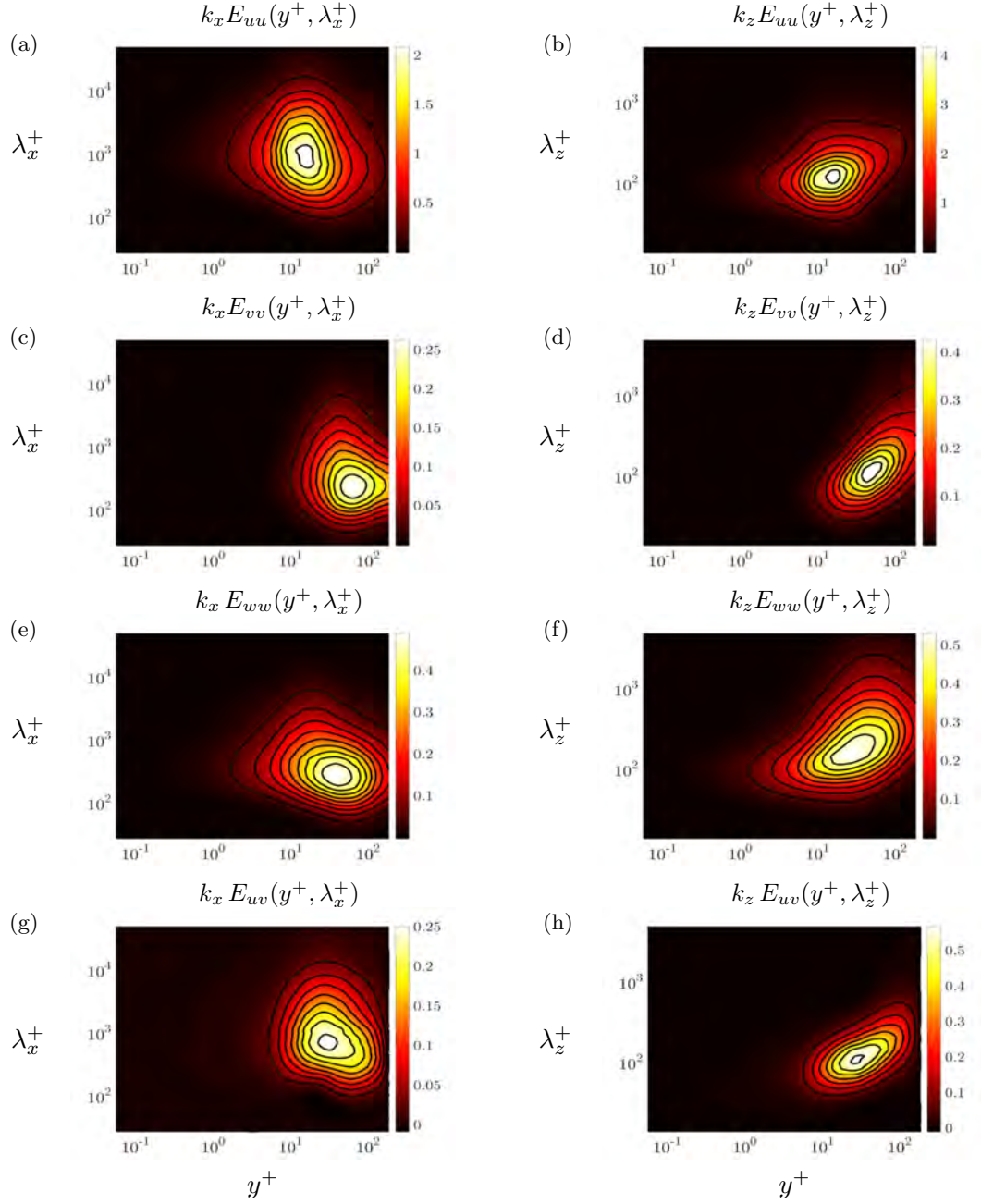


Figure 7.8: Pre-multiplied one-dimensional energy spectrum of streamwise (a,b), wall-normal (c,d), spanwise (e,f) velocity fluctuations, and the Reynolds stress co-spectrum (g,h) in terms of streamwise (left) and spanwise (right) wavelengths and the wall-normal coordinate (all in inner units). Color plots: DNS-generated spectra of turbulent channel flow with  $R_\tau = 186$ . Contour lines: spectra resulting from the solution to (7.19).

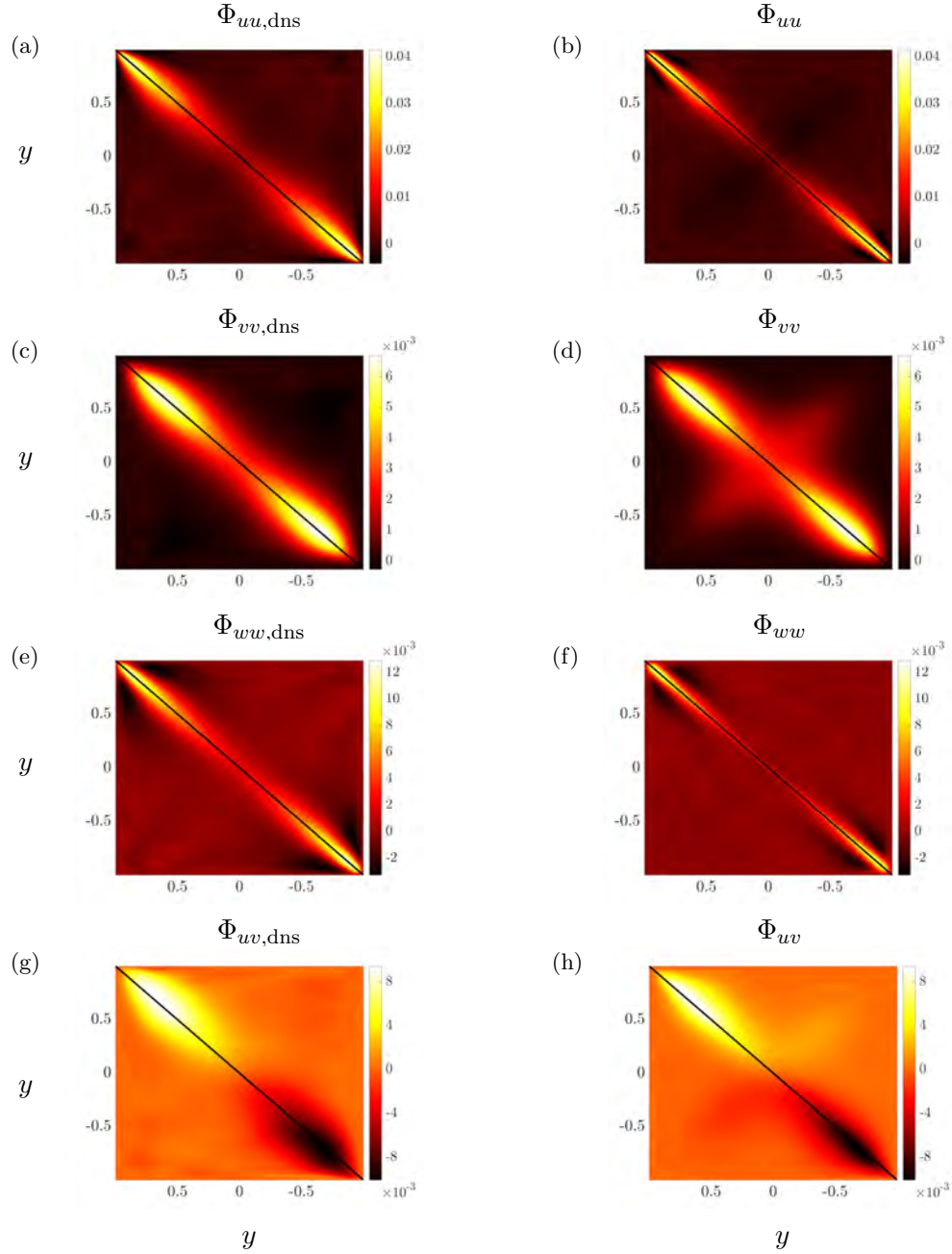


Figure 7.9: Covariance matrices resulting from DNS of turbulent channel flow with  $R_\tau = 186$  (left plots); and the solution to optimization problem (7.19) with  $\gamma = 300$  (right plots). (a, b) Streamwise  $\Phi_{uu}$ , (c, d) wall-normal  $\Phi_{vv}$ , (e, f) spanwise  $\Phi_{ww}$ , and the streamwise/wall-normal  $\Phi_{uv}$  two-point correlation matrices at  $\mathbf{k} = (2.5, 7)$ . The one-point correlation profiles that are used as problem data in (7.19) are marked by black lines along the main diagonals.

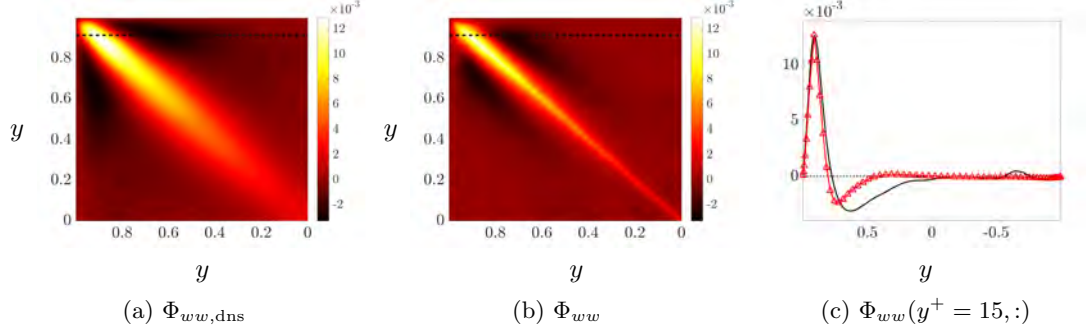


Figure 7.10: Quadrant II of the spanwise covariance matrices resulting from (a) DNS of turbulent channel flow with  $R_\tau = 186$ , and (b) the solution to optimization problem (7.19) with  $\gamma = 300$  at  $\mathbf{k} = (2.5, 7)$ . The horizontal black lines mark  $y^+ = 15$ . (c) Comparison of the two-point correlation  $\Phi_{ww}$  at  $y^+ = 15$  with other wall-normal locations: DNS (—); solution of (7.19) ( $\triangle$ ).

$\mathbf{k} = (2.5, 7)$  at which the premultiplied energy spectrum at  $R_\tau = 186$  peaks. The left column in figure 7.9 displays the streamwise  $\Phi_{uu}$ , wall-normal  $\Phi_{vv}$ , spanwise  $\Phi_{ww}$ , and the streamwise/wall-normal  $\Phi_{uv}$  covariance matrices resulting from DNS. The right column in figure 7.9 shows the same covariance matrices that are obtained from the solution to optimization problem (7.19). Although only diagonal elements of these matrices (marked by black lines in figure 7.9) were used as data in (7.19), we have good recovery of the off-diagonal entries as well. In particular, for  $\gamma = 300$ , we observe approximately 60% recovery of the DNS-generated two-point correlation matrix  $\Phi_{dns}(\mathbf{k})$ . The quality of approximation is assessed using (see appendix B.3),

$$\frac{\|\Phi(\mathbf{k}) - \Phi_{dns}(\mathbf{k})\|_F}{\|\Phi_{dns}(\mathbf{k})\|_F},$$

where  $\|\cdot\|_F$  denotes the Frobenius norm of a given matrix and  $\Phi(\mathbf{k}) = C(\mathbf{k})X(\mathbf{k})C^*(\mathbf{k})$  represents the two-point correlation matrix of the velocity fluctuations resulting from our optimization framework.

We note that the solution of optimization problem (7.19) also captures the presence of negative correlations in the covariance matrix of spanwise velocity; cf. figures 7.9e and 7.9f. Figures 7.10a and 7.10b show the second quadrants of the covariance matrices  $\Phi_{ww,dns}$  and  $\Phi_{ww}$ . In addition to matching the diagonal entries, i.e., one-point correlations of the spanwise velocity, the essential trends of two-point correlations resulting from DNS are also recovered. Figure 7.10c illustrates this by showing the dependence of the auto-correlation of the spanwise velocity at  $y^+ = 15$  on the wall-normal coordinate. This profile is obtained by extracting the corresponding row of  $\Phi_{ww}$  and is

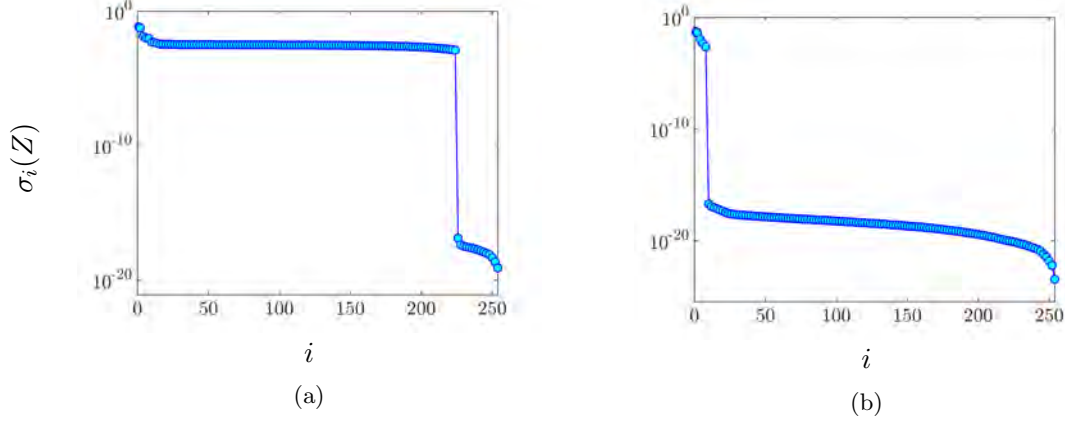


Figure 7.11: Singular values of the solution  $Z$  to (7.19) in turbulent channel flow with  $R_\tau = 186$ ,  $\mathbf{k} = (2.5, 7)$ , and  $N = 127$  for (a)  $\gamma = 300$ ; and (b)  $\gamma = 10^4$ .

marked by the black dashed line in figures 7.10a and 7.10b. Clearly, the solution to optimization problem (7.19) recovers the basic features (positive-negative-positive) of the DNS results. These features are indicators of coherent structures that reside at various wall-normal locations in the channel flow [9, 246].

It is worth noting that such *high-quality recovery of two-point correlations* would not have been possible *without incorporating the physics of the linearized NS equations as the structural constraint* (7.15) *into optimization problem* (7.19).

**Remark 4.** In optimization problem (7.19), the regularization parameter  $\gamma$  determines the importance of the nuclear norm relative to the logarithmic barrier function. Larger values of  $\gamma$  yield  $Z(\mathbf{k})$  of lower rank, but may compromise quality of completion of two-point correlations; see appendix B.3. For turbulent channel flow with  $R_\tau = 186$  and  $\mathbf{k} = (2.5, 7)$ , figure 7.11 shows the singular values of  $Z$  for two values of  $\gamma$ ,  $\gamma = 300$  and  $10^4$ . Clearly, the higher value of  $\gamma$  results in a much lower rank of the matrix  $Z$ , with 6 positive and 2 negative eigenvalues. [165] showed that the maximum number of positive or negative eigenvalues of the matrix  $Z$  bounds the number of inputs into the linearized NS model (7.6). This implies that partially available statistics can be reproduced with 6 colored-in-time inputs. However, as discussed in appendix B.3, the quality of completion is best for  $\gamma = 300$ . In this case, the matrix  $Z$  has 225 non-zero eigenvalues, 221 positive and 4 negative. Thus, for  $\gamma = 300$  and a spatial discretization with  $N = 127$  collocation points in  $y$ , 221 colored-in-time inputs are required to account for partially available statistics.

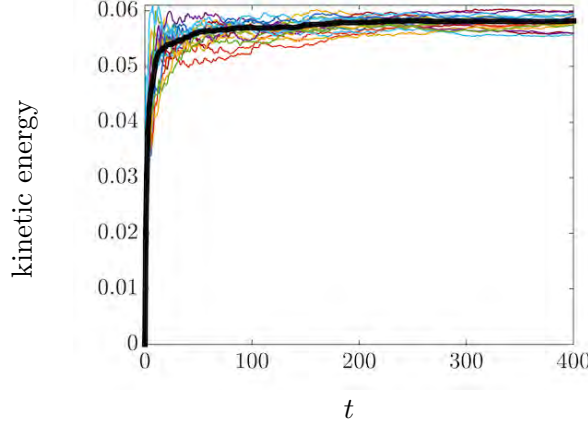


Figure 7.12: Time evolution of fluctuation's kinetic energy for twenty realizations of the forcing to the modified linearized dynamics (7.27) with  $R_\tau = 186$  and  $\mathbf{k} = (2.5, 7)$ ; the energy averaged over all simulations is marked by the thick black line.

### 7.4.3 Verification in stochastic linear simulations

We next conduct stochastic simulations of the linearized flow equations and compare the resulting statistics with DNS at  $R_\tau = 186$ . Filter (7.20) that generates colored-in-time forcing  $\mathbf{d}(\mathbf{k}, t)$  is obtained from the solution to (7.19) with  $\mathbf{k} = (2.5, 7)$  and  $\gamma = 10^4$ . This filter in conjunction with the linearized dynamics (7.6) yields representation (7.27) which is driven by white-in-time Gaussian process  $\mathbf{w}(\mathbf{k}, t)$  with zero mean and unit variance. We recall that this reduced-order representation is equivalent to the original NS equations subject to the colored-in-time stochastic forcing  $\mathbf{d}(\mathbf{k}, t)$  with properly identified power spectrum. As shown in Section 7.3.2, system (7.24) can be equivalently represented by a low-rank modification to the linearized NS dynamics (7.27), which has the same number of degrees of freedom as the finite-dimensional approximation of the original linearized NS dynamics. Here, we consider a spatial discretization with  $N = 127$  collocation points in the wall-normal direction. Thus, at each wavenumber pair, linear system (7.27) that results from our modeling framework has 254 degrees of freedom.

Stochastic linear simulations that we present next confirm that one-point correlations can indeed be recovered by stochastically forced linearized dynamics. Since the proper comparison with DNS or experiments requires ensemble-averaging, rather than comparison at the level of individual stochastic simulations, we have conducted twenty simulations of system (7.27). The total simulation time was set to 400 viscous time units.

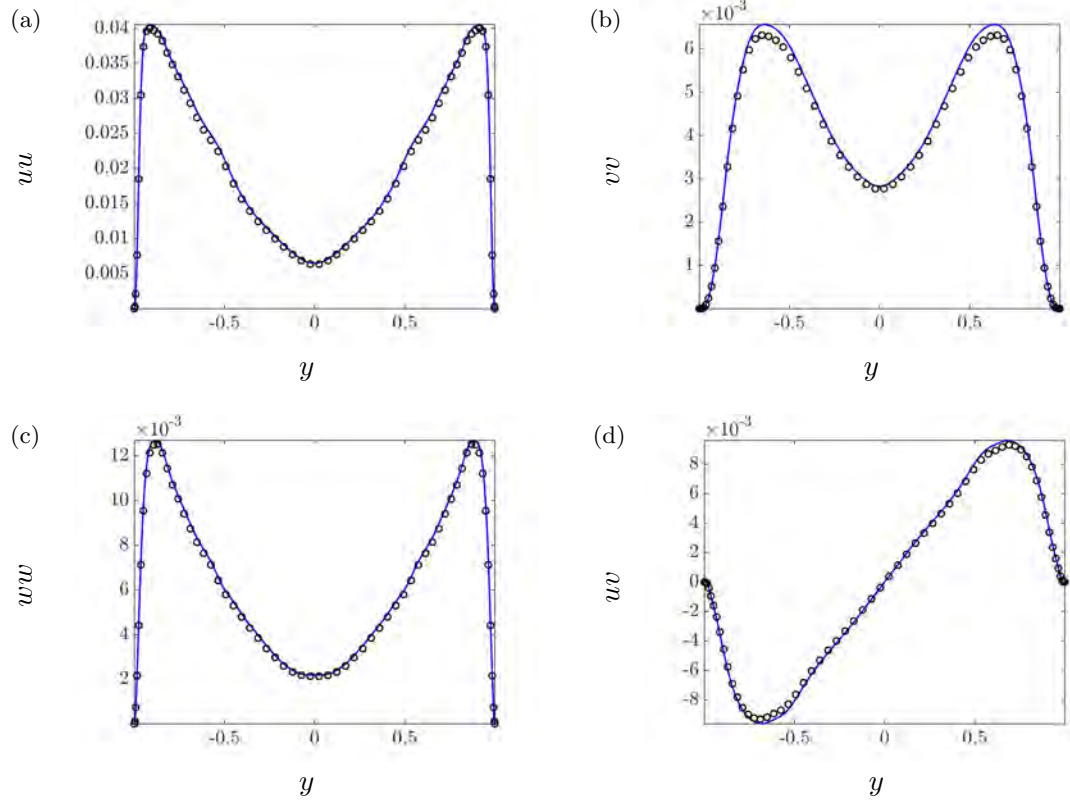


Figure 7.13: Normal stress profiles in the (a) streamwise, (b) wall-normal, (c) spanwise direction, and (d) shear stress profile resulting from DNS of turbulent channel flow with  $R_\tau = 186$  at  $\mathbf{k} = (2.5, 7)$  (—) and stochastic linear simulations ( $\circ$ ).

Figure 7.12 shows the time evolution of the energy (variance) of velocity fluctuations, for twenty realizations of white-in-time forcing  $\mathbf{w}(\mathbf{k}, t)$  to system (7.27). The variance averaged over all simulations is marked by the thick black line. Even though the responses of individual simulations differ from each other, the average of twenty sample sets asymptotically approaches the correct value of turbulent kinetic energy in the statistical steady-state,  $\text{trace}(\Phi(\mathbf{k}))$ . Figure 7.13 displays the normal and shear stress profiles resulting from DNS and from stochastic linear simulations. We see that the averaged output of twenty simulations of the linearized dynamics agrees well with DNS results. This close agreement can be further improved by running additional linear simulations and by increasing the total simulation times.

#### 7.4.4 Reproducing statistics at higher Reynolds numbers

We next apply our optimization framework to channel flows with higher Reynolds numbers [236–238]. We use  $N = 201$  collocation points to discretize differential operators for turbulent flows with  $R_\tau = 549, 934$ , and  $2003$ . We focus on a pair of wavelengths that are relevant to the study of near-wall structures, i.e.,  $\lambda_x^+ = 1000$  and  $\lambda_z^+ = 100$ . This wavelength pair is associated with the near-wall system of quasi-streamwise streaks and counter-rotating vortices which is responsible for large production of turbulent kinetic energy [247, 248]. For all Reynolds numbers, optimization problem (7.19) is solved with  $\gamma = 300$  and up to the same accuracy.

Figure 7.14 shows the normal and shear stress profiles for the aforementioned Reynolds numbers and selected wavelength pair. For illustration, these profiles have been normalized by their largest values and are presented in inner units. We see that the solution to optimization problem (7.19) achieves perfect recovery of all one-point velocity correlations.

Figure 7.15 shows the singular values of the matrix  $Z$  resulting from the solution to (7.19). At this pair of wall-parallel wavelengths, we observe that higher Reynolds numbers result in matrices  $Z$  of similar rank. For  $R_\tau = 547, 934$ , and  $2003$ , matrix  $Z$  has 84, 80, and 76 significant positive and 2, 5, and 8 significant negative eigenvalues, respectively. We thus conclude that, at higher Reynolds numbers, a similar number of inputs can be utilized to recover turbulent statistics by the linearized NS equations with colored-in-time stochastic forcing. Equivalently, the modification to the dynamical generator of the linearized NS equations which is required to capture partially available second-order statistics at higher Reynolds numbers is of similar rank.

### 7.5 Spatio-temporal analysis of the linear model

System (7.27) provides a linear model that captures second-order statistics of turbulent channel flow in statistical steady-state. As illustrated in Section 7.4.3, this model can be advanced in time by conducting linear stochastic simulations. More importantly, it can be analyzed using tools from linear systems theory. For example, dominant spatio-temporal flow structures can be easily identified and two-point correlations in time can be readily computed. These tools have provided useful insight into the dynamics of both laminar [28–30, 112, 177, 178, 181, 249] and turbulent [31, 32, 198, 200, 201, 203, 204] wall-bounded shear flows.

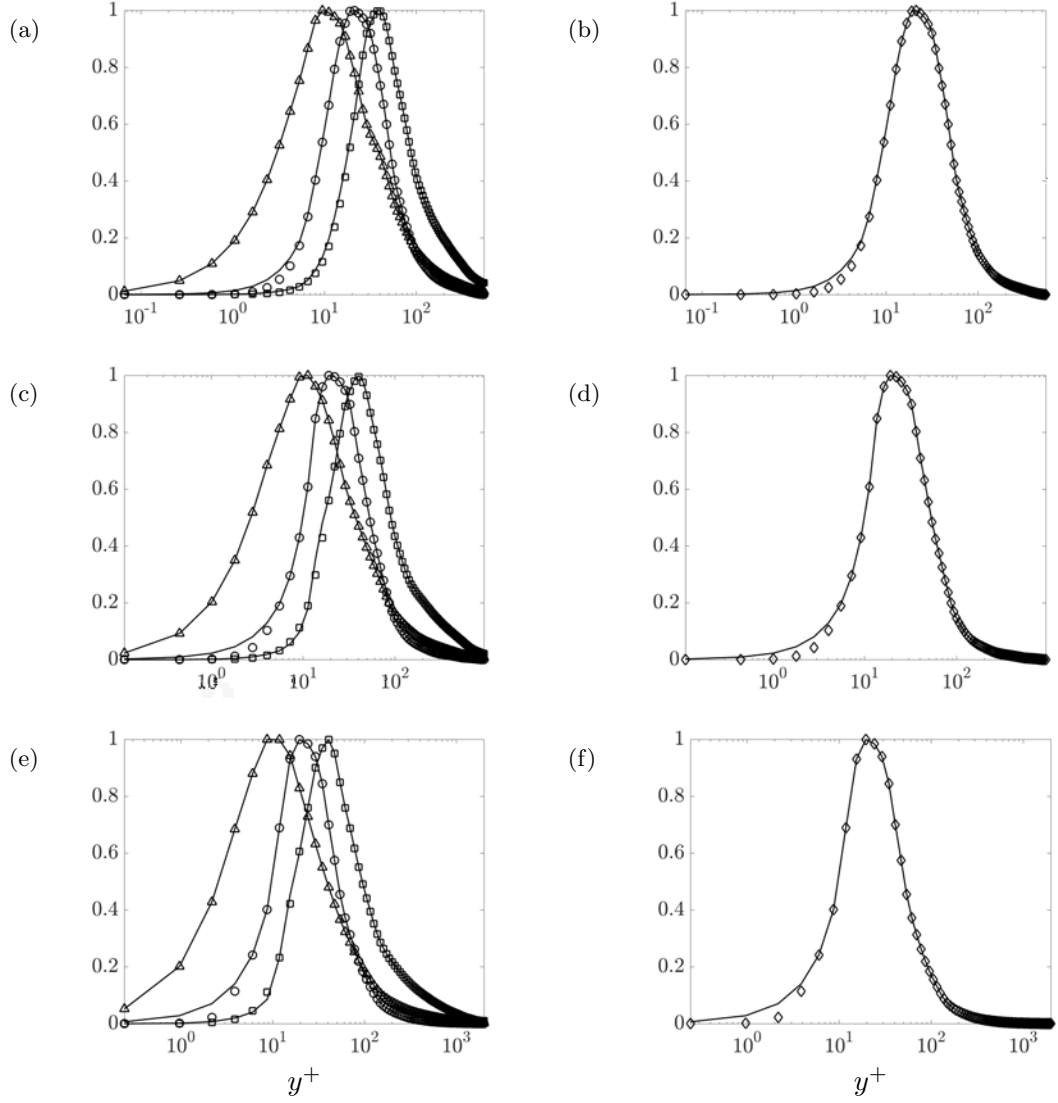


Figure 7.14: Normalized normal (left) and shear (right) stress profiles resulting from DNS (—) and from the solution to (7.19) with  $\gamma = 300$  at  $\lambda_x^+ = 1000$  and  $\lambda_z^+ = 100$  (in inner units);  $uu$  ( $\circ$ ),  $vv$  ( $\square$ ),  $ww$  ( $\triangle$ ),  $-uv$  ( $\diamond$ ). (a, b)  $R_\tau = 547$ ; (c, d)  $R_\tau = 934$ ; (e, f)  $R_\tau = 2003$ .

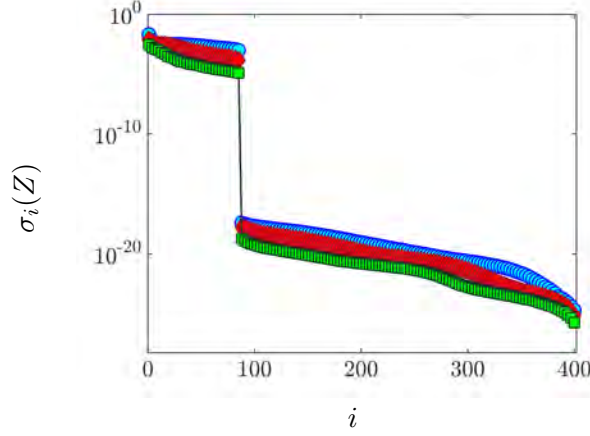


Figure 7.15: Singular values of the matrix  $Z$  resulting from the solution to (7.19) with  $\gamma = 300$  at  $R_\tau = 549$  ( $\circ$ ), 934 ( $\diamond$ ), and 2003 ( $\square$ ).

Application of the temporal Fourier transform on system (7.27) yields

$$\mathbf{v}(\mathbf{k}, \omega) = T_{\mathbf{vw}}(\mathbf{k}, \omega) \mathbf{w}(\mathbf{k}, \omega), \quad (7.31)$$

where  $\omega$  is the temporal frequency and  $T_{\mathbf{vw}}(\mathbf{k}, \omega)$  is the spatio-temporal frequency response,

$$T_{\mathbf{vw}}(\mathbf{k}, \omega) = -C(\mathbf{k}) (i\omega \mathbf{I} + A_f(\mathbf{k}))^{-1} B(\mathbf{k}). \quad (7.32)$$

Here,  $A_f(\mathbf{k})$  is the generator of linear dynamics (7.27) which result from the modeling and optimization framework of Section 7.3. Equation (7.31) facilitates decomposition of the fluctuating velocity field  $\mathbf{v}(\mathbf{k}, \omega)$  into the sum of spatio-temporal Fourier modes which correspond to physical structures with streamwise and spanwise wavelengths  $\lambda_x = 2\pi/k_x$  and  $\lambda_z = 2\pi/k_z$ . These structures convect at speed  $c = \omega/k_x$  in the streamwise direction. Since the dominant waves in turbulent channel flow travel downstream [201], the sign of the temporal frequency in (7.32) is changed relative to the convention used in (7.23). With proper definition of the matrices  $A$ ,  $B$ , and  $C$  the spatio-temporal frequency response analysis can be conducted for different linear approximations of the NS equations, e.g., the original linearized NS model (7.6) or an eddy-viscosity-enhanced linearized NS model [32, 197–200].

Singular value decomposition of the frequency response (7.32) brings input-output representation (7.31) into the following form,

$$\mathbf{v}(\mathbf{k}, \omega) = T_{\mathbf{vw}}(\mathbf{k}, \omega) \mathbf{w}(\mathbf{k}, \omega) = \sum_{j=1}^r \sigma_j(\mathbf{k}, \omega) a_j(\mathbf{k}, \omega) \tilde{\xi}_j(\mathbf{k}, \omega), \quad (7.33)$$

where  $\sigma_1 \geq \sigma_2 \geq \dots \geq \sigma_r > 0$  are the singular values of  $T_{\mathbf{vw}}(\mathbf{k}, \omega)$ ,  $\tilde{\xi}_j(\mathbf{k}, \omega)$  is the  $j$ th left singular vector of  $T_{\mathbf{vw}}(\mathbf{k}, \omega)$ , and  $a_j(\mathbf{k}, \omega)$  is the projection of the forcing  $\mathbf{w}(\mathbf{k}, \omega)$  onto the  $j$ th right singular vector. The left and right singular vectors provide insight into coherent structures of velocity and forcing fluctuations [183]. In particular, symmetries in the wall-parallel directions can be used to express velocity components as

$$u_j(x, z, t) = 4 \cos(k_z z) \operatorname{Re} \left( \tilde{u}_j(\mathbf{k}, \omega) e^{i(k_x x - \omega t)} \right), \quad (7.34a)$$

$$v_j(x, z, t) = 4 \cos(k_z z) \operatorname{Re} \left( \tilde{v}_j(\mathbf{k}, \omega) e^{i(k_x x - \omega t)} \right), \quad (7.34b)$$

$$w_j(x, z, t) = -4 \sin(k_z z) \operatorname{Im} \left( \tilde{w}_j(\mathbf{k}, \omega) e^{i(k_x x - \omega t)} \right). \quad (7.34c)$$

Here,  $\operatorname{Re}$  and  $\operatorname{Im}$  denote real and imaginary parts, and  $\tilde{u}_j(\mathbf{k}, \omega)$ ,  $\tilde{v}_j(\mathbf{k}, \omega)$ , and  $\tilde{w}_j(\mathbf{k}, \omega)$  are the streamwise, wall-normal, and spanwise components of the  $j$ th left singular vector  $\tilde{\xi}_j(\mathbf{k}, \omega)$  in (7.33).

The power spectral density (PSD) of  $\mathbf{v}(\mathbf{k}, \omega)$  quantifies amplification of white-in-time stochastic forcing  $\mathbf{w}(\mathbf{k}, t)$ , across temporal frequencies  $\omega$  and spatial wavenumbers  $\mathbf{k}$ ,

$$\Pi_{\mathbf{v}}(\mathbf{k}, \omega) = \operatorname{trace}(T_{\mathbf{vw}}(\mathbf{k}, \omega) T_{\mathbf{vw}}^*(\mathbf{k}, \omega)) = \sum_i \sigma_i^2(T_{\mathbf{vw}}(\mathbf{k}, \omega)). \quad (7.35)$$

The integration of  $\Pi_{\mathbf{v}}(\mathbf{k}, \omega)$  over temporal frequency yields the  $H_2$  norm or, equivalently, the energy spectrum as a function of wavenumbers  $\mathbf{k}$  [30]. While the PSD is given by the sum of squares of the singular values, the maximum singular value of  $T_{\mathbf{vw}}(\mathbf{k}, \omega)$  quantifies the worst-case amplification of finite energy disturbances,

$$G_{\mathbf{v}}(\mathbf{k}, \omega) := \sup_{\|\mathbf{w}\|^2 \leq 1} \frac{\|\mathbf{v}(\mathbf{k}, \omega)\|^2}{\|\mathbf{w}(\mathbf{k}, \omega)\|^2} = \sigma_{\max}^2(T_{\mathbf{vw}}(\mathbf{k}, \omega)).$$

Here,  $\|\cdot\|^2$  is the standard energy norm and the largest amplification over temporal frequencies determines the  $H_\infty$  norm [250],  $\sup_\omega \sigma_{\max}(T_{\mathbf{vw}}(\mathbf{k}, \omega))$ . For any  $\mathbf{k}$ , the  $H_\infty$  norm quantifies the worst-case amplification of purely harmonic (in  $x$ ,  $z$ , and  $t$ ) deterministic (in  $y$ ) disturbances [112].

Temporal two-point correlations of linear model (7.27) can be also computed without running stochastic simulations. For example, the autocovariance of streamwise velocity fluctuations is given by

$$\Phi_{uu}(\mathbf{k}, \tau) = \lim_{t \rightarrow \infty} \langle u(\mathbf{k}, t + \tau) u^*(\mathbf{k}, t) \rangle,$$

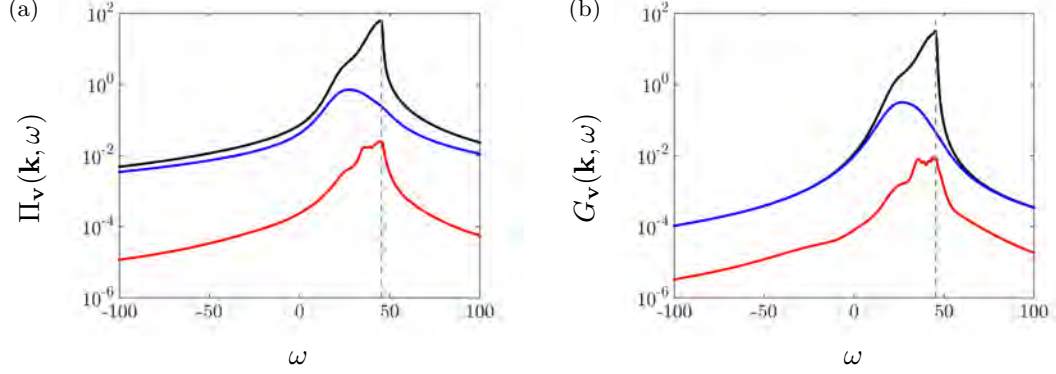


Figure 7.16: (a) Power spectral density  $\Pi_{\mathbf{v}}(\mathbf{k}, \omega)$  and (b) worst-case amplification  $G_{\mathbf{v}}(\mathbf{k}, \omega)$  as a function of temporal frequency  $\omega$  in turbulent channel flow with  $R_\tau = 186$  and  $\mathbf{k} = (2.5, 7)$ , resulting from the linearized NS model (7.6) (black curve), an eddy-viscosity-enhanced linearized NS model (blue curve), and the modified linearized dynamics (7.27) (red curve).

where  $u(\mathbf{k}, t + \tau)$  is computed from (7.27),

$$u(\mathbf{k}, t + \tau) = C_u(\mathbf{k}) e^{A_f(\mathbf{k})\tau} \psi(\mathbf{k}, t) + \int_t^{t+\tau} C_u(\mathbf{k}) e^{A_f(\mathbf{k})(t+\tau-\zeta)} B(\mathbf{k}) \mathbf{w}(\mathbf{k}, \zeta) d\zeta.$$

Since the state  $\psi(\mathbf{k}, t)$  and the white-in-time input  $\mathbf{w}(\mathbf{k}, t)$  are not correlated, we have

$$\begin{aligned} \Phi_{uu}(\mathbf{k}, \tau) &= \lim_{t \rightarrow \infty} \langle C_u(\mathbf{k}) e^{A_f(\mathbf{k})\tau} \psi(\mathbf{k}, t) \psi^*(\mathbf{k}, t) C_u^*(\mathbf{k}) \rangle \\ &= C_u(\mathbf{k}) e^{A_f(\mathbf{k})\tau} X(\mathbf{k}) C_u^*(\mathbf{k}), \end{aligned}$$

where  $X(\mathbf{k})$  is the steady-state covariance matrix of  $\psi$ . Correlations between other velocity components can be obtained in a similar way. Note that, at any  $\mathbf{k}$  and  $\tau$ , the diagonal entries of the matrix  $\Phi_{uu}(\mathbf{k}, \tau)$  provide information about two-point temporal correlations at various wall-normal locations.

### 7.5.1 Spatio-temporal frequency responses

Figure 7.16a compares the power spectral densities of three linear approximations of the NS equations in turbulent flow with  $R_\tau = 186$  and  $\mathbf{k} = (2.5, 7)$ . These are respectively given by the linearized NS equations (7.6), an eddy-viscosity-enhanced linearized NS equations, and the low-rank modification of the linearized dynamics (7.27). For

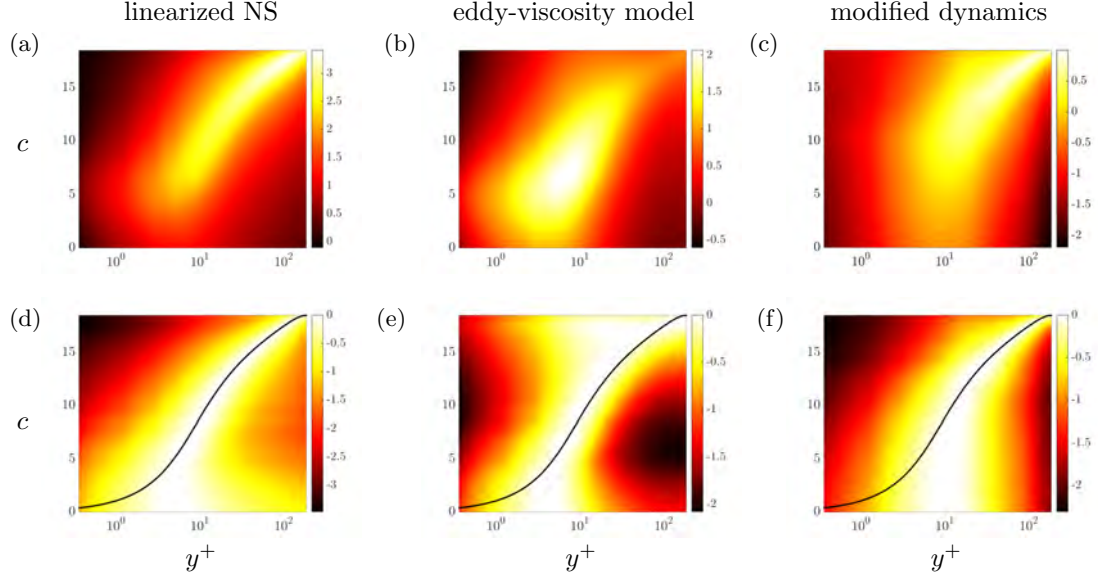


Figure 7.17: The one-dimensional energy density  $E_{\mathbf{v}\mathbf{v}}$  as a function of  $y^+$  and  $c$  computed using the linearized NS equations (7.6) (a, d), an eddy-viscosity-enhanced linearized NS model (b, e), and the modified dynamics (7.27) (c, f) for turbulent channel flow with  $R_\tau = 186$ . Plots (d-f) show the energy density normalized by its maximum value over  $y$  for fixed values of  $c$ . The colors are in logarithmic scale. The turbulent mean velocity is marked by the black curve in (d-f).

the standard and eddy-viscosity-enhanced linearizations, the input matrix  $B(\mathbf{k})$  excites all degrees of freedom in the evolution model [30]; for the modified dynamics (7.27), the input matrix  $B(\mathbf{k})$  comes from the framework of Section 7.3. While the temporal frequency at which the PSD peaks is similar for the linearized NS equations and the modified dynamics ( $\omega = 45$ ), it is smaller for the eddy-viscosity-enhanced model ( $\omega = 27$ ). Compared to the linearization around turbulent mean profile, both the eddy-viscosity-enhanced model and our model attenuate amplification of disturbances at all temporal frequencies. Thus, the low-rank modification of the linearized NS equation introduces eddy-viscosity-like features and provides additional damping across temporal frequencies.

Figure 7.16b illustrates similar trends for the worst-case amplification to harmonic forcing,  $G_{\mathbf{v}}(\mathbf{k}, \omega)$ . We recall that the PSD quantifies the total energy amplification,  $\sum_i \sigma_i^2$ , and that the worst case amplification is determined by the largest singular value of the frequency response,  $\sigma_{\max}^2$ . Clearly, in both cases, the low-rank modification reduces amplification of disturbances relative to the linearization around turbulent mean velocity but does not modify the temporal frequency at which the energy amplification peaks.

Figure 7.17 shows the one-dimensional energy density  $E_{\mathbf{v}\mathbf{v}}$  as a function of propagation speed  $c = \omega/k_x$  and  $y^+$  for turbulent channel flow with  $R_\tau = 186$ . This quantity is obtained by integrating  $\text{diag}(T_{\mathbf{v}\mathbf{w}}(\mathbf{k}, \omega) T_{\mathbf{v}\mathbf{w}}^*(\mathbf{k}, \omega))$  over  $50 \times 51$  logarithmically spaced wavenumbers with  $0 < k_x < k_{x,\max}$  and  $0 < k_z < k_{z,\max}$ , and for a range of wave speeds  $0 < c < U_c$ , where  $U_c$  is the mean centerline velocity. Here,  $k_{x,\max} = 42.5$  and  $k_{z,\max} = 84.5$  are the largest wavenumbers used in the DNS of [236] and [237]; they capture the energetically significant portion of the premultiplied turbulent energy spectrum of channel flow with  $R_\tau = 186$ . In contrast to the PSD,  $E_{\mathbf{v}\mathbf{v}}$  provides insight into the wall-normal variation of the energy amplification in stochastically forced flows. For a fixed value of  $c$ , the energy density is localized in a narrow wall-normal region; see figures 7.17(a-c). To highlight this localization, we normalize the energy density by its maximum value over  $y$  for fixed values of  $c$ . As shown in figures 7.17(d-f), the normalized energy density peaks in the vicinity of the wall-normal location where the turbulent mean velocity, marked by the thick black lines, equals the wave speed; [201] argued that the emergence of critical layers is because the resolvent norm peaks for  $c \approx U(y)$ . Our observations are in agreement with [204] where the contribution of the principal resolvent mode to the streamwise energy density was studied for the NS equations linearized around turbulent mean velocity in channel flow with  $R_\tau = 2003$ .

Figure 7.17 shows that at each wall-normal location  $y$  the modes that convect at the critical speed  $c = U(y)$  are most amplified. This observation holds in almost the entire channel and, with slight disparity, is valid for all three models. Based on Taylor’s frozen turbulence hypothesis [251], flow structures in turbulent flows propagate downstream at a speed that is close to the local mean velocity. For a large extent of the channel height our observation is in agreement with this hypothesis. However, for all three models, the scatter in the energy density increases as the wall is approached. In addition, near-wall modes peak at  $y^+ \approx 10$  and they travel at speeds that are smaller than the local mean velocity. Similar observations were made in analytical [204], experimental [252, 253] and numerical studies [254, 255], thereby suggesting that application of Taylor’s hypothesis can yield inaccurate energy spectra close to the wall.

From figure 7.17b it is evident that while eddy-viscosity enhancement reduces the scatter close to the wall, the energy density resulting from this model is less concentrated away from the wall. Even though the low-rank modification does not significantly alter the general trend in the energy density, figure 7.17f illustrates that, for  $y^+ < 15$ , the scatter in the normalized energy density increases. Namely, the highest energy amplification no longer occurs at velocities that are close to the local mean velocity near the wall.

### Principal output and forcing directions

We now utilize the singular value decomposition to analyze the principal output and forcing directions for flow with  $R_\tau = 2003$  and  $\mathbf{k} = (1, 6)$ . This wavenumber pair

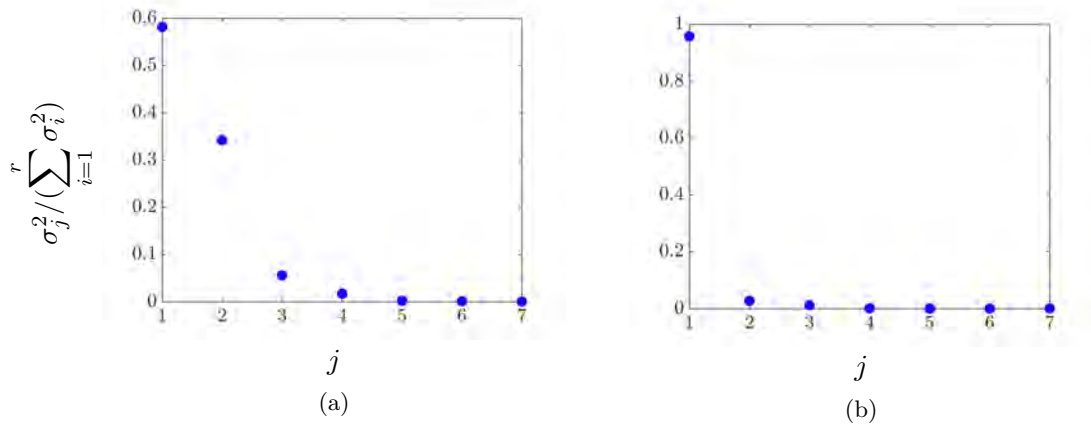


Figure 7.18: Contribution of the response directions  $\tilde{\xi}_j$  to the total energy in turbulent channel flow with  $R_\tau = 2003$  and  $\mathbf{k} = (1, 6)$ . The modified dynamics (7.27) are driven by harmonic excitation with temporal frequency (a)  $\omega = 21.4$  and (b)  $\omega = 26.5$ .

is associated with the energetic length scale of Very Large Scale Motions (VLSM) in canonical flows [246, 256, 257] and it has been previously considered in the study of coherent structures in turbulent pipes [203].

For  $N = 201$  wall-normal collocation points, the matrix  $Z(\mathbf{k})$  that results from optimization problem (7.19) with  $\gamma = 10^3$  has 7 positive and 5 negative eigenvalues. Therefore, the input matrix  $B(\mathbf{k})$ , which introduces colored-in-time forcing into the linearized NS dynamics, has 7 columns. This choice of  $\gamma$  provides a balance between the number of colored-in-time inputs and quality of completion of the two-point correlations. We examine temporal frequencies  $\omega = 21.4$  and  $26.5$  which correspond to the streamwise propagation speed  $c = \omega/k_x$  of structures that reside in the middle of the logarithmic region [258] and the peak of PSD (not shown here), respectively.

Figure 7.18 shows the contribution of each output direction  $\tilde{\xi}_j$  in (7.33) to the energy amplification,  $\sigma_j^2 / (\sum_i \sigma_i^2)$ . Since  $B(\mathbf{k})$  is a tall matrix with 7 columns, the frequency response  $T_{\mathbf{vw}}(\mathbf{k}, \omega)$  has only 7 non-zero singular values. For  $\omega = 21.4$ , the principal output direction, which corresponds to the largest singular value  $\sigma_{\max}$ , approximately contains 58% of the total energy. The second largest singular value contributes an additional 34%. Thus, the two most amplified output directions account for 92% of the total energy. For  $\omega = 26.5$ , the largest singular value contains more than 95% of the total energy. This further supports the finding that the turbulent velocity spectra and the Reynolds stress co-spectrum can be approximated with a few resolvent modes [204, 205].

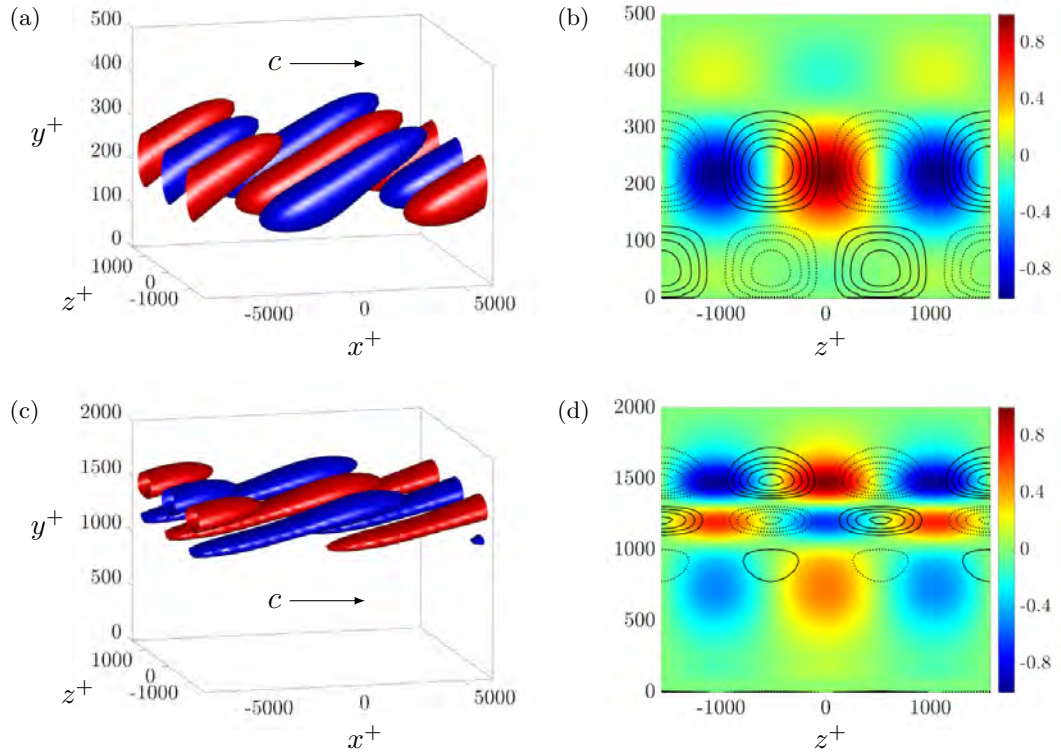


Figure 7.19: Spatial structure of the principal response directions of the frequency response  $T_{\mathbf{vw}}(\mathbf{k}, \omega)$  in turbulent channel flow with  $R_\tau = 2003$ ,  $\mathbf{k} = (1, 6)$ , at  $t = 0$  for (a,b)  $\omega = 21.4$  and (c,d)  $\omega = 26.5$ . (a,c) Isosurfaces of the streamwise velocity; red and blue colors denote regions of high and low velocity at 60% of their largest values. (b,d) Spatial structure of the streamwise velocity (color plots) and vorticity (contour lines).

Relations (7.34) can be used to visualize the spatial structure of each output direction  $\tilde{\xi}_j$ . Figures 7.19(a,b) show the spatial structure of the streamwise component of the principal output response in turbulent channel flow at  $t = 0$  and for  $\omega = 21.4$ . These streamwise elongated structures are sandwiched between counter-rotating vortical motions in the cross-stream plane (cf. figure 7.19b) and they contain alternating regions of fast- and slow-moving fluid (which are slightly inclined to the wall). We see that they reside in the logarithmic region with their largest values roughly taking place in the middle of this region. Even though these structures do not capture the full complexity of turbulent flows, they are reminiscent of VLSMs that form at large Reynolds numbers. Figures 7.19(c,d) show the spatial structure of the principal output response for the temporal frequency  $\omega = 26.5$ . Compared to  $\omega = 21.4$ , these streamwise elongated structures are longer and reside in the outer region of the channel with no protrusion to the logarithmic layer.

A similar approach can be used to study the spatial structure of colored-in-time forcing to the linearized NS equations. This is accomplished by passing the output of filter (7.23) through the input matrix  $B(\mathbf{k})$  and examining the resulting frequency response,  $B(\mathbf{k})T_f(\mathbf{k}, \omega)$ . For  $\omega = 21.4$  and  $26.5$ , the principal output directions respectively contain 62% and 88% of the total energy of the forcing to the linearized NS equations.

Figures 7.20(a,b) show the spatial structure of the principal wall-normal forcing component at  $t = 0$  and  $\omega = 21.4$ . We see that the forcing to the Orr-Sommerfeld equation affects regions of the channel that begin in the logarithmic layer and extend to the middle of the channel. The color plot in figure 7.20b shows that the largest value of the normal forcing component is in the outer layer. This suggests that the turbulent flow structures that reside in the logarithmic layer are induced by a forcing which is not limited to the logarithmic layer. Similarly, for  $\omega = 26.5$ , figures 7.20(c,d) illustrate that the most energetic component of the wall-normal forcing begins in the logarithmic layer and extends to the outer region of the channel. Compared to  $\omega = 21.4$ , these structures are shorter and do not influence the middle of the channel.

### 7.5.2 Temporal two-point correlations

Figure 7.21a shows the dependence of the main diagonal of the steady-state autocovariance of streamwise velocity  $\Phi_{uu}$  on the wall-normal coordinate  $y$  and the time lag  $\tau$  in flow with  $R_\tau = 186$  and  $\mathbf{k} = (2.5, 7)$ . Furthermore, figure 7.21b illustrates changes with  $\tau$  at  $y^+ = 15$ . We observe attenuated oscillatory  $\tau$ -dependence where the period of oscillations increases as the wall is approached. For any wall-normal location  $y$ , the fundamental frequency  $f_0$  of the corresponding diagonal entry of  $\Phi_{uu}(\mathbf{k}, \tau)$  can be used

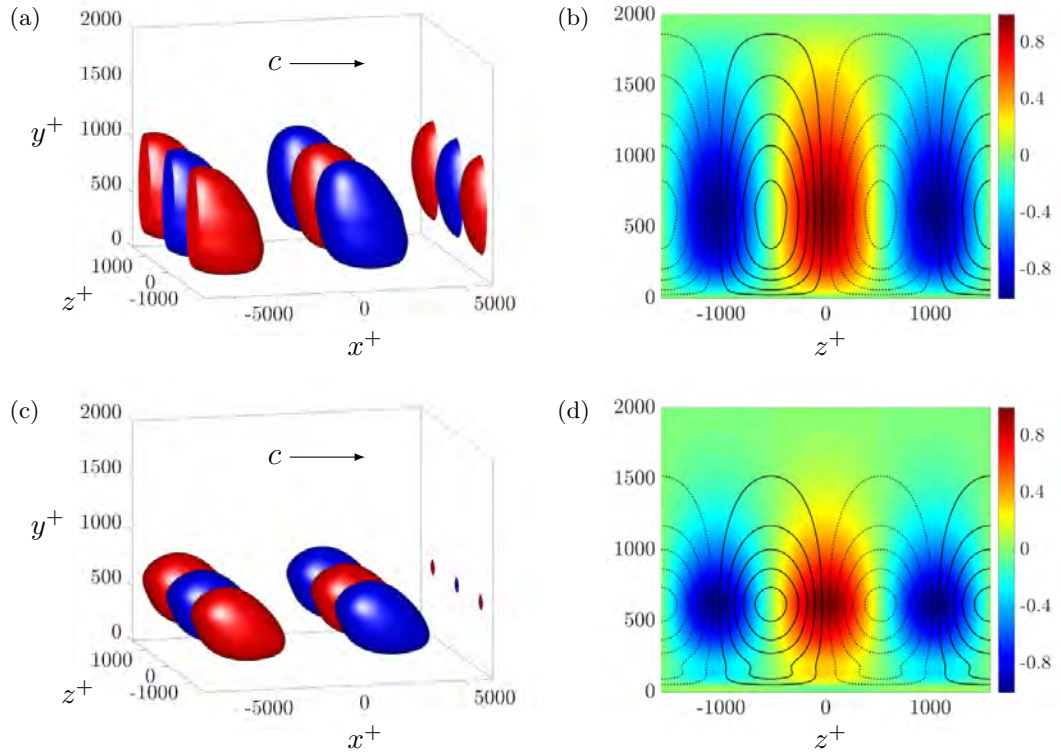


Figure 7.20: Spatial structure of the principal response of the operator  $B(\mathbf{k})T_f(\mathbf{k}, \omega)$  in turbulent channel flow with  $R_\tau = 2003$ ,  $\mathbf{k} = (1, 6)$ , at  $t = 0$  for (a,b)  $\omega = 21.4$  and (c,d)  $\omega = 26.5$ . (a,c) Isosurfaces of the streamwise velocity; red and blue colors denote regions of high and low velocity at 60% of their largest values. (b,d) Spatial structure of the streamwise component of the response (color plots) and vorticity (contour lines).

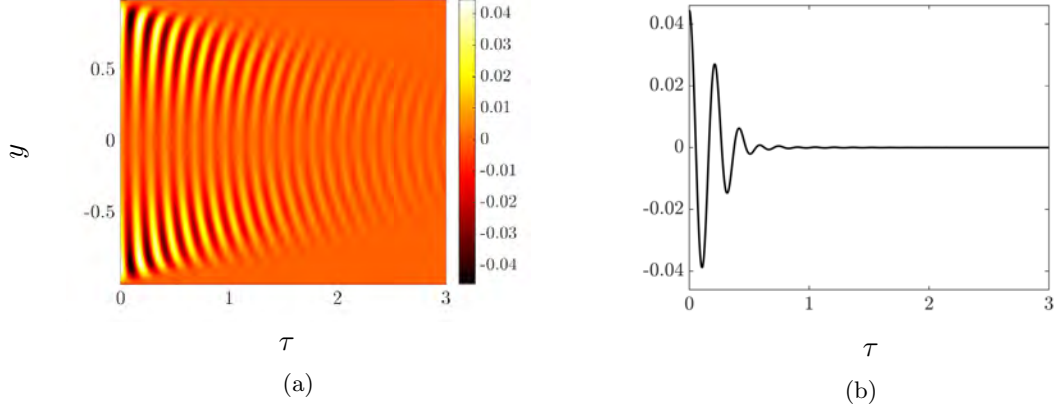


Figure 7.21: (a) The steady-state autocovariance  $\Phi_{uu}(\mathbf{k}, \tau)$  resulting from the modified dynamics (7.27) for turbulent channel flow with  $R_\tau = 186$  and  $\mathbf{k} = (2.5, 7)$ . (b) The same quantity plotted at  $y^+ = 15$ .

to estimate the streamwise convection velocity,

$$c_u(\mathbf{k}, y) = \frac{2\pi f_0}{k_x}. \quad (7.36)$$

Figure 7.22 compares this estimate of  $c_u(\mathbf{k}, y)$  to an estimate proposed by [255],

$$c_u(\mathbf{k}, y) = \int_{-1}^1 W(\eta, \mathbf{k}, y) U(\eta) d\eta, \quad (7.37)$$

where  $U$  is the mean velocity and  $W$  is a Gaussian convolution window that accounts for the wall-normal structure of eddies with wavelength  $\lambda_x = 2\pi/k_x$  and  $\lambda_z = 2\pi/k_z$ . The convolution window is tuned so that the resulting approximation agrees well with measurements of the convection velocity over a range of two-dimensional wavelengths, wall-normal distances, and Reynolds numbers [255]. The convection velocity resulting from temporal correlations of the linear dynamics (7.27) is within 12% of  $c_u(\mathbf{k}, y)$  computed from (7.37). Even though optimization problem (7.19) constrains our model to only match one-point steady-state correlations, the modified dynamics (7.27) reproduce the essential features of the convection velocity of the most energetic modes. In particular, the deviation from Taylor's frozen turbulence hypothesis as the wall is approached is captured. This is a consequence of retaining the physics of the NS equations in our modeling and optimization framework.

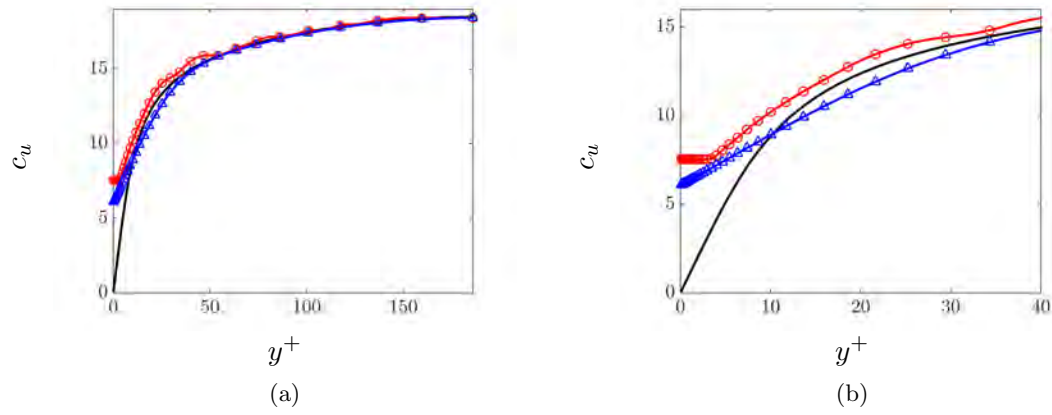


Figure 7.22: (a) Estimates of the streamwise convection velocity for  $\mathbf{k} = (2.5, 7)$  computed using (7.36) (○) and (7.37) (△) as a function of wall distance  $y^+$  for turbulent channel flow with  $R_\tau = 186$ . The mean velocity profile is plotted for comparison (—). (b) Enlargement of the same plot for  $y^+ < 40$ .

## Chapter 8

# Stochastic modeling of spatially evolving flows

Low-complexity approximations of the Navier-Stokes (NS) equations are commonly used for analysis and control of turbulent flows. In particular, stochastically forced linearized models have been successfully employed to capture structural and statistical features observed in experiments and high-fidelity simulations. In this chapter, we utilize stochastically forced linearized NS equations and the parabolized stability equations to study the dynamics of flow fluctuations in transitional boundary layers. The parabolized model can be used to efficiently propagate statistics of stochastic disturbances into statistics of velocity fluctuations. Our study provides insight into interactions of slowly-varying base flow with streamwise streaks and Tollmien-Schlichting waves. It also offers a systematic, computationally efficient framework for quantifying the influence of stochastic excitation sources (e.g., free-stream turbulence and surface roughness) on velocity fluctuations in weakly non-parallel flows.

### 8.1 Introduction

The analysis, optimization, and control of dynamical models that are based on the Navier-Stokes (NS) equations is often hindered by their complexity and large number of degrees of freedom. While the existence of coherent structures in wall-bounded shear flows [9] has inspired the development of reduced-order models using data-driven techniques, the important features of such models can be crucially altered by control actuation and sensing. This gives rise to nontrivial challenges for model-based control design [26].

In contrast, linearization of the NS equations around mean-velocity is well-suited for

analysis and synthesis using tools of modern robust control. Linearized models subject to stochastic excitation, have been employed to replicate structural and statistical features of transitional [28–30] and turbulent [32–34] wall-bounded shear flows. However, most studies have focused on parallel flow configurations in which translational invariance allows for the decoupling of the dynamical equations across streamwise and spanwise wavenumbers. This offers significant computational advantages for analysis, optimization, and control.

In the flat-plate boundary layer, streamwise and normal inhomogeneity leads to a temporal eigenvalue problem for PDEs with two spatial variables. This problem is computationally more difficult to solve than the corresponding problem for parallel flows. Previously, tools from sparse linear algebra and iterative schemes have been employed to analyze the spectra of the governing equations and provide insight into the dynamics of transitional flows [259–261]. Efforts have also been made to conduct non-modal analysis of spatially evolving flows including transient growth [260, 262] and resolvent analysis [42]. In spite of these successes, many challenges remain.

The Parabolized Stability Equations (PSE) result from the removal of elliptic components from the NS equations. The PSE respect inhomogeneity in the streamwise direction but do not propagate information upstream, which makes them computationally more efficient than conventional flow simulations based on the NS equations [263]. In particular, the resulting set of equations are convenient for marching in the downstream direction [264–266]. They are thus routinely used to compute the spatial evolution of instability modes in a wide range of engineering problems.

Despite their popularity, parabolized equations have been utilized in a rather narrow context. We revisit the modeling of spatially evolving boundary layer flow by examining the utility of such models in assessing the receptivity to different types of flow disturbances. This lays the groundwork for a systematic, computationally efficient framework for quantifying the influence of stochastic excitation sources on velocity fluctuations in weakly non-parallel flows.

The rest of this chapter is organized as follows. In Section 8.2, we describe stochastically forced linearization of the NS equations around Blasius boundary layer flow and characterize the structural constraints that the linearized equations impose on second-order statistics. In Section 8.3, we study the receptivity of the boundary layer to stochastic excitation using a parallel base flow assumption. We also perform a global stability analysis on the discretized model in two spatial directions. In Section 8.4, we adopt stochastic forcing to model the effect of excitations in the PSE.

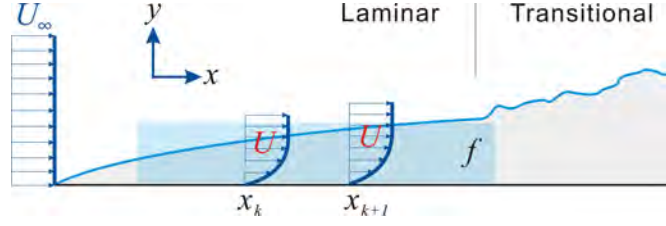


Figure 8.1: Geometry of a transitional boundary layer flow subject to stochastic forcing.

## 8.2 Background

In this section, we present the equations that govern the dynamics of flow fluctuations in incompressible flows of Newtonian fluids and characterize the structural constraints that are imposed on the second-order statistics by the linearized dynamics.

### 8.2.1 Stochastically forced linearized NS equations

In a flat-plate boundary layer, with geometry shown in figure 8.1, the dynamics linearized around the Blasius boundary layer profile  $\bar{\mathbf{u}} = [U(x, y) \ V(x, y) \ 0]^T$  are

$$\begin{aligned} \mathbf{v}_t &= -(\nabla \cdot \bar{\mathbf{u}}) \mathbf{v} - (\nabla \cdot \mathbf{v}) \bar{\mathbf{u}} - \nabla p + \frac{1}{Re_0} \Delta \mathbf{v} + \mathbf{f}, \\ 0 &= \nabla \cdot \mathbf{v}, \end{aligned} \quad (8.1)$$

where  $\mathbf{v} = [v_1 \ v_2 \ v_3]^T$  is the vector of velocity fluctuations,  $p$  denotes pressure fluctuations, and  $v_1$ ,  $v_2$  and  $v_3$  represent components of the fluctuating field in the streamwise ( $x$ ), wall-normal ( $y$ ) and spanwise ( $z$ ) directions, respectively. The Reynolds number is defined as  $Re_0 = U_\infty \delta_0 / \nu$ , where  $\delta_0$  is the initial Blasius length scale  $\delta_0 = \sqrt{\nu x_0 / U_\infty}$ ,  $U_\infty$  is the free-stream velocity, and  $\nu$  is the kinematic viscosity. Spatial coordinates are non-dimensionalized by  $\delta_0$ , velocities by  $U_\infty$ , time by  $\delta_0 / U_\infty$ , and pressure by  $\rho U_\infty^2$ , where  $\rho$  is the fluid density. The presence of the additive zero-mean stochastic body forcing  $\mathbf{f}$  can be justified in different ways and there is a rich literature on the subject [28–30]. For our purposes, we wish to compensate for the role of the neglected nonlinear interactions by introducing stochastic sources of excitation that perturb the otherwise linearly developing velocity field.

After proper spatial discretization, the dynamics of velocity and pressure fluctuations are governed by the following evolution form

$$\begin{aligned} \dot{\boldsymbol{\psi}}(t) &= A \boldsymbol{\psi}(t) + B \mathbf{f}(t), \\ \mathbf{v}(t) &= C \boldsymbol{\psi}(t), \end{aligned} \quad (8.2)$$

where  $\psi(t)$  is the state and  $\mathbf{f}(t)$  is the stochastic forcing. The matrix  $A$  is the generator of the dynamics, the matrix  $C$  establishes a kinematic relationship between the components of  $\psi$  and the components of  $\mathbf{v}$ , and the matrix  $B$  specifies the way the external excitation  $\mathbf{f}$  affects the dynamics [30].

### 8.2.2 Second-order statistics and computation of energy amplification

In statistical steady-state, the covariance matrix  $\Phi = \lim_{t \rightarrow \infty} \mathbf{E}(\mathbf{v}(t) \mathbf{v}^*(t))$ , of the velocity fluctuation vector, and the covariance matrix  $X = \lim_{t \rightarrow \infty} \mathbf{E}(\psi(t) \psi^*(t))$ , of the state in (8.2), are related as follows:

$$\Phi = C X C^*,$$

where  $*$  denotes complex-conjugate-transpose and  $\mathbf{E}$  is the expectation operator. The matrix  $\Phi$  contains information about all second-order statistics of the fluctuating velocity field.

For a stable dynamical generator  $A$ , the steady-state covariance of the state in (8.2) subject to zero-mean and white-in-time stochastic forcing with covariance  $\Omega = \Omega^* \succeq 0$ , i.e.,

$$\langle \mathbf{f}(t_1) \mathbf{f}^*(t_2) \rangle = \Omega \delta(t_1 - t_2),$$

is determined as the solution to the standard Lyapunov equation,

$$A X + X A^* = -B \Omega B^*. \quad (8.3)$$

The Lyapunov equation relates covariance  $\Omega$  of white-in-time forcing to the state covariance  $X$  via system matrices  $A$  and  $B$ . The energy spectrum of velocity fluctuations that obey (8.2) can be computed from the  $H_2$  norm as

$$E = \text{trace}(C X C^*).$$

## 8.3 Local and global analysis of stochastically forced linearized NS equations

In this section, we first examine the dynamics of flow fluctuations in the stochastically forced Blasius boundary layer under a locally parallel base flow assumption. This assumption entails linearization around the Blasius profile evaluated at a fixed streamwise location  $x_0$ . Since the resulting base flow only depends on the wall-normal coordinate  $y$ , this also allows for the parameterization of the corresponding evolution model over

horizontal wavenumbers and reduces the computational complexity of studying the amplification of streamwise streaks and Tollmien-Schlichting (TS) waves. We then repeat the same exercise for the NS equations linearized around a base flow which is a function of both streamwise and wall-normal coordinates. In fluids literature this approach is called *global analysis* and it is typically a computationally challenging problem. For the initial study presented here, we use a coarse grid to discretize the differential operators in the streamwise and wall-normal coordinates and provide insight into the results that can come out of global analysis.

### 8.3.1 Parallel Blasius boundary layer flow subject to free-stream turbulence

We perform an input-output analysis to quantify the energy amplification of velocity fluctuations subject to free-stream turbulence. This excitation is modeled as white-in-time stochastic forcing into the linearized NS equations around the parallel Blasius base flow profile, i.e., the Blasius profile evaluated at one streamwise location  $x_0$  with no dependence on the streamwise coordinate. This choice is motivated by previous studies which show that transient growth exhibits similar trends for parallel and non-parallel boundary layer flows [267, 268].

Under the assumption of a parallel base flow, translational invariance allows us to apply Fourier transform in the plate-parallel directions, which brings the state-space representation of the linearized NS around the nominal base profile to the form

$$\begin{aligned}\dot{\boldsymbol{\psi}}(\mathbf{k}, t) &= A(\mathbf{k}) \boldsymbol{\psi}(\mathbf{k}, t) + B(\mathbf{k}) \mathbf{f}(\mathbf{k}, t), \\ \mathbf{v}(\mathbf{k}, t) &= C(\mathbf{k}) \boldsymbol{\psi}(\mathbf{k}, t).\end{aligned}\tag{8.4}$$

Here,  $\boldsymbol{\psi} = [v_2^T \ \eta^T]^T \in \mathbb{C}^{2N}$  is the state, which contains the wall-normal velocity  $v_2$  and vorticity  $\eta = \partial_z v_1 - \partial_x v_3$ , and  $\mathbf{v} \in \mathbb{C}^{3N}$  with  $N$  being the number of collocation points in the finite dimensional approximation of the differential operators. Equations (8.4) are parameterized by the spatial wavenumber pair  $\mathbf{k} = (k_x, k_z)$ ; see [30] for the expressions of  $A$ ,  $B$ , and  $C$ . We consider no-slip and no-penetration boundary conditions. The receptivity to external forcing that enters at various wall-normal locations can be evaluated by computing the energy spectrum of the velocity fluctuations. To specify the wall-normal region in which the forcing enters, we define  $\mathbf{f} := f(y)\mathbf{f}_s$  where  $\mathbf{f}_s$  represents the forcing from free-stream turbulence and  $f(y)$  is the smooth function defined as

$$f(y) := \frac{1}{\pi} (\text{atan}(y - y_1) - \text{atan}(y - y_2)), \tag{8.5}$$

where  $y_1$  and  $y_2$  determine the shape of  $f(y)$ . The energy amplification of the stochastically forced flow can be computed using the solution to the Lyapunov equation (8.3)

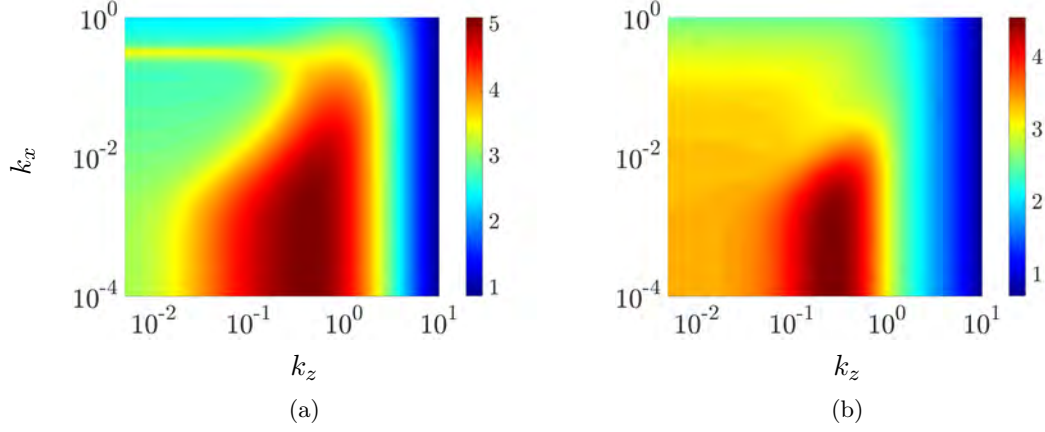


Figure 8.2: Plots of  $\log_{10}(E(\mathbf{k}))$  in the Blasius boundary layer flow with  $Re_0 = 400$  subject to white-in-time stochastic excitation in different wall-normal regions; (a)  $y_1 = 0, y_2 = 5$  (b)  $y_1 = 5, y_2 = 10$  in equation (8.5).

with  $\Omega$  being the covariance of the filtered stochastic forcing  $\mathbf{f}$ .

We present results obtained by computing the energy spectrum of stochastically excited parallel Blasius boundary layer flow with  $Re_0 = 400$ . This implies that the Blasius profile is computed at  $x_0 = 400$ . Here, we consider a wall-normal region of  $L_y = 25$ . A solenoidal white-in-time excitation is first introduced to the region in the immediate vicinity of the wall by choosing  $y_1 = 0$  and  $y_2 = 5$  in equation (8.5). Figure 8.2a shows that the energy of velocity fluctuations is most amplified at low streamwise wavenumbers ( $k_x \approx 0$ ) with a global peak at  $k_z \approx 0.42$ . Clearly, the energy spectrum is dominated by streamwise elongated flow structures, with a trace of TS waves observed at  $k_x \approx 0.35$ . As the forcing region moves away from the wall the amplification of streamwise elongated structures persists while the amplification of the TS waves weakens; see figure 8.2b. It is also observed that as the region of excitation moves away from the wall, energy amplification becomes weaker and the peak of the energy spectrum shifts to lower values of  $k_z$ . These observations are in agreement with the global analysis of boundary layer flow presented next.

### 8.3.2 Global analysis of stochastically forced linearized NS equations

We consider the linearized NS equations around a spatially evolving Blasius boundary layer profile and introduce forcing at various wall-normal locations. To capture the spatially evolving nature of the boundary layer, we employ finite dimensional spatial discretization using a pseudospectral scheme [240] in both streamwise and wall-normal

directions. The linearized NS generator is globally stable for the particular Reynolds number and spanwise wavenumbers we consider in this study. Thus, the steady-state covariance of the perturbation field of the stochastically forced system (8.2) can be obtained from the solution to the Lyapunov equation (8.3).

The computational region is a rectangular box with  $L_x \times L_y = 900 \times 25$  and the initial Reynolds number is set to  $Re_0 = 400$ . We consider the linearized dynamics (8.2), homogenous Dirichlet boundary conditions on  $\eta$  and Dirichlet/Neumann boundary conditions on  $v_2$ , and we also introduce sponge layers in the streamwise direction [269, 270]. Similar to Section 8.3.1, we assume that white-in-time stochastic forcing is filtered by the function  $f(y)$  in (8.5).

Our computational experiments show that the energy amplification increases as the region of influence for the external forcing approaches the wall; the principal eigenvalues of the steady-state covariance matrices  $X$  for perturbations that enter in the vicinity of the wall ( $y_1 = 0$  and  $y_2 = 5$  in equation (8.5)) and away from the wall ( $y_1 = 5$  and  $y_2 = 10$ ) are  $3.1 \times 10^5$  and  $4.9 \times 10^4$ , respectively. This suggests that perturbations entering in the vicinity of the wall are the most amplified. Figures 8.3a and 8.3b show the spatial structure of the streamwise component of the principal response when white-in-time stochastic forcing enters in the vicinity of the wall and away from the wall, respectively. The streamwise growth of the streak structure can be observed in these figure. Figures 8.3c and 8.3d display the cross-section of these streamwise elongated structures at  $z = 0$ . As figures 8.3e and 8.3f demonstrate, these streaky structures are sandwiched between counter-rotating vortical motions in the cross-stream plane; and they contain alternating regions of fast- and slow-moving fluid that are slightly inclined to the wall.

## 8.4 Stochastically forced linear parabolized stability equations

While it is customary to use the parallel-flow approximation to study the stability of boundary layer flows to small amplitude perturbations, this approximation does not accurately capture the effect of the spatially evolving base flow on the stability of the boundary layer. This issue can be addressed by examining the spatial growth of specific wave structures. Furthermore, in the absence of body forcing and neutrally stable modes, linearized models that do not account for the spatial evolution of the base flow, predict either asymptotic decay or unbounded growth of fluctuations. On the other hand, the global analysis and direct numerical simulation of spatially evolving flows may be prohibitively expensive for analysis and control purposes.

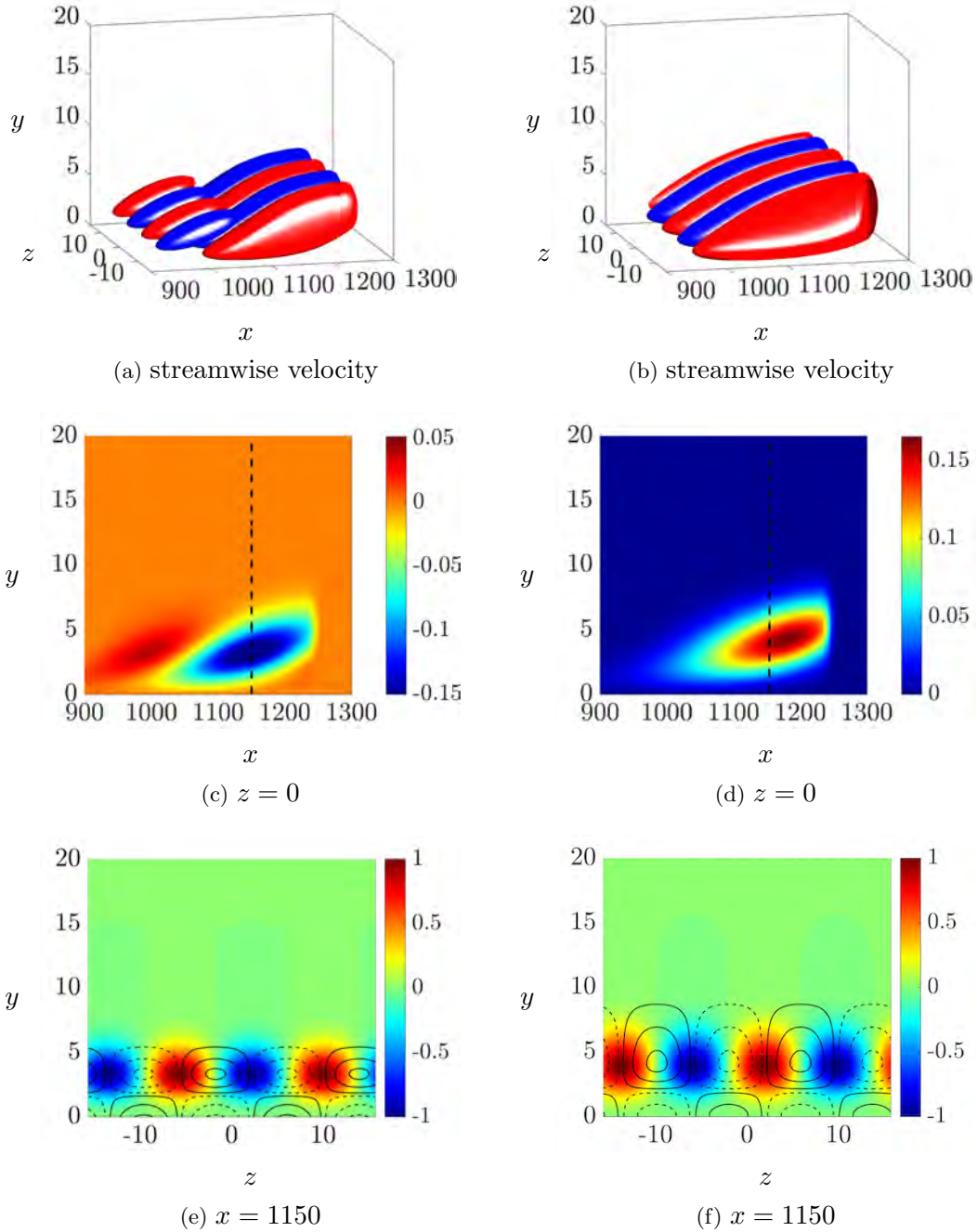


Figure 8.3: Principal modes with  $k_z = 0.4$ , resulting from excitation in the vicinity (a,c,e) ( $y_1 = 0$  and  $y_2 = 5$  in (8.5)) and away from the wall (b,d,f) ( $y_1 = 5$  and  $y_2 = 10$  in (8.5)). (a,b) Streamwise velocity components; (c,d) streamwise velocity at  $z = 0$ ; (e,f)  $y$ - $z$  slice of streamwise velocity (color plots) and vorticity (contour lines) at  $x = 1150$ .

To refine predictions of parallel flow analysis, we utilize the Parabolized Stability Equations (PSE) to study the dynamics of flow fluctuations in flat-plate boundary layers. These equations are obtained by removing elliptic components from the NS equations and they can be easily advanced downstream via marching procedure. This approach is significantly more efficient than conventional flow simulations based on the NS equations. In contrast to standard PSE-based analysis, we introduce a stochastic forcing term and show that linear PSE can be used to march covariance matrices downstream in a computationally efficient manner.

We next provide a brief overview of the stochastically forced linear PSE. Additional details regarding the PSE can be found in [264, 265].

#### 8.4.1 Linear parabolized stability equations

In weakly non-parallel flows, e.g. the pre-transitional boundary layer, flow fluctuations can be separated into slowly and rapidly varying components [264]. This is achieved by considering the following decomposition for the fluctuation field  $\hat{\mathbf{q}} = [v_1 \ v_2 \ v_3 \ p]^T$  in (8.1),

$$\begin{aligned}\hat{\mathbf{q}}(x, y, z, t) &= \mathbf{q}(x, y) \chi(x, z, t), \\ \chi(x, z, t) &= \exp(i(\theta(x) + k_z z - \omega t)), \\ \theta(x) &= \int_{x_0}^x \alpha(\xi) d\xi,\end{aligned}$$

where  $\mathbf{q}(x, y)$  and  $\chi(x, z, t)$  are the shape and phase functions,  $k_z$  and  $\omega$  are the spanwise wavenumber and temporal frequency, and  $\alpha(x)$  is the streamwise varying generalization of the wavenumber [264]. The ambiguity arising from the streamwise variation of both  $\mathbf{q}$  and  $\alpha$  is resolved by imposing the condition  $\int_{\Omega_y} \mathbf{q}^* \mathbf{q}_x dy = 0$  [264]. The PSE approximation assumes that the streamwise variation of  $\mathbf{q}$  and  $\alpha$  are sufficiently small to neglect  $\mathbf{q}_{xx}$ ,  $\alpha_{xx}$ ,  $\alpha_x \mathbf{q}_x$ , and their higher order derivatives with respect to  $x$ . The stochastically forced linear PSE thus take the form

$$L \mathbf{q} + M \mathbf{q}_x + \alpha_x N \mathbf{q} = \mathbf{f}, \quad (8.6)$$

with

$$L = \begin{bmatrix} C + U_x + V \partial_y & U' & 0 & i\alpha \\ 0 & C + V' + V \partial_y & 0 & \partial_y \\ 0 & 0 & C + V \partial_y & i k_z \\ i\alpha & \partial_y & i k_z & 0 \end{bmatrix},$$

$$C = -\frac{1}{Re_0}(\partial_{yy} - \alpha^2 - k_z^2) + i(\alpha U - \omega),$$

and

$$M = \begin{bmatrix} U - \frac{2i\alpha}{Re_0} & 0 & 0 & 1 \\ 0 & U - \frac{2i\alpha}{Re_0} & 0 & 0 \\ 0 & 0 & U - \frac{2i\alpha}{Re_0} & 0 \\ 1 & 0 & 0 & 0 \end{bmatrix}, \quad N = \begin{bmatrix} -\frac{i}{Re_0} & 0 & 0 & 0 \\ 0 & -\frac{i}{Re_0} & 0 & 0 \\ 0 & 0 & -\frac{i}{Re_0} & 0 \\ 0 & 0 & 0 & 0 \end{bmatrix}.$$

Matrices  $L$ ,  $M$  and  $N$  result from applying PSE assumptions to the operators in the linearized NS equations (8.2); see [239, 265] for additional details.

In what follows, we use the PSE to propagate the spatially evolving state covariance,

$$X(x) = \mathbf{E}(\mathbf{q}(x) \mathbf{q}^*(x)),$$

via the Lyapunov equation

$$X_{k+1} = \bar{A}_{k+1} X_k \bar{A}_{k+1}^* + \bar{B} \Omega_{k+1} \bar{B}^*, \quad (8.7)$$

where  $\mathbf{E}$  is the expectation operator,  $k$  identifies the streamwise location, and  $\Omega_k$  represents the covariance of the white stochastic disturbance  $\mathbf{f}$ . The dynamical matrix  $\bar{A}$  and the input matrix  $\bar{B}$  result from a rearrangement of the stochastically forced linear PSE (8.6) with a constant streamwise wavenumber  $\alpha$ ,

$$\mathbf{q}_x = \underbrace{(-M^{-1}L)}_{\bar{A}} \mathbf{q} + \underbrace{(-M^{-1})}_{\bar{B}} \mathbf{f}.$$

These equations provide a good approximation of perturbations with slowly-varying streamwise wavenumbers [271]. The streamwise dependence of our equations follows from the dependence of the state  $\mathbf{q}$ , and matrices  $L$  and  $M$  on the streamwise location  $x_k$ . Propagation of the state covariance  $X_k$  using equation (8.7) offers significant computational advantage over computation of the covariance from the ensemble average of many stochastic simulations.

We next consider the streamwise evolution of a two-dimensional TS wave and provide a comparison of the results obtained using linear PSE with and without stochastic forcing and nonlinear PSE.

#### 8.4.2 Streamwise evolution of a two-dimensional TS wave

We study the streamwise evolution of a two-dimensional TS wave ( $k_z = 0$ ) with an initial amplitude of  $2.5 \times 10^{-3}$  and temporal frequency  $\omega = 0.0344$ . All computations

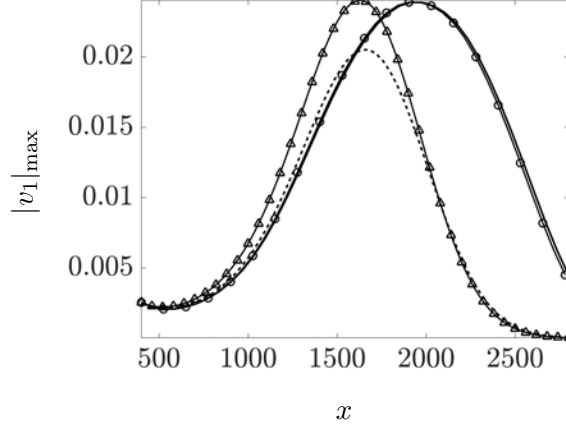


Figure 8.4: Amplitude of TS waves at  $\omega = 0.0344$  in a flat-plate boundary layer flow; nonlinear PSE (solid), linear PSE without forcing (dashed), linear PSE with white forcing ( $\triangle$ ), and linear PSE with white, but  $x$ -dependent forcing designed using the procedure explained in Section 8.4.2 ( $\circ$ ).

are initialized at  $x_0 = 400$  with the streamwise wavenumber  $\alpha$  and shape function corresponding to the TS-mode which is identified by the eigenvalue with the largest imaginary part in the spatial eigenvalue problem. This problem studies the stability of the linearized NS equations around the base flow profile at  $x_0$ , for a particular Reynolds number, spanwise wavenumber, and temporal frequency. The initial Reynolds number is 400 and the computational domain is  $L_x \times L_y = 2400 \times 60$  with homogenous Dirichlet boundary conditions applied in the wall-normal direction. We have conducted 400 simulations of stochastically forced linear PSE (8.6), with different realizations of white stochastic forcing. As in Section 8.3.1, we filter the forcing using the function  $f(y)$  in (8.5) with  $y_1 = 0$  and  $y_2 = 10$ . The resulting velocity profiles and covariances are compared with the results of linear PSE with no stochastic forcing and nonlinear PSE under the same parameter space and initial conditions.

Figure 8.4 shows the peak amplitude of the streamwise velocity component of the TS wave. Relative to nonlinear PSE, linear PSE with and without a white stochastic forcing with covariance that is a scalar multiple of the identity underestimates the streamwise location of the peak. Figure 8.5 shows the covariance matrices of the streamwise and streamwise/wall-normal velocity components at the outflow ( $x = 2800$ ). These are obtained using simulations of nonlinear PSE and propagation of equation (8.7). We see that the outflow velocity covariances resulting from linear PSE with white forcing capture the essential trends observed in nonlinear PSE.

Our computations show that it is not feasible to exactly match velocity correlations

and growth trends with white stochastic excitation of the linear PSE with a covariance that is a scalar multiple of identity. This necessitates the use of  $x$ -dependent and/or colored stochastic forcing. As an example, we consider a forcing field which is streamwise dependent but uncorrelated in the wall-normal direction. This allows us to better predict the location of the peak amplitude in figure 8.4.

In order to obtain this stochastic forcing, we first use  $X_k$  and  $X_{k+1}$  resulting from nonlinear PSE to compute the covariance  $Z_k := \bar{B} \Omega_k \bar{B}^*$ . This covariance corresponds to a spatially correlated process in the streamwise direction and is thus  $x$ -dependent and not necessarily positive semi-definite. We then project these forcing correlations onto the positive-definite cone to achieve uncorrelated noise. The result of incorporating this white, but  $x$ -dependent, stochastic forcing is also shown in figure 8.4. Clearly, the peak amplitude resulting from this model matches the curve from nonlinear PSE simulations.

To further evaluate the performance of this model, we examine the error in matching the full state covariance matrix  $X$  and the amplitude of the streamwise velocity profile  $|v_1|$  as a function of the streamwise location  $x$ ; see figure 8.6. Although we are able to reliably approximate the location of the peak, exact amplitudes and velocity covariances cannot be achieved. Figures 8.7a and 8.7b show the amplitude of the streamwise velocity  $|v_1|$  at the location with highest error ( $x = 1840$ ) and the outflow ( $x = 2800$ ), respectively. While the profiles perfectly match for  $y < 30$ , the profiles resulting from linear PSE with  $x$ -dependent forcing experience significant deviations in the outer flow region.

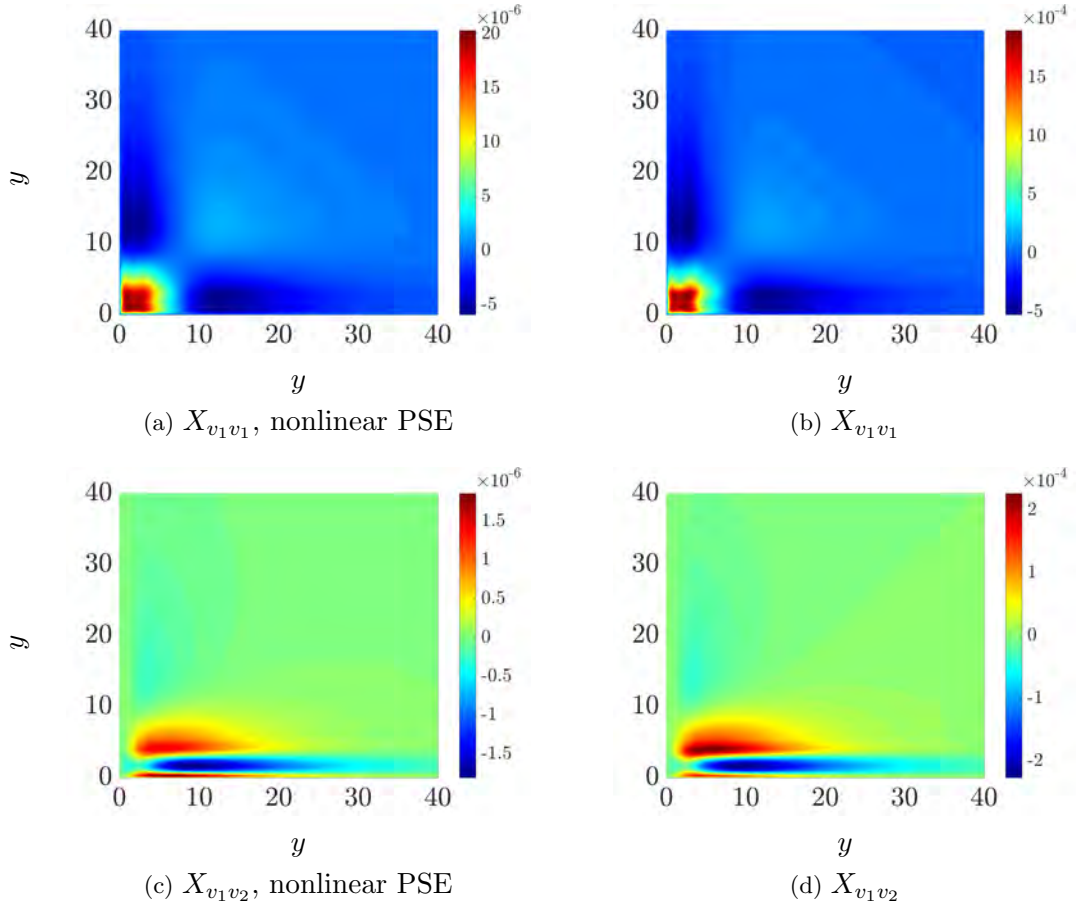


Figure 8.5: Velocity covariance matrices at  $x = 2800$  resulting from (a,c) simulation of nonlinear PSE, and (b,d) from propagation of equation (8.7) in Blasius boundary layer flow with TS mode initialization. (a,b) The streamwise correlation matrix  $X_{v_1 v_1}$ , and (c,d) the streamwise/wall-normal cross correlation matrix  $X_{v_1 v_2}$ .

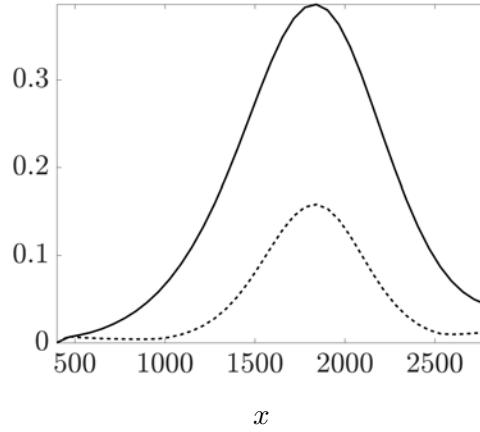


Figure 8.6: Relative error in matching the amplitude of streamwise velocity (solid) and in matching the state covariance  $X(x)$  (dashed) using the linear PSE with  $x$ -dependent white stochastic forcing in the spatial evolution of a 2D TS wave with  $\omega = 0.0344$ .

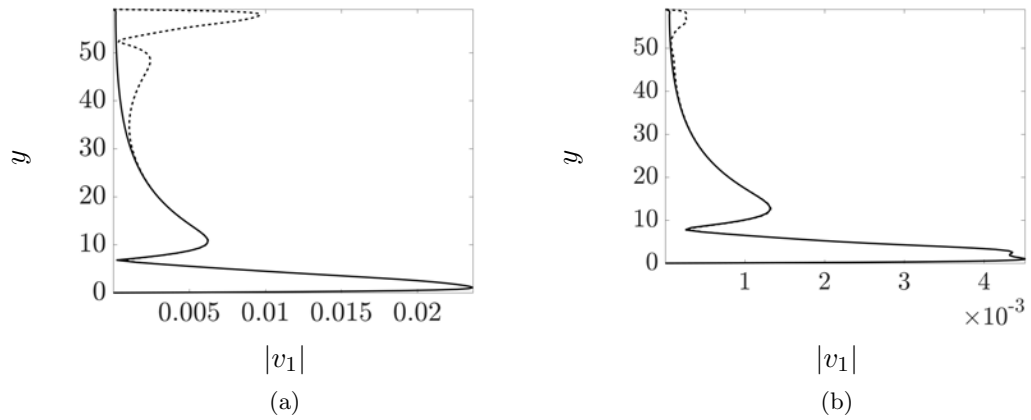


Figure 8.7: The amplitude of the streamwise component of a 2D TS waves with  $\omega = 0.0344$  at (a)  $x = 1840$  and (b)  $x = 2800$ , which results from nonlinear PSE (solid) and linear PSE with  $x$ -dependent stochastic forcing (dashed).

## Chapter 9

# Conclusions and future directions

### Conclusions

We are interested in accounting for statistical signatures of turbulent flows using low-complexity linear stochastic models. The complexity is quantified by the number of degrees of freedom in the NS equations that are directly influenced by stochastic forcing. Models for colored-in-time forcing are obtained using a maximum entropy formulation together with a regularization that serves as a penalty for model complexity. We show that colored-in-time excitation of the NS equations can also be interpreted as a low-rank modification to the generator of the linearized dynamics. Schematically, the correspondence between the nonlinear and stochastically-driven linearized NS equations is shown in figure 9.1. The modified dynamics are designed to be equivalent, at the level of second-order statistics, to DNS of turbulent channel flow.

Our motivation has been to develop a framework to complete unavailable statistics in a way that is consistent with the linearized dynamics around turbulent mean velocity. The resulting dynamical model can be used for time-dependent linear stochastic simulations and analyzed using tools from linear systems theory. We have verified the ability to match statistics of turbulent channel flow using such simulations. We have also analyzed the spatio-temporal responses to stochastic and deterministic excitation sources. In particular, by examining the power spectral density of velocity fluctuations, we have shown that the dynamical modification attenuates the amplification over all temporal frequencies. A similar effect has been observed in eddy-viscosity-enhanced linearization of the NS equations. Although our models are based on one-point correlations in statistical steady-state, we have computed two-point temporal correlations to demonstrate that the essential features of the convection velocities of individual modes are reproduced.

Full scale physics-based models are often prohibitively complex. An advantage of our

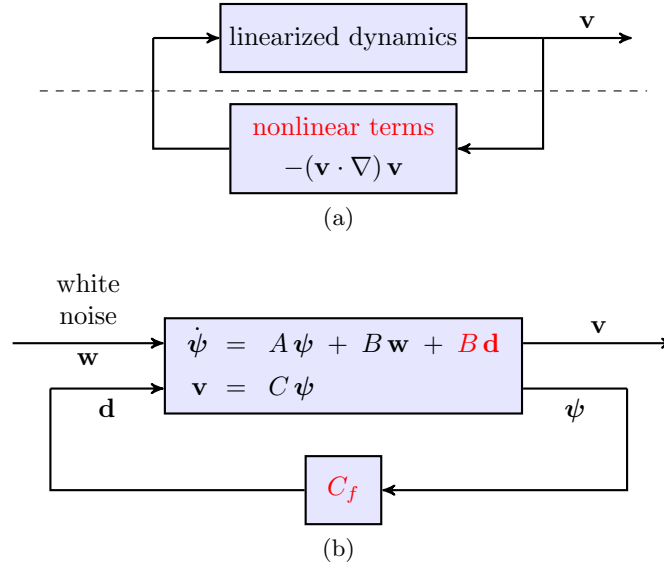


Figure 9.1: (a) Nonlinear NS equations as a feedback interconnection of the linearized dynamics with the nonlinear term; (b) Stochastically-driven linearized NS equations with low-rank state-feedback modification. The two representations can be made equivalent, at the level of second-order statistics, by proper selection of  $B$  and  $C_f$ .

method is that it provides a data-driven refinement of models that originate from first principles. The method captures complex dynamics in a way that is tractable for analysis, optimization and control design. We have focused on a canonical flow configuration to demonstrate the ability to generate statistically consistent velocity fluctuations. The framework opens up the possibility to guide experimental data collection in an economic manner that, at the same time, allows faithful representation of structural and statistical flow features.

In Chapter 8, we have utilized stochastically forced linearized NS equations and stochastically forced linear PSE to study the dynamics of flow fluctuations in the Blasius boundary layer. In particular, we have examined the receptivity of the spatially-evolving Blasius boundary layer flow to free-stream disturbances which we model as stochastic excitations that enter at specific wall-normal locations. We also incorporate stochastic forcing into the linear PSE to study the streamwise evolution of TS waves. While white stochastic excitation with a covariance that is a scalar multiple of the identity matrix is not able to improve predictions relative to the conventional linear PSE, we achieve

better predictions of transient peaks using an  $x$ -dependent white stochastic forcing.

## Extensions and future directions

**Higher-order statistics and sub-scale modeling.** The colored-in-time stochastic noise modeling framework presented in this thesis allows for the matching of second-order statistics of the fluctuating velocity field using the linearized NS model. However, the extension of this framework for explaining higher-order statistics that are of relevance in a broader context, e.g., acoustic source modeling [272, 273], is still an open problem.

Apart from accounting for partially-observed flow statistics, which are typically constrained to a narrow region of the spectrum, the predictive capability of such stochastic models should also be examined. In particular, it would be of interest to explore the utility of this modeling framework in developing new classes of subgrid-scale models.

**The role of the colored-in-time forcing.** As noted in Chapter 7, the colored-in-time forcing introduces a low-rank modification to the dynamics of the linearized NS equations around turbulent mean velocity. This should be compared and contrasted to alternative modifications proposed in the literature. For instance, one such modification is obtained by augmenting molecular viscosity with turbulent eddy viscosity [31, 32, 197–200]. Another modification adds a source of constant [212, 215, 216, 221] or dynamical [208, 209] dissipation. The colored-in-time forcing similarly alters the dynamics but rather than postulating relations between Reynolds stresses and mean velocity gradients, it generates perturbations in a *data-driven* manner.

More specifically, in the linearized NS model, the generator  $A(\mathbf{k})$  is lower block triangular. This means that wall-normal vorticity does not influence the dynamics of wall-normal velocity [239]. In the context of channel flow, standard eddy-viscosity and dissipation models do not alter this structural feature. In contrast, the low-rank term  $B(\mathbf{k})C_f(\mathbf{k})$  not only modifies the structure of the Orr-Sommerfeld, Squire, and coupling operators but it also introduces an additional feedback term  $\tilde{A}_{12}$  as illustrated in figure 9.2. Thereby, besides an interpretation of colored-in-time forcing as a data-driven generalized eddy-viscosity refinement, the new framework points to potentially missing dynamical interactions in the linearized model. The nature and physical basis for such interactions calls for additional in-depth examination.

**Closure of the mean flow equations.** It is well known that the nonlinear nature of the NS equations makes the  $n$ th velocity moment depend on the  $(n + 1)$ th. Colored-in-time forcing provides an alternative mechanism for developing a new class of *data-driven* turbulence closure models. More specifically, as shown in figure 9.3, the turbulent mean velocity enters as a coefficient into the linearized flow equations. In turn these equations are used to compute second-order statistics which feed back into the mean

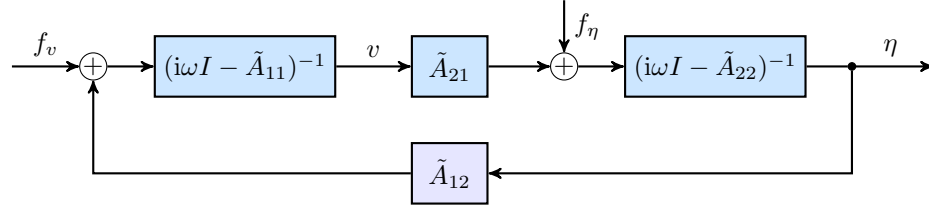


Figure 9.2: Partitioning the state in (7.27) as  $\psi = (v, \eta)$ , and conformably the forcing  $B\mathbf{w}$  as  $(f_v, f_\eta)$ , the term  $BC_f$  in (7.27) modifies the Orr-Sommerfeld, Squire, and coupling operators into  $\tilde{A}_{11}$ ,  $\tilde{A}_{22}$ , and  $\tilde{A}_{21}$ , respectively. It also introduces an additional feedback term  $\tilde{A}_{12}$ .

flow equations.

A contribution of this work is to identify power spectra of forcing to the linearized NS equations that yield velocity fluctuation statistics that are consistent with the DNS data in statistical steady state. The output of our model can be used to drive the mean flow equations in time-dependent simulations. Thus, a correction to the mean velocity profile can be sought which perturbs the linearized NS dynamics. This completes the loop by incorporating a two-way interaction between the mean flow and second-order statistics of the fluctuating velocity field. An important topic is to identify conditions under which the feedback connection of mean flow equations with stochastically-forced linearized equations, shown in figure 9.3, converges.

Our methodology is conceptually related to recent work where streamwise-constant NS equations are combined with linearized flow equations driven by white-in-time forcing [229–231]. It was demonstrated that self-sustained turbulence can indeed be maintained with such a model, although, correct statistics are not necessarily obtained. In this context, our approach offers a systematic framework for embedding data into physics-based models in order to capture correct turbulent statistics.

#### **Kinematic simulation of turbulent flow and turbulent inflow generation.**

Kinematic simulations of fully developed turbulence have been extensively used to generate synthetic flow fields. These typically involve the superposition of randomized Fourier modes that obey prescribed one- and two-point correlations [274–279]. Likewise, generating statistically consistent turbulent inflow conditions for numerical simulations of transitional/turbulent flows as well as flow control has been a topic of great interest [280, 281]. A common theme in these studies is that, in contrast to direct simulations, prescribed spatial and temporal correlations are used to generate statistically consistent flow fields.

Our approach is in line with this general theme in that it provides a data-driven method

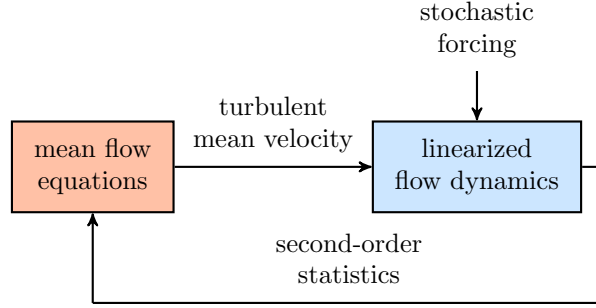


Figure 9.3: For the linearized dynamics of fluctuations around turbulent mean velocity, the appropriate forcing is sought to reproduce partially available velocity correlations and complete the statistical signature of the turbulent flow field. Completed second-order statistics can then be brought into the mean flow equations in order to give turbulent mean velocity and provide equilibrium configuration.

to generate statistically consistent velocity fluctuations using stochastically-driven linearized NS equations. The output of our modeling framework is a velocity field which can be calculated via *inexpensive stochastic linear simulations*. While we only use one-point correlations as problem data, we have demonstrated that two-point spatial and temporal features are reasonably recovered. This can be attributed to two elements of our framework. First, the underlying physics are intrinsic in the problem formulation and, second, the sought modifications of the linearized NS equations around turbulent mean velocity are of *low rank*.

**Extension to complex geometries.** Channel and pipe flows allow Fourier transform techniques to exploit translational invariance in the homogeneous directions and, thereby, simplify computational aspects of the problem. In such cases, the governing equations for fluctuations around mean velocity can be decoupled across spatial wavenumbers. As a result, the optimization step in our theory deals with one pair of wall-parallel wavenumbers at a time; cf. (7.19). Non-parallel flows are spatially-developing and flows in more complex geometries may not be homogeneous in even a single spatial direction. One such example is that of boundary layer flows where experiments [257, 258, 282–284] and simulations [285–288] have provided insight into coherent flow structures and statistics.

Non-parallel flows and flows in complex geometries require treating a much higher number of degrees of freedom. Although our framework is pertinent to refining physics-based models of low complexity using data-driven methods, our current algorithms require  $O(n^3)$  computations for an  $n$ -state discretized evolution model and fall short of dealing with the added computational overhead. At this point, development of more efficient optimization algorithms appears challenging. Thus, a possible direction is to examine

approximations of the governing equations. Examples of such approximations, that have been used for the control and stability analysis of boundary layer flow, can be found in [264, 266, 289, 290]. In general, model reduction techniques [10–13, 15–17, 19–21] can also be used for this purpose.

**Stochastic modeling of spatially-evolving flows.** The results of Chapter 8 demonstrate the necessity of spatially correlated stochastic excitation of the linear PSE for the purpose of capturing transient peaks in the streamwise intensity of the flow. The predictive power of our approach can be further improved by utilizing the theoretical framework developed for identifying the spatio-temporal spectrum of stochastic excitation sources; see Chapters 2, 3 and 7 as well as [34, 164]. On the other hand, while the spatial evolution of the base flow is prominent in the laminar region of the transitional boundary layer, this is not the case in the turbulent region. In fact, a parallel flow assumption can be utilized to develop low-complexity stochastic models that are statistically consistent with the result of nonlinear simulations in this region of the flow. The problem of employing such a framework in order to recover partially-observed statistical signatures of spatially-evolving flows via low-complexity stochastic models is an open problem and will be studied in our future work.

## **Part III**

# **Flow control**

## Chapter 10

# Turbulent drag reduction by streamwise traveling waves

For a turbulent channel flow with zero-net-mass-flux surface actuation in the form of streamwise traveling waves we develop a model-based approach to design control parameters that can reduce skin-friction drag. In contrast to the traditional approach that relies on numerical simulations and experiments, we use turbulence modeling in conjunction with stochastically forced linearized equations to determine the effect of small amplitude traveling waves on the drag. Our simulation-free approach is capable of identifying drag reducing trends in traveling waves with various control parameters. High-fidelity simulations are used to verify the quality of our theoretical predictions.

### 10.1 Introduction

Sensor-free flow control strategies are capable of reducing drag in turbulent flows; examples of these strategies include spanwise wall oscillations [291], riblets, and streamwise traveling waves [292, 293]. Recently, numerical simulations of turbulent channel flows were used to demonstrate that upstream traveling waves can provide sustained levels of drag that are lower than in the laminar flow [292]. These numerical simulations have provided motivation for the development of a model-based framework for designing traveling waves to control the onset of turbulence [108, 109]. Furthermore, the results of [108, 109] have recently been extended to turbulent channel flows subject to spanwise wall-oscillations [33]. Theoretical predictions obtained in [33] were able to capture the behavior of the controlled turbulent flow which was previously observed in high fidelity simulations [291]. In this chapter, we utilize a similar computationally efficient model-based method to study the effects of streamwise traveling waves on turbulent channel

flows. This is achieved by combining turbulence modeling with stochastically forced linearized dynamics to determine the effect of small amplitude traveling waves on skin-friction drag. Our approach is capable of identifying drag reducing trends in traveling waves with various control parameters. We use high fidelity numerical simulations as a means for verifying trustworthiness of our theoretical predictions.

The rest of this chapter is organized as follows: in Section 10.2, we present the governing equations along with the turbulent viscosity model; in Section 10.3, we describe the procedure for determining an approximation to the turbulent mean velocity in flow with control using turbulent viscosity of the uncontrolled flow; in Section 10.4, we use linearized Navier-Stokes (NS) equations to obtain second-order statistics of velocity fluctuations in controlled flow and to show how they influence the turbulent viscosity and skin-friction drag; and finally, in Section 10.4.4, we demonstrate the utility of our method in capturing drag-reducing trends of streamwise traveling waves.

## 10.2 Problem formulation

### 10.2.1 Governing equations

We consider a three-dimensional turbulent channel flow of an incompressible viscous Newtonian fluid; see figure 10.1a for geometry. The flow is driven by a pressure gradient and is governed by the NS and continuity equations

$$\begin{aligned}\mathbf{u}_t &= -(\mathbf{u} \cdot \nabla)\mathbf{u} - \nabla P + (1/R_\tau) \Delta \mathbf{u}, \\ 0 &= \nabla \cdot \mathbf{u},\end{aligned}\tag{10.1}$$

where  $\mathbf{u}$  is the velocity vector,  $P$  is the pressure,  $\nabla$  is the gradient,  $\Delta = \nabla \cdot \nabla$  is the Laplacian. The streamwise, wall-normal, and spanwise coordinates are represented by  $\bar{x}$ ,  $\bar{y}$ , and  $\bar{z}$ , and time is denoted by  $\bar{t}$ . Equation (10.1) has been non-dimensionalized by scaling spatial coordinates with the channel half-height  $h$ , velocity with the friction velocity  $u_\tau = \sqrt{\tau_w/\rho}$ , time with inertial time scale  $h/u_\tau$ , and pressure with  $\rho u_\tau^2$ . The important parameter in (10.1) is the friction Reynolds number,  $R_\tau = u_\tau h/\nu$ , which determines the ratio of inertial to viscous forces. Here,  $\rho$  is the fluid density and  $\nu$  is the kinematic viscosity.

In addition to pressure gradient, the flow with control is subject to a zero-net-mass-flux surface blowing and suction; see figure 10.1b. This imposes the following boundary conditions on the velocity fields,

$$\mathbf{u}(\bar{x}, \bar{y} = \pm 1, \bar{z}, \bar{t}) = [0 \mp 2\alpha \cos(\omega_x(\bar{x} - c\bar{t})) \ 0]^T, \tag{10.2}$$

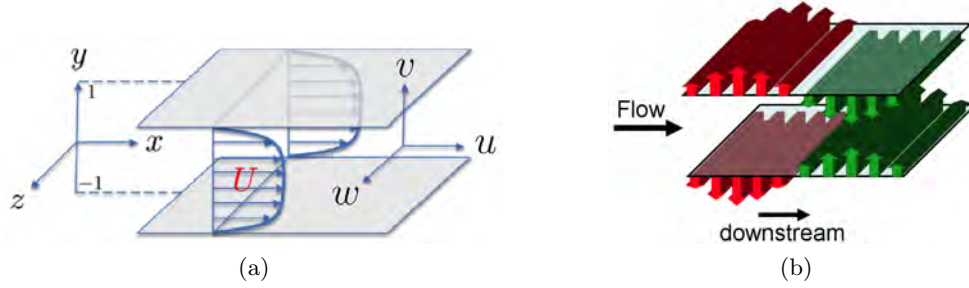


Figure 10.1: (a) Pressure driven turbulent channel flow. (b) Boundary actuation of blowing and suction along the walls.

where  $\omega_x$ ,  $c$ , and  $\alpha$  denote the frequency, speed, and amplitude of the traveling wave. Positive (negative) values of  $c$  define a wave that travels in the downstream (upstream) direction. We can eliminate the time dependence in (10.2) using a simple coordinate transformation,  $(x = \bar{x} - c\bar{t}, y = \bar{y}, z = \bar{z}, t = \bar{t})$ , which adds an additional convective term to (10.1)

$$\begin{aligned} \mathbf{u}_t &= c \mathbf{u}_x - (\mathbf{u} \cdot \nabla) \mathbf{u} - \nabla P + (1/R_\tau) \Delta \mathbf{u}, \\ 0 &= \nabla \cdot \mathbf{u}. \end{aligned} \quad (10.3)$$

### 10.2.2 Navier-Stokes equations augmented with turbulent viscosity

Following a similar procedure as in [33], we augment the molecular viscosity in (10.3) with turbulent viscosity  $\nu_T$

$$\begin{aligned} \mathbf{u}_t &= c \mathbf{u}_x - (\mathbf{u} \cdot \nabla) \mathbf{u} - \nabla P + (1/R_\tau) \nabla \cdot ((1 + \nu_T) (\nabla \mathbf{u} + (\nabla \mathbf{u})^T)), \\ 0 &= \nabla \cdot \mathbf{u}. \end{aligned} \quad (10.4)$$

This model has been used in [33] for model-based design of transverse wall oscillations for the purpose of drag reduction. Moarref and Jovanović [33] showed that this model is capable of capturing the essential features of the turbulent flow with control that were previously observed in high fidelity numerical simulations.

In order to determine the influence of traveling waves on skin-friction drag we need to develop robust models for approximating the turbulent viscosity,  $\nu_T$ , in the presence of control. Several studies [196, 245, 294] have attempted to find expressions for  $\nu_T$  that yield the turbulent mean velocity in flows without control. For example, the following

model for the turbulent viscosity was developed in [196],

$$\nu_{T0}(y) = \frac{1}{2} \left( \left( 1 + \left( \frac{c_2}{3} R_\tau (1 - y^2) (1 + 2y^2) (1 - e^{-(1-|y|) R_\tau / c_1}) \right)^2 \right)^{1/2} - 1 \right) \quad (10.5)$$

where the parameters  $c_1$  and  $c_2$  are selected to minimize least squares deviation between the mean streamwise velocity obtained with  $\tau_w = 1$  and turbulent viscosity (10.5), and the mean streamwise velocity obtained in experiments and simulations.

Our model-based design of streamwise traveling waves for drag reduction involves two tasks:

- (i) [Section 10.3] **Mean flow analysis:** *assuming that (10.5) reliably approximates turbulent viscosity in the controlled flow, we determine the turbulent mean velocity in the flow subject to traveling waves;*
- (ii) [Section 10.4] **Fluctuation dynamics:** *we quantify the effect of fluctuations around the mean velocity determined in (i) on turbulent viscosity and drag reduction.*

In Section 10.3, we use perturbation analysis to determine the steady-state solution to (10.4) with turbulent viscosity given by (10.5) in the presence of small-amplitude boundary actuation (10.2). Using high-fidelity simulations of nonlinear flow dynamics we show that this approximation to turbulent mean velocity does not reliably predict the drag reducing effects of streamwise traveling waves. In Section 10.4, we then demonstrate that predictive capability of our analysis can be improved by examining stochastically forced linearization of system (10.4)-(10.5) around its steady-state solution.

### 10.3 Turbulent mean velocity in flow with $\nu_{T0}$

The first step in our analysis requires determination of an approximation to the turbulent mean velocity,

$$\mathbf{U} = \begin{bmatrix} U(x, y) & V(x, y) & 0 \end{bmatrix}^T,$$

in the presence of blowing and suction along the walls. This is achieved by finding the steady-state solution to (10.4)-(10.5),

$$\begin{aligned} 0 &= c \mathbf{U}_x - (\mathbf{U} \cdot \nabla) \mathbf{U} - \nabla P + (1/R_\tau) \nabla \cdot ((1 + \nu_{T0}) (\nabla \mathbf{U} + (\nabla \mathbf{U})^T)), \\ 0 &= \nabla \cdot \mathbf{U}, \end{aligned} \quad (10.6)$$

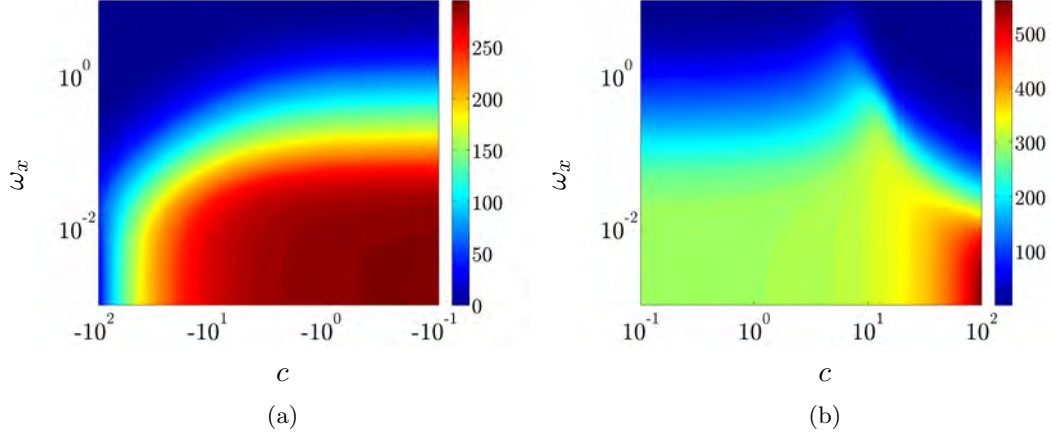


Figure 10.2: Second-order correction to the skin-friction drag  $D_2$  as a function of traveling wave speed  $c$  and frequency  $\omega_x$ : (a) upstream traveling waves; and (b) downstream traveling waves. Predictions are obtained using the solution to (10.6)-(10.7) with turbulent viscosity determined by (10.5).

with boundary conditions

$$V(x, y = \pm 1) = \mp 2\alpha \cos(\omega_x x), \quad U(x, \pm 1) = 0. \quad (10.7)$$

For small amplitude actuation,  $\alpha \ll 1$ , a perturbation analysis can be employed to solve (10.6) subject to (10.7) and determine the corrections to the mean velocities,

$$\begin{aligned} U(x, y) &= U_0(y) + \alpha U_1(x, y) + \alpha^2 U_2(x, y) + \mathcal{O}(\alpha^3), \\ V(x, y) &= \alpha V_1(x, y) + \alpha^2 V_2(x, y) + \mathcal{O}(\alpha^3). \end{aligned} \quad (10.8)$$

Here,  $U_0(y)$  represents the base velocity in the uncontrolled turbulent flow and it is determined from the solution to

$$\begin{aligned} 0 &= (1 + \nu_{T0}) U_0'' + \nu_{T0}' U_0' + R_\tau, \\ 0 &= U_0(y = \pm 1), \end{aligned} \quad (10.9)$$

where prime denotes differentiation with respect to the wall-normal coordinate  $y$ . Higher

harmonics of the mean velocity can be represented as

$$\begin{aligned} U_1(x, y) &= U_{1,-1}(y) e^{-i\omega_x x} + U_{1,1}(y) e^{i\omega_x x}, \\ V_1(x, y) &= V_{1,-1}(y) e^{-i\omega_x x} + V_{1,1}(y) e^{i\omega_x x}, \\ U_2(x, y) &= U_{2,0}(y) + U_{2,-2}(y) e^{-2i\omega_x x} + U_{2,2}(y) e^{2i\omega_x x}, \\ V_2(x, y) &= V_{2,-2}(y) e^{-2i\omega_x x} + V_{2,2}(y) e^{2i\omega_x x}. \end{aligned}$$

Under the assumption of the fixed bulk,

$$\int_{-1}^1 \overline{U(x, y)} dy = \int_{-1}^1 U_0(y) dy,$$

the skin-friction drag is determined by the slope of the streamwise mean velocity at the walls,

$$D = \frac{1}{2} \left( \left. \frac{d\overline{U}}{dy} \right|_{-1} - \left. \frac{d\overline{U}}{dy} \right|_1 \right), \quad (10.10)$$

where the overline denotes the average value obtained by integration in the  $x$ -direction. Thus, up to a second-order in  $\alpha$ , the only terms that influence  $D$  are  $U_0$  and  $U_{2,0}$ ,

$$\begin{aligned} D &= D_0 + \alpha^2 D_2 + \mathcal{O}(\alpha^4), \\ D_0 &:= \frac{1}{2} (U'_0(-1) - U'_0(1)), \\ D_2 &:= \frac{1}{2} (U'_{2,0}(-1) - U'_{2,0}(1)), \end{aligned}$$

Figure 10.2 shows the second order correction to skin-friction drag  $D_2$ , as a function of the traveling wave speed and frequency. We observe that both upstream and downstream traveling waves increase drag. This is in contrast to the results obtained using simulations of the nonlinear flow dynamics [109, 292] where it was shown that drag reduction can be obtained for certain values of traveling wave parameters. For an upstream traveling wave with  $c = -2$  and  $\omega_x = 0.5$ , figure 10.3 also demonstrates increase in drag for all values of the wave amplitude  $\alpha$ . We observe close correspondence between the results obtained from the solution to (10.6)-(10.7) with  $\nu_{T0}$  determined by (10.5) using terms up to a second order in  $\alpha$ , fourth order in  $\alpha$ , and Newton's method.

The results of this section show the inability of the above conducted mean flow analysis to capture the drag reducing effects of streamwise traveling waves. In Section 10.4, we demonstrate that the gap between our predictions and the results of high-fidelity numerical simulations can be significantly reduced by analyzing the dynamics of fluctuations around the mean velocity profile determined here.

## 10.4 Dynamics of velocity fluctuations

In this section, we use a framework for the input-output analysis of PDEs with spatially-periodic coefficients developed in [295] to examine the dynamics of fluctuations around the turbulent mean profile  $\mathbf{U}$  determined in Section 10.3. The second-order statistics of the flow with control are obtained using stochastically forced NS equations. For small amplitude actuation, we employ perturbation analysis to determine turbulent viscosity and the resulting correction to the skin-friction drag from these statistics.

### 10.4.1 Linearized Navier-Stokes equations

The dynamics of infinitesimal velocity fluctuations  $\mathbf{v} = [u \ v \ w]^T$  around the turbulent mean velocity  $\mathbf{U}$  are governed by

$$\begin{aligned} \mathbf{v}_t &= c \mathbf{v}_x - (\mathbf{U} \cdot \nabla) \mathbf{v} - (\mathbf{v} \cdot \nabla) \mathbf{U} - \nabla p + \mathbf{f} \\ &\quad + (1/R_\tau) \nabla \cdot ((1 + \nu_{T0}) (\nabla \mathbf{v} + (\nabla \mathbf{v})^T)), \\ 0 &= \nabla \cdot \mathbf{v}. \end{aligned} \tag{10.11}$$

Equation (10.11) is driven by zero-mean temporally white stochastic forcing  $\mathbf{f}$ . Since the boundary conditions (10.2) are satisfied by turbulent mean velocity, the velocity fluctuations  $\mathbf{v}$  assume no-slip boundary conditions. Following a similar procedure as in [108], we can bring the set of spatially periodic PDEs (10.11) into the following evolution form

$$\begin{aligned} \partial_t \boldsymbol{\psi}_\theta(y, k_z, t) &= A_\theta(k_z) \boldsymbol{\psi}_\theta(y, k_z, t) + \mathbf{f}_\theta(y, k_z, t), \\ \mathbf{v}_\theta(y, k_z, t) &= C_\theta(k_z) \boldsymbol{\psi}_\theta(y, k_z, t), \end{aligned} \tag{10.12}$$

where  $\boldsymbol{\psi} = [v \ \eta]^T$  is the state vector with  $\eta = \partial_z u - \partial_x w$  being the wall-normal vorticity. Homogenous Dirichlet boundary conditions are imposed on  $\eta$ , while homogeneous Dirichlet and Neumann boundary conditions are imposed on  $v$ .

We note that  $\boldsymbol{\psi}$ ,  $\mathbf{v}$ , and  $\mathbf{f}$  are bi-infinite column vectors parameterized by  $\theta$  and  $k_z$ , e.g.,  $\boldsymbol{\psi}_\theta(y, k_z, t) = \text{col}\{\boldsymbol{\psi}(\theta_n, y, k_z, t)\}_{n \in \mathbb{N}}$ . Furthermore, for each  $\theta$  and  $k_z$ ,  $A_\theta(k_z)$  and  $C_\theta(k_z)$  are bi-infinite matrices whose elements are integro-differential operators in  $y$ . The operator  $A_\theta$  can be written as  $A_\theta = A_{0\theta} + \sum_{\ell=1}^{\infty} \alpha^\ell A_{\ell\theta}$  where the definition of  $A_{\ell\theta}$  can be found in [108]. In the next section, we exploit the structure of the operator  $A_\theta$  and use perturbation analysis to determine the auto-correlation operator of  $\boldsymbol{\psi}_\theta$  for small values of the traveling wave amplitude,  $\alpha$ .

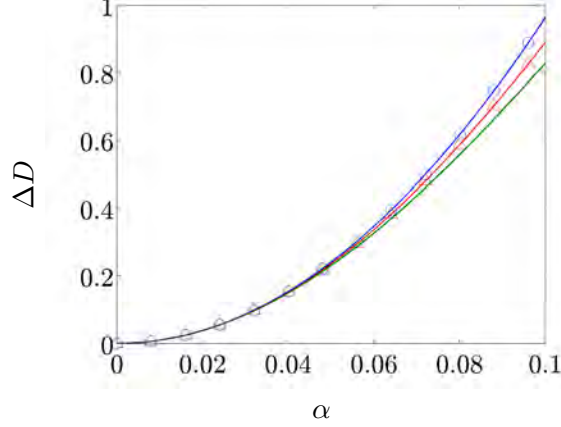


Figure 10.3: Drag variation,  $\Delta D = D - D_0$ , as a function of wave amplitude  $\alpha$  for an upstream traveling wave with  $c = -2$  and  $\omega_x = 0.5$ . Predictions are obtained from the solution to (10.6)-(10.7) with turbulent viscosity determined by (10.5) using terms up to a second order in  $\alpha$  ( $\circ$ ), fourth order in  $\alpha$  ( $\nabla$ ), and Newton's method (solid curve).

#### 10.4.2 Second-order statistics of velocity fluctuations

Consider the linearized system (10.12) driven by zero-mean temporally white stochastic forcing with second-order statistics,

$$\mathcal{E}(\mathbf{f}(\cdot, \boldsymbol{\kappa}, t_1) \otimes \mathbf{f}(\cdot, \boldsymbol{\kappa}, t_2)) = M(\boldsymbol{\kappa}) \delta(t_1 - t_2).$$

Here,  $\boldsymbol{\kappa} = (\theta, k_z)$  denotes the wave-numbers,  $\delta$  is the Dirac delta function,  $\mathbf{f} \otimes \mathbf{f}$  is the tensor product of  $\mathbf{f}$  with itself, and  $M(\boldsymbol{\kappa})$  is the spatial spectral-density of forcing. We follow [33] and select  $M$  so that the two-dimensional energy spectra of the stochastically forced linearized NS equations match those of the uncontrolled turbulent flow. For this purpose, we use the energy spectrum of the uncontrolled flow  $E(y, \boldsymbol{\kappa})$  resulting from numerical simulations of the nonlinear flow dynamics [236, 237] to define

$$M(\boldsymbol{\kappa}) = \frac{\bar{E}(\boldsymbol{\kappa})}{\bar{E}_0(\boldsymbol{\kappa})} M_0(\boldsymbol{\kappa}),$$

$$M_0(\boldsymbol{\kappa}) = \begin{bmatrix} \sqrt{E} I & 0 \\ 0 & \sqrt{E} I \end{bmatrix} \begin{bmatrix} \sqrt{E} I & 0 \\ 0 & \sqrt{E} I \end{bmatrix}^\dagger,$$

where  $\bar{E}(\boldsymbol{\kappa}) = (1/2) \int_{-1}^1 E(y, \boldsymbol{\kappa}) dy$  represents the two-dimensional energy spectrum of the uncontrolled flow and  $\bar{E}_0$  is the energy spectrum obtained from the linearized NS equations subject to white-in-time forcing with spatial spectrum  $M_0(\boldsymbol{\kappa})$ . The  $\dagger$  sign

denotes the adjoint of an operator which should be determined with respect to the appropriate inner product; for additional details see [30].

For the linearized system (10.12), the steady-state auto-correlation operator of  $\psi_\theta$  can be determined from the solution to the Lyapunov equation,

$$A_\theta(k_z) \mathcal{X}_\theta(k_z) + \mathcal{X}_\theta(k_z) A_\theta^+(k_z) + M_0(\theta, k_z) = 0,$$

and the energy spectrum is given by

$$E_0(\kappa) = \text{trace}(\mathcal{X}_\theta(k_z)) = \sum_{n=-\infty}^{\infty} \text{trace}(X_d(\theta_n, k_z)),$$

where  $X_d(\theta_n, k_z)$  represents the elements on the main diagonal of  $\mathcal{X}_\theta$ . For small amplitude actuation, perturbation analysis in conjunction with the special structure of the operator  $A_\theta$  can be used to express  $\mathcal{X}_\theta(k_z)$  as

$$\mathcal{X}_\theta(k_z) = \mathcal{X}_{\theta,0}(k_z) + \alpha^2 \mathcal{X}_{\theta,2}(k_z) + \mathcal{O}(\alpha^4),$$

where  $\mathcal{X}_{\theta,0}(k_z)$  and  $\mathcal{X}_{\theta,2}(k_z)$  are the solutions to a set of coupled operator-valued Lyapunov and Sylvester equations [296]. The auto-correlation operator  $\mathcal{X}_{\theta,0}(k_z)$  contains the contribution of the flow with no control, and  $\mathcal{X}_{\theta,2}(k_z)$  captures the effect of control (up to second-order in  $\alpha$ ).

### 10.4.3 Influence of fluctuations on turbulent viscosity and skin-friction drag

We next show how velocity fluctuations in the flow with control introduce a second order correction to turbulent viscosity and skin-friction drag. We use the kinetic energy of velocity fluctuations,  $k$ , and its rate of dissipation,  $\epsilon$ , to determine the influence of fluctuation on the turbulent viscosity,

$$\nu_T = C_\mu R_\tau^2 (k^2/\epsilon), \quad (10.13)$$

where  $C_\mu = 0.09$  is a model constant. Both  $k$  and  $\epsilon$  are determined by the second-order statistics of velocity fluctuations,

$$\begin{aligned} k(y) &= (1/2) (\overline{uu} + \overline{vv} + \overline{ww}), \\ \epsilon(y) &= 2(\overline{u_x u_x} + \overline{v_y v_y} + \overline{w_z w_z} + \overline{u_y v_x} + \overline{u_z w_x} + \overline{v_z w_y}) + \overline{u_y u_y} + \overline{w_y w_y} \\ &\quad + \overline{v_x v_x} + \overline{w_x w_x} + \overline{u_z u_z} + \overline{v_z v_z}. \end{aligned} \quad (10.14)$$

The overline in (10.14) denotes averaging in the streamwise and spanwise directions.

In the flow subject to small amplitude traveling waves,  $k$  and  $\epsilon$  can be expressed as

$$\begin{aligned} k &= k_0 + \alpha^2 k_2 + \mathcal{O}(\alpha^4), \\ \epsilon &= \epsilon_0 + \alpha^2 \epsilon_2 + \mathcal{O}(\alpha^4), \end{aligned} \tag{10.15}$$

where the subscript 0 denotes the corresponding quantities in the uncontrolled flow, and the subscript 2 denotes the influence of fluctuations at the level of  $\alpha^2$ .

By substituting (10.15) into (10.13) and applying the Neumann series expansion we obtain an expression that establishes the dependence of the second-order correction to  $\nu_T$  on  $k_2$  and  $\epsilon_2$ ,

$$\begin{aligned} \nu_T &= \nu_{T0} + \alpha^2 \nu_{T2} + \mathcal{O}(\alpha^4), \\ \nu_{T2} &= \nu_{T0} \left( \frac{2k_2}{k_0} - \frac{\epsilon_2}{\epsilon_0} \right). \end{aligned} \tag{10.16}$$

The influence of fluctuations on turbulent mean velocity (and consequently the skin-friction drag) can be obtained by substituting  $\nu_T$  from (10.16) into (10.4) and finding the resulting steady-state solution.

#### 10.4.4 Results: turbulent drag reduction and net efficiency

We next examine the effect of an upstream traveling wave with  $c = -2$  and  $\omega_x = 0.5$  on the skin-friction drag in a turbulent channel flow with  $R_\tau = 186$ . For this choice of traveling wave parameters, numerical simulations of nonlinear flow dynamics at  $R_\tau \approx 63$  have demonstrated the drag-reducing ability of upstream traveling waves [109, 292].

Figure 10.4 shows the time dependence of the skin-friction drag for the uncontrolled turbulent flow and for the flow subject to an upstream traveling wave with  $c = -2$ ,  $\omega_x = 0.5$ , and three wave amplitudes ( $\alpha = 0.01$ ,  $\alpha = 0.05$ , and  $\alpha = 0.125$ ). The solid lines are obtained using simulations of the nonlinear NS equations, and the black dots indicate the corresponding steady-state values of drag resulting from the model-based approach of Section 10.4. Compared to the flow with no control, from figure 10.4 it appears that the traveling wave with  $\alpha = 0.01$  slightly increases drag. However, numerical simulation conducted over longer time horizon (not shown here) indicates a very small discrepancy between the uncontrolled flow results and the results obtained for the upstream traveling wave with  $\alpha = 0.01$ . For  $\alpha = 0.05$ , our results (obtained using perturbation analysis up to second-order in  $\alpha$ ) show that upstream traveling waves are able to reduce turbulent drag. More interestingly, for traveling waves with amplitude  $\alpha = 0.125$ , our predictions from perturbation analysis capture the ability of upstream traveling waves in reducing skin-friction drag to sub-laminar levels. This is in agreement with the results of [292].

Even though our predictions are verified in numerical simulations of the nonlinear NS

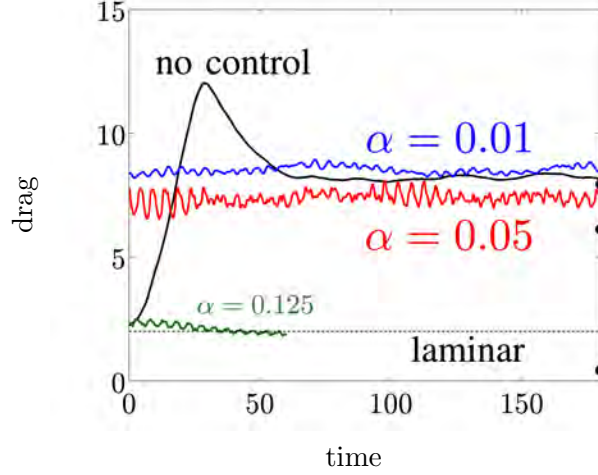


Figure 10.4: Drag in a turbulent channel flow obtained from high-fidelity simulations with  $R_\tau = 186$  subject to an upstream traveling wave ( $c = -2$ ,  $\omega_x = 0.5$ ) at three wave amplitudes,  $\alpha = 0.01$  (blue),  $\alpha = 0.05$  (red), and  $\alpha = 0.125$  (green). The black dots denote the drag computed using the model-based framework of Section 10.4. Also shown are the laminar drag (dashed line) and turbulent drag in the absence of control (black solid line).

equations (see red and green curves in figure 10.4), we observe a mismatch between numerically obtained values of the drag and those resulting from our analysis. However, the effect of higher-order corrections to the turbulent viscosity in our perturbation analysis remains to be examined.

## Chapter 11

# Model-based analysis of the effect of spanwise wall oscillations on drag reduction at high Reynolds numbers

Experiments and numerical simulations have shown that the drag-reducing ability of spanwise wall oscillations in turbulent channels deteriorates as the Reynolds number increases. Recent work by Moarref and Jovanovic [33] has demonstrated the predictive power of a model-based approach for controlling turbulent channel flow using spanwise wall oscillations. In the present chapter, we use a linearized stochastically-forced model to reveal the Reynolds number independent effects of wall oscillations on drag reduction. This allows us to extend the predictive capability of our simulation-free approach to high Reynolds numbers. We show that the influence of wall oscillations at low Reynolds numbers is confined to the streamwise and spanwise wavelengths that correspond to the universal inner-scaled eddies in wall turbulence. Since wall oscillations do not suppress large-scale eddies, which are responsible for increased drag in the uncontrolled flow, we conclude that wall oscillations have weaker influence on drag reduction at higher Reynolds numbers. In addition, our observations enable predictions of drag reduction trends at high Reynolds numbers.

### 11.1 Introduction

In the last two decades, an extensive amount of research has been dedicated to understanding the mechanisms that are responsible for maintaining the laminar flow and

reducing skin-friction drag via active and passive control [1, 2]. In particular, experiments and numerical simulations of turbulent channel flows have respectively recorded up to 40 and 45% drag reduction using transverse wall oscillations [297–301]. The basic setup for this flow control strategy involves oscillation of channel walls, which can be characterized by the amplitude  $\alpha$  and period of oscillations  $T$ ; see figure 11.1b. In this vein, an interesting observation is that as the Reynolds number in the channel flow setup increases, the drag reducing ability of spanwise wall oscillations gradually deteriorates [33, 302–304]. Although many have provided useful insight into this phenomenon, few have provided an analytical framework for quantifying such an effect. In this chapter, we utilize the recently developed model-based framework for the design of spanwise wall oscillations in turbulent channel flow [33] to study the drag reducing trends of this control strategy as higher Reynolds number flows are considered.

In [33], the second-order statistics of a stochastically forced linearized model of turbulent channel flow were used to determine the modification to turbulent viscosity in the presence of control via perturbation analysis. This study considers an eddy-viscosity enhanced variation of the linearized NS equations. In addition, the spatial power spectrum of white-in-time forcing is selected to ensure that in the absence of control, the stochastically forced linear model reproduces the energy spectrum resulting from DNS of a turbulent channel flow [236, 237]. The second-order flow statistics that are collected from the stochastically forced linearized dynamics of the flow subject to wall oscillation are used, via perturbative methods, to compute second-order corrections (in control amplitude  $\alpha$ ) to the kinetic energy and dissipation of kinetic energy. These corrections are subsequently utilized to compute the influence of control on the turbulent eddy viscosity and approximately quantify the effect of control on turbulent drag.

The rest of this chapter is organized as follows. In Section 11.2, we present the governing equations along with the turbulent viscosity model. We also briefly overview how perturbation analysis can be used to predict the influence of control on the turbulent eddy viscosity, the streamwise mean velocity, and the turbulent drag. In Section 11.3, we examine some common trends observed in the energy spectrum of turbulent channel flow at high Reynolds numbers. We also quantify the effect of spanwise wall oscillations at high Reynolds numbers by computing the production and dissipation of turbulent kinetic energy. Based on the observations made in Section 11.3, we predict the drag reducing trends of spanwise wall oscillations at high Reynolds numbers in Section 11.4.

## 11.2 Background

We consider a pressure-driven turbulent channel flow of an incompressible viscous Newtonian fluid; see figure 11.1a for geometry. The flow is driven by a pressure gradient

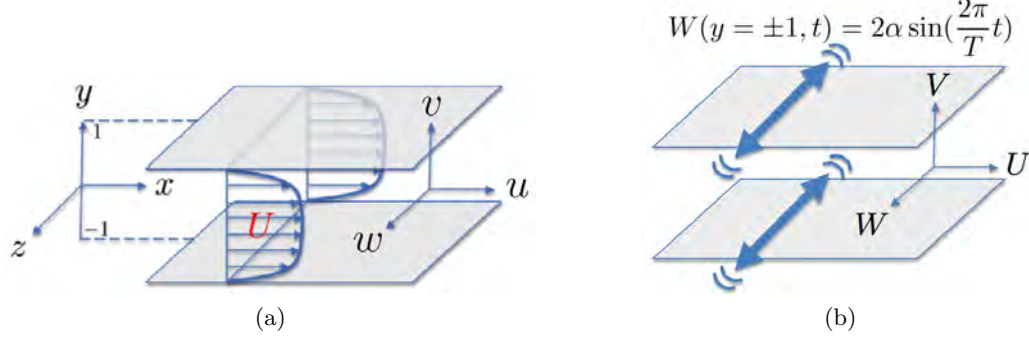


Figure 11.1: (a) Pressure driven turbulent channel flow, and (b) channel flow subject to spanwise wall oscillations of amplitude  $\alpha$  and period  $T$ .

and is governed by the NS and continuity equations

$$\begin{aligned} \mathbf{u}_t &= -(\mathbf{u} \cdot \nabla) \mathbf{u} - \nabla P + (1/R_\tau) \Delta \mathbf{u}, \\ 0 &= \nabla \cdot \mathbf{u}, \end{aligned} \quad (11.1)$$

where  $\mathbf{u} = [u \ v \ w]^T$  is the velocity vector,  $P$  is the pressure,  $\nabla$  is the gradient,  $\Delta = \nabla \cdot \nabla$  is the Laplacian. Equation (11.1) has been non-dimensionalized by scaling spatial coordinates with the channel half-height  $h$ , velocity with the friction velocity  $u_\tau = \sqrt{\tau_w/\rho}$ , time with inertial time scale  $h/u_\tau$ , and pressure with  $\rho u_\tau^2$ . The friction Reynolds number,  $R_\tau = u_\tau h/\nu$ , determines the ratio of inertial to viscous forces. Here,  $\rho$  is the fluid density and  $\nu$  is the kinematic viscosity.

In addition to pressure gradient, the flow is subject to zero-mean spanwise wall oscillations; see figure 11.1b. This imposes the following boundary conditions on the velocity field,

$$\mathbf{u}(x, y = \pm 1, z, t) = [0 \ 0 \ 2\alpha \sin(\frac{2\pi}{T}t)]^T, \quad (11.2)$$

where  $\alpha$  denotes the amplitude of oscillations and the period of oscillations is given by  $T$  when computed in outer units (normalized by  $h/u_\tau$ ) and by  $T^+ = R_\tau T$  when computed in viscous units (normalized by  $\nu/u_\tau^2$ ). While the uniform pressure gradient  $P_x$  balances the wall-shear stress [186, 206] and induces a streamwise mean velocity  $U(y)$ , wall oscillations give rise to a spanwise mean velocity component  $W(y)$ ; see [33] for the governing equations of the mean velocity  $\bar{\mathbf{u}} = [U(y) \ 0 \ W(y, t)]^T$ .

The skin-friction coefficient can be computed as [206, 305]

$$C_f = 2|P_x|/U_B^2. \quad (11.3)$$

We consider a constant bulk flux  $U_B$ . As a result, reduction (increase) in  $|P_x|$  results in drag reduction (increase). Changes to the skin-friction coefficient relative to the uncontrolled flow can be quantified as

$$\% C_f = 100 \frac{C_{f,u} - C_{f,c}}{C_{f,u}} = 100 (1 + P_{x,c}), \quad (11.4)$$

where the subscripts  $c$  and  $u$  respectively represent quantities in the controlled and uncontrolled flows. As a result, our control strategy leads to drag reduction in cases which  $P_{x,c} > -1$ .

The dynamics of fluctuations around the time-periodic mean velocity  $\mathbf{u}$  is governed by the evolution form of the linearized NS (7.6), with operator  $A$  given by

$$A(\mathbf{k}, t) = A_0(\mathbf{k}) + \alpha \left( A_{-1}(\mathbf{k}) e^{-i\frac{2\pi}{T}t} + A_1(\mathbf{k}) e^{i\frac{2\pi}{T}t} \right), \quad (11.5)$$

where,  $A_0$  is the generator of the eddy-viscosity enhanced linearized NS equations in the absence of control, and  $A_{-1}$  and  $A_1$  represent modifications induced by the harmonic boundary conditions. Expressions for  $A_0$ ,  $A_{-1}$  and  $A_1$  can be found in [33, Appendix B].

In order to determine the influence of wall oscillations on skin-friction drag we need to develop robust models for approximating the turbulent viscosity,  $\nu_T$ , in the presence of control. Several studies [196, 245, 294] have attempted to find expressions for  $\nu_T$  that yield the turbulent mean velocity in flows without control. For example, the following model for the turbulent viscosity was developed in [196],

$$\nu_{T0}(y) = \frac{1}{2} \left( \left( 1 + \left( \frac{c_2}{3} R_\tau (1 - y^2) (1 + 2y^2) (1 - e^{-(1-|y|) R_\tau / c_1}) \right)^2 \right)^{1/2} - 1 \right) \quad (11.6)$$

where the parameters  $c_1$  and  $c_2$  are selected to minimize the least squares deviation between the mean streamwise velocity obtained with  $\tau_w = 1$  and turbulent viscosity (11.6), and the mean streamwise velocity obtained in experiments and simulations; see [33] for values of  $c_1$  and  $c_2$  at various Reynolds numbers.

### 11.2.1 Second-order statistics of velocity fluctuations in the presence of control

For small-amplitude wall oscillations, perturbation analysis in  $\alpha$  can be used to quantify the average effect of forcing (over one period  $T$ ) on the the auto-correlation operator of the state  $\psi$ , i.e.,

$$X(\mathbf{k}) = X_0(\mathbf{k}) + \alpha^2 X_2(\mathbf{k}) + O(\alpha^4). \quad (11.7)$$

While  $X_0$  contains the second-order statistics of uncontrolled flow,  $X_2$  represents the influence of control at the level of  $\alpha^2$  and can be obtained from a set of decoupled Lyapunov equations [107, 306]; also see [33, Appendix D] for additional details.

### 11.2.2 Turbulent viscosity model and drag reduction

While we utilize the Reynolds-Tiederman turbulent eddy-viscosity profile for the equations with no control (cf. (11.6)), we quantify the effect of velocity fluctuations in the flow with control on the turbulent viscosity and skin-friction drag via the steps outlined in Section 10.4.3. A perturbation series for the turbulent viscosity is thus deduced from the perturbation series (11.7),

$$\nu_T = \nu_{T0} + \alpha^2 \nu_{T2} + O(\alpha^4). \quad (11.8)$$

Here,  $\nu_{T2}$  represents the second-order correction to the turbulent viscosity, which depends on second-order corrections to the kinetic energy  $k_2$  and dissipation of kinetic energy  $\epsilon_2$ , i.e.,

$$\nu_{T2} = 2k_2 \left( \frac{\nu_{T0}}{k_0} \right) + \left( \frac{\epsilon_2}{R_\tau^2} \right) \left( \frac{\nu_{T0}}{k_0} \right)^2. \quad (11.9)$$

This equation separates the dependence of  $\nu_{T2}$  on the turbulent viscosity and kinetic energy of the uncontrolled flow via the ratio  $\nu_{T0}/k_0$ , and the second-order correction to the kinetic energy  $k_2$  and the scaled correction to the dissipation of kinetic energy  $\epsilon_2/R_\tau^2$  in the presence of control.

Following the perturbation series considered for  $\nu_T$  in (11.8), the mean streamwise velocity and the pressure gradient can be written as

$$U(y) = U_0(y) + \alpha^2 U_2(y) + O(\alpha^4), \quad (11.10a)$$

$$P_x = -1 + \alpha^2 P_{x,2} + O(\alpha^4). \quad (11.10b)$$

Here,  $U_0$  is the turbulent mean velocity of the channel flow in the absence of control, and  $U_2$  and  $P_{x,2}$  are correction terms to the mean streamwise velocity and the pressure gradient at the level of  $\alpha^2$ . These correction terms can be computed by substituting the perturbation series (11.8) into the governing equations for the streamwise mean velocity  $U(y)$ . By substituting equation (11.10b) into (11.4), we arrive at the the second-order correction to turbulent drag  $C_f$

$$C_{f,2} = -\frac{1}{2U_B} \int_{-1}^1 \int_{-1}^y \frac{\nu_{T2}(\xi) U_0'(\xi)}{1 + \nu_{T0}} d\xi dy. \quad (11.11)$$

See [33, Appendix E] for additional details.

### 11.3 High Reynolds number trends

Recent improvements in high-fidelity numerical simulations [236, 237, 285–288, 307] and the construction of high Reynolds number facilities for gathering experimental measurements [257, 258, 282–284, 308–316] have provided the opportunity to answer many questions regarding the structural features of wall turbulence at high Reynolds numbers. This has led to an improved understanding of the physics of energetically relevant turbulent length-scales as well as universality laws for the trends observed in the turbulent mean velocity profile in a variety of shear flow configurations [9, 257].

In this section, we first examine the DNS-generated energy spectrum of a turbulent channel flow with  $R_\tau = 186, 547, 934, \text{ and } 2003$  [236, 237]. We then explore the spectrum of kinetic energy and its dissipation in the controlled channel flow and use these observations to predict drag reducing trends of this control strategy at higher Reynolds numbers.

#### 11.3.1 Turbulent energy spectrum of uncontrolled flow

Figure 11.2 shows the premultiplied energy spectrum of uncontrolled flow from numerical simulations [236, 237] of the turbulent channel flow at various Reynolds numbers. The spectra are displayed in terms of the streamwise and spanwise wavelengths and the wall-normal coordinate (all in inner units). The energy is concentrated within a certain range of wavelengths and in a certain wall-normal region and away from the wall. As the Reynolds number is increased, flow structures with longer wavelengths that form farther away from the wall become more significant. This observation is in agreement with experimental measurements that have shown that as the Reynolds number increases, the contribution to the production of turbulent kinetic energy shifts from fluid structures that reside in the near-wall region ( $0 < y^+ < 30$ ) to ones that are farther away from the wall and within the logarithmic region ( $70 < y^+ < 0.15R_\tau$ ) [315]; see figure 11.3.

#### 11.3.2 Effect of control on the production and dissipation of turbulent kinetic energy at high Reynolds numbers

In this subsection, we use the model-based framework described in Section 11.2 to examine the effect of control on the turbulent kinetic energy and the dissipation of kinetic energy. We focus on wall oscillations with a period of  $T^+ = 100$  for which numerical studies at  $R_\tau = 200$  have shown largest drag reduction for control amplitudes of  $\alpha = 3.1$  and  $6.2$  [291].

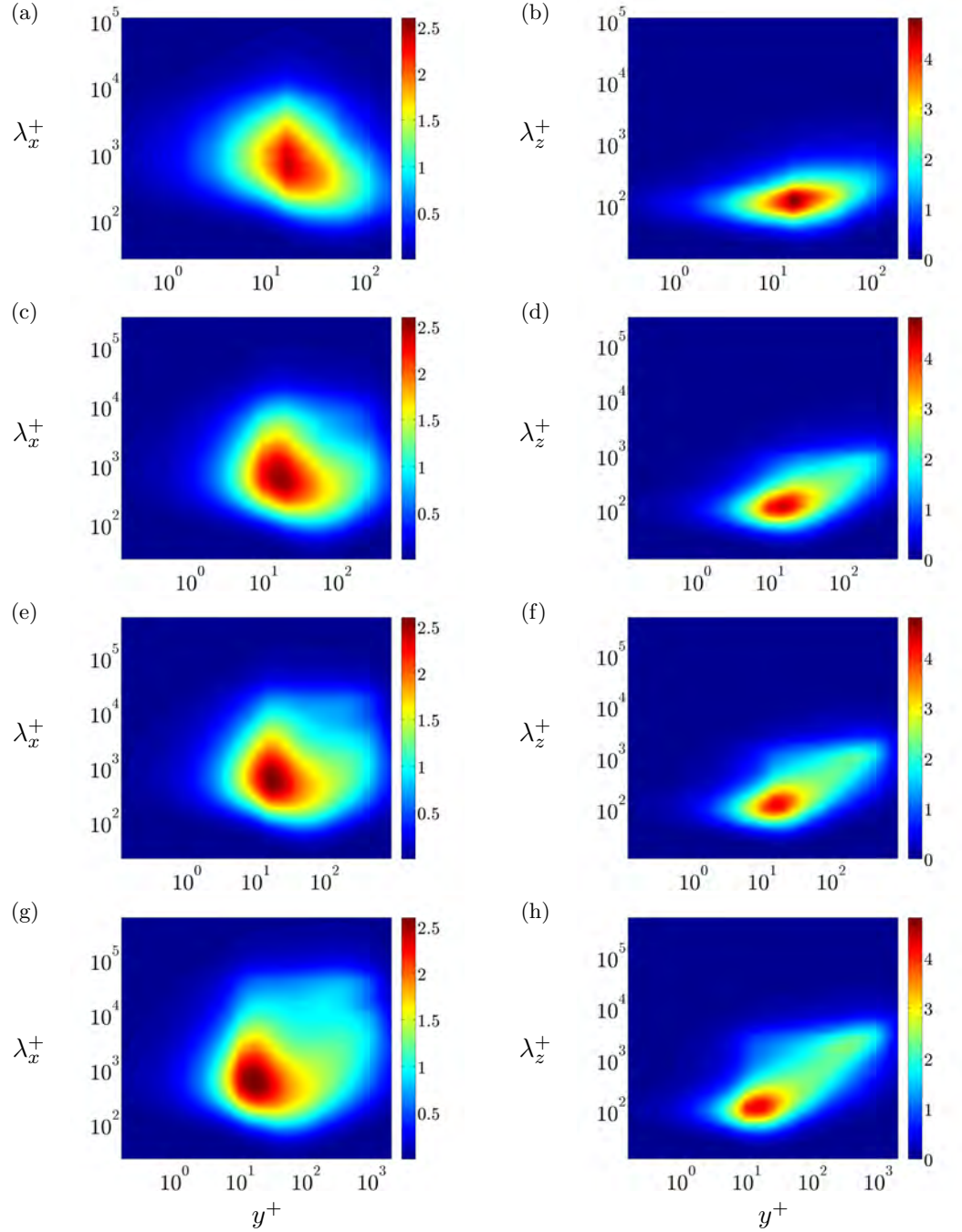


Figure 11.2: Premultiplied energy spectrum of uncontrolled flow from DNS of turbulent channel flow [236, 237] in terms of streamwise (left) and spanwise (right) wavelengths and the wall-normal coordinate (all in inner units) at (a, b)  $R_\tau = 186$ , (c, d)  $R_\tau = 547$ , (e, f)  $R_\tau = 934$ , and (g, h)  $R_\tau = 2003$ .

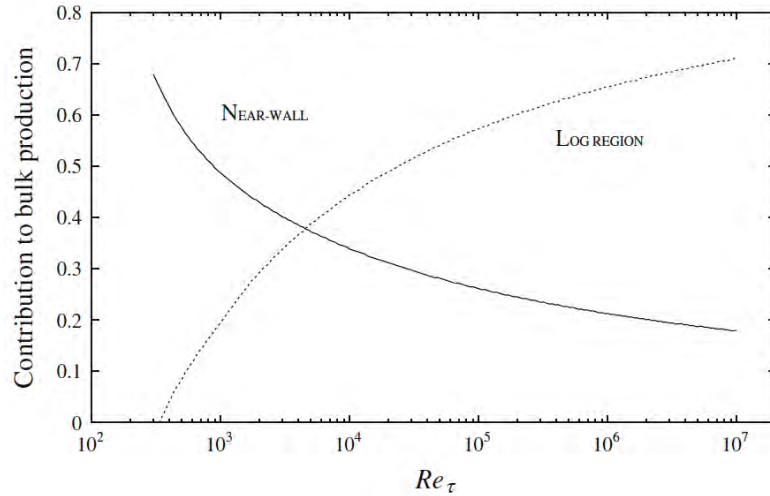


Figure 11.3: Ratio of contribution to kinetic energy production to bulk production. As the Reynolds number increases, contribution to the production of kinetic energy shifts from structures that lie in the near-wall region to those that lie farther away from the wall and in the logarithmic region; figure from Marusic *et al.* [315].

Figure 11.4 shows the premultiplied second-order correction to the turbulent kinetic energy in terms of the streamwise and spanwise wavelengths and the wall-normal coordinate (all in inner units) for turbulent channels with various Reynolds numbers. We observe that as the Reynolds number is increased, the effect of control on the production of turbulent kinetic energy is confined to a certain region close to the wall ( $1 < y^+ < 100$ ). It is also limited to a certain range of streamwise and spanwise wavelengths. A similar collapse with inner units is observed in the premultiplied second-order correction to the dissipation of kinetic energy divided by  $R_\tau^2$ ; see figure 11.5.

## 11.4 Drag reduction in higher Reynolds numbers flows

Based on the trends observed in the previous section, the effect of control on the premultiplied second-order corrections to the turbulent kinetic energy and its dissipation are approximately invariant with respect to changes in the Reynolds number<sup>1</sup>; cf. figures 11.4 and 11.5. Based on this and the dependence of equation (11.9) on the ratio  $\nu_{T0}/k_0$  we arrive at the following conclusion.

<sup>1</sup>Currently, this claim is confined to the range of Reynolds numbers considered in this study.

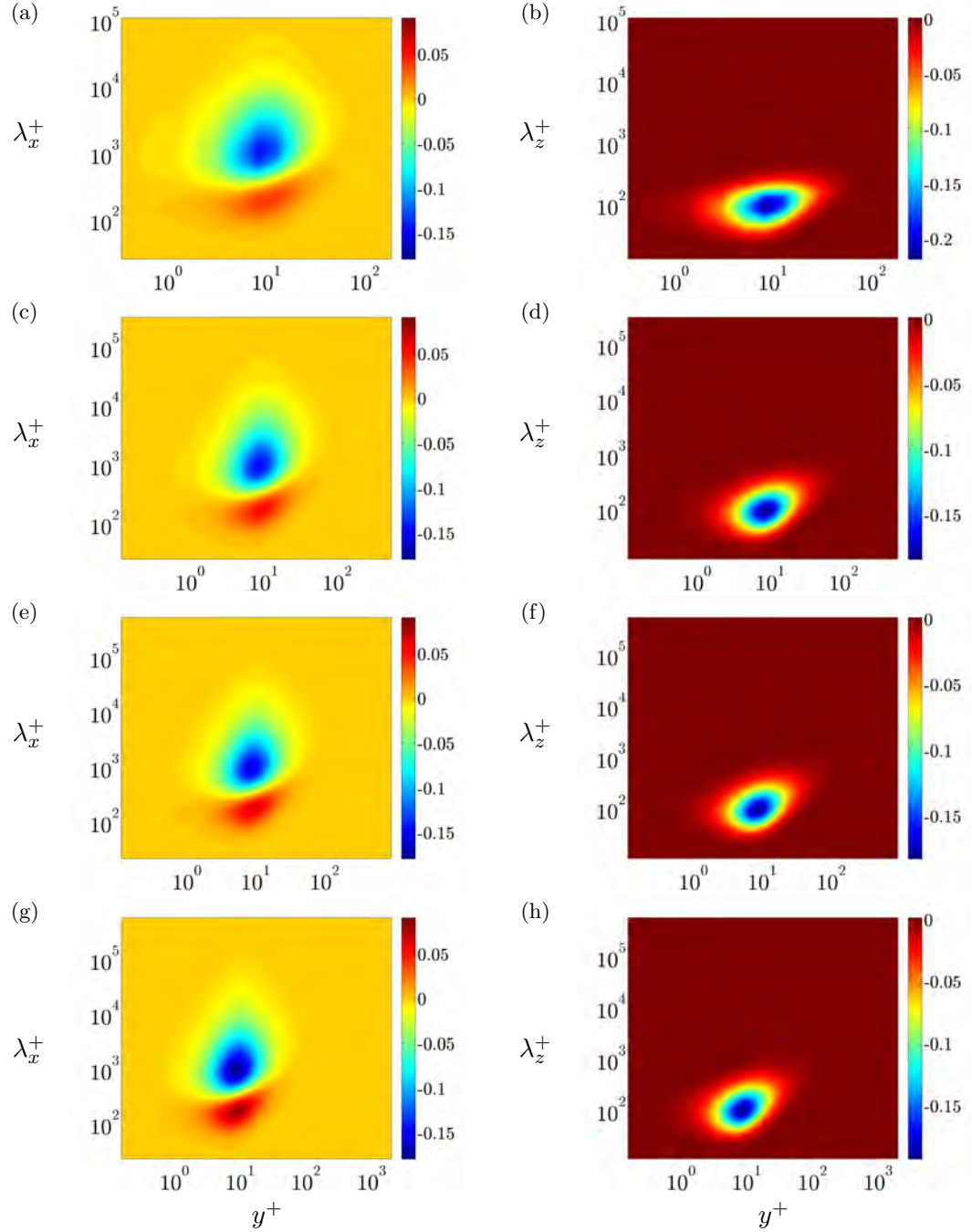


Figure 11.4: Premultiplied second-order correction to the kinetic energy spectrum of velocity fluctuations in turbulent channel flow subject to spanwise wall oscillations with period  $T^+ = 100$ ;  $k_x k_2(y, k_x)$  (left) and  $k_z k_2(y, k_z)$  (right). (a, b)  $R_\tau = 186$ , (c, d)  $R_\tau = 547$ , (e, f)  $R_\tau = 934$ , and (g, h)  $R_\tau = 2003$ .

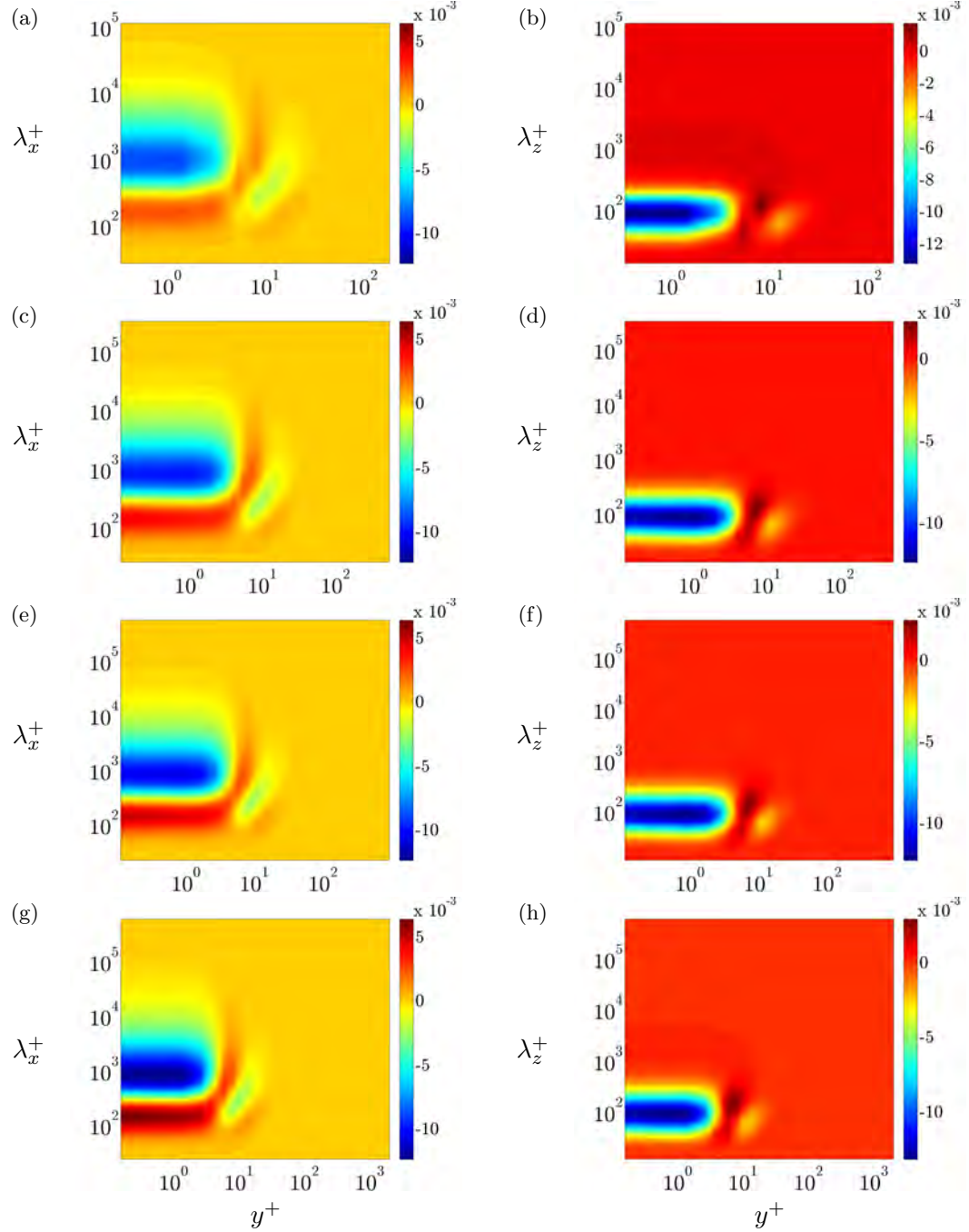


Figure 11.5: Premultiplied second-order correction to the dissipation of kinetic energy in turbulent channel flow subject to spanwise wall oscillations with period  $T^+ = 100$ ;  $k_x \epsilon_2(y, k_x)/R_\tau^2$  (left) and  $k_z \epsilon_2(y, k_z)/R_\tau^2$  (right). (a, b)  $R_\tau = 186$ , (c, d)  $R_\tau = 547$ , (e, f)  $R_\tau = 934$ , and (g, h)  $R_\tau = 2003$ .

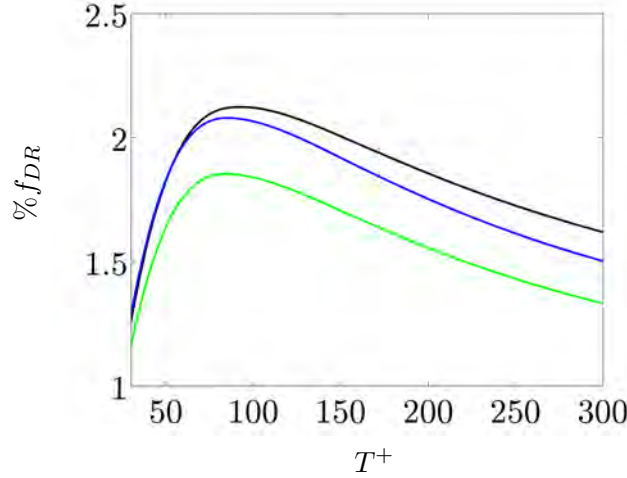


Figure 11.6: Turbulent drag reduction normalized by  $\alpha^2$  at  $R_\tau = 934$  (black),  $R_\tau = 2003$  (blue), and  $R_\tau = 4000$  (green) in terms of period of oscillations  $T^+$ .

**Remark 5.** Given the spectrum of turbulent kinetic energy  $k_0$  of the uncontrolled flow from DNS, and the turbulent kinetic energy  $\nu_{T0}$  from (11.6), the second-order correction to the turbulent viscosity  $\nu_{T2}$  and skin-friction drag  $C_{f,2}$  (cf. equations (11.9) and (11.11)) can be predicted at higher Reynolds numbers based on the spectra of  $k_2$  and  $\epsilon_2/R_\tau^2$  at lower Reynolds numbers.

Figure 11.6 shows the percentage of drag reduction normalized by  $\alpha^2$  for various Reynolds numbers

$$\%f_{DR} = -100 C_{f,2},$$

where  $C_{f,2}$  is computed from equation (11.11). We have used  $k_2$  and  $\epsilon_2/R_\tau^2$  from the model-based analysis conducted at  $R_\tau = 2003$  to predict drag reduction at  $R_\tau = 4000$ . In addition, we have used the turbulent kinetic energy  $k_0$  from DNS of turbulent channel flow<sup>2</sup> with  $R_\tau = 4000$  and used equation (11.6) for  $\nu_{T0}$ . It is clear that the ability of wall oscillations to reduce skin-friction drag in the turbulent channel flow reduces as the Reynolds number is increased. This is in agreement with DNS studies that have confirmed deterioration in drag reduction as the friction Reynolds number increases [302–304, 317]. Figure 11.6 also shows that the optimal period of oscillations  $T^+$  slightly decreases in higher Reynolds number flows. Therefore, as  $R_\tau$  increases, optimal drag reduction is obtained by wall oscillation with larger frequency.

<sup>2</sup>The DNS-based kinetic energy is taken from <http://torroja.dmt.upm.es/ftp/channels/data/> and interpolated in the wall-normal direction.

The deterioration in drag reduction as Reynolds number increases, can be explained by experimental and computational observations. As previously reported in experiments [301], and confirmed by the analysis of [33], wall oscillations reduce the spatial spread and magnitude of the dominant characteristic eddies and suppress the spanwise vorticity in the viscous sublayer. However, as the Reynolds number increases, the role of longer (and wider) eddy structures that lie farther away from the wall (in the logarithmic region) becomes more prominent in the production of kinetic energy; cf. figure 11.3. Similarly, the results of Section 11.3.2 showed that as the Reynolds number increases, the effect of control on the production and dissipation of kinetic energy is confined to a certain range of wavelengths that lie in the close proximity of the wall ( $y^+ < 100$ ). Furthermore, figures 11.4 and 11.5 show that at higher Reynolds numbers, corrections to the spectrum of turbulent kinetic energy and its dissipation due to the effect of control at the level of  $\alpha^2$  become more concentrated.

## Chapter 12

# Conclusions and future directions

### Conclusions

In Chapter 10, we have developed a model-based framework to design streamwise traveling waves for drag reduction in a turbulent channel flow. Our approach consists of two steps: (1) we use the turbulent viscosity of the uncontrolled flow to approximate the influence of control on the turbulent mean velocity; and (2) we use second-order statistics of stochastically forced equations linearized around this mean profile to examine the influence of velocity fluctuations on the turbulent viscosity and skin-friction drag. We demonstrate that the mean flow analysis alone is not capable of capturing the essential drag-reducing trends of streamwise traveling waves. In order to improve the quality of predictions, we need to incorporate the influence of fluctuations on the turbulent viscosity and skin-friction drag. For an upstream traveling wave with  $c = -2$  and  $\omega_x = 0.5$  we have employed perturbation analysis in the traveling wave amplitude to demonstrate that analysis of dynamics can reduce the gap between theoretical predictions and results of high-fidelity numerical simulations. Moreover, we have demonstrated the ability of our model-based framework in capturing the sub-laminar drag observed in the DNS of turbulent channel flow subject to upstream traveling waves of amplitude 0.25 ( $\alpha = 0.125$ ).

In Chapter 11, we have utilized a previously developed model-based framework for the design of spanwise wall oscillations to examine the efficacy of this control strategy at high Reynolds numbers. For this, we have used perturbation analysis to show that the influence of control on the production and dissipation of kinetic energy is confined to a range of wavelengths that correspond to the universal inner-scaled eddies. These energetic structures typically lie within the inner layer of the flow. Given the mean profiles of the streamwise, wall-normal, and spanwise intensities (or the turbulent kinetic energy) from DNS, these observations allow us to predict the drag reducing capability of spanwise wall oscillations at higher Reynolds numbers. In particular, we are able to

capture the deterioration in drag reduction as the friction Reynolds number increases.

## Extensions and future directions

**Stochastic modeling for the purpose of control design.** Despite initial successes of model-based feedback [106, 318–323] and sensor-free [33, 107–109, 324] control at low Reynolds numbers in wall-bounded flows, many important challenges remain. One source of the problem is that, typically, sensing and actuation of the flow field is restricted to the surface of the domain. Thus, this limited actuation needs to rely on estimation of the flow field based on available noisy measurements of wall-shear stresses and pressure. The importance of modeling the statistics of flow disturbances for obtaining well-behaved estimation gains has been previously recognized [325, 326]. However, these initial studies, rely on assumptions on flow disturbances, e.g., whiteness-in-time, which often fail to hold in turbulent flows. In this vein, the colored-in-time stochastic modeling approach of Chapter 7 demonstrates that by departing from the white-in-time restriction on stochastic excitations, turbulent flow statistics can be matched by linearized NS equations. This methodology fits nicely into a Kalman filter estimation framework for turbulent flows and has the potential to open the door for a successful feedback control design at higher Reynolds numbers.

Another aspect which remains to be studied is the possibility to improve predictions from our model-based framework by incorporating higher-order corrections to the turbulent viscosity. This can be effectively thought of as closing the loop in the simulation-free approach presented in [33]; see Figure 12.1. In this, higher-order corrections are fed back into the RANS model for the mean velocity which subsequently modifies the linearized flow dynamics. This closed-loop methodology in conjunction with appropriate stochastic noise modeling for higher-order statistics can potentially improve predictions of skin-friction drag, which is critically important in model-based flow control design. The development of the appropriate computational framework for these purposes is a topic of future research.

**Numerical simulations.** Direct numerical simulations play a critical role in verifying our simulation-free predictions. While many numerical studies have examined the drag reducing effects of wall oscillations in turbulent boundary layers, channels and pipes [291, 303, 317, 327–330], our recent efforts to predict skin-friction drag reduction at higher Reynold numbers call for additional efforts in this direction.

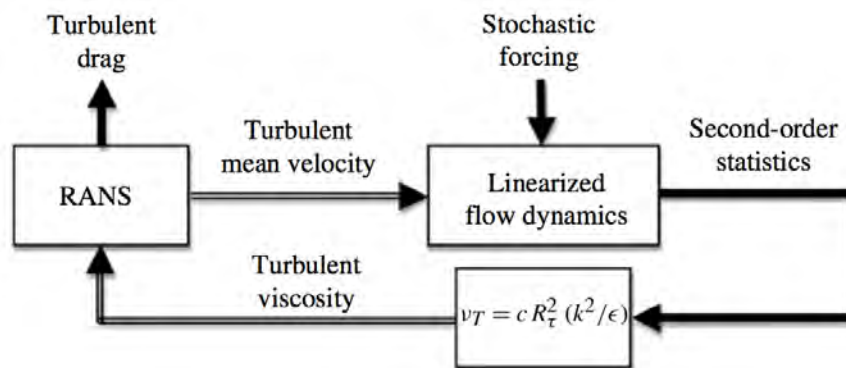


Figure 12.1: Block diagram representing the various steps involved in the simulation-free approach for determining the effect of control on skin-friction drag in turbulent flows; figure taken from [33].

# References

- [1] M. Gad-el Hak. *Flow control: passive, active, and reactive flow management*. Cambridge Univ. Press, New York, 2000.
- [2] R. D. Joslin. Aircraft laminar flow control. *Annu. Rev. Fluid Mech.*, 30:1–29, 1998.
- [3] P. Moin and J. Kim. Tackling turbulence with supercomputers. *Scient. Amer*, 276(1):46–52, 1997.
- [4] M. Matsubara and P. H. Alfredsson. Disturbance growth in boundary layers subjected to free-stream turbulence. *J. Fluid Mech.*, 430:149–168, 2001.
- [5] J. Slotnick, A. Khodadoust, J. Alonso, D. Darmofal, W. Gropp, E. Lurie, and D. Mavriplis. Cfd vision 2030 study: A path to revolutionary computational aerosciences. *Tech. Rep. CR-2014-218178*, NASA, 2014.
- [6] D. C. Wilcox. *Turbulence modeling for CFD*. La Canada, CA: DCW Ind., 1998.
- [7] S. K. Robinson. Coherent motions in the turbulent boundary layer. *Annu. Rev. Fluid Mech.*, 23(1):601–639, 1991.
- [8] R. J. Adrian. Hairpin vortex organization in wall turbulence. *Phys. Fluids*, 19(4):041301, 2007.
- [9] A. J. Smits, B. J. McKeon, and I. Marusic. High-Reynolds number wall turbulence. *Annu. Rev. Fluid Mech.*, 43:353–375, 2011.
- [10] L. Sirovich. Turbulence and the dynamics of coherent structures. Part I: Coherent structures. *Quart. Appl. Math.*, 45:561–571, 1987.
- [11] G. Berkoo, P. Holmes, and J. L. Lumley. The proper orthogonal decomposition in the analysis of turbulent flows. *Annu. Rev. Fluid Mech.*, 25(1):539–575, 1993.
- [12] J. L. Lumley. *Stochastic Tools in Turbulence*. Dover Publications, 2007.
- [13] C. W. Rowley. Model reduction for fluids using balanced proper orthogonal decomposition. *Intl J. Bifurcation Chaos*, 15(3):997–1013, 2005.

- [14] M. Ilak and C. W. Rowley. Modeling of transitional channel flow using balanced proper orthogonal decomposition. *Phys. Fluids*, 20(3):034103, 2008.
- [15] I. Mezić. Spectral properties of dynamical systems, model reduction and decompositions. *Nonlinear Dyn.*, 41:309–325, 2005.
- [16] C. W. Rowley, I. Mezić, S. Bagheri, P. Schlatter, and D. S. Henningson. Spectral analysis of nonlinear flows. *J. Fluid Mech.*, 641:115–127, 2009.
- [17] I. Mezić. Analysis of fluid flows via spectral properties of Koopman operator. *Annu. Rev. Fluid Mech.*, 45(1):357–378, 2013.
- [18] S. Bagheri. Koopman-mode decomposition of the cylinder wake. *J. Fluid Mech.*, 726:596–623, 2013.
- [19] P. J. Schmid. Dynamic mode decomposition of numerical and experimental data. *J. Fluid Mech.*, 656:5–28, 2010.
- [20] K. K. Chen, J. H. Tu, and C. W. Rowley. Variants of dynamic mode decomposition: boundary condition, Koopman, and Fourier analyses. *J. Nonlinear Sci.*, 22(6):887–915, 2012.
- [21] M. R. Jovanović, P. J. Schmid, and J. W. Nichols. Sparsity-promoting dynamic mode decomposition. *Phys. Fluids*, 26(2):024103, 2014.
- [22] P. Holmes, J. L. Lumley, and G. Berkooz. *Turbulence, coherent structures, dynamical systems and symmetry*. Cambridge Univ. Press, 1998.
- [23] B. R. Noack, K. Afanasiev, M. Morzyński, G. Tadmor, and F. Thiele. A hierarchy of low-dimensional models for the transient and post-transient cylinder wake. *J. Fluid Mech.*, 497:335–363, 2003.
- [24] B. R. Noack, P. Papas, and P. A. Monkewitz. The need for a pressure-term representation in empirical Galerkin models of incompressible shear flows. *J. Fluid Mech.*, 523:339–365, 2005.
- [25] G. Tadmor, O. Lehmann, B. R. Noack, and M. Morzyński. Mean field representation of the natural and actuated cylinder wake. *Phys. Fluids*, 22:034102, 2010.
- [26] B. R. Noack, M. Morzyński, and G. Tadmor. *Reduced-order modelling for flow control*, volume 528 of *CISM Courses and Lectures*. Springer, 2011.
- [27] G. Tadmor and B. R. Noack. Bernoulli, Bode, and Budgie [Ask the Experts]. *IEEE Contr. Syst. Mag.*, 31(2):18–23, 2011.
- [28] B. F. Farrell and P. J. Ioannou. Stochastic forcing of the linearized Navier-Stokes equations. *Phys. Fluids A*, 5(11):2600–2609, 1993.

- [29] B. Bamieh and M. Dahleh. Energy amplification in channel flows with stochastic excitation. *Phys. Fluids*, 13(11):3258–3269, 2001.
- [30] M. R. Jovanović and B. Bamieh. Componentwise energy amplification in channel flows. *J. Fluid Mech.*, 534:145–183, 2005.
- [31] Y. Hwang and C. Cossu. Amplification of coherent streaks in the turbulent Couette flow: an input-output analysis at low Reynolds number. *J. Fluid Mech.*, 643:333–348, 2010.
- [32] Y. Hwang and C. Cossu. Linear non-normal energy amplification of harmonic and stochastic forcing in the turbulent channel flow. *J. Fluid Mech.*, 664:51–73, 2010.
- [33] R. Moarref and M. R. Jovanović. Model-based design of transverse wall oscillations for turbulent drag reduction. *J. Fluid Mech.*, 707:205–240, 2012.
- [34] A. Zare, M. R. Jovanović, and T. T. Georgiou. Color of turbulence. *J. Fluid Mech.*, 2016. doi:10.1017/jfm.2016.682; also arXiv:1602.05105.
- [35] W. Ran, A. Zare, M. J. P. Hack, and M. R. Jovanović. Low-complexity stochastic modeling of spatially-evolving flows. In *Proceedings of the 2016 Summer Program*, Center for Turbulence Research, Stanford University/NASA, 2016. To appear.
- [36] N. Hoda, M. R. Jovanović, and S. Kumar. Energy amplification in channel flows of viscoelastic fluids. *J. Fluid Mech.*, 601:407–424, April 2008.
- [37] N. Hoda, M. R. Jovanović, and S. Kumar. Frequency responses of streamwise-constant perturbations in channel flows of oldroyd-b fluids. *J. Fluid Mech.*, 625:411–434, April 2009.
- [38] M. R. Jovanović and S. Kumar. Transient growth without inertia. *Phys. Fluids*, 22(2):023101, February 2010.
- [39] M. R. Jovanović and S. Kumar. Nonmodal amplification of stochastic disturbances in strongly elastic channel flows. *J. Non-Newtonian Fluid Mech.*, 166(14-15):755–778, August 2011.
- [40] B. K. Lieu, M. R. Jovanović, and S. Kumar. Worst-case amplification of disturbances in inertialess couette flow of viscoelastic fluids. *J. Fluid Mech.*, 723:232–263, May 2013.
- [41] G. Gallino, L. Zhu, and F. Gallaire. The stability of a rising droplet: an inertialess non-modal growth mechanism. *J. Fluid Mech.*, 786, 2016.
- [42] J. Jeun, J. W. Nichols, and M. R. Jovanović. Input-output analysis of high-speed axisymmetric isothermal jet noise. *Phys. Fluids*, 28(4):047101, 2016.

- [43] R. Bell, J. Bennett, Y. Koren, and C. Volinsky. The million dollar programming prize. *IEEE Spectrum*, 5(46):28–33, 2009.
- [44] Y. Koren, R. Bell, and C. Volinsky. Matrix factorization techniques for recommender systems. *IEEE Computer*, 42(8):30–37, 2009.
- [45] E. J. Candès and B. Recht. Exact matrix completion via convex optimization. *Found. Comput. Math.*, 9(6):717–772, 2009.
- [46] E. J. Candès and T. Tao. The power of convex relaxation: Near-optimal matrix completion. *IEEE Trans. Inform. Theory*, 56(5):2053–2080, 2010.
- [47] D. Gross. Recovering low-rank matrices from few coefficients in any basis. *IEEE Trans. Inform. Theory*, 57(3):1548–1566, 2011.
- [48] B. Recht. A simpler approach to matrix completion. *J. Mach. Learn. Res*, 12:3413–3430, 2011.
- [49] A. M.-C. So and Y. Ye. Theory of semidefinite programming for sensor network localization. *Math. Program.*, 109(2-3):367–384, 2007.
- [50] A. Singer. A remark on global positioning from local distances. *Proc. Natl. Acad. Sci. USA*, 105(28):9507–9511, 2008.
- [51] A. Javanmard and A. Montanari. Localization from incomplete noisy distance measurements. *Found. Comput. Math.*, 13(3):297–345, 2013.
- [52] E. J. Candès, Y. C. Eldar, T. Strohmer, and V. Voroninski. Phase retrieval via matrix completion. *SIAM Rev.*, 57(2):225–251, 2015.
- [53] M. Fazel, H. Hindi, and S. P. Boyd. Log-det heuristic for matrix rank minimization with applications to Hankel and Euclidean distance matrices. In *Proceedings of the 2003 American Control Conference*, volume 3, pages 2156–2162, 2003.
- [54] Z. Liu, A. Hansson, and L. Vandenberghe. Nuclear norm system identification with missing inputs and outputs. *Syst. Control Lett.*, 62(8):605–612, 2013.
- [55] C. Tomasi and T. Kanade. Shape and motion from image streams under orthography: a factorization method. *Int. J. Comput. Vision.*, 9(2):137–154, 1992.
- [56] P. Chen and D. Suter. Recovering the missing components in a large noisy low-rank matrix: Application to SFM. *IEEE Trans. Pattern Anal. Mach. Intell.*, 26(8):1051–1063, 2004.
- [57] Y. Amit, M. Fink, N. Srebro, and S. Ullman. Uncovering shared structures in multiclass classification. In *Proceedings of the 24th international conference on Machine learning*, pages 17–24. ACM, 2007.
- [58] A. Evgeniou and M. Pontil. Multi-task feature learning. *NIPS*, 19:41, 2007.

- [59] Y. Chen and Y. Chi. Spectral Compressed Sensing via Structured Matrix Completion. In *ICML (3)*, pages 414–422, 2013.
- [60] E. J. Candès and Y. Plan. Matrix completion with noise. *Proc. IEEE*, 98(6):925–936, 2010.
- [61] R. H. Keshavan. *Efficient algorithms for collaborative filtering*. PhD thesis, Stanford University, 2012.
- [62] E. J. Candès, X. Li, Y. Ma, and J. Wright. Robust principal component analysis? *J. ACM*, 58(3):11, 2011.
- [63] Y. Peng, A. Ganesh, J. Wright, W. Xu, and Y. Ma. RASL: robust alignment by sparse and low-rank decomposition for linearly correlated images. *IEEE Trans. Pattern Anal. Mach. Intell.*, 34(11):2233–2246, 2012.
- [64] M. Mardani, G. Mateos, and G. B. Giannakis. Recovery of low-rank plus compressed sparse matrices with application to unveiling traffic anomalies. *IEEE Trans. Info. Th.*, 59(8):5186–5205, 2013.
- [65] R. Otazo, E. J. Candès, and D. K. Sodickson. Low-rank plus sparse matrix decomposition for accelerated dynamic MRI with separation of background and dynamic components. *Magn. Reson. Med.*, 73(3):1125–1136, 2015.
- [66] D. D. Lee and H. S. Seung. Algorithms for non-negative matrix factorization. *NIPS*, pages 556–562, 2001.
- [67] S. Gandy, B. Recht, and I. Yamada. Tensor completion and low-n-rank tensor recovery via convex optimization. *Inverse Problems*, 27(2):025010, 2011.
- [68] C. Mu, B. Huang, J. Wright, and D. Goldfarb. Square Deal: Lower Bounds and Improved Relaxations for Tensor Recovery. In *ICML*, pages 73–81, 2014.
- [69] S. Negahban and M. J. Wainwright. Restricted strong convexity and weighted matrix completion: Optimal bounds with noise. *J. Mach. Learn. Res.*, 13(May):1665–1697, 2012.
- [70] R. Keshavan, A. Montanari, and S. Oh. Matrix completion from a few entries. *IEEE Trans. on Inform. Theory*, 56(6):2980–2998, 2010.
- [71] R. Sun and Z.-Q. Luo. Guaranteed matrix completion via nonconvex factorization. In *Foundations of Computer Science (FOCS), 2015 IEEE 56th Annual Symposium on*, pages 270–289, 2015.
- [72] M. Fazel. *Matrix rank minimization with applications*. PhD thesis, Stanford University, 2002.

- [73] B. Recht, M. Fazel, and P. A. Parrilo. Guaranteed minimum-rank solutions of linear matrix equations via nuclear norm minimization. *SIAM Rev.*, 52(3):471–501, 2010.
- [74] J.-F. Cai, E. J. Candès, and Z. Shen. A singular value thresholding algorithm for matrix completion. *SIAM J. Optim.*, 20(4):1956–1982, 2010.
- [75] K.-C. Toh and S. Yun. An accelerated proximal gradient algorithm for nuclear norm regularized linear least squares problems. *Pacific J. Optimization*, 6(615–640):15, 2010.
- [76] S. Ma, D. Goldfarb, and L. Chen. Fixed point and Bregman iterative methods for matrix rank minimization. *Math. Program.*, 128(1-2):321–353, 2011.
- [77] A. Agarwal, S. Negahban, and M. J. Wainwright. Fast global convergence rates of gradient methods for high-dimensional statistical recovery. *NIPS*, pages 37–45, 2010.
- [78] K. Hou, Z. Zhou, A. M.-C. So, and Z.-Q. Luo. On the linear convergence of the proximal gradient method for trace norm regularization. *NIPS*, pages 710–718, 2013.
- [79] C. Grussler and A. Rantzer. On optimal low-rank approximation of non-negative matrices. In *Proceedings of the 54th IEEE Conference on Decision and Control*, pages 5278–5283, 2015.
- [80] X. V. Doan and S. Vavasis. Finding the largest low-rank clusters with Ky Fan 2-k-norm and  $\ell_1$ -norm. *SIAM J. Optim.*, 26(1):274–312, 2016.
- [81] A. M. McDonald, M. Pontil, and D. Stamos. New Perspectives on  $k$ -Support and Cluster Norms. *arXiv preprint arXiv:1512.08204*, 2015.
- [82] A. Argyriou, R. Foygel, and N. Srebro. Sparse prediction with the  $k$ -support norm. *NIPS*, pages 1466–1474, 2012.
- [83] A. Eriksson, T. Thanh Pham, T.-J. Chin, and I. Reid. The  $k$ -support norm and convex envelopes of cardinality and rank. In *Proceedings of the IEEE Conference on Computer Vision and Pattern Recognition*, pages 3349–3357, 2015.
- [84] H. Lai, Y. Pan, C. Lu, Y. Tang, and S. Yan. Efficient  $k$ -support matrix pursuit. In *Computer Vision–ECCV 2014*, pages 617–631. Springer, 2014.
- [85] C. Grussler, A. Rantzer, and P. Giselsson. Low-rank Optimization with Convex Constraints. *arXiv preprint arXiv:1606.01793*, 2016.
- [86] C. Grussler and P. Giselsson. Low-Rank Inducing Norms with Optimality Interpretations. *arXiv preprint arXiv:1612.03186*, 2016.

- [87] C. Grussler, A. Zare, M. R. Jovanović, and A. Rantzer. The use of the  $r^*$  heuristic in covariance completion problems. In *Proceedings of the 55th IEEE Conference on Decision and Control*, pages 1978–1983, 2016.
- [88] R. Salakhutdinov and A. Mnih. Probabilistic matrix factorization. *NIPS*, pages 1257–1264, 2007.
- [89] I. Pilászy, D. Zibriczky, and D. Tikk. Fast ALS-based Matrix Factorization for Explicit and Implicit Feedback Datasets. In *Proceedings of the fourth ACM conference on Recommender systems*, pages 71–78. ACM, 2010.
- [90] H.-F. Yu, C.-J. Hsieh, S. Si, and I. Dhillon. Scalable coordinate descent approaches to parallel matrix factorization for recommender systems. In *2012 IEEE 12th International Conference on Data Mining*, pages 765–774, 2012.
- [91] A. Paterek. Improving regularized singular value decomposition for collaborative filtering. In *Proceedings of KDD cup and workshop*, volume 2007, pages 5–8, 2007.
- [92] R. Gemulla, E. Nijkamp, P. J. Haas, and Y. Sismanis. Large-scale matrix factorization with distributed stochastic gradient descent. In *Proceedings of the 17th ACM SIGKDD international conference on Knowledge discovery and data mining*, pages 69–77. ACM, 2011.
- [93] B. Recht and C. Ré. Parallel stochastic gradient algorithms for large-scale matrix completion. *Math. Program. Comput.*, 5(2):201–226, 2013.
- [94] Y. Zhuang, W.-S. Chin, Y.-C. Juan, and C.-J. Lin. A fast parallel SGD for matrix factorization in shared memory systems. In *Proceedings of the 7th ACM conference on Recommender systems*, pages 249–256. ACM, 2013.
- [95] R. Sun. *Matrix Completion via Nonconvex Factorization: Algorithms and Theory*. PhD thesis, University of Minnesota, 2015.
- [96] T. Yoshino, Y. Suzuki, and N. Kasagi. Drag reduction of turbulence air channel flow with distributed micro sensors and actuators. *J. Fluid Sci. Tech.*, 3(1):137–148, 2008.
- [97] C.-M. Ho and Y.-C. Tai. Review: MEMS and its applications for flow control. *J. Fluids Eng.*, 118:437447, 1996.
- [98] C.-M. Ho and Y.-C. Tai. Micro-electro-mechanical-systems (MEMS) and fluid flows. *Annu. Rev. Fluid Mech.*, 30:579–612, 1998.
- [99] N. Kasagi, Y. Suzuki, and K. Fukagata. Microelectromechanical systems-based feedback control of turbulence for skin friction reduction. *Annu. Rev. Fluid Mech.*, 41:231–251, 2009.

- [100] G. Karniadakis and K.-S. Choi. Mechanisms on transverse motions in turbulent wall flows. *Annu. Rev. Fluid Mech.*, 35:45–62, 2003.
- [101] D. M. Bushnell and K. J. Moore. Drag reduction in nature. *Annu. Rev. Fluid Mech.*, 23:65–79, 1991.
- [102] M. J. Walsh. Riblets as a viscous drag reduction technique. *AIAA J.*, 21(4):485–486, 1983.
- [103] J. P. Rothstein. Slip on superhydrophobic surfaces. *Annu. Rev. Fluid Mech.*, 42:89–109, 2010.
- [104] F. E. Fish and G. V. Lauder. Passive and active flow control by swimming fishes and mammals. *Annual Review of Fluid Mechanics*, 38:193–224, 2006.
- [105] E. Coustols and A. M. Savill. Resume of important results presented at the third turbulent drag reduction working party. *App. Sci. Res.*, 46(3):183–196, 1989.
- [106] J. Kim and T. R. Bewley. A linear systems approach to flow control. *Annu. Rev. Fluid Mech.*, 39:383–417, 2007.
- [107] M. R. Jovanović. Turbulence suppression in channel flows by small amplitude transverse wall oscillations. *Phys. Fluids*, 20(1):014101, 2008.
- [108] R. Moarref and M. R. Jovanović. Controlling the onset of turbulence by streamwise traveling waves. part 1: Receptivity analysis. *J. Fluid Mech.*, 663:70–99, 2010.
- [109] B. K. Lieu, R. Moarref, and M. R. Jovanović. Controlling the onset of turbulence by streamwise traveling waves. part 2: Direct numerical simulations. *J. Fluid Mech.*, 663:100–119, 2010.
- [110] A. Zare, B. K. Lieu, and M. R. Jovanović. Turbulent drag reduction by streamwise traveling waves. In *Proceedings of the 51st IEEE Conference on Decision and Control*, pages 3122–3126, 2012.
- [111] M. R. Jovanović and B. Bamieh. The spatio-temporal impulse response of the linearized navier-stokes equations. In *Proceedings of the 2001 American Control Conference*, pages 1948–1953, 2001.
- [112] M. R. Jovanović. *Modeling, analysis, and control of spatially distributed systems*. PhD thesis, University of California, Santa Barbara, 2004.
- [113] M. R. Jovanović and B. Bamieh. Modelling flow statistics using the linearized navier-stokes equations. In *Proceedings of the 40th IEEE Conference on Decision and Control*, pages 4944–4949, 2001.

- [114] M. R. Jovanović and T. T. Georgiou. Reproducing second order statistics of turbulent flows using linearized Navier-Stokes equations with forcing. In *Bulletin of the American Physical Society*, November 2010.
- [115] M. Fazel, H. Hindi, and S. Boyd. A rank minimization heuristic with application to minimum order system approximation. In *Proceedings of the 2001 American Control Conference*, pages 4734–4739, 2001.
- [116] V. Chandrasekaran, S. Sanghavi, P. A. Parrilo, and A. S. Willsky. Rank-sparsity incoherence for matrix decomposition. *SIAM J. Optim.*, 21(2):572–596, 2011.
- [117] R. E. Kalman. *Realization of covariance sequences*. Birkhäuser Basel, 1982.
- [118] T. T. Georgiou. *Partial realization of covariance sequences*. PhD thesis, University of Florida, 1983.
- [119] T. T. Georgiou. Realization of power spectra from partial covariance sequences. *IEEE Trans. Acoust. Speech Signal Processing*, 35(4):438–449, 1987.
- [120] C. I. Byrnes and A. Lindquist. Toward a solution of the minimal partial stochastic realization problem. *Comptes rendus de l'Académie des sciences. Série 1, Mathématique*, 319(11):1231–1236, 1994.
- [121] T. T. Georgiou. The structure of state covariances and its relation to the power spectrum of the input. *IEEE Trans. Autom. Control*, 47(7):1056–1066, 2002.
- [122] T. T. Georgiou. Spectral analysis based on the state covariance: the maximum entropy spectrum and linear fractional parametrization. *IEEE Trans. Autom. Control*, 47(11):1811–1823, 2002.
- [123] A. Hotz and R. E. Skelton. Covariance control theory. *Int. J. Control*, 46(1):13–32, 1987.
- [124] Y. Chen, T. T. Georgiou, and M. Pavon. Optimal steering of a linear stochastic system to a final probability distribution, Part II. *IEEE Trans. Automat. Control*, 61(5):1170–1180, 2016.
- [125] P. Dai Pra. A stochastic control approach to reciprocal diffusion processes. *Appl. Math. Opt.*, 23(1):313–329, 1991.
- [126] Y. Chen, T. T. Georgiou, and M. Pavon. Optimal steering of a linear stochastic system to a final probability distribution, Part I. *IEEE Trans. Automat. Control*, 61(5):1158–1169, 2016.
- [127] Y. Chen, T. T. Georgiou, and M. Pavon. Fast cooling for a system of stochastic oscillators. *J. Math. Phys.*, 56(11):113302, 2015.

- [128] O. Taussky. A generalization of a theorem of Lyapunov. *SIAM J. Appl. Math.*, 9(4):640–643, 1961.
- [129] A. Ostrowski and H. Schneider. Some theorems on the inertia of general matrices. *J. Math. Anal. Appl.*, 4(1):72–84, 1962.
- [130] L. M. DeAlba and C. R. Johnson. Possible inertia combinations in the Stein and Lyapunov equations. *Lin. Alg. Appl.*, 222:227–240, 1995.
- [131] F. C. Silva and R. Simões. On the Lyapunov and Stein equations. *Lin. Alg. Appl.*, 420(2):329–338, 2007.
- [132] C.-T. Chen. *Linear system theory and design*. Oxford Univ. Press, 1995.
- [133] R. A. Horn and C. R. Johnson. *Matrix Analysis*. Cambridge Univ. Press, 1990.
- [134] M. Grant and S. Boyd. CVX: Matlab software for disciplined convex programming, version 2.1. <http://cvxr.com/cvx>, March 2014.
- [135] S. Boyd and L. Vandenberghe. *Convex optimization*. Cambridge Univ. Press, 2004.
- [136] F. Lin, M. R. Jovanović, and T. T. Georgiou. An admm algorithm for matrix completion of partially known state covariances. In *Proceedings of the 52nd IEEE Conference on Decision and Control*, pages 1684–1689, 2013.
- [137] A. Zare, M. R. Jovanović, and T. T. Georgiou. Completion of partially known turbulent flow statistics. In *Proceedings of the 2014 American Control Conference*, pages 1680–1685, 2014.
- [138] P. Tseng. Applications of a splitting algorithm to decomposition in convex programming and variational inequalities. *SIAM J. Control Optim.*, 29(1):119–138, 1991.
- [139] T. Goldstein, B. O’Donoghue, S. Setzer, and R. Baraniuk. Fast alternating direction optimization methods. *SIAM J. Imaging Sci.*, 7(3):1588–1623, 2014.
- [140] O. A. Dalal and B. Rajaratnam. G-AMA: Sparse Gaussian graphical model estimation via alternating minimization. *arXiv preprint arXiv:1405.3034*, 2014.
- [141] M. Tao and X. Yuan. Recovering low-rank and sparse components of matrices from incomplete and noisy observations. *SIAM J. Optim.*, 21(1):57–81, 2011.
- [142] X. Yuan. Alternating direction method for covariance selection models. *J. Sci. Comput.*, 51(2):261–273, 2012.
- [143] T. Goldstein and S. Osher. The split Bregman method for  $\ell_1$ -regularized problems. *SIAM J. Imaging Sci.*, 2(2):323–343, 2009.

- [144] F. Lin, M. Fardad, and M. R. Jovanović. Sparse feedback synthesis via the alternating direction method of multipliers. In *Proceedings of the 2012 American Control Conference*, pages 4765–4770, 2012.
- [145] F. Lin, M. Fardad, and M. R. Jovanović. Design of optimal sparse feedback gains via the alternating direction method of multipliers. *IEEE Trans. Automat. Control*, 58(9):2426–2431, 2013.
- [146] M. R. Jovanović and N. K. Dhingra. Controller architectures: tradeoffs between performance and structure. *Eur. J. Control*, 30:76–91, July 2016.
- [147] M. Ayazoglu and M. Sznaier. An algorithm for fast constrained nuclear norm minimization and applications to systems identification. In *Proceedings of the 51th IEEE Conference on Decision and Control*, pages 3469–3475, 2012.
- [148] A. Hansson, Z. Liu, and L. Vandenberghe. Subspace system identification via weighted nuclear norm optimization. In *Proceedings of the 51st IEEE Conference on Decision and Control*, pages 3439–3444, 2012.
- [149] Z. Wen, D. Goldfarb, and W. Yin. Alternating direction augmented Lagrangian methods for semidefinite programming. *Math. Program. Comp.*, 2(3-4):203–230, 2010.
- [150] S. Boyd, N. Parikh, E. Chu, B. Peleato, and J. Eckstein. Distributed optimization and statistical learning via the alternating direction method of multipliers. *Found. Trends Mach. Learn.*, 3(1):1–122, 2011.
- [151] B. O’Donoghue, E. Chu, N. Parikh, and S. Boyd. Operator splitting for conic optimization via homogeneous self-dual embedding. *arXiv preprint arXiv:1312.3039*, 2013.
- [152] O. Banerjee, L. E. Ghaoui, and A. d’Aspremont. Model selection through sparse maximum likelihood estimation for multivariate gaussian or binary data. *J. Mach. Learn. Res.*, 9:485–516, 2008.
- [153] J. Barzilai and J. M. Borwein. Two-point step size gradient methods. *IMA J. Numer. Anal.*, 8(1):141–148, 1988.
- [154] N. Parikh and S. Boyd. Proximal algorithms. *Found. Trends Optim.*, 1(3):123–231, 2013.
- [155] P. L. Combettes and V. R. Wajs. Signal recovery by proximal forward-backward splitting. *Multiscale Model. Simul.*, 4(4):1168–1200, 2005.
- [156] D. R. Hunter and K. Lange. A tutorial on mm algorithms. *The American Statistician*, 58(1):30–37, 2004.

- [157] G. H. G. Chen and R. T. Rockafellar. Convergence rates in forward-backward splitting. *SIAM J. Optim.*, 7(2):421–444, 1997.
- [158] Y. Nesterov. Gradient methods for minimizing composite objective function. In *CORE discussion papers*, Universit e catholique de Louvain, Center for Operations Research and Econometrics (CORE), 2007.
- [159] B. O’Donoghue and E. Candès. Adaptive restart for accelerated gradient schemes. *Found. Comput. Math.*, pages 1–18, 2013.
- [160] A. Zare, M. R. Jovanović, and T. T. Georgiou. Alternating direction optimization algorithms for covariance completion problems. In *Proceedings of the 2015 American Control Conference*, pages 515–520, 2015.
- [161] F. Lin and M. R. Jovanović. Least-squares approximation of structured covariances. *IEEE Trans. Automat. Control*, 54(7):1643–1648, 2009.
- [162] A. Ferrante, M. Pavon, and M. Zorzi. A maximum entropy enhancement for a family of high-resolution spectral estimators. *IEEE Trans. Automat. Control*, 57(2):318–329, 2012.
- [163] M. Zorzi and A. Ferrante. On the estimation of structured covariance matrices. *Automatica*, 48(9):2145–2151, 2012.
- [164] A. Zare, Y. Chen, M. R. Jovanović, and T. T. Georgiou. Low-complexity modeling of partially available second-order statistics: theory and an efficient matrix completion algorithm. *IEEE Trans. Automat. Control*, 2016. doi:10.1109/TAC.2016.2595761; also arXiv:1412.3399.
- [165] Y. Chen, M. R. Jovanović, and T. T. Georgiou. State covariances and the matrix completion problem. In *Proceedings of the 52nd IEEE Conference on Decision and Control*, pages 1702–1707, 2013.
- [166] A. Zare, M. R. Jovanović, and T. T. Georgiou. Completion of partially known turbulent flow statistics via convex optimization. In *Proceedings of the 2014 Summer Program*, pages 345–354, Center for Turbulence Research, Stanford University/NASA, 2014.
- [167] C. Berge. *Topological Spaces: including a treatment of multi-valued functions, vector spaces, and convexity*. Courier Corporation, 1963.
- [168] B. Polyak, M. Khlebnikov, and P. Shcherbakov. An LMI approach to structured sparse feedback design in linear control systems. In *Proceedings of the 2013 European Control Conference*, pages 833–838, 2013.

- [169] N. K. Dhingra, M. R. Jovanović, and Z. Q. Luo. An admm algorithm for optimal sensor and actuator selection. In *Proceedings of the 53rd IEEE Conference on Decision and Control*, pages 4039–4044, 2014.
- [170] G. E. Dullerud and F. Paganini. *A course in robust control theory: a convex approach*. Springer-Verlag, New York, 2000.
- [171] E. J. Candès, M. B. Wakin, and S. P. Boyd. Enhancing sparsity by reweighted  $\ell_1$  minimization. *J. Fourier Anal. Appl.*, 14(5-6):877–905, 2008.
- [172] P. S. Klebanoff, K. D. Tidstrom, and L. M. Sargent. The three-dimensional nature of boundary-layer instability. *J. Fluid Mech.*, 12:1–34, 1962.
- [173] P. S. Klebanoff. Effect of free-stream turbulence on the laminar boundary layer. *Bull. Am. Phys. Soc.*, 16(11):1323, 1971.
- [174] B. G. B. Klingmann. On transition due to three-dimensional disturbances in plane Poiseuille flow. *J. Fluid Mech.*, 240:167–195, 1992.
- [175] K. J. A. Westin, A. V. Boiko, B. G. B. Klingmann, V. V. Kozlov, and P. H. Alfredsson. Experiments in a boundary layer subjected to free stream turbulence. Part 1. Boundary layer structure and receptivity. *J. Fluid Mech.*, 281:193–218, 1994.
- [176] L. H. Gustavsson. Energy growth of three-dimensional disturbances in plane Poiseuille flow. *J. Fluid Mech.*, 98:149, 1991.
- [177] K. M. Butler and B. F. Farrell. Three-dimensional optimal perturbations in viscous shear flow. *Phys. Fluids A*, 4(8):1637–1650, 1992.
- [178] S. C. Reddy and D. S. Henningson. Energy growth in viscous channel flows. *J. Fluid Mech.*, 252:209–238, 1993.
- [179] D. S. Henningson and S. C. Reddy. On the role of linear mechanisms in transition to turbulence. *Phys. Fluids*, 6(3):1396–1398, 1994.
- [180] P. J. Schmid and D. S. Henningson. Optimal energy density growth in Hagen-Poiseuille flow. *J. Fluid Mech.*, 277:197–225, 1994.
- [181] L. N. Trefethen, A. E. Trefethen, S. C. Reddy, and T. A. Driscoll. Hydrodynamic stability without eigenvalues. *Science*, 261:578–584, 1993.
- [182] B. F. Farrell and P. J. Ioannou. Perturbation growth in shear flow exhibits universality. *Phys. Fluids A*, 5(9):2298–2300, 1993.
- [183] P. J. Schmid. Nonmodal stability theory. *Annu. Rev. Fluid Mech.*, 39:129–162, 2007.

- [184] M. T. Landahl. Wave breakdown and turbulence. *SIAM J. Appl. Math.*, 28:735–756, 1975.
- [185] M. J. Lee, J. Kim, and P. Moin. Structure of turbulence at high shear rate. *J. Fluid Mech.*, 216:561–583, 1990.
- [186] S. B. Pope. *Turbulent flows*. Cambridge Univ. Press, 2000.
- [187] J. Kim and J. Lim. A linear process in wall-bounded turbulent shear flows. *Phys. Fluids*, 12(8):1885–1888, 2000.
- [188] S. I. Chernyshenko and M. F. Baig. The mechanism of streak formation in near-wall turbulence. *J. Fluid Mech.*, 544:99–131, 2005.
- [189] K. M. Butler and B. F. Farrell. Optimal perturbations and streak spacing in wall-bounded turbulent shear flow. *Phys. Fluids A*, 5(3):774–777, 1993.
- [190] B. F. Farrell and P. J. Ioannou. Optimal excitation of three-dimensional perturbations in viscous constant shear flow. *Phys. Fluids A*, 5(6):1390–1400, 1993.
- [191] B. F. Farrell and P. J. Ioannou. Perturbation structure and spectra in turbulent channel flow. *Theoret. Comput. Fluid Dynamics*, 11:237–250, 1998.
- [192] W. Schoppa and F. Hussain. Coherent structure generation in near-wall turbulence. *J. Fluid Mech.*, 453:57–108, 2002.
- [193] J. Hœpfner, L. Brandt, and D. S. Henningson. Transient growth on boundary layer streaks. *J. Fluid Mech.*, 537:91–100, 2005.
- [194] J. M. Hamilton, J. Kim, and F. Waleffe. Regeneration mechanisms of near-wall turbulence structures. *J. Fluid Mech.*, 287:317–348, 1995.
- [195] F. Waleffe. On a self-sustaining process in shear flows. *Phys. Fluids*, 9(4):883–900, 1997.
- [196] W. C. Reynolds and W. G. Tiederman. Stability of turbulent channel flow with application to Malkus’s theory. *J. Fluid Mech.*, 27(2):253–272, 1967.
- [197] W. C. Reynolds and A. K. M. F. Hussain. The mechanics of an organized wave in turbulent shear flow. Part 3. Theoretical models and comparisons with experiments. *J. Fluid Mech.*, 54(2):263–288, 1972.
- [198] J. C. Del Álamo and J. Jiménez. Linear energy amplification in turbulent channels. *J. Fluid Mech.*, 559:205–213, 2006.
- [199] C. Cossu, G. Pujals, and S. Depardon. Optimal transient growth and very large-scale structures in turbulent boundary layers. *J. Fluid Mech.*, 619:79–94, 2009.

- [200] G. Pujals, M. García-Villalba, C. Cossu, and S. Depardon. A note on optimal transient growth in turbulent channel flows. *Phys. Fluids*, 21(1):015109, 2009.
- [201] B. J. McKeon and A. S. Sharma. A critical-layer framework for turbulent pipe flow. *J. Fluid Mech.*, 658:336–382, 2010.
- [202] B. J. McKeon, A. S. Sharma, and I. Jacobi. Experimental manipulation of wall turbulence: A systems approach. *Phys. Fluids*, 25(3):031301, 2013.
- [203] A. S. Sharma and B. J. McKeon. On coherent structure in wall turbulence. *J. Fluid Mech.*, 728:196–238, 2013.
- [204] R. Moarref, A. S. Sharma, J. A. Tropp, and B. J. McKeon. Model-based scaling of the streamwise energy density in high-Reynolds-number turbulent channels. *J. Fluid Mech.*, 734:275–316, 2013.
- [205] R. Moarref, M. R. Jovanović, J. A. Tropp, A. S. Sharma, and B. J. McKeon. A low-order decomposition of turbulent channel flow via resolvent analysis and convex optimization. *Phys. Fluids*, 26(5):051701, May 2014.
- [206] W. D. McComb. *The Physics of Fluid Turbulence*. Oxford Univ. Press, 1991.
- [207] P. A. Durbin and B. A. Petterson-Reif. *Theory and modeling of turbulent flows*. Wiley, 2000.
- [208] R. H. Kraichnan. The structure of isotropic turbulence at very high Reynolds numbers. *J. Fluid Mech.*, 5(04):497–543, 1959.
- [209] R. H. Kraichnan. An almost-Markovian Galilean-invariant turbulence model. *J. Fluid Mech.*, 47(03):513–524, 1971.
- [210] S. A. Orszag. Analytical theories of turbulence. *J. Fluid Mech.*, 41(02):363–386, 1970.
- [211] A. S. Monin and A. M. Yaglom. *Statistical Fluid Mechanics*, volume 2. MIT Press, 1975.
- [212] B. F. Farrell and P. J. Ioannou. Stochastic dynamics of baroclinic waves. *J. Atmos. Sci.*, 50(24):4044–4057, 1993.
- [213] B. F. Farrell and P. J. Ioannou. A theory for the statistical equilibrium energy spectrum and heat flux produced by transient baroclinic waves. *J. Atmos. Sci.*, 51(19):2685–2698, 1994.
- [214] B. F. Farrell and P. J. Ioannou. Stochastic dynamics of the midlatitude atmospheric jet. *J. Atmos. Sci.*, 52(10):1642–1656, 1995.

- [215] T. DelSole and B. F. Farrell. A stochastically excited linear system as a model for quasigeostrophic turbulence: Analytic results for one-and two-layer fluids. *J. Atmos. Sci.*, 52(14):2531–2547, 1995.
- [216] T. DelSole and B. F. Farrell. The quasi-linear equilibration of a thermally maintained, stochastically excited jet in a quasigeostrophic model. *J. Atmos. Sci.*, 53(13):1781–1797, 1996.
- [217] T. DelSole. Can quasigeostrophic turbulence be modeled stochastically? *J. Atmos. Sci.*, 53(11):1617–1633, 1996.
- [218] A. J. Majda, I. Timofeyev, and E. V. Eijnden. Models for stochastic climate prediction. *Proc. Natl. Acad. Sci.*, 96(26):14687–14691, 1999.
- [219] A. J. Majda, I. Timofeyev, and E. V. Eijnden. A mathematical framework for stochastic climate models. *Commun. Pure Appl. Math.*, 54:891–974, 2001.
- [220] T. DelSole. A fundamental limitation of Markov models. *J. Atmos. Sci.*, 57(13):2158–2168, 2000.
- [221] T. DelSole. Stochastic models of quasigeostrophic turbulence. *Surv. Geophys.*, 25(2):107–149, 2004.
- [222] J. Hoepffner. Modeling flow statistics using convex optimization. In *Proceedings of the 2005 European Control Conference and the 44th IEEE Conference on Decision and Control*, pages 4287–4292, 2005.
- [223] R. Moarref. *Model-based control of transitional and turbulent wall-bounded shear flows*. PhD thesis, University of Minnesota, 2012.
- [224] B. F. Farrell and P. J. Ioannou. Structural stability of turbulent jets. *J. Atmos. Sci.*, 60(17):2101–2118, 2003.
- [225] B. F. Farrell and P. J. Ioannou. Structure and spacing of jets in barotropic turbulence. *J. Atmos. Sci.*, 64(10):3652–3665, 2007.
- [226] N. A. Bakas and P. J. Ioannou. Structural stability theory of two-dimensional fluid flow under stochastic forcing. *J. Fluid Mech.*, 682:332–361, 2011.
- [227] N. C. Constantinou, B. F. Farrell, and P. J. Ioannou. Emergence and equilibration of jets in beta-plane turbulence: applications of Stochastic Structural Stability Theory. *J. Atmos. Sci.*, 71(5):1818–1842, 2014.
- [228] N. A. Bakas and P. J. Ioannou. A theory for the emergence of coherent structures in beta-plane turbulence. *J. Fluid Mech.*, 740:312–341, 2014.
- [229] B. F. Farrell and P. J. Ioannou. Dynamics of streamwise rolls and streaks in turbulent wall-bounded shear flow. *J. Fluid Mech.*, 708:149–196, 2012.

- [230] V. L. Thomas, B. K. Lieu, M. R. Jovanović, B. F. Farrell, P. J. Ioannou, and D. F. Gayme. Self-sustaining turbulence in a restricted nonlinear model of plane couette flow. *Phys. Fluids*, 26(10):105112, 2014.
- [231] N. C. Constantinou, A. Lozano-Durán, M.-A. Nikolaidis, B. F. Farrell, P. J. Ioannou, and J. Jiménez. Turbulence in the highly restricted dynamics of a closure at second order: comparison with DNS. *J. Phys.: Conf. Ser.*, 506:012004, 2014.
- [232] J. U. Bretheim, C. Meneveau, and D. F. Gayme. Standard logarithmic mean velocity distribution in a band-limited restricted nonlinear model of turbulent flow in a half-channel. *Phys. Fluids*, 27(1):011702, 2015.
- [233] V. L. Thomas, B. F. Farrell, P. J. Ioannou, and D. F. Gayme. A minimal model of self-sustaining turbulence. *Phys. Fluids*, 27(10):105104, 2015.
- [234] J. Kim, P. Moin, and R. Moser. Turbulence statistics in fully developed channel flow at low Reynolds number. *J. Fluid Mech.*, 177:133–166, 1987.
- [235] R. D. Moser, J. Kim, and N. N. Mansour. DNS of turbulent channel flow up to  $Re_\tau = 590$ . *Phys. Fluids*, 11(4):943–945, 1999.
- [236] J. C. Del Álamo and J. Jiménez. Spectra of the very large anisotropic scales in turbulent channels. *Phys. Fluids*, 15(6):41–44, 2003.
- [237] J. C. Del Álamo, J. Jiménez, P. Zandonade, and R. D. Moser. Scaling of the energy spectra of turbulent channels. *J. Fluid Mech.*, 500(1):135–144, 2004.
- [238] S. Hoyas and J. Jiménez. Scaling of the velocity fluctuations in turbulent channels up to  $Re_\tau = 2003$ . *Phys. Fluids*, 18(1):011702, 2006.
- [239] P. J. Schmid and D. S. Henningson. *Stability and Transition in Shear Flows*. Springer-Verlag, New York, 2001.
- [240] J. A. C. Weideman and S. C. Reddy. A MATLAB differentiation matrix suite. *ACM Trans. Math. Software*, 26(4):465–519, 2000.
- [241] P. Moin and R. D. Moser. Characteristic-eddy decomposition of turbulence in a channel. *J. Fluid Mech.*, 200(41):509, 1989.
- [242] H. Kwakernaak and R. Sivan. *Linear optimal control systems*. Wiley-Interscience, 1972.
- [243] G. C. Goodwin and R. L. Payne. *Dynamic system identification: experiment design and data analysis*. Academic press, 1977.
- [244] A. Zare, M. R. Jovanović, and T. T. Georgiou. Perturbation of system dynamics and the covariance completion problem. In *Proceedings of the 55th IEEE Conference on Decision and Control*, pages 7036–7041, 2016.

- [245] W. V. R. Malkus. Outline of a theory of turbulent shear flow. *J. Fluid Mech.*, 1(5):521–539, 1956.
- [246] J. P. Monty, J. A. Stewart, R. C. Williams, and M. S. Chong. Large-scale features in turbulent pipe and channel flows. *J. Fluid Mech.*, 589:147–156, 2007.
- [247] S. J. Kline, W. C. Reynolds, F. A. Schraub, and P. W. Runstadler. The structure of turbulent boundary layers. *J. Fluid Mech.*, 30(04):741–773, 1967.
- [248] C. R. Smith and S. P. Metzler. The characteristics of low-speed streaks in the near-wall region of a turbulent boundary layer. *J. Fluid Mech.*, 129:27–54, 1983.
- [249] S. C. Reddy, P. J. Schmid, and D. S. Henningson. Pseudospectra of the Orr-Sommerfeld operator. *SIAM J. Appl. Math.*, 53(1):15–47, 1993.
- [250] K. Zhou, J. C. Doyle, and K. Glover. *Robust and Optimal Control*. Prentice Hall, 1996.
- [251] G. I. Taylor. The spectrum of turbulence. In *Proc. R. Soc. Lond. A*, volume 164, pages 476–490, 1938.
- [252] J. P. Monty and M. S. Chong. Turbulent channel flow: comparison of streamwise velocity data from experiments and direct numerical simulation. *J. Fluid Mech.*, 633:461–474, 2009.
- [253] J. LeHew, M. Guala, and B. J. McKeon. A study of the three-dimensional spectral energy distribution in a zero pressure gradient turbulent boundary layer. *Exp. Fluids*, 51(4):997–1012, 2011.
- [254] J. Kim and F. Hussain. Propagation velocity of perturbations in turbulent channel flow. *Phys. Fluids A*, 5(3):695–706, 1993.
- [255] J. C. Del Álamo and J. Jiménez. Estimation of turbulent convection velocities and corrections to Taylor’s approximation. *J. Fluid Mech.*, 640:5–26, 2009.
- [256] N. Hutchins and I. Marusic. Evidence of very long meandering features in the logarithmic region of turbulent boundary layers. *J. Fluid Mech.*, 579:1–28, 2007.
- [257] J.P. Monty, N. Hutchins, H. C. H. Ng, I. Marusic, and M. S. Chong. A comparison of turbulent pipe, channel and boundary layer flows. *J. Fluid Mech.*, 632:431–442, 2009.
- [258] I. Marusic, J. P. Monty, M. Hultmark, and A. J. Smits. On the logarithmic region in wall turbulence. *J. Fluid Mech.*, 716:R3, 2013.
- [259] U. Ehrenstein and F. Gallaire. On two-dimensional temporal modes in spatially evolving open flows: the flat-plate boundary layer. *J. Fluid Mech.*, 536:209–218, 2005.

- [260] E. Åkervik, U. Ehrenstein, F. Gallaire, and D. S. Henningson. Global two-dimensional stability measures of the flat plate boundary-layer flow. *Eur. J. Mech. B*, 27(5):501–513, 2008.
- [261] G. P. Paredes. *Advances in global instability computations: from incompressible to hypersonic flow*. PhD thesis, Technical University of Madrid, 2014.
- [262] A. Monokrousos, E. Åkervik, L. Brandt, and D. S. Henningson. Global three-dimensional optimal disturbances in the blasius boundary-layer flow using time-steppers. *J. Fluid Mech.*, 650:181–214, 2010.
- [263] M. J. P. Hack and P. Moin. Towards modeling boundary layer transition in large-eddy simulations. In *Annual Research Briefs*, pages 137–144, Center for Turbulence Research, Stanford University, 2015.
- [264] F. P. Bertolotti, T. Herbert, and P. R. Spalart. Linear and nonlinear stability of the Blasius boundary layer. *J. Fluid Mech.*, 242:441–474, 1992.
- [265] T. Herbert. Parabolized stability equations. In *Special Course on Progress in Transition Modelling*, chapter 4, pages 1–34. AGARD Rep., 1994. No. 793.
- [266] T. Herbert. Parabolized stability equations. *Annu. Rev. Fluid Mech.*, 29(1):245–283, 1997.
- [267] P. Andersson, M. Berggren, and D. S. Henningson. Optimal disturbances and bypass transition in boundary layers. *Phys. Fluids*, 11(1):134–150, 1999.
- [268] A. Tumin and E. Reshokto. Spatial theory of optimal disturbances in boundary layers. *Phys. Fluids*, 13:2097–2104, 2001.
- [269] J. W. Nichols and S. K. Lele. Global modes and transient response of a cold supersonic jet. *J. Fluid Mech.*, 669:225–241, 2011.
- [270] A. Mani. Analysis and optimization of numerical sponge layers as a nonreflective boundary treatment. *J. Comput. Phys.*, 231(2):704–716, 2012.
- [271] A. Towne. *Advancements in jet turbulence and noise modeling: accurate one-way solutions and empirical evaluation of the nonlinear forcing of wavepackets*. PhD thesis, California Institute of Technology, 2016.
- [272] S. J. Leib and M. E. Goldstein. Hybrid source model for predicting high-speed jet noise. *AIAA J.*, 49(7):1324–1335, 2011.
- [273] J. R. Kreitzman and J. W. Nichols. Acoustic source analysis of a supersonic rectangular chevron jet. In *21st AIAA/CEAS Aeroacoustics Conference*, page 2838, 2015.

- [274] J. C. H. Fung, J. C. R. Hunt, N. A. Malik, and R. J. Perkins. Kinematic simulation of homogeneous turbulence by unsteady random Fourier modes. *J. Fluid Mech.*, 236:281–318, 1992.
- [275] F. W. Elliott and A. J. Majda. Pair dispersion over an inertial range spanning many decades. *Phys. Fluids*, 8(4):1052–1060, 1996.
- [276] N. A. Malik and J. C. Vassilicos. A Lagrangian model for turbulent dispersion with turbulent-like flow structure: Comparison with direct numerical simulation for two-particle statistics. *Phys. Fluids*, 11(6):1572–1580, 1999.
- [277] J. C. H. Fung and J. C. Vassilicos. Two-particle dispersion in turbulent-like flows. *Phys. Rev. E*, 57(2):1677–1690, 1998.
- [278] C. Cambon, F. S. Godeferd, F. C. G. A. Nicolleau, and J. C. Vassilicos. Turbulent diffusion in rapidly rotating flows with and without stable stratification. *J. Fluid Mech.*, 499:231–255, 2004.
- [279] N. R. Clark and J. C. Vassilicos. Kinematic simulation of fully developed turbulent channel flow. *Flow, Turbul. Combust.*, 86(2):263–293, 2011.
- [280] A. Keating, U. Piomelli, E. Balaras, and H.-J. Kaltenbach. A priori and a posteriori tests of inflow conditions for large-eddy simulation. *Phys. Fluids*, 16(12):4696–4712, 2004.
- [281] J. Höpfner, Y. Naka, and K. Fukagata. Realizing turbulent statistics. *J. Fluid Mech.*, 676:54–80, 2011.
- [282] N. Hutchins and I. Marusic. Evidence of very long meandering features in the logarithmic region of turbulent boundary layers. *J. Fluid Mech.*, 579:1–28, 2007.
- [283] R. Mathis, N. Hutchins, and I. Marusic. Large-scale amplitude modulation of the small-scale structures in turbulent boundary layers. *J. Fluid Mech.*, 628:311–337, 2009.
- [284] M. Guala, M. Metzger, and B. J. McKeon. Interactions within the turbulent boundary layer at high Reynolds number. *J. Fluid Mech.*, 666:573–604, 2011.
- [285] X. Wu and P. Moin. Direct numerical simulation of turbulence in a nominally zero-pressure-gradient flat-plate boundary layer. *J. Fluid Mech.*, 630:5–41, 2009.
- [286] P. Schlatter and R. Örlü. Assessment of direct numerical simulation data of turbulent boundary layers. *J. Fluid Mech.*, 659:116–126, 2010.
- [287] J. A. Sillero, J. Jiménez, and R. D. Moser. One-point statistics for turbulent wall-bounded flows at Reynolds numbers up to  $\delta^+ \approx 2000$ . *Phys. Fluids*, 25:105102, 2013.

- [288] J. A. Sillero, J. Jiménez, and R. D. Moser. Two-point statistics for turbulent boundary layers and channels at Reynolds numbers up to  $\delta^+ \approx 2000$ . *Phys. Fluids*, 26:105109, 2014.
- [289] H. L. Reed, W. S. Saric, and D. Arnal. Linear stability theory applied to boundary layers. *Annu. Rev. Fluid Mech.*, 28(1):389–428, 1996.
- [290] M. Högberg and D. S. Henningson. Linear optimal control applied to instabilities in spatially developing boundary layers. *J. Fluid Mech.*, 470:151–179, 2002.
- [291] M. Quadrio and P. Ricco. Critical assessment of turbulent drag reduction through spanwise wall oscillations. *J. Fluid Mech.*, 521:251–271, 2004.
- [292] T. Min, S. M. Kang, J. L. Speyer, and J. Kim. Sustained sub-laminar drag in a fully developed channel flow. *J. Fluid Mech.*, 558:309–318, 2006.
- [293] J. Höpfner and K. Fukagata. Pumping or drag reduction? *J. Fluid Mech.*, 635:171–187, 2009.
- [294] R. D. Cess. A survey of the literature on heat transfer in turbulent tube flow. *Westinghouse Research, Rep. 8-0529-R24*, 1958.
- [295] M. Fardad, M. R. Jovanović, and B. Bamieh. Frequency analysis and norms of distributed spatially periodic systems. *IEEE Trans. Automat. Control*, 53(10):2266–2279, November 2008.
- [296] M. Fardad and B. Bamieh. Perturbation methods in stability and norm analysis of spatially periodic systems. *SIAM J. Control Optim.*, 47:997–1021, 2008.
- [297] W. J. Jung, N. Mangiavacchi, and R. Akhavan. Suppression of turbulence in wall-bounded flows by high-frequency spanwise oscillations. *Phys. Fluids A*, 4(8):1605–1607, 1992.
- [298] F. Laadhari, L. Skandaji, and R. Morel. Turbulence reduction in a boundary layer by a local spanwise oscillating surface. *Phys. Fluids*, 6(10):3218–3220, 1994.
- [299] K.-S. Choi, J.-R. DeBisschop, and B. R. Clayton. Turbulent boundary-layer control by means of spanwise-wall oscillation. *AIAA J.*, 36(7):1157–1163, 1998.
- [300] K.-S. Choi. Near-wall structure of turbulent boundary layer with spanwise-wall oscillation. *Phys. Fluids*, 14(7):2530–2542, 2002.
- [301] P. Ricco. Modification of near-wall turbulence due to spanwise wall oscillations. *J. Turbul.*, 5:20–20, 2004.
- [302] J.-I. Choi, C.-X. Xu, and H. J. Sung. Drag reduction by spanwise wall oscillation in wall-bounded turbulent flows. *AIAA J.*, 40(5):842–850, 2002.

- [303] P. Ricco and M. Quadrio. Wall-oscillation conditions for drag reduction in turbulent channel flow. *Int. J. Heat Fluid Flow*, 29(4):891–902, 2008.
- [304] E. Touber and M. A. Leschziner. Near-wall streak modification by spanwise oscillatory wall motion and drag-reduction mechanisms. *J. Fluid Mech.*, 693:150–200, 2012.
- [305] R. L. Panton. *Incompressible flows*. John Wiley & Sons, Inc., New York, 1996.
- [306] M. R. Jovanović and M. Fardad.  $H_2$  norm of linear time-periodic systems: a perturbation analysis. *Automatica*, 44(8):2090–2098, 2008.
- [307] M. Lee and R. D. Moser. Direct numerical simulation of turbulent channel flow up to  $Re_\tau = 5200$ . *J. Fluid Mech.*, 774:395–415, 2015.
- [308] M. V. Zagarola and A. J. Smits. Mean-flow scaling of turbulent pipe flow. *J. Fluid Mech.*, 373:33–79, 1998.
- [309] J. C. Klewicki, J. F. Foss, and J. M. Wallace. High Reynolds number [ $R_\theta = O(10^6)$ ] boundary layer turbulence in the atmospheric surface layer above Western Utah’s salt flats. In *Flow at Ultra-High Reynolds and Rayleigh Numbers*, pages 450–466. Springer, 1998.
- [310] J. M. Österlund. *Experimental studies of zero pressure-gradient turbulent boundary layer flow*. PhD thesis, Royal Institute of Technology, Department of Mechanics, 1999.
- [311] D. B. DeGraaff and J. K. Eaton. Reynolds-number scaling of the flat-plate turbulent boundary layer. *J. Fluid Mech.*, 422:319–346, 2000.
- [312] J. Carlier and M. Stanislas. Experimental study of eddy structures in a turbulent boundary layer using particle image velocimetry. *J. Fluid Mech.*, 535(36):143–188, 2005.
- [313] T. B. Nickels, I. Marusic, S. Hafez, and M. S. Chong. Evidence of the  $k_t^{-1}$  law in a high-Reynolds-number turbulent boundary layer. *Phys. Rev. Lett.*, 95(7):074501, 2005.
- [314] H. M. Nagib, K. A. Chauhan, and P. A. Monkewitz. Approach to an asymptotic state for zero pressure gradient turbulent boundary layers. *Philos. Trans. Roy. Soc. Lond. A*, 365(1852):755–770, 2007.
- [315] I. Marusic, R. Mathis, and N. Hutchins. High Reynolds number effects in wall turbulence. *Intl J. Heat Fluid Flow*, 31(3):418–428, 2010.
- [316] M. P. Schultz and K. A. Flack. Reynolds-number scaling of turbulent channel flow. *Phys. Fluids*, 25:025104, 2013.

- [317] P. Ricco and S. Wu. On the effects of lateral wall oscillations on a turbulent boundary layer. *Exper. Therm. Fluid Sc.*, 29(1):41–52, 2004.
- [318] S. S. Joshi, J. L. Speyer, and J. Kim. A systems theory approach to the feedback stabilization of infinitesimal and finite-amplitude disturbances in plane Poiseuille flow. *J. Fluid Mech.*, 332:157–184, 1997.
- [319] L. Cortelezzi and J. L. Speyer. Robust reduced-order controller of laminar boundary layer transitions. *Phys. Rev. E*, 58(2):1906–1910, 1998.
- [320] T. R. Bewley and S. Liu. Optimal and robust control and estimation of linear paths to transition. *J. Fluid Mech.*, 365:305–349, 1998.
- [321] K. H. Lee, L. Cortelezzi, J. Kim, and J. Speyer. Application of reduced-order controller to turbulent flows for drag reduction. *Phys. Fluids*, 13(5):1321–1330, 2001.
- [322] M. Högberg, T. R. Bewley, and D. S. Henningson. Linear feedback control and estimation of transition in plane channel flow. *J. Fluid Mech.*, 481:149–175, 2003.
- [323] M. Högberg, T. R. Bewley, and D. S. Henningson. Relaminarization of  $Re_\tau = 100$  turbulence using linear state-feedback control. *Phys. Fluids*, 15(11):3572–3575, 2003.
- [324] J. H. M. Fransson, A. Talamelli, L. Brandt, and C. Cossu. Delaying transition to turbulence by a passive mechanism. *Phys. Rev. Lett.*, 96(6):064501, 2006.
- [325] J. Hoepffner, M. Chevalier, T. R. Bewley, and D. S. Henningson. State estimation in wall-bounded flow systems. Part 1. Perturbed laminar flows. *J. Fluid Mech.*, 534:263–294, 2005.
- [326] M. Chevalier, J. Hoepffner, T. R. Bewley, and D. S. Henningson. State estimation in wall-bounded flow systems. Part 2. Turbulent flows. *J. Fluid Mech.*, 552:167–187, 2006.
- [327] M. Quadrio and S. Sibilla. Numerical simulation of turbulent flow in a pipe oscillating around its axis. *J. Fluid Mech.*, 424:217–241, 2000.
- [328] A. Baron and M. Quadrio. Turbulent drag reduction by spanwise wall oscillations. *Appl. Sci. Res.*, 55(4):311–326, 1996.
- [329] M. Quadrio and P. Ricco. Initial response of a turbulent channel flow to spanwise oscillation of the walls. *J. Turbul.*, 4(7):1–23, 2003.
- [330] M. Quadrio. Drag reduction in turbulent boundary layers by in-plane wall motion. *Phil. Trans. R. Soc. Lond. A*, 369(1940):1428–1442, 2011.

- [331] R. T. Rockafellar. Monotone operators and the proximal point algorithm. *SIAM J. Control Optim.*, 14(5):877–898, 1976.

# Appendix A

## A.1 Proof of Lemma 1

Without loss of generality, let us consider  $Z$  of the following form (see Section 2.3.2 for further justification)

$$Z = 2 \begin{bmatrix} I_\pi & 0 & 0 \\ 0 & -I_\nu & 0 \\ 0 & 0 & 0 \end{bmatrix}. \quad (\text{A.1})$$

Given any  $S$  that satisfies  $Z = S + S^*$  we can decompose it into

$$S = M + N$$

with  $M$  Hermitian and  $N$  skew-Hermitian. It is easy to see that

$$M = \frac{1}{2} Z = \begin{bmatrix} I_\pi & 0 & 0 \\ 0 & -I_\nu & 0 \\ 0 & 0 & 0 \end{bmatrix}.$$

By partitioning  $N$  as

$$N = \begin{bmatrix} N_{11} & N_{12} & N_{13} \\ N_{21} & N_{22} & N_{23} \\ N_{31} & N_{32} & N_{33} \end{bmatrix},$$

we have

$$S = \begin{bmatrix} I_\pi + N_{11} & N_{12} & N_{13} \\ N_{21} & -I_\nu + N_{22} & N_{23} \\ N_{31} & N_{32} & N_{33} \end{bmatrix}.$$

Clearly,

$$\text{rank}(S) \geq \text{rank}(I_\pi + N_{11}).$$

Since  $N_{11}$  is skew-Hermitian, all its eigenvalues are on the imaginary axis. This implies that all the eigenvalues of  $I_\pi + N_{11}$  have real part 1 and therefore  $I_\pi + N_{11}$  is a full rank matrix. Hence, we have

$$\text{rank}(S) \geq \text{rank}(I_\pi + N_{11}) = \pi(Z)$$

which completes the proof.

## A.2 Proof of Proposition 2

The inequality

$$\min\{\text{rank}(S) \mid Z = S + S^*\} \geq \max\{\pi(Z), \nu(Z)\}$$

follows from Lemma 1. To establish the proposition we need to show that the bounds are tight, i.e.,

$$\min\{\text{rank}(S) \mid Z = S + S^*\} \leq \max\{\pi(Z), \nu(Z)\}.$$

Given  $Z$  in (A.1), for  $\pi(Z) \leq \nu(Z)$ ,  $Z$  can be written as

$$Z = 2 \begin{bmatrix} I_\pi & 0 & 0 & 0 \\ 0 & -I_\pi & 0 & 0 \\ 0 & 0 & -I_{\nu-\pi} & 0 \\ 0 & 0 & 0 & 0 \end{bmatrix}.$$

By selecting  $S$  in the form (2.15) we conclude that

$$\begin{aligned} \text{rank}(S) &= \text{rank}\left(\begin{bmatrix} I_\pi & -I_\pi \\ I_\pi & -I_\pi \end{bmatrix}\right) + \text{rank}(-I_{\nu-\pi}) \\ &= \pi(Z) + \nu(Z) - \pi(Z) = \nu(Z). \end{aligned}$$

Therefore

$$\min\{\text{rank}(S) \mid Z = S + S^*\} \leq \nu(Z).$$

Similarly, for the case  $\pi(Z) > \nu(Z)$ ,

$$\min\{\text{rank}(S) \mid Z = S + S^*\} \leq \pi(Z).$$

Hence,

$$\min\{\text{rank}(S) \mid Z = S + S^*\} \leq \max\{\pi(Z), \nu(Z)\}$$

which completes the proof.

### A.3 Proof of Lemma 2

The second-order approximation of  $\log \det \mathcal{A}^\dagger(Y)$  yields

$$\begin{aligned} \log \det \mathcal{A}^\dagger(Y + \Delta Y) &= \log \det \mathcal{A}^\dagger(Y) + \text{trace}(\mathcal{A}^\dagger(Y)^{-1} \mathcal{A}^\dagger(\Delta Y)) - \\ &\quad \frac{1}{2} \text{trace}(\mathcal{A}^\dagger(Y)^{-1} \mathcal{A}^\dagger(\Delta Y) \mathcal{A}^\dagger(Y)^{-1} \mathcal{A}^\dagger(\Delta Y)) + O(\|\Delta Y\|_F^2). \end{aligned}$$

To show Lipschitz continuity of the gradient it is sufficient to show that the approximation to the Hessian is bounded by the Lipschitz constant  $L$ , i.e.,

$$\text{trace}(\mathcal{A}^\dagger(Y)^{-1} \mathcal{A}^\dagger(\Delta Y) \mathcal{A}^\dagger(Y)^{-1} \mathcal{A}^\dagger(\Delta Y)) \leq L \|\Delta Y\|_F^2.$$

From the left-hand-side we have

$$\begin{aligned} \text{trace}(\mathcal{A}^\dagger(Y)^{-1} \mathcal{A}^\dagger(\Delta Y) \mathcal{A}^\dagger(Y)^{-1} \mathcal{A}^\dagger(\Delta Y)) &= \text{trace}\left(\mathcal{A}^\dagger(Y)^{-\frac{1}{2}} \mathcal{A}^\dagger(\Delta Y) \mathcal{A}^\dagger(Y)^{-1} \mathcal{A}^\dagger(\Delta Y) \mathcal{A}^\dagger(Y)^{-\frac{1}{2}}\right) \\ &\leq \frac{1}{\alpha} \text{trace}\left(\mathcal{A}^\dagger(Y)^{-\frac{1}{2}} \mathcal{A}^\dagger(\Delta Y) \mathcal{A}^\dagger(\Delta Y) \mathcal{A}^\dagger(Y)^{-\frac{1}{2}}\right) \\ &= \frac{1}{\alpha} \text{trace}(\mathcal{A}^\dagger(\Delta Y) \mathcal{A}^\dagger(Y)^{-1} \mathcal{A}^\dagger(\Delta Y)) \\ &\leq \frac{1}{\alpha^2} \text{trace}(\mathcal{A}^\dagger(\Delta Y) \mathcal{A}^\dagger(\Delta Y)) \\ &\leq \frac{\sigma_{\max}^2(\mathcal{A}^\dagger)}{\alpha^2} \|\Delta Y\|_F^2. \end{aligned}$$

Here, we have utilized the fact that  $\mathcal{A}^\dagger(Y)^{-1}$  is a positive-definite matrix and that  $Y \in \mathcal{D}_{\alpha\beta}$ . This completes the proof.

### A.4 Proof of Lemma 3

We begin by substituting the expressions for  $Y_1^+$ ,  $Y_2^+$ ,  $\bar{Y}_1$ , and  $\bar{Y}_2$ . Utilizing the non-expansive property of the proximal operator  $\mathcal{T}_\gamma$  [331] we have

$$\begin{aligned} \|Y_1^+ - \bar{Y}_1\|_F &= \|\mathcal{T}_\gamma(Y_1 + \rho \mathcal{A}_1(\mathcal{A}^\dagger(Y_1, Y_2)^{-1})) - \mathcal{T}_\gamma(\bar{Y}_1 + \rho \mathcal{A}_1(\mathcal{A}^\dagger(\bar{Y}_1, \bar{Y}_2)^{-1}))\|_F \\ &\leq \|Y_1 + \rho \mathcal{A}_1(\mathcal{A}^\dagger(Y_1, Y_2)^{-1}) - \bar{Y}_1 - \rho \mathcal{A}_1(\mathcal{A}^\dagger(\bar{Y}_1, \bar{Y}_2)^{-1})\|_F \\ \|Y_2^+ - \bar{Y}_2\|_F &= \|Y_2 + \rho(\mathcal{A}_2(\mathcal{A}^\dagger(Y_1, Y_2)^{-1}) - G) - \\ &\quad \bar{Y}_2 - \rho(\mathcal{A}_2(\mathcal{A}^\dagger(\bar{Y}_1, \bar{Y}_2)^{-1}) - G)\|_F, \end{aligned}$$

from which we obtain

$$\|Y^+ - \bar{Y}\|_F \leq \|h_\rho(Y) - h_\rho(\bar{Y})\|_F,$$

where

$$h_\rho(Y) = Y + \rho \mathcal{A}(\mathcal{A}^\dagger(Y)^{-1}).$$

The first order approximation of the linear map  $h_\rho$  gives

$$h_\rho(Y + \Delta Y) - h_\rho(Y) \approx \Delta Y - \rho \mathcal{A}(\mathcal{A}^\dagger(Y)^{-1} \mathcal{A}^\dagger(\Delta Y) \mathcal{A}^\dagger(Y)^{-1}).$$

From this we conclude that its Jacobian at  $Y$  is  $\leq 1$  if

$$\langle \mathcal{A}(\mathcal{A}^\dagger(Y)^{-1} \mathcal{A}^\dagger(\Delta Y) \mathcal{A}^\dagger(Y)^{-1}), \Delta Y \rangle \geq 0,$$

and the step-size  $0 < \rho \leq \frac{2\alpha^4}{\beta^2 \sigma_{\max}^2(\mathcal{A})}$  satisfies

$$\frac{\rho}{2} \|\mathcal{A}(\mathcal{A}^\dagger(Y)^{-1} \mathcal{A}^\dagger(\Delta Y) \mathcal{A}^\dagger(Y)^{-1})\|_F^2 \leq \langle \mathcal{A}(\mathcal{A}^\dagger(Y)^{-1} \mathcal{A}^\dagger(\Delta Y) \mathcal{A}^\dagger(Y)^{-1}), \Delta Y \rangle$$

for any perturbation  $\Delta Y$ . The former follows from

$$\begin{aligned} & \langle \mathcal{A}^\dagger(Y)^{-1} \mathcal{A}^\dagger(\Delta Y) \mathcal{A}^\dagger(Y)^{-1}, \mathcal{A}^\dagger(\Delta Y) \rangle \\ &= \text{trace}(\mathcal{A}^\dagger(Y)^{-1} \mathcal{A}^\dagger(\Delta Y) \mathcal{A}^\dagger(Y)^{-1} \mathcal{A}^\dagger(\Delta Y)) \\ &= \text{trace}(\mathcal{A}^\dagger(Y)^{-1/2} \mathcal{A}^\dagger(\Delta Y) \mathcal{A}^\dagger(Y)^{-1} \mathcal{A}^\dagger(\Delta Y) \mathcal{A}^\dagger(Y)^{-1/2}), \end{aligned}$$

and the latter follows from

$$\begin{aligned} & \frac{\rho}{2} \|\mathcal{A}(\mathcal{A}^\dagger(Y)^{-1} \mathcal{A}^\dagger(\Delta Y) \mathcal{A}^\dagger(Y)^{-1})\|_F^2 \\ & \leq \frac{\rho \sigma_{\max}^2(\mathcal{A})}{2} \|\mathcal{A}^\dagger(Y)^{-1} \mathcal{A}^\dagger(\Delta Y) \mathcal{A}^\dagger(Y)^{-1}\|_F^2 \\ & \leq \frac{\rho \sigma_{\max}^2(\mathcal{A})}{2\alpha^4} \|\mathcal{A}^\dagger(\Delta Y)\|_F^2 \\ & \leq \frac{\rho \beta^2 \sigma_{\max}^2(\mathcal{A})}{2\alpha^4} \langle \mathcal{A}^\dagger(Y)^{-1} \mathcal{A}^\dagger(\Delta Y) \mathcal{A}^\dagger(Y)^{-1}, \mathcal{A}^\dagger(\Delta Y) \rangle \\ & = \frac{\rho \beta^2 \sigma_{\max}^2(\mathcal{A})}{2\alpha^4} \langle \mathcal{A}(\mathcal{A}^\dagger(Y)^{-1} \mathcal{A}^\dagger(\Delta Y) \mathcal{A}^\dagger(Y)^{-1}), \Delta Y \rangle \\ & \leq \langle \mathcal{A}(\mathcal{A}^\dagger(Y)^{-1} \mathcal{A}^\dagger(\Delta Y) \mathcal{A}^\dagger(Y)^{-1}), \Delta Y \rangle. \end{aligned}$$

Thus, we conclude  $J_{h_\rho}(Y) \leq 1$  for all  $Y \in \mathcal{D}_{\alpha\beta}$ . Finally, from the mean value theorem, we have

$$\begin{aligned} \|Y^+ - \bar{Y}\|_F &\leq \|h_\rho(Y) - h_\rho(\bar{Y})\|_F \\ &\leq \sup_{\delta \in [0,1]} J_{h_\rho}(Y_\delta) \|Y - \bar{Y}\|_F, \\ &\leq \|Y - \bar{Y}\|_F \end{aligned}$$

where  $Y_\delta = \delta Y + (1 - \delta) \bar{Y} \in \mathcal{D}_{\alpha\beta}$ . This completes the proof.

## A.5 Proof of Lemma 4

We first show that

$$\alpha I \preceq \mathcal{A}^\dagger(Y^0) \preceq \beta I.$$

The upper bound follows from

$$\begin{aligned} \|\mathcal{A}^\dagger(Y^0)\|_2 &= \|\mathcal{A}^\dagger(Y^0)\|_2 - \|\mathcal{A}^\dagger(\bar{Y})\|_2 + \|\mathcal{A}^\dagger(\bar{Y})\|_2 \\ &\leq \|\mathcal{A}^\dagger(Y^0) - \mathcal{A}^\dagger(\bar{Y})\|_2 + \|\mathcal{A}^\dagger(\bar{Y})\|_2 \\ &\leq \|\mathcal{A}^\dagger(Y^0) - \mathcal{A}^\dagger(\bar{Y})\|_F + \|\mathcal{A}^\dagger(\bar{Y})\|_2 \\ &\leq \sigma_{\max}(\mathcal{A}^\dagger) \|Y^0 - \bar{Y}\|_F + \|\mathcal{A}^\dagger(\bar{Y})\|_2 = \beta. \end{aligned}$$

To see the lower bound, note that for any  $X \in \mathbb{H}^n$ ,

$$\frac{1}{\sqrt{n}} \|X\|_F \leq \|X\|_2 \leq \|X\|_F. \quad (\text{A.2})$$

Using this property and the dual constraint  $\|Y_1^0\|_2 \leq \gamma$  we have

$$\begin{aligned} \|\mathcal{A}_1^\dagger(Y_1^0)\|_2 &\leq \|\mathcal{A}_1^\dagger(Y_1^0)\|_F \leq \sigma_{\max}(\mathcal{A}_1^\dagger) \|Y_1^0\|_F \\ &\leq \sqrt{n} \sigma_{\max}(\mathcal{A}_1^\dagger) \|Y_1^0\|_2 \leq \gamma \sqrt{n} \sigma_{\max}(\mathcal{A}_1^\dagger). \end{aligned}$$

Since  $\mathcal{A}_1^\dagger(Y_1^0) + \mathcal{A}_2^\dagger(Y_2^0) \succ 0$ , we also have

$$\mathcal{A}_2^\dagger(Y_2^0) \succeq -\gamma \sqrt{n} \sigma_{\max}(\mathcal{A}_1^\dagger) I.$$

Noting  $G = \mathcal{A}_2(\bar{X})$  for the optimal solution  $\bar{X} \succ 0$ , we obtain

$$\langle G, Y_2^0 \rangle = \langle \mathcal{A}_2(\bar{X}), Y_2^0 \rangle = \langle \bar{X}, \mathcal{A}_2^\dagger(Y_2^0) \rangle \geq -\gamma \sqrt{n} \sigma_{\max}(\mathcal{A}_1^\dagger) \text{trace}(\bar{X}). \quad (\text{A.3})$$

Let  $a = \lambda_{\min}(\mathcal{A}^\dagger(Y^0))$ . Since  $\beta$  gives a bound on the largest eigenvalue of  $\mathcal{A}^\dagger(Y^0)$ , we have

$$\log \det \mathcal{A}^\dagger(Y^0) \leq \log(a) + (n-1) \log(\beta)$$

Combining this and

$$\begin{aligned} \log \det \mathcal{A}^\dagger(Y^0) &\geq \log \det \mathcal{A}^\dagger(Y^0) - \langle G, Y_2^0 \rangle + \langle G, Y_2^0 \rangle \\ &\geq \log \det \mathcal{A}^\dagger(Y^0) - \langle G, Y_2^0 \rangle - \gamma \sqrt{n} \sigma_{\max}(\mathcal{A}_1^\dagger) \text{trace}(\bar{X}). \end{aligned}$$

gives  $\lambda_{\min}(\mathcal{A}^\dagger(Y^0)) = a \geq \alpha$ .

The proof of  $\alpha I \preceq \mathcal{A}^\dagger(Y^k) \preceq \beta I$  for  $k > 0$  follows similar lines. We use inductive argument to prove this. Assume that  $\alpha I \preceq \mathcal{A}^\dagger(Y^\ell) \preceq \beta I$  holds for all  $0 \leq \ell \leq k-1$ . For the upper bound, we have

$$\begin{aligned} \|\mathcal{A}^\dagger(Y^k)\|_2 &= \|\mathcal{A}^\dagger(Y^k)\|_2 - \|\mathcal{A}^\dagger(\bar{Y})\|_2 + \|\mathcal{A}^\dagger(\bar{Y})\|_2 \\ &\leq \|\mathcal{A}^\dagger(Y^k) - \mathcal{A}^\dagger(\bar{Y})\|_F + \|\mathcal{A}^\dagger(\bar{Y})\|_2 \\ &\leq \sigma_{\max}(\mathcal{A}^\dagger) \|Y^k - \bar{Y}\|_F + \|\mathcal{A}^\dagger(\bar{Y})\|_2. \end{aligned}$$

By repeatedly applying Lemma 3 for  $\|Y^j - \bar{Y}\|_F \leq \|Y^{j-1} - \bar{Y}\|_F$ , for all  $1 \leq j \leq k$  we have

$$\|\mathcal{A}^\dagger(Y^k)\|_2 \leq \sigma_{\max}(\mathcal{A}^\dagger) \|Y^0 - \bar{Y}\|_F + \|\mathcal{A}^\dagger(\bar{Y})\|_2 = \beta.$$

To see the lower bound, note that (A.3) holds for all  $k \geq 0$ , namely,

$$\langle G, Y_2^k \rangle = \langle \mathcal{A}_2(\bar{X}), Y_2^k \rangle = \langle \bar{X}, \mathcal{A}_2^\dagger(Y_2^k) \rangle \geq -\gamma \sqrt{n} \sigma_{\max}(\mathcal{A}_1^\dagger) \text{trace}(\bar{X}), \quad (\text{A.4})$$

with the same argument. Let  $a = \lambda_{\min}(\mathcal{A}^\dagger(Y^k))$ . Since  $\beta$  gives a bound on the largest eigenvalue of  $\mathcal{A}^\dagger(Y^k)$ , we have

$$\log \det \mathcal{A}^\dagger(Y^k) \leq \log(a) + (n-1) \log(\beta) \quad (\text{A.5})$$

The dual ascent property

$$\log \det \mathcal{A}^\dagger(Y^k) - \langle G, Y_2^k \rangle \geq \log \det \mathcal{A}^\dagger(Y^0) - \langle G, Y_2^0 \rangle,$$

together with inequality (A.4) gives

$$\begin{aligned} \log \det \mathcal{A}^\dagger(Y^k) &\geq \log \det \mathcal{A}^\dagger(Y^0) - \langle G, Y_2^0 \rangle + \langle G, Y_2^k \rangle \\ &\geq \log \det \mathcal{A}^\dagger(Y^0) - \langle G, Y_2^0 \rangle - \gamma \sqrt{n} \sigma_{\max}(\mathcal{A}_1^\dagger) \text{trace}(\bar{X}). \end{aligned} \quad (\text{A.6})$$

From (A.5) and (A.6) we thus have

$$\lambda_{\min}(\mathcal{A}^\dagger(Y^k)) = a \geq \det \mathcal{A}^\dagger(Y^0) \beta^{1-n} e^{-\langle G, Y_2^0 \rangle - \gamma \sqrt{n} \sigma_{\max}(\mathcal{A}_1^\dagger) \operatorname{trace}(\bar{X})} = \alpha,$$

which completes the proof.

# Appendix B

## B.1 Change of coordinates

The kinetic energy of velocity fluctuations in the linearized NS equations (7.5) is determined by,

$$E = \langle \varphi, \varphi \rangle_e = \frac{1}{2} \int_{-1}^1 \varphi^* \mathbf{Q} \varphi \, dy =: \langle \varphi, \mathbf{Q} \varphi \rangle, \quad (\text{B.1})$$

where  $\langle \cdot, \cdot \rangle$  is the standard  $L_2$  inner product and  $\mathbf{Q}$  is the operator that determines energy on the state-space  $\mathbb{H}_{\text{OS}} \times L_2[-1, 1]$  [30, 178]. After wall-normal discretization, the energy norm is determined by  $E = \varphi^* Q \varphi$ , where  $Q$  is the finite-dimensional representation of the operator  $\mathbf{Q}$ .

Since the matrix  $Q$  is positive-definite, the state of the linearized NS equations (7.5) can be transformed into a set of coordinates in which the energy is determined by the standard Euclidean norm, i.e.,  $E = \psi^* \psi$  with  $\psi := Q^{1/2} \varphi$ . Equation (7.6) results from the application of this change of coordinates on the discretized state-space matrices  $\bar{A}$ ,  $\bar{B}$ , and  $\bar{C}$

$$A = Q^{1/2} \bar{A} Q^{-1/2}, \quad B = Q^{1/2} \bar{B} I_W^{-1/2}, \quad C = I_W^{1/2} \bar{C} Q^{-1/2}, \quad (\text{B.2})$$

and the discretized input  $\bar{\mathbf{d}}$  and velocity  $\bar{\mathbf{v}}$  vectors

$$\mathbf{d} = I_W^{1/2} \bar{\mathbf{d}}, \quad \mathbf{v} = I_W^{1/2} \bar{\mathbf{v}}. \quad (\text{B.3})$$

Here,  $I_W$  is a diagonal matrix of integration weights on the set of Chebyshev collocation points. The form of the input and output matrices in (B.3) follows from the definition of their respective energy norms which are given by the standard  $L_2[-1, 1]$  inner product.

## B.2 Interpretation of the matrix $H$ solving (7.12)

From (7.25) we see that the state  $\phi(\mathbf{k}, t)$  of the linear filter (7.20) is

$$\phi(\mathbf{k}, t) = \psi(\mathbf{k}, t) + \chi(\mathbf{k}, t), \quad (\text{B.4})$$

where  $\chi(\mathbf{k}, t)$  represents uncontrollable asymptotically stable modes of the cascade connection of the linearized NS equations and the filter given in (7.24). Thus,  $\chi(\mathbf{k}, t) \rightarrow 0$  as  $t \rightarrow \infty$  and, consequently,

$$\lim_{t \rightarrow \infty} \langle \psi(\mathbf{k}, t) \phi^*(\mathbf{k}, t) \rangle = \lim_{t \rightarrow \infty} \langle \psi(\mathbf{k}, t) \psi^*(\mathbf{k}, t) \rangle = X(\mathbf{k}). \quad (\text{B.5})$$

On the other hand, the cross-correlation between the colored-in-time forcing and the state of the linearized NS equations (7.6) becomes

$$\begin{aligned} \lim_{t \rightarrow \infty} \langle \psi(\mathbf{k}, t) \mathbf{d}^*(\mathbf{k}, t) \rangle &= \lim_{t \rightarrow \infty} \langle \psi(\mathbf{k}, t) (\phi^*(\mathbf{k}, t) C_f^*(\mathbf{k}) + \mathbf{w}^*(\mathbf{k}, t)) \rangle \\ &= X(\mathbf{k}) C_f^*(\mathbf{k}), \end{aligned} \quad (\text{B.6})$$

where we have used the fact that the state  $\psi(\mathbf{k}, t)$  and the white-in-time input  $\mathbf{w}(\mathbf{k}, t)$  are not correlated. From the definition of  $C_f(\mathbf{k})$  in (7.21) we now have

$$H(\mathbf{k}) = \lim_{t \rightarrow \infty} \langle \psi(\mathbf{k}, t) \mathbf{d}^*(\mathbf{k}, t) \rangle + \frac{1}{2} B(\mathbf{k}) \Omega(\mathbf{k}). \quad (\text{B.7})$$

Therefore, the solution  $H(\mathbf{k})$  of (7.12) can be seen to be directly related to the cross-correlation between the forcing  $\mathbf{d}(\mathbf{k}, t)$  and the state  $\psi(\mathbf{k}, t)$ ; see also [121].

## B.3 The role of the regularization parameter $\gamma$

When the true covariance matrices are not known, the regularization parameter  $\gamma$  is typically chosen on an empirical basis or by cross-validation. In fact, the selection of the optimal value of  $\gamma$  is an open theoretical challenge. If the DNS-generated two-point correlation matrix  $\Phi_{\text{dns}}(\mathbf{k})$  is known, we can use the following error criterion:

$$\frac{\|\Phi(\mathbf{k}) - \Phi_{\text{dns}}(\mathbf{k})\|_F}{\|\Phi_{\text{dns}}(\mathbf{k})\|_F} \times 100, \quad (\text{B.8})$$

to assess the quality of approximation.

For turbulent channel flow with  $R_\tau = 186$  and  $\mathbf{k} = (2.5, 7)$ , figure B.1a shows the  $\gamma$  dependence of the above measure. The smallest error is achieved for  $\gamma \approx 300$ . On the

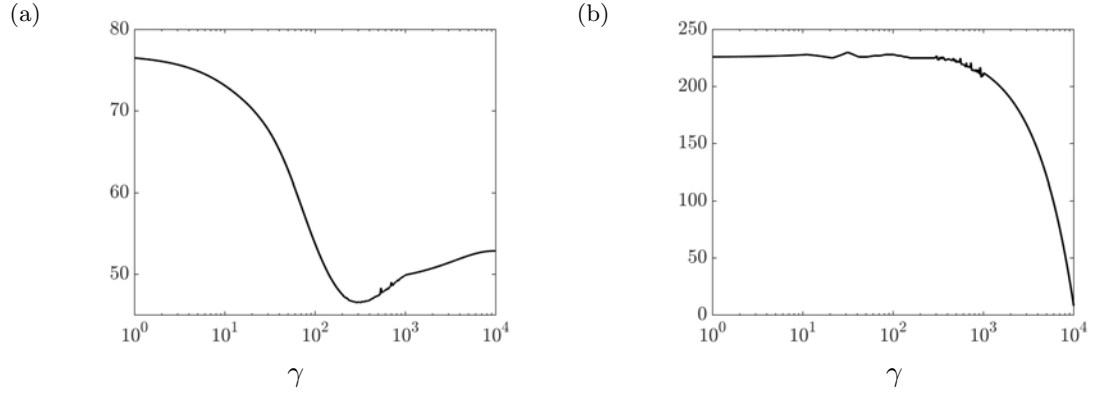


Figure B.1: The  $\gamma$ -dependence of (a) the relative error (B.8); and (b) the rank of the matrix  $Z$  resulting from (7.19) for turbulent channel flow with  $R_\tau = 186$  and  $\mathbf{k} = (2.5, 7)$ .

other hand, figure B.1b shows the  $\gamma$  dependence of the rank of the matrix  $Z$ . Clearly, much larger values of  $\gamma$  are needed to achieve  $Z$  of lower rank.

